Thieno[3,2-*b*]thiophene Based Conjugated Polymers for High Performance Organic Photovoltaic and Field Effect Transistor Applications

Iain Meager

Submitted in partial fulfilment of the requirements for the degree of Doctor of Philosophy in Chemistry

Department of Chemistry, Imperial College London

September 2014

To my parents for their encouragement and support throughout the duration of this work

Acknowledgements

I would first like to thank Prof. Iain McCulloch for providing me with such a fantastic opportunity and for his excellent supervision, motivation and advise over the last three years. I would also like to thank Dr. Hugo Bronstein for helping me adjust to life as a PhD student and for teaching me how to make a polymer.

This PhD would not have been possible without the finances in place to support the research. As such I would like to extend my gratitude to Dr. Henry Leventis and the philanthropic Leventis Foundation whose generous funding allowed me to pursue this great opportunity.

The duration of my PhD has been very enjoyable in large part due to the great people I have worked with. My fellow PhD cohort; Dr Joe Rumer, Daniel Beatrup and Sarah Holliday have been great companions since day one. My fellow group members Dr. Bob Schroeder, Dr. Christian Nielsen, Dr. Raja Shahid Ashraf, Dr. Weimin Zhang, Dr. Laure Biniek, Dr Mindaugas Kirkus, Dr Miquel Planells, Dr Astrid Knall, Dr. David James, Dr. Jenny Donnaghey, Sam Cryer, Michael Hurghangee, Alex Giovannitti, Tibi Sbircea as well as each member of the Martin Heeney group have all made the laboratory a highly enjoyable working environment.

I would also like to thank Dick Sheppard and Pete Haycock for running an efficient NMR service and Dr. Lisa Haigh for her help with mass spectrometry. Finally, I am extremely grateful to Jessica Shaw, Dr. Joe Rumer and Dr. David James for their generous help with proof reading this thesis.

Contributions

Much of the work detailed in this thesis contains collaborative efforts that would not have been possible without the work of a number of people.

All organic solar cell devices reported in this thesis were fabricated at Imperial College London by Dr. Raja Shahid Ashraf (Imperial College London).

Organic field effect transistor devices in Chapter Two were fabricated by Stephen Rossbauer under the supervision of Professor Thomas Anthopoulos (Imperial College London). In Chapter Three by Sonya Mollinger under the supervision of Professor Alberto Salleo (Stanford University) and in Chapter Four by Mark Nikolka under the supervision of Professor Henning Sirringhaus in the Cavendish Laboratory (University of Cambridge).

Atomic force microscopy was performed either by Stephen Rossbauer or Dr. Christian Nielsen (both Imperial College London). X-ray diffraction was performed either by Dr. Miquel Planells, Dr. Christian Nielsen (both Imperial College London), or Sonya Mollinger (Stanford University). Photothermal deflecftion spectroscopy was performed by Aditya Sadhanala (University of Cambridge). Stock laboratory co-monomers used throughout the thesis were synthesised by Dr. Bob Schroeder (Imperial College London). PESA measurements were carried out either by Dr. Scott Watkins (CSIRO, Australia) or Sarah Holliday (Imperial College London).

Declaration

The work described in this thesis was carried out in the laboratory of Professor Iain McCulloch, Department of Chemistry, Imperial College London between October 2011 and September 2014. Unless otherwise stated, the work is my own.

Copyright Declaration

Publications

Much of the work described in this thesis has been published.

The following publications have arisen directly as a result of the work described in this thesis:

1. I. Meager et al. *Macromolecules*, 2013, **46**, 15, 5961-5967.
2. I. Meager et al. *J. Am. Chem. Soc.*, 2013, **135**, 11537-11540.
3. I. Meager et al. *Adv. Funct. Mater.*, 2014.
4. I. Meager et al. *J. Mater. Chem. C.*, 2014, **2**, 8593-8598.
5. R. S. Ashraf, I. Meager et al. *Manuscript in preparation*, 2014.

Patent: Thieno[3,2-*b*]thiophene isoindigo polymers for OFET applications.

The following publications have arisen during the course of my PhD but are not related to the work described in this thesis:

6. H. Bronstein et al. *Adv. Funct. Mater.*, 2013 **23**, 5647-5654.
7. J. Marshall et al. *Macromolecules*, 2013, **47**, 89-96.
8. J. W. Rumer et al. *J. Org. Semiconductors*, 2013, 1, 30-35.
9. J. W. Rumer et al. *Thin solid films*, 2014, 560, 82-85.
10. J. W. Rumer et al. 2014, *Adv. Energy Mater.* Submitted
11. Z. Huang et al. 2014, *J. Mater. Chem. A.*, 2014.

Abstract

The design, synthesis and characterisation of thirteen new semiconducting polymers for use in organic photovoltaic (OPV) and field effect transistor (OFET) devices are reported. The rational design of each polymer is discussed and their structures related to their varying chemical and physical properties, which are further used to rationalise the specific device performances. Various structural modifications are investigated with a focus on the electron-deficient bis-lactam structures diketopyrrolopyrrole (**DPP**) and isoindigo, that are flanked by thieno[3,2-*b*]thiophene donor groups.

Alkyl chain optimisation of thieno[3,2-*b*]thiophene diketopyrrolopyrrole (**DPPTT**) based co-polymers was thoroughly examined and it was found that increased alkyl chain size affords improved solubility and a wider range of accessible co-monomer units. Exploiting this improved solubility, the new **DPPTT-T** polymer was fractionated using recycling gel permeation chromatography (GPC). This gave fractions with increased molecular weights and narrowed mass distributions resulting in OPV power conversion efficiency (PCE) ehancements of greater than 50 %. Continuing with **DPPTT-T** alkyl chains, a new OPV structural design consideration is introduced in which the alkyl chain branching position is systematically moved further from the polymer backbone. This resulted in higher molecular weight polymers with stronger π - π interactions and significantly enhanced device performances due to increased intermolecular interactions, with PCEs in excess of 8 %. Using the new higher performing branched alkyl chains the role of differing chalcogenophene co-monomers OPV devices was also investigated and was found that increased heteroatomic size, from thiophene to selenophene to tellurophene, resulted in narrowed optical band gaps and increased heteroatom – heteroatom interchain interactions. When these differences are taken into consideration, thiophene is shown to be the highest performing chalcogenophene comonomer of the series.

Moving to isoindigo, a new thieno[3,2-*b*]thiophene flanked structure (**iITT**) was designed and synthesised for the first time. The resultant narrow band gap co-polymers were shown to be excellent candidate materials for ambipolar OFET applications. Through a comparative literature and computational study, the new **iITT** unit is shown to be one of the highest performing units within this family of polymer structures.

Contents

List of Figures

Chapter One

Chapter Two

Chapter Three

Chapter Four

Chapter Five

List of Tables

Chapter Two

Chapter Three

Chapter Four

List of Abbreviations

$C_{10}C_{12}$	2-decyl-1-tetradecyl
C_8H_{10}	2-octyl-1-dodecyl
λ_{max}	Absorption maximum
λ_{onset}	Absorption onset
A_{LUMO}	Acceptor LUMO
Å	Angstrom
AFM	Atomic force microscopy
E_g	Band gap
BT	Benzo[*c*][1,2,5] thiadiazole
2T	2,2'-bithiophene
BLA	Bond length alternation
Btu	British thermal units
Calc.	Calculated
C	Celcius
δ	Chemical shift
PhCl	Chlorobenzene
$CHCl_3$	Chloroform
$CDCl_3$	Chloroform-d
J	Coupling constant
J–V curve	Current – voltage curve
CPDT	Cyclopentadithiophene
DFT	Density functional theory
°	Degrees
DCM	Dichloromethane
Et_2O	Diethyl ether
DSC	Differential scanning calorimetry
DPP	Diketopyrrolopyrrole
DMF	Dimethylformamide
D / A	Donor / Acceptor
D_{HOMO}	Donor HOMO
V_D	Drain voltage
EDG	Electron-donating group
EI	Electron ionisation
μ_e	Electron mobility
eV	Electron volts
EWG	Electron-withdrawing group
EtOAc	Ethyl acetate
EQE	External quantum efficiency
FET	Field effect transistor
FF	Fill Factor
p	Fracftional monomer conversion
FWHM	Full width half maximum
V_G	Gate voltage
GPC	Gel permeation chromatography
GIXD	Grazing incidence x-ray diffraction
$(Sn(Me_3))_2$	Hexamethylditin
HOMO	Highest occupied molecular orbital
μ_e	Hole mobility
E_{HOMO}	HOMO energy level
IDT-BT	Indacenodithiophene-co-benzothiadiazole
ITO	Indium tine oxide
J	Joules
kDa	Kilo Dalton
$LiAlH_4$	Lithium aluminium tetrahydride
LiF	Lithium fluoride
LUMO	Lowest unoccupied molecular orbital
E_{LUMO}	LUMO energy level
m/z	Mass to charge
MALDI	Matrix assisted desorption / ionisation
P_{max}	Maximum power output
μ	Micro
μW	Microwave
mg	Miligram
mL	Militre
M_i	Molar mass
M_0	Monomer molar mass
*n*BuLi	*n*-butyl lithium
NMP	*N*-methyl-2-pyrrolidone
nm	nanometer
NMR	Nuclear magnetic resonance
DP_n	Number average degree of polymerisation
M_n	Number average molecular weight
N_i	Number of moles
*o*DCB	*o*-dichlorobenzene
I_{on} / I_{off}	On / off ratio
V_{oc}	Open circuit voltage
OFET	Organic field effect transistor
OPV	Organic photovoltaic
$Pd(Ph_3)_4$	Tetrakis(triphenylphosphine) palladium(0)
ppm	Parts per million
Ph	Phenyl
iIP	Phenyl isoindigo
PC[61]BM	[6,6]-Phenyl C_{61} butyric acid methyl ester
PC[71]BM	[6,6]-Phenyl C_{71} butyric acid methyl ester
PESA	Photoelectron spectroscopy in air
PDS	Photothermal deflection spectroscopy
PV	Photovoltaic
P3HT	Poly(3-hexyl)thiophene
PDI	Polydispersity index
PPV	polyphenylene vinylene
PEDOT : PSS	Poly(3,4-ethylenedioxythiophene)-polystyrene sulfonate
K_2CO_3	Potassium carbonate
K_3PO_4	Potassium phosphate tribasic
PCE	Power conversion efficiency
P_{in}	Power input

rpm	Revolutions per minute	TD	Time dependent
RT	Room temperature	TOF	Time of flight
RMS	Root mean squared	PhMe	Toluene
Se	Selenophene	PPh_3	Triphenylphosphine
J_{sc}	Short circuit current	$Pd_2(dba)_3$	tris(dibenzylideneacetone)di palladium(0)
r	Stoichiometric ratio		
Te	Tellurophene	$P(o\text{-tol})_3$	tri(*o*-tolyl)phosphine
THF	Tetrahydrofuran	λ	Wavelength
DPPTT	Thieno[3,2-*b*]thiophene Diketopyrrolopyrrole	DP_w	Weight average degree of polymerisation
iITT	Thieno[3,2-*b*]thiophene isoindigo	M_w	Weight average molecular weight
TT	Thieno[3,2-*b*]thiophene	w/v	Weight by volume
iIT	Thiophene isoindigo	XRD	X-ray diffraction
V_T	Threshold voltage	ZnO	Zinc oxide

Chapter One

Introduction

1.1. Why Solar?

Our current dependence on fossil fuels is not sustainable. A rapidly increasing global population means that the finite nature of these resources are fast becoming recognised as one of the single most important challenges faced in modern times. United Nations predicts that by 2050 there will be 9.6 billion people on Earth whilst a recent *International Energy Outlook 2013* study estimated that the world's energy consumption will grow by 56 % between 2010 and 2040.[1,2] As shown in **Figure 1.1** this growth in consumption is estimated to be largely originating from developing countries where demand is driven by long-term economic growth and modernisation, with fossil fuels currently making up in the region 80 % of this usage.[3] Considering the natural anaerobic decomposition processes that create fossil fuels take millions of years, it is an inevitability that global fossil fuel resources are soon to be depleted.

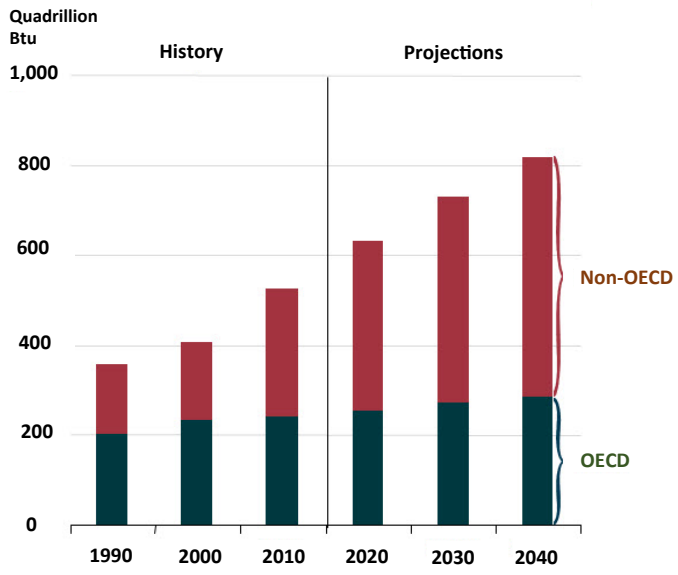

Figure 1.1. World energy consumption and predicted world energy consumption between 1990 and 2040 as estimated in 2013 by *U.S. Energy Information Administration*.[1] Btu = British thermal units (1 Btu ~ 1055 J).

The non-sustainable nature of this dependence is not the only concern. Fossil fuels are made up primarily of hydrocarbons and the products of their combustion include large amounts of greenhouse gases and pollutants such as carbon dioxide, nitrous oxides, sulphur dioxide and other volatile organic compounds.

Radiative forcing is one of the major consequences of these emissions and is a term that is coined in order to quantify anthropogenic effects on the Earth's surface temperature. The presence of greenhouse gases such as CO_2 in the Earth's atmosphere absorb solar radiation that is reflected from the Earth's surface, which has an insulating effect on surface temperatures. Increased concentrations of these species in the atmosphere therefore result in rising surface and lower atmosphere temperatures, or global warming, which has a destructive effect on many of the world's environments and ecosystems. There are a multitude of reports and findings that demonstrate the unequivocal and detrimental phenomena of global warming. Among these, **Figure 1.2** illustrates this effect as changing surface temperatures since the industrial revolution over the past 150 years using data from the *Met Office Hadley Centre and Climate Research Unit*.[4]

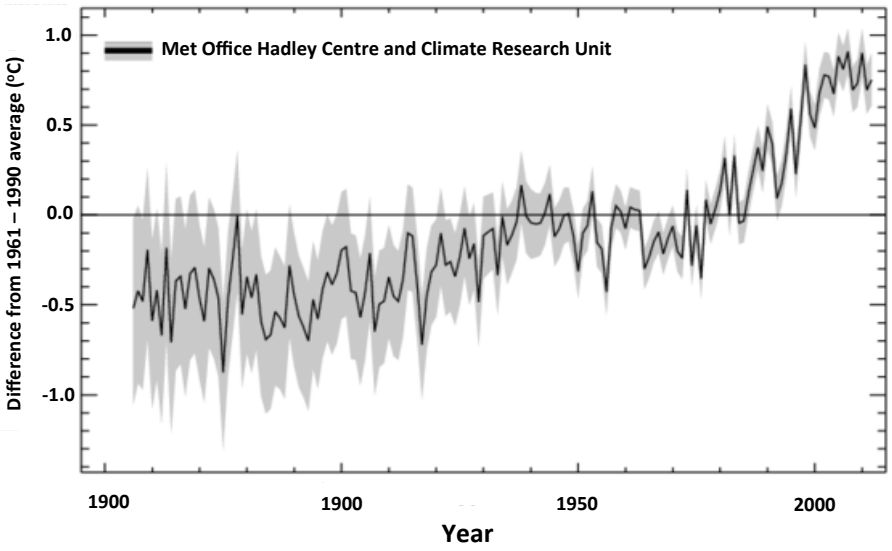

Figure 1.2. Changing global surface temperatures from 1860 – 2012.[4]

The only viable solution to this non-sustainable dependence is a dramatic restructuring of global energy markets, which needs to be proactive not reactive in nature. The *Renewables 2014 Global Status Report* estimates that renewable energy constituted 19 % of the global energy consumption in 2012 with biomass combustion, wind, hydroelectric, geothermal and solar energy technologies all making significant progress in recent years.[5] Despite these advances, renewables are still generally neglected and it is unlikely that they will become dominant until driving market forces accelerate their development.

Out of all of these emerging energy solutions the abundant nature of the sun as a primary energy source makes it an excellent candidate in the strive towards sustainability. The amount of solar radiation intensity reaching the Earth, known as the solar flux constant, is measured at about 1369 watts per square metre. Taking into account atmospheric effects, this can be equated to 3.2 million exajoules (EJ = 10^{18} J) reaching the Earth's surface annually. Figures vary in the interpretation of this value with estimates approximating it to be between 7000 – 8000 times the annual global usages.[6]

The potential of harvesting the sun's omnipresent energy in an economically viable manner is therefore clear. Photovoltaic (PV) technologies based upon crystalline silicon semiconductors have been continually improving since the first silicon PV solar cell was developed in the Bell Laboratories in 1954.[7] Despite decades of research advancements in the field and international commercialisation of the technology, silicon PV still only occupies a small portion of the market.[8] The limiting factor remains the production costs associated with the supply of electronic grade silicon, which requires exceptionally high levels of material purity to allow the efficient transfer of electrons across the material. Despite silicon being one of the most abundant materials on the planet its purification and fabrication remains costly and energy intensive with fabrication processes often paradoxically releasing various carbon-based greenhouse gases themselves. This means that when production costs and emissions are accounted for, several years of usage are usually required for a silicon PV solar cell to become 'carbon neutral'.[9] Therefore if the potential of solar energy is to be realised, a low cost solution that is suitable for large-scale mass production is essential.

This provides the motivation for the research described in this thesis. Organic photovoltaic (OPV) materials offer an opportunity to tackle each of the previously described problems associated with silicon based solar cells and a thorough understanding of the benefits and limitations of these new materials is essential. A move towards devices consisting of solution processable organic materials has the potential to revolutionise the photovoltaics industry by opening up the possibility of a multitude of new fabrication techniques and applications. After an introduction to some of the fundamental principles underpinning the research, a brief history of the

development or OPV will be introduced and the physical and chemical operating principles discussed later in sections **1.4** and **1.5** respectively.

1.2. Polymer properties and synthesis

1.2.1. Polymer properties

A polymer is a long chain molecule that is made up of repeating monomer units with the total mass of each polymer chain being the sum of its individual units. There are a huge variety of polymers both synthetic and naturally occurring, from proteins to plastics, they are essential to a wide range of applications in everyday life. Regardless of the nature of the polymer, the individual chains in a polymer batch are rarely the same size which leads to a degree of difficulty in classifying a polymer's molecular weight.

A polymer's weight is therefore best described as a statistical distribution around an average and it is necessary to introduce the terms number average molecular weight (M_n), weight average molecular weight (M_w) and polydispersity index (PDI). A comprehensive evaluation of these values can be essential when drawing comparisons between different polymer batches. Perhaps the most widely used descriptor is the number average molecular weight (M_n) which is given by

$$M_n = \frac{\Sigma M_i N_i}{\Sigma N_i} \qquad \textbf{Equation 1.1}$$

Where N_i is the number of moles of each polymer species and M_i is the molar mass of that species. This is averaged across all the different sized polymer species in a polymer batch. The weight average molecular weight (M_w) is always higher than M_n as it is a weighted average of all the values in a polymer batch and is given by

$$M_w = \frac{\Sigma N_i {M_i}^2}{\Sigma N_i M_i} \qquad \textbf{Equation 1.2}$$

Figure 1.3 shows a general comparison of M_n and M_w statistical averages of a generic polymer batch with a Gaussian-type distribution of masses.

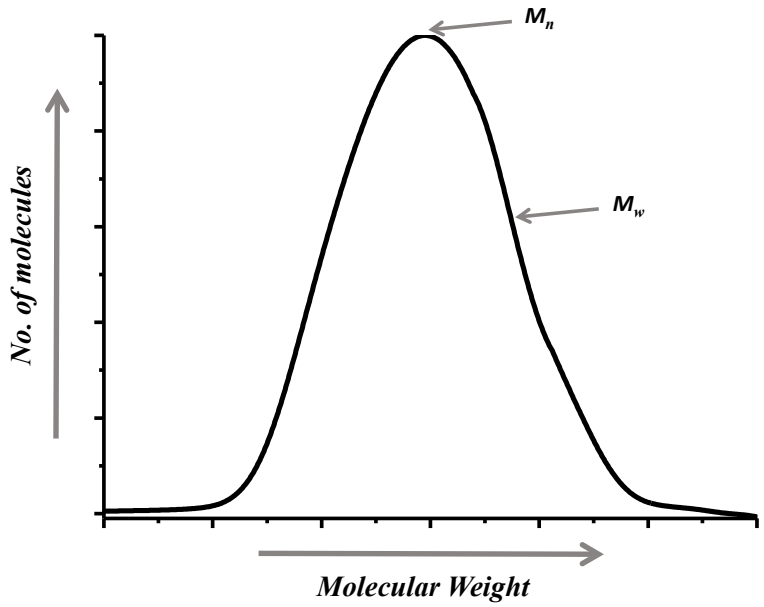

Figure 1.3. Gaussian-type mass disribution of a generic polymer sample showing M_n and M_w.

The polydispersity index (PDI) is a quantification of the heterogeneity of a polymer batch containing various different sized polymer chains. A sample with polymer chains that are all the same size would have PDI = 1. PDI is given by

$$PDI = \frac{M_w}{M_n} \qquad \textbf{Equation 1.3}$$

An additional way to approximate the size of a polymer is to quantify the degree of polymerisation, which is effectively a measure of how many repeat units there are in a polymer chain. As with molecular weight it is possible to define number average and weight average values, DP_n and DP_w respectively, which are given by

$$DP_n = \frac{M_n}{M_0} \qquad \textbf{Equation 1.4}$$

$$DP_w = \frac{M_w}{M_0} \qquad \textbf{Equation 1.5}$$

Where M_0 is the molecular weight of an individual repeating monomer unit.

1.2.2. Polymer synthesis

1.2.2.1. Step growth and chain growth

Polymers can be broadly characterised into two classifications based upon the manner in which the polymer chains are formed. Step-growth or condensation polymerisations are formed by the sequential reaction of bi-functional or multi-functional monomers and oligomers with the elimination of small molecule by-products. Monomers form dimers, which then form trimers or oligomers and combine to form more oligomers. The growth of polymer chains is generally slow and a high extent of reaction is required to reach larger molecular weights. The monomer concentration diminishes very early on in the polymerisation process and after each combination the reactive sites remain active with no termination step.

Chain growth polymerisations occur via the propagation of monomers with an active centre (often ionic or radical in nature). Monomers are sequentially added to the active chain resulting in the formation of higher molecular weight material at an earlier stage than in step-growth synthesis whilst monomer species are present throughout the duration of the polymerisation process. Different mechanistic steps operate at different stages of the polymerisation; initiation, propagation, chain transfer, termination. A living chain growth polymerisation describes a chain-growth mechanism where the ability of a polymer chain to terminate has been removed. **Figure 1.4** shows how the molecular weight of a polymer grows during different polymerisation mechanisms.

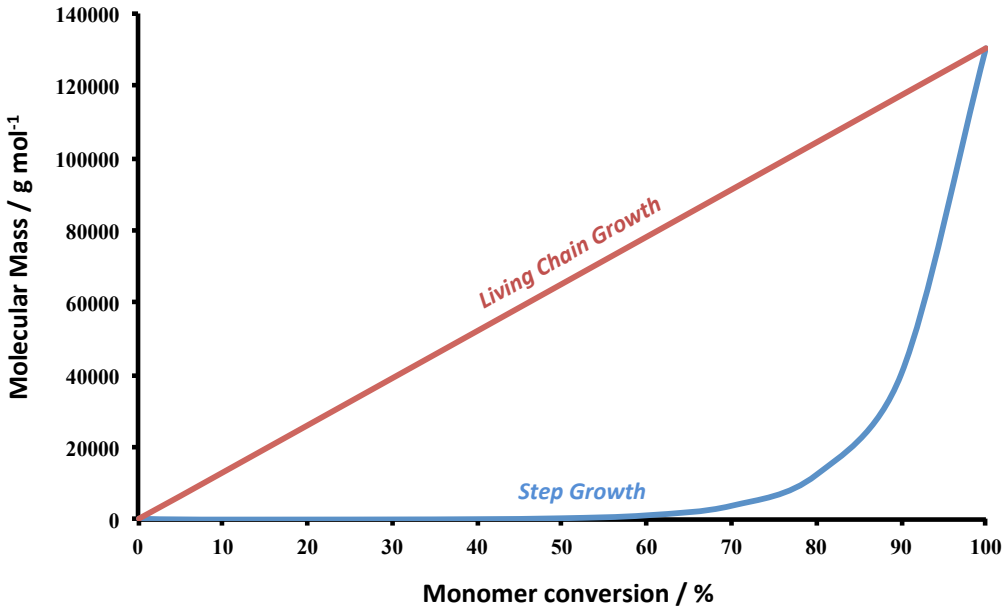

Figure 1.4. Polymer chain growth as a function of percentage monomer conversion during different polymerisation mechanisms.

Semiconducting polymers are generally synthesised by the step-growth polymerisation of bi-functional monomers. These are described to good effect by the Carothers equation where DP_n is estimated for a specific fractional monomer conversion (***p***). For two monomers in equimolar quantities

$$DP_n = \frac{1}{1-p} \qquad \textbf{Equation 1.6}$$

and ***p*** is described by

$$p = \frac{N_0 - N}{N_0} \qquad \textbf{Equation 1.7}$$

Where N_0 is initial monomer number and N is the number of monomers at a given time. This equation demonstrates the requirement of high monomer conversion in order to achieve polymers of high molecular weights. The equation can also be adjusted to take into account non-equimolar amounts of monomers where ***r*** gives the stoichiometric ratio of reactants, taking the excess reactant as the denominator. This gives

$$DP_n = \frac{1+r}{1+r-2rp}$$ **Equation 1.8**

As the reaction tends towards complete monomer conversion ($\boldsymbol{p \rightarrow 1}$) then

$$DP_n \rightarrow \frac{1+r}{1-r}$$ **Equation 1.9**

This demonstrates how a stoichiometric excess of one monomer can be used to carefully control the degree of a step-growth polymerisation and hence the molecular weight of a polymer batch.

1.2.2.2 Palladium-catalysed cross-coupling polymerisations

There are a large number of mechanisms used in the synthesis of polymers. Perhaps the most frequently encountered synthetic route in the field of organic electronics is the use of carbon – carbon bond formation via transition metal mediated cross-coupling. Transition metal atoms such as palladium have vacant d-orbitals which can accept electron density and participate in redox reactions with organic monomers. These interactions can be harnessed to catalyse reactions between two different bi-functional monomers and under the right conditions consecutive cross-coupling cycles can result in the build-up of polymer chains. Palladium-catalysed Stille couplings and Suzuki couplings are frequently used throughout this thesis, as a result of this and the desire to remain concise, other transition metal mediated cross-coupling reactions will not be discussed further.

Stille couplings are a highly versatile carbon – carbon bond forming method between organotin and organohalide functionalities at sp^2 hybridised carbons, a general catalytic mechanism of which is shown in **Figure 1.5**. The first mechanistic step is the rate-determining oxidative addition of the organohalide to the transition metal centre, which goes from Pd^0 to Pd^{II}. The addition normally occurs in a *cis*-fashion with the *cis* intermediate rapidly isomerising to its more thermodynamically favourable *trans* equivalent. Next, transmetalation occurs between the intermediate formed from the previous oxidative addition step and the organotin compound which is driven by the formation of the stannylhalide by-product. This is then followed by *trans* / *cis* isomerism to give alkyl groups that are in mutually *cis* coordination sites and are

amenable towards the next step. The final reductive elimination step results in the coupling of the two alkyl groups and regeneration of the Pd^0 species.

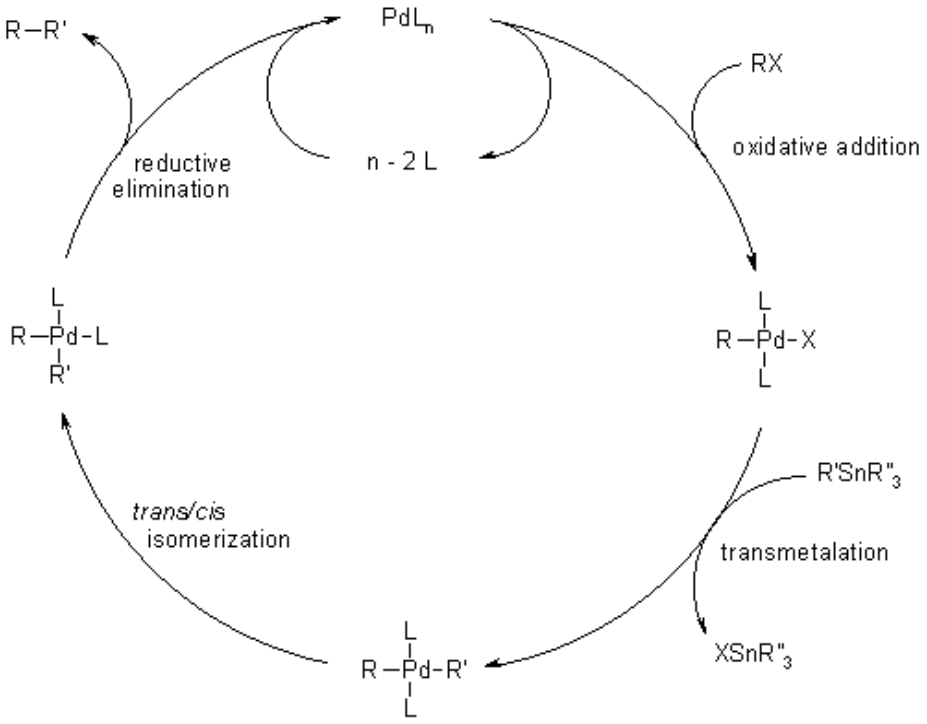

Figure 1.5. Stille catalysed cross-coupling reaction between an organotin and organohalide compound. L = Ligand.

The catalytic species can be formed *in situ* by the combination of a palladium source such as $Pd_2(dba)_3$ or $Pd(OAc)_2$ and a sterically bulky ligand such as triphenyl phosphine (PPh_3) or tri-(*o*-tolyl)phosphine ($P(otol)_3$) or alternatively a preformed catalyst such as $Pd(PPh_3)_4$ can be used. The ligand choice can be used to enhance a number of the previously described catalytic steps. Strong electron donors such as PPh_3, or the ionic OAc^-, serve to increase the electron density at the metal centre which enhances its nucleophilicity and accelerates the rate determining oxidative addition step. The requirement for sterically demanding ligands is also used to influence the reductive elimination step by accelerating isomerisation from the *trans* to *cis* positions.

In comparison, Suzuki couplings occur between organoboron and organohalide compounds at sp^2 hybridised carbons and proceed in a similar mechanistic manner to Stille coupling. A noteable difference is the requirement for activation of the boron species by a mild base, usually 1 M or 2 M concentrations. This base serves to

enhance the polarisation of the organic ligand for the transmetalation step and the biphasic reaction does not begin until the addition of the basic phase. Whilst Suzuki couplings can be favourable compared to Stille couplings as they avoid the use of the toxic organotin compounds, they also have their disadvantages. The main limitation being a consequence of the requirement for basic conditions meaning Suzuki couplings are less tolerant than the pH-neutral Stille coupling to various monomer functional groups.

1.3. Semiconducting polymers

1.3.1. Conjugation

Organic compounds consist largely of carbon and hydrogen atoms, a single C - H or C - C bond is known as a sigma (σ) bond and is the sharing of an electron pair through the head-on overlap of two atomic orbitals with one electron coming from each atom. A pi (π) bond involves the overlap of the two lobes of one atom's p-orbital with the two lobes of another atom's p-orbital. As shown in **Figure 1.6**, a carbon carbon (C = C) double bond is made up of one σ-bond that is localised within the molecular plane and one π-bond that is above and below that molecular plane. A carbon atom that has only σ-bonds to other atoms is said to be sp^3 hybridised whilst two σ-bonds and one π-bond describes an sp^2 hybridised carbon.

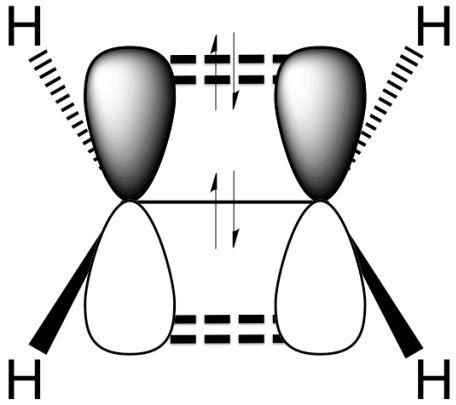

Figure 1.6. π-orbital formation by overlap of p orbitals on sp^2 hybridised carbon atoms in ethene.

It is these differences at the molecular orbital level that differentiate semiconducting and insulating organic compounds from one another. Organic compounds consisting of only sp^3 hybridised carbon atoms have each of their bonding electrons localized within σ-bonds. These bonds guarantees the molecule's integrity but also means the electrons are not able to participate in conductivity as free charges. Consequently many organic compounds have insulating properties, which are exploited in a wide number of commercial synthetic plastics such as Teflon and Nylon.

Conjugated organic compounds (including aromatics) are those that contain alternating single and double bonds, giving predominantly sp^2 carbons. The electrons in the π-bonds within these conjugated systems are able to delocalize across the conjugated electron cloud of the whole molecule. This delocalisation of π-electrons is the origin of electrical semiconductivity in organic compounds and through the synthesis of large conjugated polymers this becomes extended across a large number of atoms to give highly delocalised molecular orbitals.

Depending on their phase, adjacent p-orbitals in a conjugate system can be either in phase (bonding) or out of phase (anti-bonding) relative to one another. The possible bonding and anti-bonding arrangements can be visualised as molecular orbitals of different energies. The frontier molecular orbitals are defined as the Highest Occupied Molecular Orbital (HOMO) and the Lowest Unoccupied Molecular Orbital (LUMO). **Figure 1.7** shows how extension of the conjugation length, ie through consecutive monomer unit addition from thiophene to bi-thiophene, results in the splitting of energy levels with HOMO and LUMO levels that become closer together as polymer chain size is increased.

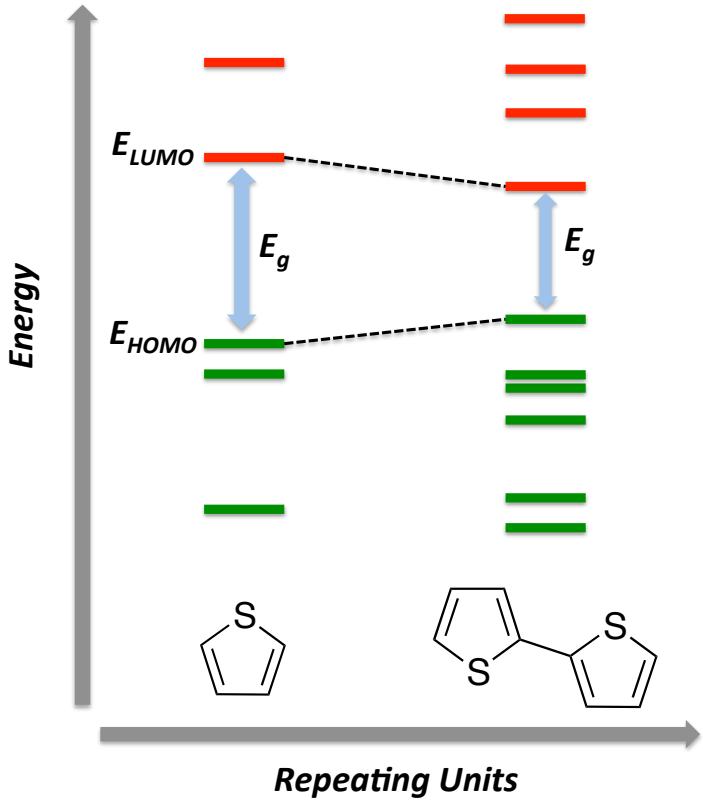

Figure 1.7. Band gap redution with extended conjugation length from thiophene to bi-thiophene.

Light absorption results in the photoexcitation of an electron from the HOMO to the LUMO level (E_{HOMO} and E_{LUMO} respectively) and the energetic difference between these frontier orbital energy levels is defined as the optical band gap (E_g). The size of E_g dictates the energy, and hence the wavelength, of light that is absorbed by the material. Narrowed band gaps therefore resulting in a shift of the absorption profile of a polymer material to longer wavelengths.

As shown in **Figure 1.8** the solar flux spectrum has a maximum at around 600 - 700 nm. The shifting of absorption towards the infrared region to cover a larger portion of the cumulative photon flux is an effective route towards increased light absorption of a photoactive polymer. In addition to the narrowing of E_g by extending the conjugation length of a material, there are also several other key features that are known to be effective techniques towards finer tuning of energy levels and theresultant light absorption, which are discussed in the next section.

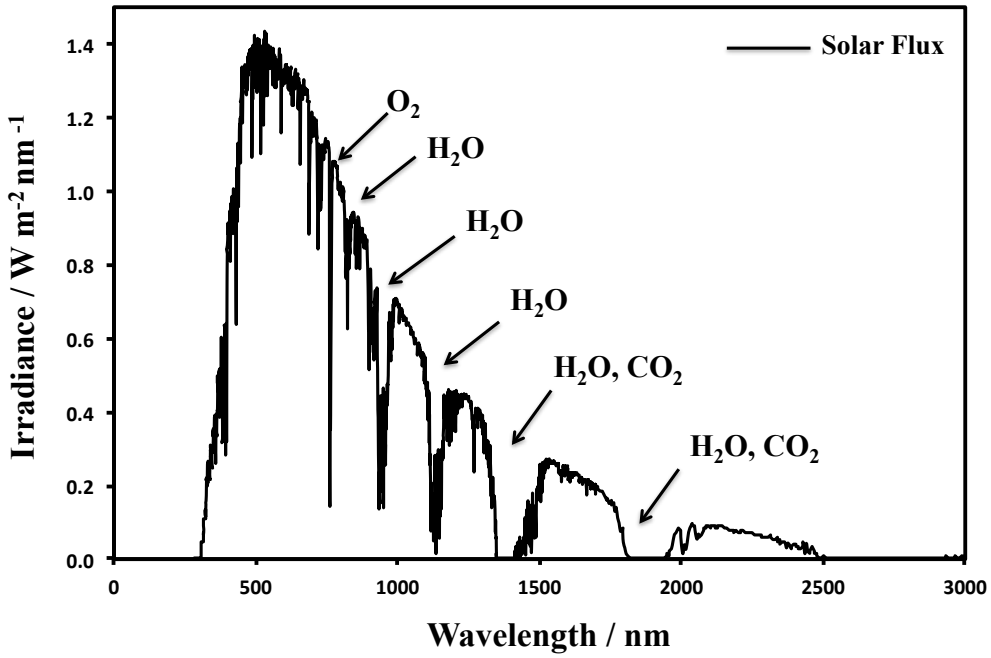

Figure 1.8. Solar flux spectrum with the strongest atmospheric absorbers indicated.

1.3.2. Band gap engineering

One key physical parameter to consider when modifying a polymer's band gap is the Bond Length Alternation (BLA). The concept of BLA arises from the existence of two different resonance structures in aromatic compounds. These are known as the aromatic and quinoidal forms and are interchangeable through single bonds becoming double bonds and vice versa. The quinoidal resonance structure corresponds to a loss of aromatic stability and this energetic destabilisation results in a raised E_{HOMO} and lowered E_{LUMO} giving narrowed E_g values. The ratio of the aromatic to quinoidal form is quantified by BLA where a higher quinoidal contribution corresponds to a decreased BLA value. E_g decreases linearly with decreasing BLA and a polymer that has a greater tendency to exist in the quinoidal form is therefore highly desirable for increased photon absorption. This is exemplified when comparing phenyl and thiophene based polymers (**Figure 1.9**); phenyl rings are highly aromatic which corresponds to wider E_g values, whilst thiophene rings are less aromatic and generally have a larger quinoidal contribution and narrowed band gaps.

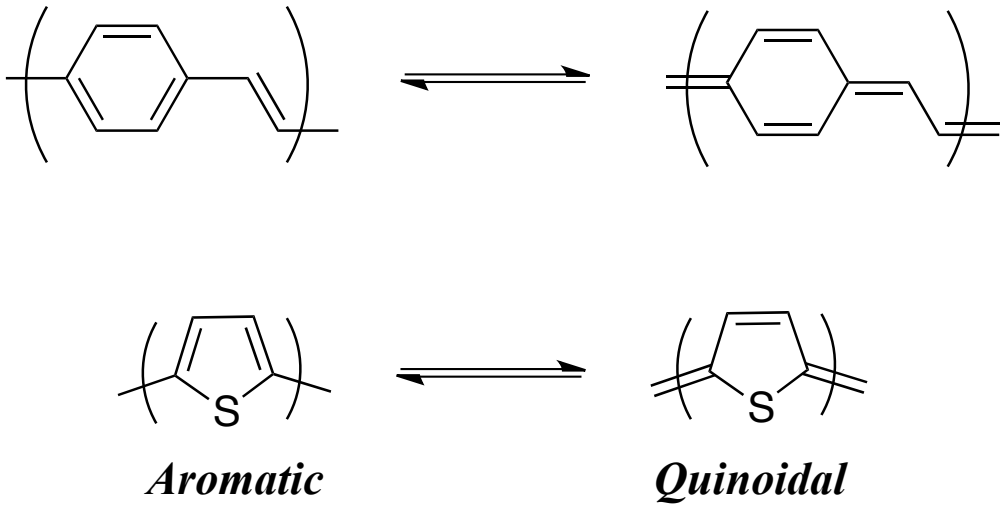

Figure 1.9. Aromatic and quinoidal forms of polyphenylene vinylene (**PPV**) (above) and polythiophene (below).

Other techniques successfully employed in band gap engineering relate to the use of main chain substituents and backbone planarity. Through introducing electron-withdrawing or electron-donating groups (EWG / EDG) along the polymer backbone, it is possible to influence the electronic populations of the molecular orbitals to afford energetic stabilisation or destabilisation. Numerous examples can be seen throughout the literature, in particular strongly electron-withdrawing groups such as halogens and units such as benzothiadiazole are successfully employed to stabilise a polymer's E_{HOMO} value.[10-12]

In addition to a consideration of the electronic contributions of different structural features, the effect that these features have on polymer backbone planarity can also be essential. Fused aromatic systems have highly planar structures with good overlap of adjacent orbitals and efficient conjugation, whilst the bonds that connect the aromatic units to one another often have a degree of rotational freedom which can result in a reduction in planarity. This can disrupt the conjugation along a polymer's backbone and result in wider E_g values. Planarising structural features such as extended fused systems and intramolecular H-bonds are therefore highly effective in the design of narrow band gap materials.

Although they generally play little to no role in affecting the polymer molecular orbitals, solubilising alkyl chains can also affect a material's band gap through

influencing the planarity in the solid state. It is essential to have alkyl chains tethered to the repeating monomeric units to guarantee solution processability via steric disruption of the strong interactions between the electron clouds of different polymer chains, known as π - π interactions. The density of these solubilising alkyl groups, their branched or linear nature and their size are key features in influencing electrostatic interactions between chains which in turn can dictate polymer coplanarity and band gap size.

Each of the factors described that are frequently used to modify the band gap of a polymer are nearly always present to varying extents and there is often a complex interplay between these and other parameters. To further complicate the delicate balance in the design of low band gap polymers, 'push-pull' or 'D / A' polymers are now one of the most frequently used routes towards the narrowest E_g values. As shown in **Figure 1.10**, it is speculated that alternating electron-rich donor and electron-poor acceptor structural features interact with each other through the hybridisation of molecular orbitals, which enhances the double bond character along the polymer backbone. Besides the narrowing of E_g values, the alternating donor and acceptor segments also serve as local dipoles, which enhance intermolecular ordering favourable for charge transport.

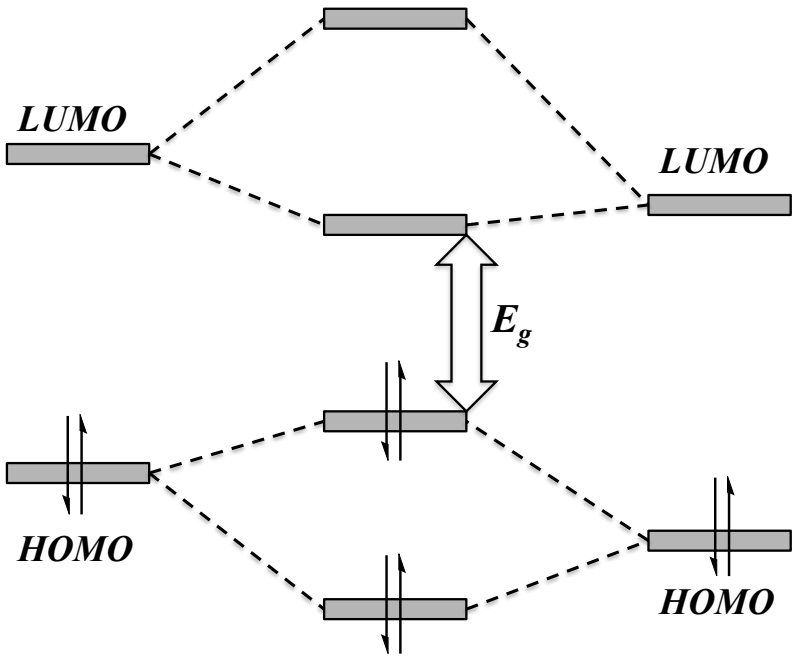

Figure 1.10. E_g reduction as a result of the hybridisation of adjacent donor and acceptor molecular orbitals.

1.4. History of conjugated polymers for organic photovoltaics

The field of organic photovoltaics is vast and ever expanding and there are several different types of organic solar cells based upon different materials. Devices based upon small molecule, dye-sensitized, and most recently perovskite materials are widely studied and offer highly promising alternatives to conjugated polymers. To remain within the context of the research aims of this thesis, these introduction sections will be focussed exclusively on polymer-based solar cells.

In response to the need to meet the economic requirements of cheap solar energy that is industrially viable for mass production there was huge excitement generated, within both industrial and academic circles, when *A. Heeger et al*. reported the first example of semiconducting polymers in 1977.[13] It was found that oxidized iodine-doped polyacetylene exhibited electrical conductivity that was several orders of magnitude larger than the original polymer. This lead to a handful of studies using heavily doped conjugated materials sandwiched between two electrodes with power conversion efficiencies (PCE) as high as 0.3 %.[6] The potential of using conjugated organics as photovoltaic materials was immediately apparent. Being able to fabricate solar cells from solution processable organic materials could allow for cheap, large-scale production. Manufacturing processes could be developed so that devices could be printed in a roll-to-roll manner on to flexible substrates due to the high temperature processing conditions associated with silicon PV no longer being necessary.

A major breakthrough came in 1986 when *C. W. Tang et al.* achieved a PCE of 1 % using a bilayer donor / acceptor device.[14] The two different materials of the photoactive bi-layer consisted of a copper pthalocyanine (CuPc) electron donor and a perylene tetracarboxylate (PTC) based electron acceptor. The bilayer was placed between two electrodes of different work functions and irradiated under stimulated illumination. Light absorption by the CuPc donor material resulted in the creation of a coulombically bound electron – hole pair, known as an exciton. If this exciton reaches the donor / acceptor interface (CuPC / PTC) within it's short-lived lifetime then it is able to dissociate into free electrons and holes which can then migrate to their respective electrodes. The operating principles will be discussed in further detail in a later section.

It soon became apparent that bilayer devices are limited by the small donor / acceptor interfacial region and the next major milestone came with the discovery of polymer / fullerene (C_{60}) bulk heterojunctions (BHJ).[15] As with bilayer devices, charge generation is a consequence of excitonic dissociation at the interface of the donor and acceptor materials.[16] Unlike bilayer devices, the photoactive layer consists of a mixture of the two materials as a finely intermixed blend. The surface area of the interfacial region is therefore substantially increased which results in a large improvement in the generation of photocurrent.

Research into bulk heterojunctions began to accelerate dramatically with new conjugated polymer structures being synthesised and screened for solar cell performance. The fullerene acceptor was also modified over time, the addition of substituents to the previously bare fullerene cage were used to prevent crystallisation of acceptor domains and increase miscibility with the polymer donor material. PC[61]BM and the larger PC[71]BM are the two most frequently used acceptor materials and to date they remain dominant, with the volume of research into new acceptors being far surpassed by their donor counterparts.

In 2001 a high efficiency of 2.5 % in a BHJ device was reported by *J. C. Hummelen et al.* using a polyphenylene vinylene (PPV) based polymer donor material.[17] PPV as a polymer for OPV applications had already been reported several times however this research was one of the first important examples of how a high level of control over the degree of intermixing of the D / A blend is crucial in achieving the highest performing devices. The current benchmark material combination of the polymer / fullerene BHJ field came in 2002 when a poly(3-hexylthiophene) (P3HT) / fullerene device achieved a PCE of 2.8 %.[18] Due to its good solubility, efficient conjugation and ease of synthesis and structural modification, P3HT / fullerene research flourished over the next decade with thousands of papers published each year and efficiencies over 6.5 % reported.[19-21]

The next generation of conjugated polymers saw the development of alternating D / A backbone structures. As previously described, these consist of alternating electron-rich and electron-deficient segments along the polymer chain which afford narrow optical band gaps through the hybridisation of molecular orbitals. With the development of these low band gap polymer materials efficiencies have continued to

rise to above 9 % in single junction BHJs.[22] Whilst efficiencies are now approaching, and in the case of multi-junction devices exceeding, the 'magic 10 %' milestone which has long been heralded as the final hurdle towards commercialisation it is clear that there still remain many obstacles.[23] The synthetic complexity associated with the design of polymer donor materials as well as poor device operational stability means that affordable OPV energy production is a long way from reality and further research into these materials and devices are in great demand.

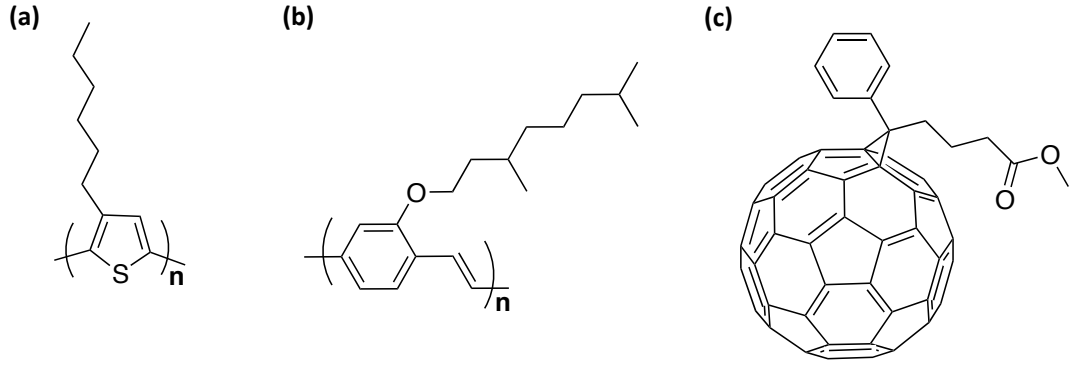

Figure 1.11. Chemical structures of some of the previously described OPV benchmark materials. **(a)** P3HT **(b)** MDMO-PPV **(c)** PC[61]BM

1.5. Polymer / fullerene bulk heterojunction solar cells

1.5.1. Mechanism of charge generation

Organic solar cells are known as excitonic solar cells due to one of the primary differences between photovoltaic devices based upon organic materials (eg. polymers, small molecules) and those based upon inorganics (eg. silicon). Photoexcitation in conjugated organic materials gives the formation of a coulombically bound electon and hole pair (an exciton) as opposed to the generation of free charges in inorganic devices. This is a consequence of the low permittivity of organic compounds and the separation of these short-lived species into free charges is key to the operation of bulk heterojunction solar cells.

The active layer of a BHJ solar cell consists of a bicontinuous interpenetrating network of electron donor (polymer) and acceptor (fullerene) materials. As shown in

Figure **1.12** photoexcitation promotes an electron from the donor material's HOMO into it's LUMO, leaving behind a hole and thus creating an exciton. Once it has been formed, the exciton diffuses through the active layer towards a donor / acceptor heterojunction. If it reaches this heterojunction within it's short-lived lifetime the excited electron can dissociate into the LUMO of the acceptor providing the energetic offset is greater than the couloumbic attraction between the hole and electron. Following dissociation, the free hole and electron charges are able to migrate to the respective electrodes.

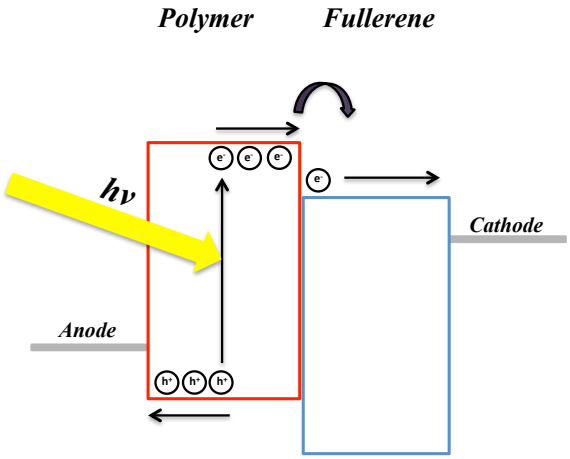

Figure 1.12. Simplified mechanism of charge generation in polymer / fullerene BHJ solar cells.

There are however several complications that prevent the smooth operation of the bulk heterojunction solar cell. The exciton is a very short-lived species that is only able to travel small distances, with estimates ranging from 5 – 10 nm, before relaxation to the ground state occurs.[24-27] This means that any excitons formed at a greater distance than this from a heterojunction will not dissociate into free charges. In order to enhance dissociation a finely intermixed active layer is required so that as many excitons reach a boundary within their lifetime as possible. Several studies report various optimised device processing conditions in attempts to improve charge separation through finer blend intermixing. However, it is also necessary to have percolated pathways for the separated holes and electrons to migrate to the electrodes without encountering traps.[28,29] These percolation pathways can be reduced if the

intermixing is too fine and therefore there is often a carefully balanced trade-off between the two.

1.5.2. Device parameters

The manner in which a solar cell device's performance is reported is essential when comparing the calibre of photovoltaic materials and devices that are produced in different laboratories under different fabrication conditions. The power conversion efficiency (PCE %) of a device provides a way to easily describe its performance and is generally quoted to provide an overall picture. The PCE is defined as the percentage conversion of incident light into electrical power and is given as the ratio between the useful power output (P_{max}) and the power input / solar radiation (P_{in}) under standard test conditions (temperature = 25 °C, irradiance = 100 W / m^2, air mass = 1.5 (AM1.5 spectrum)). The value of P_{max} is a product of the cell's internal properties and is given mathematically by

$$P_{max} = FF \times J_{sc} \times V_{oc} \qquad \textbf{Equation 1.10}$$

which gives

$$PCE = \frac{FF \times J_{sc} \times V_{oc}}{P_{in}} \qquad \textbf{Equation 1.11}$$

Whilst each of these individual device characteristics can be defined in further mathematical detail, for the purpose of this thesis their definitions will remain qualitative. The short circuit current (J_{sc}) is given in mA cm^{-2} and is the current density through the cell when the voltage is zero (short circuited). Also referred to as the photocurrent, it is a measure of the generation and collection of charge carriers. It is heavily influenced by the amount of light that is absorbed as well as the various loss mechanisms that prevent the collection of charges at the electrodes. The open circuit voltage (V_{oc}) gives the maximum voltage of a device when there is zero current (open circuited) and is largely influenced by the energetic offset between the HOMO level of the donor material and the LUMO level of the acceptor material. The final term in the equation is the fill factor (FF), which is defined as the ratio of the maximum power from the solar cell to the product of V_{oc} and J_{sc}.

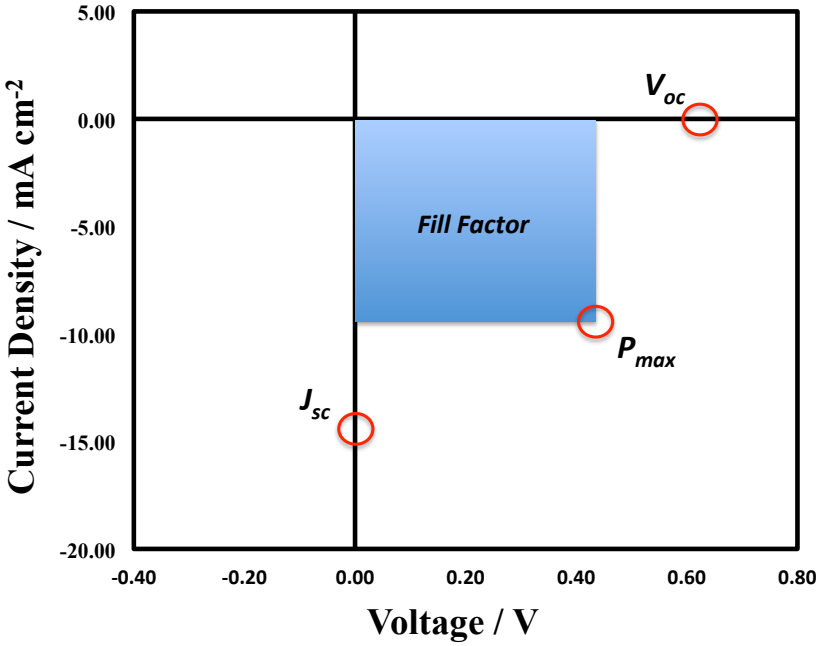

Figure 1.13. Typical *J-V* curve extracted from an OPV device under simulated illumination. FF is indicated by the blue square.

Testing of a device under simulated illumination conditions allows for the extraction of a current density *vs* voltage (*J-V*) curve. V_{oc} and J_{sc} correspond to the curve crossing the *x* and *y* axes respectively whilst the 'squareness' of the *J-V* curve gives a graphical representation of the FF of a device. The external quantum efficiency (EQE) of a device is defined as the ratio of the number charge carriers collected at the electrodes to the number of incident photons at a given wavelength. The EQE can be plotted across the visible spectrum where the integrated area under the curve is equal to the J_{sc} of the device. Many researchers choose to correct their observed J_{sc} using the value of this area under an EQE spectral curve so that a more accurate J_{sc} value is obtained. As a result EQE spectra are generally reported along side *J-V* curves throughout the literature.[30]

1.5.3. Device architecture

As mentioned earlier, the first organic solar cells comprised a planar heterojunction of electron donor and acceptor layers. This active bilayer is typically sandwiched between two conducting metallic electrodes of differing work functions for the extraction of generated charges. These comprise a low work function top electrode / cathode (Al, Ca) and a high work function anode such as indium tin oxide (ITO) that is transparent so that incident light can pass through. As shown in **Figure 1.13** BHJ devices have a similar basic structure with the difference that the active layer is instead a bi-continuous blend mixture of the donor and acceptor materials.

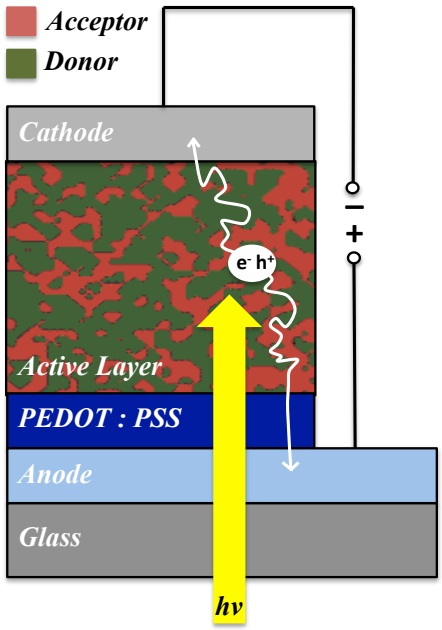

Figure 1.14. Graphical representation of the different layers in a BHJ device with conventional architecture

The active blend layer, generally a polymer / fullerene mixture, receives by far the most research attention. Control over the material properties of the active layer allows for control to be exerted over the light absorption, charge separation and charge transport to the electrodes and is therefore of huge importance. When fabricating a BHJ device the importance of good intermixing of donor and materials cannot be stressed enough. In addition to the use of different donor / acceptor ratios, variation of solvent systems from which the active layer is deposited from as well as the use of low vapour pressure processing additives and high temperature annealing conditions

have been shown to significantly affect the microstructure of the blend and its resultant photovoltaic operation.[31-37]

With the development of multi-layer BHJ devices came the introduction of interfacial charge transport layers. An electron interfacial layer or electron transport layer such as LiF or ZnO is deposited between the active layer blend and the cathode whilst a hole transport layer, most commonly poly(3,4-ethylenedioxythiophene)-polystyrene sulfonate (PEDOT : PSS), is deposited between the active layer blend and the anode. Interfacial layers primarily function to adjust the energy level offsets between the active layers and the electrodes and thus increase preferential charge extraction of a specific charge carrier.[38] Additionally, they can also serve as protecting layers to inhibit reactions and material degradation at the active layer / electrode interfacial regions.[39]

The long-term oxidative stability of the low work function cathodes used in conventional architectures are often of significant detriment to the device's operation. With the construction of inverted device architectures this undesirable feature can be greatly reduced through reversing the polarities of the electrodes. The low work function top electrode is replaced by a higher work function material (Ag, Au) that is less prone to oxidation and the position of the hole and electron transport materials are swapped. Long-term device stabilities and overall performances are often significantly improved through the inversion of architecture and they are now frequently reported in parallel with conventional devices.[40,41]

1.6. Organic Field Effect Transistors

Transistors, like solar cells, are another silicon-based technology that have the potential to be revolutionised by semiconducting organic materials. Transistor devices underpin modern circuitry and are used to switch or amplify an electric signal. When these functions are modulated by an applied electric field the devices are known as field effect transistors (FETs). Organic field effect transistors (OFETs) are FETs in which the semiconducting channel consists of conjugated organics as opposed to crystalline silicon or other semiconducting inorganics. A transition to OFETs offers much of the same benefits as the OPV devices previously discussed. Large-scale

solution processing and roll-to-roll printing could significantly reduce the costs associated with many electronic devices whilst the possibility of printed transistors on flexible substrates is particularly exciting for the development of a new generation of flexible electronic devices.[42,43]

1.6.1. Operating principles

An OFET device has three terminals; source, drain and gate electrodes. A semiconducting channel, that is insulated from the gate electrode by a dielectric layer, bridges the source and drain electrodes that serve to inject and extract charges respectively. When a potential is applied between the gate electrode and source / drain electrodes an electric field is created which results in an accumulation of charge carriers in the semiconducting channel at the interface with the dielectric layer. Variation of the applied potential is used to modulate the flow of these charge carriers between the source and drain electrodes and switching between negative and positive bias is used to dictate the nature of the charge carriers that are accumulated.

When the gate voltage (V_G) is zero, the transistor is considered in the OFF state with little to no current flowing between source and drain electrodes. Holes can be accumulated in at the semiconducting channel / dielectric interface by the application of a negative gate bias. On application of a negative bias at the drain electrode (V_D), accumulated holes flow between the source and drain electrodes (p-type conduction) and the transistor is switched to ON. As the magnitude of the drain-source voltage is increased, the drain-source current also increased until V_D reached V_G, at which point the current saturates. For the accumulation and transport of electrons (n-type conduction) the current-voltage behaviour is similar, with positive values as opposed to negative.

1.6.2. Device architectures

As with OPV devices, there are multiple architectures that are used in OFET device fabrication. **Figure 1.15** shows the four device structures generally used, each of which has a different arrangement of the semiconducting channel, dielectric layer and

electrodes relative to the substrate. Top gate / bottom contact, top gate / top contact, bottom gate / top contact and bottom gate / bottom contact devices are commonly reported where the position of the source and drain contacts are described relative to the semiconducting channel and the position of the gate electrode described relative to the dielectric. Performances and fabrication costs can vary dramatically depending on the device architecture.[44,45]

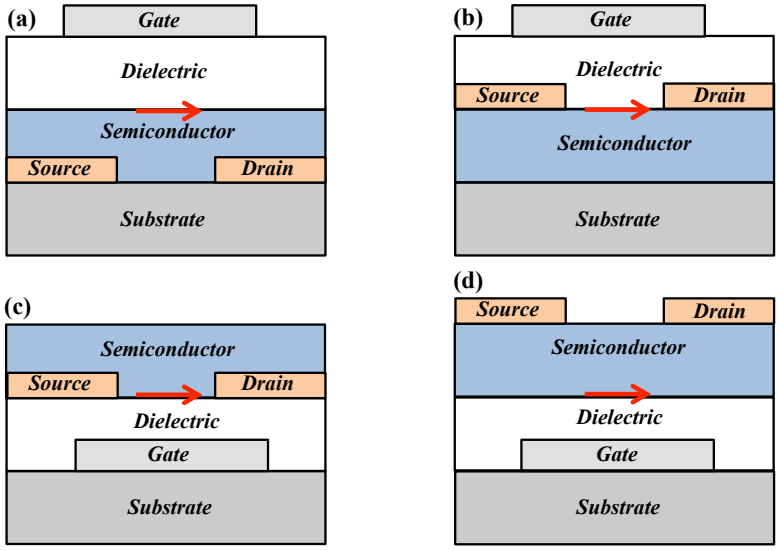

Figure 1.15. Typical OFET devices architectures **(a)** top gate / bottom contact **(b)** top gate / top contact **(c)** bottom gate / bottom contact **(d)** bottom gate / top contact.

1.6.3. Performance parameters

OFET research is generally focused on the optimisation of three important parameters; charge carrier (hole or electron) mobility, on / off current ratio (I_{on} / I_{off}) and threshold voltage (V_T). Hole mobilities (μ_h) and electron mobilities (μ_e) are directly proportional to the conductivity of the semiconducting channel and are often quoted when describing the overal performance of an OFET device. Mobility values are known to vary by orders of magnitudes with electron and hole mobilities now frequently reported between 1.0 and 10.0 cm^2 / Vs.[46-49] The value of I_{on} / I_{off} is determined by the ratio of the saturation current to the leakage current when the transistor is off and describes the ability of the device to function effectively as a switch. A high I_{on} / I_{off} value is desirable for reduction of losses through leakage currents. The threshold voltage (V_T) gives a measure of the voltage between source

and gate electrodes that is required for to turn the device on and result in the accumulation of charge carriers.

In the synthetic design of candidate semiconducting polymers for OFET applications it is generally the mobility values that are discussed due to close relationship between their magnitude and a semiconductor's chemical and physical properties. There are indeed a number of design criteria that are common to both OPV and OFET applications and consequently it is common to see the same polymer structures screened for both applications. Like OPV materials, the ability of electrons to delocalise conjugatively is key and structural features that enhance the transport of charges through a polymer's conjugate system are highly desirable. Efficient orbital overlap throughout a polymer due to highly planar, fused structures frequently demonstrate some of the highest charge carrier mobilities.[50] Contrastingly, backbones in which there is significant twisting or folding can inhibit charge transport and often result in large reduction in mobilities.[51]

For a high performing OFET device, the transport of charge carriers along the length of a polymer backbone must operate in conjunction with the transport of charge between polymer chains. This in turn is closely related to the intermolecular interactions and packing between polymer chains in the solid state. Generally, highly ordered semicrystalline polymers are favourable for interchain transport although several amorphous polymer systems demonstrating high mobilities are known. Features that promote close packing of chains and π - π interactions such as D / A type backbone structures and shorter linear alkyl chains, amongst others, are often the first port of call when designing a conjugated polymer with good transport characteristics.[52]

In contrast to OPV, a polymer's optical band gap is no longer a dominant consideration. The frontier molecular orbital energies do however remain important as they determine the ease of which charge carriers are injected from the source electrode. Sufficiently deep LUMO levels can accommodate the injection of electrons giving n-type semiconductors whilst higher lying HOMO levels accommodates good hole injection for p-type semiconductors. Materials that accommodate both hole and injection electron, with mobilities on a similar order of magnitude are known as ambipolar.

A majority of OFET polymers reported historically exhibit high hole transporting properties with electron mobilities that are several orders of magnitude lower due to the polymer E_{LUMO} values being too high lying to facilitate injection from the high work function electrode. OFET electron mobilities have since reached values of comparable magnitude through various techniques including synthetic LUMO stabilisation and varying of the electrode material.[53] Unlike OPV, the performances of OFET devices based upon conjugated polymers are now rivalling traditional silicon based technologies and examples of industrial prototype electronic devices based upon these materials are beginning to surface.[54]

1.7. Scope of thesis

The primary aim of this thesis is the synthesis of new D / A type semiconducting polymer for application in OPV and OFET devices. These new materials will have in common the general structural feature of a thieno[3,2-*b*]thiophene (TT) donor group, whilst the acceptor group will be based upon a bis-lactam core with a diketopyrrolopyrrole (**DPP**) or isoindigo structure. Both **DPP** and isoindigo based polymers receive much research attention due to their impressive charge transport properties, highly planar structures, strong intermolecular interactions and relative ease of synthetic structural modification.[55,56]

Thieno[3,2-*b*]thiophene flanked **DPP** polymers (**DPPTT**) have previously been reported by *H. Bronstein et al.* and several more recent publications have expanded the depth of knowledge of the structure.[57-60] Through small and targeted modifications of the solubilising branched alkyl chains, detailed structure – property relationships will be established specifically with a view to improving the OPV device morphological arrangement and subsequent performance.

Concerning the branched alkyl chains, specific focus will be paid to the critical role the alkyl chain branching position plays with regards to a variety of physical properties that are key to the operation of organic electronic devices. During the undertaking of this research it was demonstrated by *T. Lei et al.* how modification of these branching positions was beneficial to the OFET performance of a variety of polymers through influencing $\pi - \pi$ stacking interactions.[61,62] The evaluation of this

structural modification in materials for OPV applications however has not been reported and is of significant interest to the field.

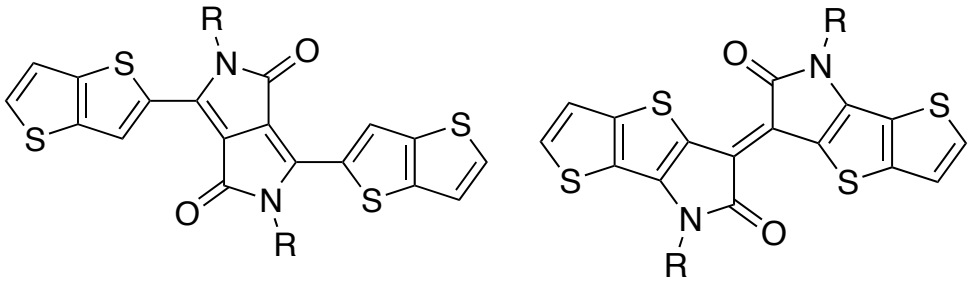

Thieno[3,2-b]thiophene diketoypyrrolopyrrole (DPPTT)

Thieno[3,2-b]thiophene isoindigo (iITT)

Figure 1.16. Chemical structures of **DPPTT** and **iITT** units.

Further to the tuning of alkyl chains, the **DPPTT** structure will be used as a basis for investigating the effect of heavy atom substitution with regards to increasing heteroatomic size (T, Se, Te) in a series of chalcogenophene based co-monomers. There is a significant lack of work investigating the effect of chalcogen atomic variation on organic electronic applications. In particular the reduced aromaticity down the series will be used to obtained narrowed E_g values whilst closer heteroatomic contacts between polymer chains will influence polymer interactions in solution and the solid state.

Moving attention to the structurally similar electron-deficient isoindigo unit, the same thieno[3,2-*b*]thiophene donor group will be introduced and a series of di-thienothienyl isoindigo (**iITT**) co-polymers will be targeted. The equivalent di-thienyl flanked polymers are established as some of the highest performing isoindigo structures in OFET applications.[63,47] The introduction of the more fused thieno[3,2-*b*]thiophene unit will serve to extend orbital delocalisation and increase polymer coplanarity. Considering the improvements observed with the progression from **DPPT** to **DPPTT**, it is reasonable to anticipate this new **iITT** structure will exhibit the potential to establish itself among the leaders within this specific family of polymers.

1.8. References

1. U.S. Energy Information Administration, *International energy outlook 2013*, 2013.
2. United Nations Department of Economic and Social Affairs, *World population prospects: 2012 revision*, 2012.
3. BP, *BP Statistical review of world energy 2014*, 2014.
4. Met Office, *Met Off. Hadley Cent. Obs. datases HadCRUT.4.2.0.0*, 2012.
5. REN21 Network, *Renewables global status report*, 2014.
6. R. Nielsen, *Solar Radiation*, 2005.
7. D. M. Chapin, C. S. Fuller and G. L. Pearson, *J. Appl. Phys.*, 1954, **25**, 676.
8. European Photovoltaic Industry Association, *Global market outlook for photovoltaics 2014-2018*, 2014.
9. E. Alsema, *Photovoltaics and the environment Keystone Colorado workshop proceedings July 1998*, 1998.
10. B. C. Schroeder, Z. Huang, R. S. Ashraf, J. Smith, P. D'Angelo, S. E. Watkins, T. D. Anthopoulos, J. R. Durrant and I. McCulloch, *Adv. Funct. Mater.*, 2012, **22**, 1663–1670.
11. H. Zhou, L. Yang, A. C. Stuart, S. C. Price, S. Liu and W. You, *Angew. Chemie-International Ed.*, 2011, **50**, 2995–2998.
12. S. C. Price, A. C. Stuart, L. Yang, H. Zhou and W. You, *J. Am. Chem. Soc.*, 2011, **133**, 4625–4631.
13. C. K. Chiang, C. R. Fincher, Y. W. Park, A. J. Heeger, H. Shirakawa, E. J. Louis, S. C. Gau and A. G. MacDiarmid, *Phys. Rev. Lett.*, 1977, **39**, 1098–1101.
14. C. W. Tang, *Appl. Phys. Lett.*, 1986, **48**, 183-185
15. G. Yu, J. Gao, J. C. Hummelen, F. Wudl and A. J. Heeger, *Science*, 1995, **270**, 1789–1791.
16. J. J. M. Halls, C. A. Walsh, N. C. Greenham, E. A. Marseglia, R. H. Friend, S. C. Moratti and A. B. Holmes, *Nature*, 1995, **376**, 498–500.
17. S. E. Shaheen, C. J. Brabec, N. S. Sariciftci, F. Padinger, T. Fromherz and J. C. Hummelen, *Appl. Phys. Lett.*, 2001, **78**, 841-843.
18. P. Schilinsky, C. Waldauf and C. J. Brabec, *Appl. Phys. Lett.*, 2002, **81**, 3885.
19. D. Minh Trung, L. Hirsch and G. Wantz, *Adv. Mater.*, 2011, **23**, 3597–3602.
20. S.-H. Lee, J.-H. Kim, T.-H. Shim and J.-G. Park, *Electron. Mater. Lett.*, 2009, **5**, 47–50.
21. S.-H. Lee, D.-H. Kim, J.-H. Kim, G.-S. Lee and J.-G. Park, *J. Phys. Chem. C*, 2009, **113**, 21915–21920.
22. C. Z. Zhicai He, Shijian Su, Miao Xu, Hongbin Wu & Yong Cao, *Nat. Photonics*, 2012, **6**, 591–595.
23. J. You, L. Dou, K. Yoshimura, T. Kato, K. Ohya, T. Moriarty, K. Emery, C.-C. Chen, J. Gao, G. Li and Y. Yang, *Nat. Commun.*, 2013, **4**, 1446.
24. D. E. Markov, E. Amsterdam, P. W. M. Blom, A. B. Sieval, and J. C. Hummelen, *J. Phys. Chem. A*, 2005, **109**, 5266–5274.
25. R. R. Lunt, N. C. Giebink, A. A. Belak, J. B. Benziger and S. R. Forrest, *J. Appl. Phys.*, 2009, **105**.
26. H. Hoppe and N. S. Sariciftci, *J. Mater. Chem.*, 2006, **16**, 45–61.
27. W. A. Luhman and R. J. Holmes, *Adv. Funct. Mater.*, 2011, **21**, 764–771.
28. K. Vakhshouri, D. R. Kozub, C. Wang, A. Salleo and E. D. Gomez, *Phys. Rev. Lett.*, 2012, **108**, 26601.
29. B. A. Collins, E. Gann, L. Guignard, X. He, C. R. McNeill and H. Ade, J. *Phys. Chem. Lett.*, 2010, **1**, 3160–3166.

30. M. C. Scharber, D. Wuhlbacher, M. Koppe, P. Denk, C. Waldauf, A. J. Heeger and C. L. Brabec, *Adv. Mater.*, 2006, **18**, 789.
31. S. Bertho, G. Janssen, T. J. Cleij, B. Conings, W. Moons, A. Gadisa, J. D'Haen, E. Goovaerts, L. Lutsen, J. Manca, and D. Vanderzande, *Sol. Energy Mater. Sol. Cells*, 2008, **92**, 753–760.
32. K. Kawano, J. Sakai, M. Yahiro and C. Adachi, *Sol. Energy Mater. Sol. Cells*, 2009, **93**, 514–518.
33. K. R. Graham, P. M. Wieruszewski, R. Stalder, M. J. Hartel, J. Mei, F. So and J. R. Reynolds, *Adv. Funct. Mater.*, 2012, **22**, 4801–4813.
34. G. Li, Y. Yao, H. Yang, V. Shrotriya, G. Yang and Y. Yang, *Adv. Funct. Mater.*, 2007, **17**, 1636–1644.
35. H. C. Yang, T. J. Shin, Z. N. Bao, K. Cho and C. Y. Ryu, *229th National meeting of the American Chemical Society San Diego CA 2005*, 2005, 336.
36. J. K. Lee, W. L. Ma, C. J. Brabec, J. Yuen, J. S. Moon, J. Y. Kim, K. Lee, G. C. Bazan and A. J. Heeger, *J. Am. Chem. Soc.*, 2008, **130**, 3619–3623.
37. J. Razzell-Hollis, W. C. Tsoi and J.-S. Kim, *J. Mater. Chem. C*, 2013, **1**, 6235–6243.
38. H. Peisert, M. Knupfer and J. Fink, *Appl. Phys. Lett.*, 2002, **81**, 2400–2402.
39. R. Steim, F. R. Kogler and C. J. Brabec, *J. Mater. Chem.*, 2010, 20, 2499–2512.
40. J. Zou, H.-L. Yip, Y. Zhang, Y. Gao, S.-C. Chien, K. O'Malley, C.-C. Chueh, H. Chen and A. K. Y. Jen, *Adv. Funct. Mater.*, 2012, **22**, 2804-2811.
41. S. K. Hau, H.-L. Yip and A. K.-Y. Jen, *Polym. Rev.*, 2010, **50**, 474–510.
42. T. Sekitani, U. Zschieschang, H. Klauk and T. Someya, *Nat. Mater.*, 2010, **9**, 1015–1022.
43. S. J. Benight, C. Wang, J. B. H. Tok and Z. Bao, *Prog. Polym. Sci.*, 2013, **38**, 1961–1977.
44. S. Holliday, J. E. Donaghey and I. McCulloch, *Chem. Mater.*, 2013, **26**, 647–663.
45. M. E. Roberts, A. N. Sokolov and Z. N. Bao, *J. Mater. Chem.*, 2009, **19**, 3351–3363.
46. J. Li, Y. Zhao, H. S. Tan, Y. L. Guo, C. A. Di, G. Yu, Y. Q. Liu, M. Lin, S. H. Lim, Y. H. Zhou, H. B. Su and B. S. Ong, *Sci. Rep.*, 2012, **2**.
47. G. Kim, S.-J. Kang, G. K. Dutta, Y.-K. Han, T. J. Shin, Y.-Y. Noh and C. Yang, *J. Am. Chem. Soc.*, 2014, **136**, 9477–9483.
48. H. Chen, Y. Guo, G. Yu, Y. Zhao, J. Zhang, D. Gao, H. Liu and Y. Liu, *Adv. Mater.*, 2012, **24**, 4618–4622.
49. H.-R. Tseng, H. Phan, C. Luo, M. Wang, L. A. Perez, S. N. Patel, L. Ying, E. J. Kramer, T.-Q. Nguyen, G. C. Bazan and A. J. Heeger, *Adv. Mater.*, 2014, **26**, 2993–2998.
50. W. Zhang, J. Smith, S. E. Watkins, R. Gysel, M. McGehee, A. Salleo, J. Kirkpatrick, S. Ashraf, T. Anthopoulos, M. Heeney and I. McCulloch, *J. Am. Chem. Soc.*, 2010, **132**, 11437–11439.
51. C. B. Nielsen, M. Turbiez, and I. McCulloch, *Adv. Mater.*, 2012, **25**, 1859-1880.
52. L. Biniek, B. C. Schroeder, C. B. Nielsen, and I. McCulloch, *J. Mater. Chem.*, 2012, **22**, 14803–14813.
53. X. Cheng, Y.-Y. Noh, J. Wang, M. Tello, J. Frisch, R.-P. Blum, A. Vollmer, J. P. Rabe, N. Koch and H. Sirringhaus, *Adv. Funct. Mater.*, 2009, **19**, 2407–2415.
54. Sony, *Sony Press Release 26/05/10*, 2010.
55. D. Chandran and K.-S. Lee, *Macromol. Res.*, 2013, **21**, 272–283.
56. L. A. Estrada, R. Stalder, K. A. Abboud, C. Risko, J.-L. Brédas and J. R. Reynolds, *Macromolecules*, 2013, **46**, 8832–8844.
57. Y. Li, S. P. Singh and P. Sonar, *Adv. Mater.*, 2010, **22**, 4862–4866.
58. H. Bronstein, E. Collado-Fregoso, A. Hadipour, Y. W. Soon, Z. Huang, S. D. Dimitrov, R. S. Ashraf, B. P. Rand, S. E. Watkins, P. S. Tuladhar, I. Meager, J. R. Durrant and I. McCulloch, *Adv. Funct. Mater.*, 2013, **23**, 5647–5654.

59. Z. Chen, M. J. Lee, R. Shahid Ashraf, Y. Gu, S. Albert-Seifried, M. Meedom Nielsen, B. Schroeder, T. D. Anthopoulos, M. Heeney, I. McCulloch and H. Sirringhaus, *Adv. Mater.*, 2012, **24**, 647–52.
60. H. Bronstein, Z. Chen, R. S. Ashraf, W. Zhang, J. Du, J. R. Durrant, P. S. Tuladhar, K. Song, S. E. Watkins, Y. Geerts, M. M. Wienk, R. A. J. Janssen, T. Anthopoulos, H. Sirringhaus, M. Heeney and I. McCulloch, *J. Am. Chem. Soc.*, 2011, **133**, 3272–3275.
61. J.-H. Dou, Y.-Q. Zheng, T. Lei, S.-D. Zhang, Z. Wang, W.-B. Zhang, J.-Y. Wang and J. Pei, *Adv. Funct. Mater.*, **2014**, ASAP, DOI: 10.1002/adfm.201401822
62. T. Lei, J.-H. Dou and J. Pei, *Adv. Mater.*, 2012, **24**, 6457–6461.
63. Y. Koizumi, M. Ide, A. Saeki, C. Vijayakumar, B. Balan, M. Kawamoto and S. Seki, *Polym. Chem.*, 2013, **4**, 484–494.

Chapter Two

Alkyl Chain Extension and Polymer Fractionation as Routes Towards Novel Thieno[3,2-*b*]thiophene Flanked Diketopyrrolopyrrole Polymers for High Performance OPV and OFET Applications

2.1. Introduction

Diketopyrrolopyrrole (**DPP**) is a versatile structural unit for the design of semiconducting conjugated polymers. Its electron-deficient core comprises two fused ketopyrrole rings which are generally flanked by an electron-rich aromatic unit. It's D / A type structure facilitates strong interchain interactions, whilst the nitrogen atoms on the ketopyrrole core are readily alkylated to ensure solution processability. The first **DPP** based polymers were reported with phenyl flanking units giving a di-phenyl **DPP** structure that has been widely studied and characterised in a variety of different applications.[1,2] Subsequent structural variations in the **DPP** flanking units, solubilising *N*-alkyl chains and co-monomers were rapidly investigated and a seemingly natural progression to di-thienyl **DPP** was observed.[3,4] Introduction of the thiophene unit reduced the steric clash observed in di-phenyl **DPP** between lactam oxygen atoms on the **DPP** core and phenyl α-hydrogens, whilst the increased planarity gave some of the most promising results in both OPV and OFET applications at the time.[5,6] In 2011 *H. Bronstein et al.*, reported a further progression in **DPP** based polymers with the synthesis and characterisation of the thieno[3,2-*b*]thiophene (TT) flanked diketopyrrolopyrrole (**DPPTT**) unit and its subsequent application in homo- and co- polymers for OPV and OFET devices (**Figure 2.1**).[7]

The **DPPTT** core was synthesised by the condensation of thieno[3,2-*b*]thiophene-2-carbonitrile with diisopropyl succinate and alkylated with a branched 2-octyl-dodecyl (C_8C_{10}) group before brominattion. Polymerisation of the brominated monomer with thiophene by palladium-catalysed Stille coupling afforded the first reported example of the polymer **DPPTT-T**. The analogous **DPPTT** homo-polymer was also synthesised using palladium-catalysed 'Stille-like' homo-polymerisation.

The resultant co- and homo- polymers were screened for their performance in bulk OPV and OFET devices giving solar cell efficiencies in excess of 5 % and hole mobilities > 1 cm^2 / Vs in top gate / bottom contact devices. The introduction of the electron-rich thieno[3,2-*b*]thiophene ring gives the D / A type polymer a stronger donor unit relative to the previously reported di-thienyl and di-phenyl **DPP** polymers. This resulted in an optical band gap reduction due to enhanced molecular orbital hybridization between the adjacent donor and acceptor units which corresponds to a significantly red-shifted UV-Vis absorption profile.[8,9] The fused structure of the TT

unit was also seen to extend the coplanarity of the polymer structure and promote a more delocalized HOMO distribution along the polymer backbone. In combination with increased intermolecular association between polymer chains this proved beneficial for the charge transport properties of the polymer.

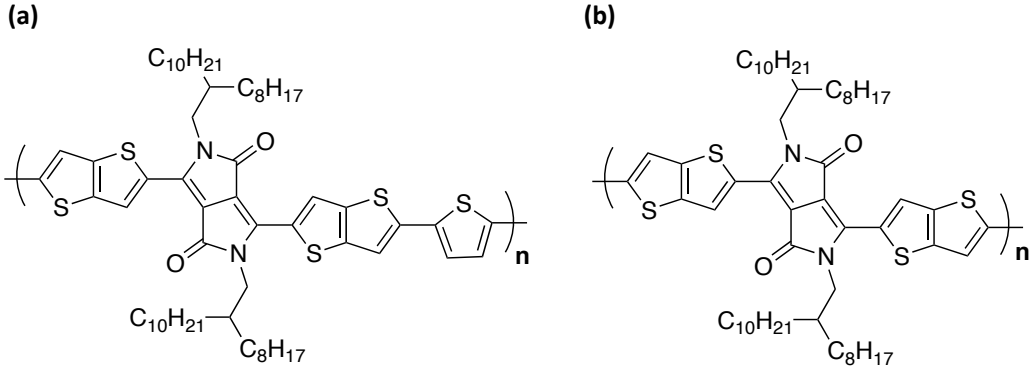

Figure 2.1. Chemical structures of **(a) DPPTT-T** co-polymer and **(b) DPPTT** homo-polymer reported by *H. Bronstein et al*.[7]

Whilst the reported OPV and OFET performance were good, the polymers had fairly poor intrinsic solubility in common organic solvents. This resulted in limitations regarding the choice of co-monomer units that could be employed, which in turn prevented a comprehensive exploration of the material properties of the **DPPTT** unit. The number average molecular weights (M_n) achieved with these polymers were also limited (14 kDa and 16 kDa for co- and homo- polymers respectively), due to polymeric material crashing-out of solution during the polymerisation process. The molecular weight of a polymer has long been established as a critical factor in influencing the OPV and OFET device performances of a material and can be a key parameter when tuning the material's morphology both in the pristine film and the polymer / fullerene blend. Consequently with the low M_n values reported it is not clear whether the best device performance of **DPPTT** is being achieved.[10,11]

A further consequence of the limited solubility was that the polydispersity indexes (PDI) of the polymers were also fairly broad (5.4 and 4.9 for co- and homo- polymers respectively). The PDI of a polymer has been shown to influence their performance in both OPV and OFET devices and values as narrow as 2 are often seen as desirable. The reduced variation in polymer chain size can lead to greater uniformity over the morpohological and microstructural arrangement of polymer chains which is generally beneficial for control over the charge transport properties of polymers.[12] As

a result, several synthetic strategies and approaches towards reduced mass distributions are often reported throughout the literature.[13]

It was therefore of interest to observe whether increasing the intrinsic solubility of the **DPPTT** unit would facilitate the synthesis of higher M_n and narrowed PDI materials and whether this would be beneficial for the performances of the resultant OPV and OFET devices.

2.2. Aim

Through the synthesis of the branched 2-decyltetradecyl ($C_{10}C_{12}$) alkyl chain and its subsequent attachment to the lactam nitrogen of **DPPTT** it is hoped that this extension in alkyl chain size, C_8C_{10} to $C_{10}C_{12}$, with four extra carbon atoms per alkyl chain will result in improved solubility of **DPPTT** based polymers. The enhanced solubility should improve the polymerisation process giving higher molecular weight materials with narrowed polydispersities.[14]

The improved solubility of the **DPPTT** co-monomer should also enable polymerisation with a wider range of co-monomers than were previously accessible. In the case of C_8C_{10} alkylated **DPPTT**, thiophene is the only co-monomer unit that resulted in solution processable polymers. When co-polymerisations with monomer units containing a more fused or larger aromatic structure were attempted it was not possible to obtain a sufficiently soluble polymer. Through the introduction of a larger, more solubilising alkyl chain it is hoped that the synthesis of **DPPTT** based polymers with thiophene (T), thieno[3,2-*b*]thiophene (TT), benzothiadiazole (BT) and phenyl (P) can be attempted.

Thiophene and thienothiophene were chosen as co-monomer units to achieve highly planar polymer backbones beneficial for charge transport, the fused nature of thieno[3,2-*b*]thiophene in particular offering increased planarity. Benzothiadiazole and phenyl units were chosen as previous work in analogous **DPP-BT** and **DPP-P** polymers have shown excellent ambipolar OFET mobilities and good solar cell efficiencies respectively.[15,16]

2.3. Synthesis of polymers P1 - P4

2.3.1. Monomer synthesis

The synthesis of the **DPPTT** core is reproduced as according to literature procedures (**Figure 2.2**) using a synthetic route in which a carbonitrile is condensed with a succinate group. This route is general for **DPP** structures regardless of the nature of the flanking aromatic unit.[17-19] Commercially available thieno[3,2-*b*]thiophene was lithiated at the activated *2* position in tetrahydrofuran (THF) at -78 ºC using *n*BuLi with care being taken to use only one equivalent of the organolithium reagent so as not to over lithiate the starting material. The lithiation proceeded for one hour at -78 ºC before it was quenched with dimethylformamide (DMF). Allowing the solution to warm to room temperature overnight followed by a subsequent short silica column with hexane as the eleuent afforded the formylated product thieno[3,2-*b*]thiophene-2-carbaldehyde **2.1** in good yield. ^{1}H NMR characterisation of the product showed the strongly de-shielded aldehyde proton appearing at 10.00 ppm.

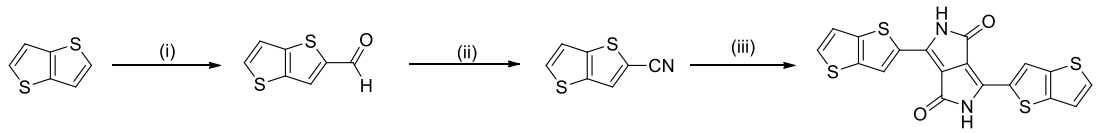

2.1 **2.2** **2.3**

Figure 2.2. Synthesis of **DPPTT** core. *Reagents and conditions*: **(i)** *n*BuLi, THF, DMF, -78 ºC **(ii)** NH_3 (aq), THF / MeCN, I_2, 0 ºC **(iii)** Na, 2-methyl-2-butanol, $FeCl_3$, diisopropyl succinate, 80 ºC.

Once isolated, thieno[3,2-*b*]thiophene-2-carbaldehyde **2.1** was converted to thieno[3,2-*b*]thiophene-2-carbonitrile **2.2** using iodine in aqueous ammonia via formation and subsequent oxidation of the corresponding imine with elimination of an HI molecule to give the desired carbonitrile functionality.[20] Aqueous work-up afforded the product thieno[3,2-*b*]thiophene-2-carbonitrile **2.2** in good yield and no further purification was necessary. As shown in **Figure 2.3** ^{1}H NMR shows the disappearance of the characteristically de-shielded aldehyde proton at 10.00 ppm whilst the three aromatic peaks observed in the starting material remain.

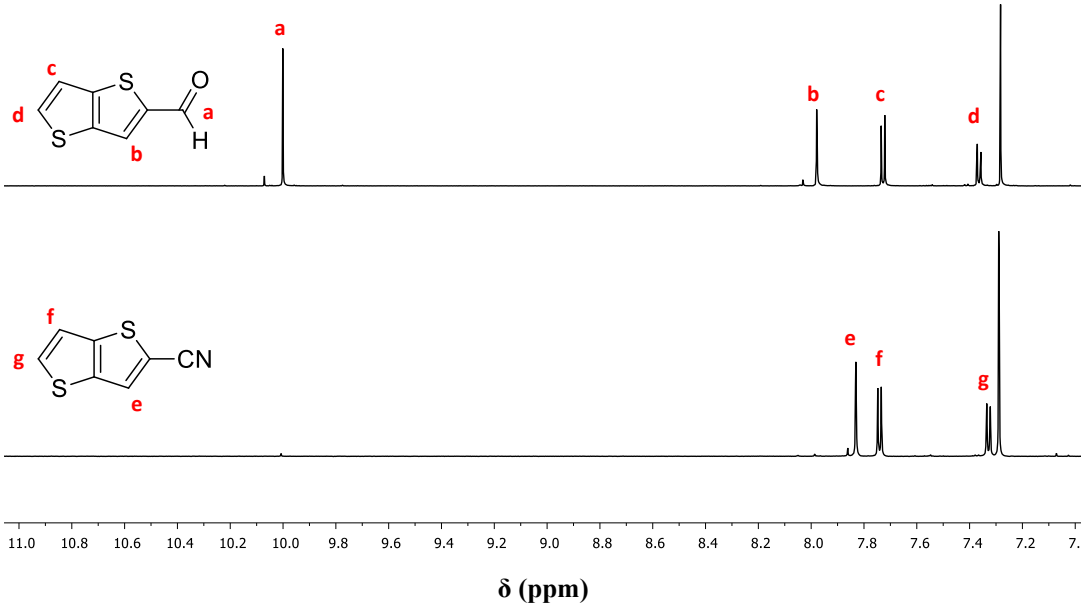

Figure 2.3. ^{1}H NMR in $CDCl_3$ at 25 ºC of compounds **2.1** and **2.2** showing the characteristic changes associated with each transformation.

The ring closing condensation reaction of thieno[3,2-*b*]thiophene-2-carbonitirile **2.2** with diisopropyl succinate was performed at 80 ºC under basic conditions. Following an acidic quench the mixture was cooled to room temperature and filtered to afford the poorly soluble dark blue / black solid **DPPTT** core **2.3**. The product was washed repeatedly in multiple solvents to remove any inorganic or organic impurities or side products from the reaction and used without any further purification or characterisation.

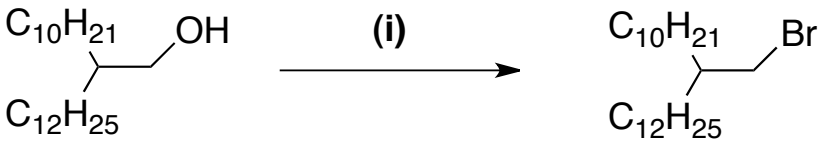

2.4

Figure 2.4. Synthesis of $C_{10}C_{12}$ alkyl chain **2.4.** *Reagents and conditions*: **(i)** NBS, PPh_3, DCM, 0 ºC.

As shown in **Figure 2.4** the larger alkyl chain 2-decyl-1-tetradecyl bromide **2.4** was synthesised under mild conditions from the commercially available alcohol using N-bromosuccinimide (NBS) before subsequent attachment to the **DPPTT** core **2.3**.

Next, the synthesised **DPPTT** core was deprotonated under basic conditions in DMF and alkylated via nucleophilic attack at the previously synthesised alkyl chain **2.4**. Relatively harsh heating conditions of 120 ºC for 18 hours were necessary due to the steric hindrance resulting from the bulky nature of the branched $C_{10}H_{21}$ / $C_{12}H_{25}$ alkyl groups inhibiting nucleophilic attack combined with the poor solubility of the **DPPTT** unit in common laboratory solvents. The solubilised product was easily isolated from the remaining non-alkylated **DPPTT** and the excess unreacted alkyl iodide removed by column chromatography. Even with the harsh conditions employed, a fairly low 35 % yield of alkylated product was obtained as a shiny deep red / purple solid. Branched alkylations of this nature generally proceed at lower yields than their linear counterparts due to the increased steric demand of the alkyl groups hindering the nucleophilic attack of the deprotonated nitrogen.[21] ^{1}H NMR shows an aromatic region with two doublets and a singlet, each of equal integration, corresponding to the three inequivelant thieno[3,2-*b*]thiophene protons.

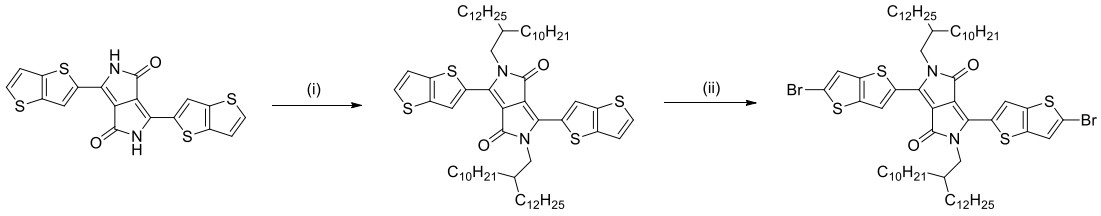

2.4 **2.5** **2.6**

Figure 2.5. Alkylation of **DPPTT** core to give compound **2.5** and subsequent bromination to compound **2.6**. *Reagents and conditions*: **(i)** 2-decyl-tetradecyl bromide **2.4**, K_2CO_3, 18-crown-6, DMF, 120 ºC **(ii)** Br_2, $CHCl_3$, 80 ºC.

Bromination of the two α-positions of the flanking thieno[3,2-*b*]thiophene units was achieved by facile electrophilic aromatic substitution using two equivalents of elemental bromine in chloroform. Care was taken to carefully control the stoichiometry of the reaction so as to avoid excessive over / under bromination. The di-brominated monomer was isolated from any non- and mono- brominated impurities by column chromatography as a shiny deep purple solid in good yield. Analysis by ^{1}H NMR shows the aromatic region to contain two singlets of equal integration corresponding to the two remaining inequivalent thieno[3,2-*b*]thiophene protons (**Figure 2.6**).

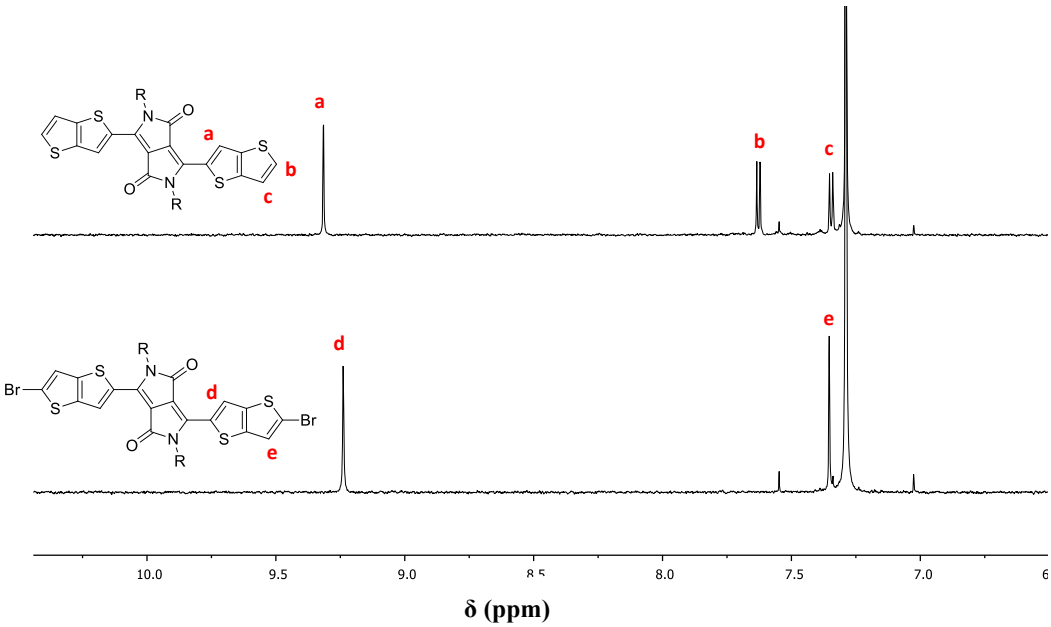

Figure 2.6. ^{1}H NMR in $CDCl_3$ at 25 ºC of compounds **2.5** and **2.6** showing the characteristic changes associated with each transformation.

2.3.2. Synthesis of polymers P1 and P2 by Stille coupling

Thiophene as a co-monomer is widely used in the synthesis of semiconducting polymers with a large number of structures based upon polythiophenes.[22] Its electron-rich nature can be used to good effect to decrease BLA and increase the electron density of the HOMO energy levels, resulting in narrowed E_g values. Synthetically, the use of the thiophene co-monomer is generally limited to Stille coupling as opposed to the less toxic Suzuki coupling which is not as frequently encountered for thiophene based co-monomers. This is understood to be a result of the electron-rich thiophene unit having an increased tendency for hydrolytic de-borolation before aryl – aryl coupling can occur, thus limiting the formation of the desired products.[23-25] Stille coupling is therefore generally preferably employed and it is believed that the electron-donating nature of the sulphur heteroatom accelerates the rate determining transmetalation step to afford highly efficient couplings.[14]

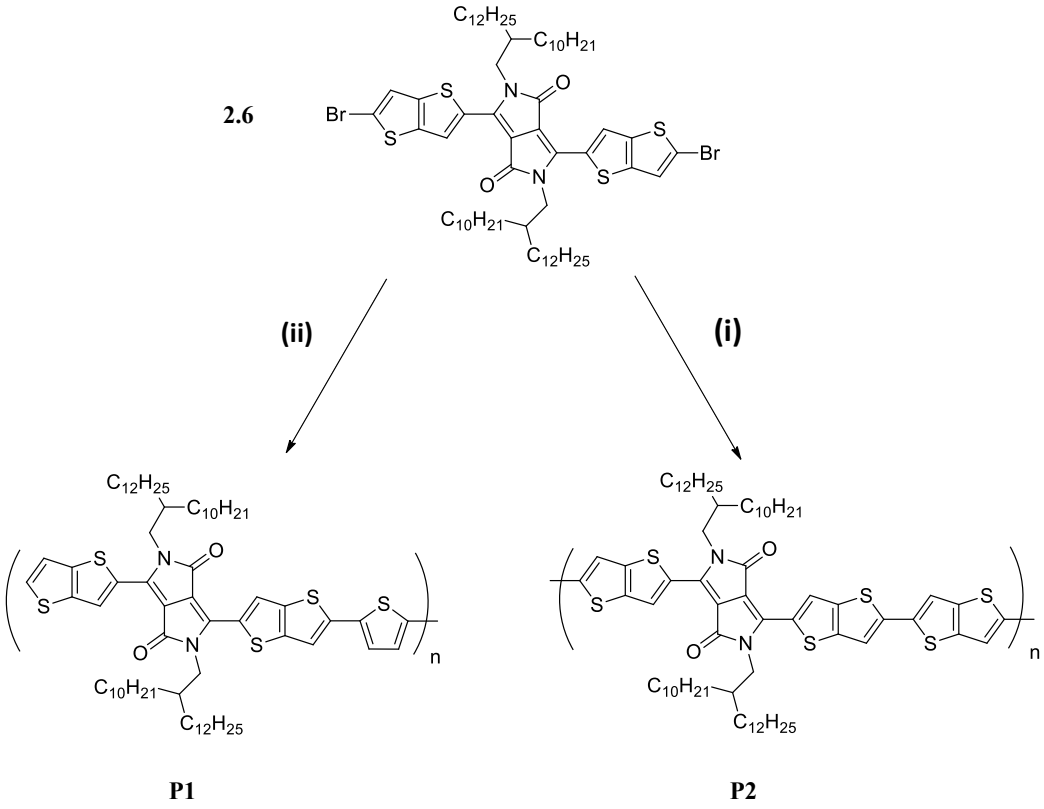

Figure 2.7. Synthesis of polymers **P1** and **P2** by palladium-catalysed Stille co-polymerisation of **2.6**. *Reagents and conditions*: **(i)** 2,5-bis(trimethylstannyl)thiophene, $Pd_2(dba)_3$, P(*o*Tol)$_3$, PhCl, μW **(ii)** 2,5-bis(trimethylstannyl)thieno[3,2-*b*]thiophene, $Pd_2(dba)_3$, P(*o*Tol)$_3$, PhCl, μW.

The thiophene and thieno[3,2-*b*]thiophene co-monomers with trimethyltin groups at the two α-positions were co-polymerised with equimolar amounts of the dibrominated **DPPTT** monomer **2.6** via microwave assisted palladium-catalysed Stille cross-coupling to afford **DPPTT-T P1** and **DPPTT-TT P2** co-polymers respectively. Both polymerisations were performed using microwave radiation in sealed microwave vials under argon in thoroughly degassed chlorobenzene. Sealed microwave vials allow the heating of high boiling point solvents such as chlorobenzene, toluene and DMF to temperatures significantly above their boiling point due to the internal pressure created within the vial, with significantly reduced reaction times relative to conventional heating techniques.[26] The chlorobenzene monomer solution was heated in successive intervals of increasing duration from 100 ºC up to 200 ºC with a total heating time of 1 ½ hours.

Upon cooling the viscous dark green gel was precipitated into vigorously stirring methanol and the polymeric precipitate filtered into a glass fibre Soxhlet thimble. Catalytic impurities and low molecular weight oligomers were removed from the polymeric mixture by Soxhlet extraction in methanol, acetone and hexane. The remaining high molecular weight polymeric material was removed from the thimble by solvation in chloroform and chlorobenzene. The dark green solutions obtained were concentrated and re-precipitated into methanol before filtration and drying in a high vacuum environment. The resultant polymer material was characterised by analytical gel permeation chromatography (GPC) in chlorobenzene and their physical properties are reported in **Table 2.1**.

Table 2.1. Physical properties of polymers **P1** and **P2**.

Polymer	M_n (kDa)[a]	M_w (kDa)[a]	PDI[a]	DP_n[a]
P1	148	385	2.6	126.7
P2	100	280	2.8	81.7

[a] M_n, M_w, PDI (M_w / M_n) and DP_n (M_n / M_0) determined by GPC at 80 ºC using low PDI (<1.10) polystyrene standards and chlorobenzene as the eluent.

2.3.3. Synthesis of polymers P3 and P4 by Suzuki coupling

Phenyl and benzothiadiazole are two aromatic units that can be used to afford less electron dense co-monomers and therefore offer the choice between the use of Stille or Suzuki coupling conditions. With its reduced electron density, the phenyl ring serves as a slightly weaker donor than thiophene with generally lower lying HOMO levels. This lowering of polymer HOMO levels can be a desirable feature when it comes to band gap engineering considerations as it is known that the V_{oc} of a bulk heterojunction solar cell is closely related to the energetic offset between the polymer HOMO level and the fullerene LUMO level.[27,28] The V_{oc} enhancement however often comes at the cost of a widened optical band gap which can be unfavourable for light absorption. Benzothiadiazole has a strongly electron-withdrawing thiadiazole unit that is fused to the benzene ring, which makes the BT unit a co-monomer with strong acceptor characteristics. This electron-withdrawing nature results in the lowering of E_{HOMO} and E_{LUMO} by varying amounts and is a useful tool towards enhancing a material's donor / acceptor characteristics.[16]

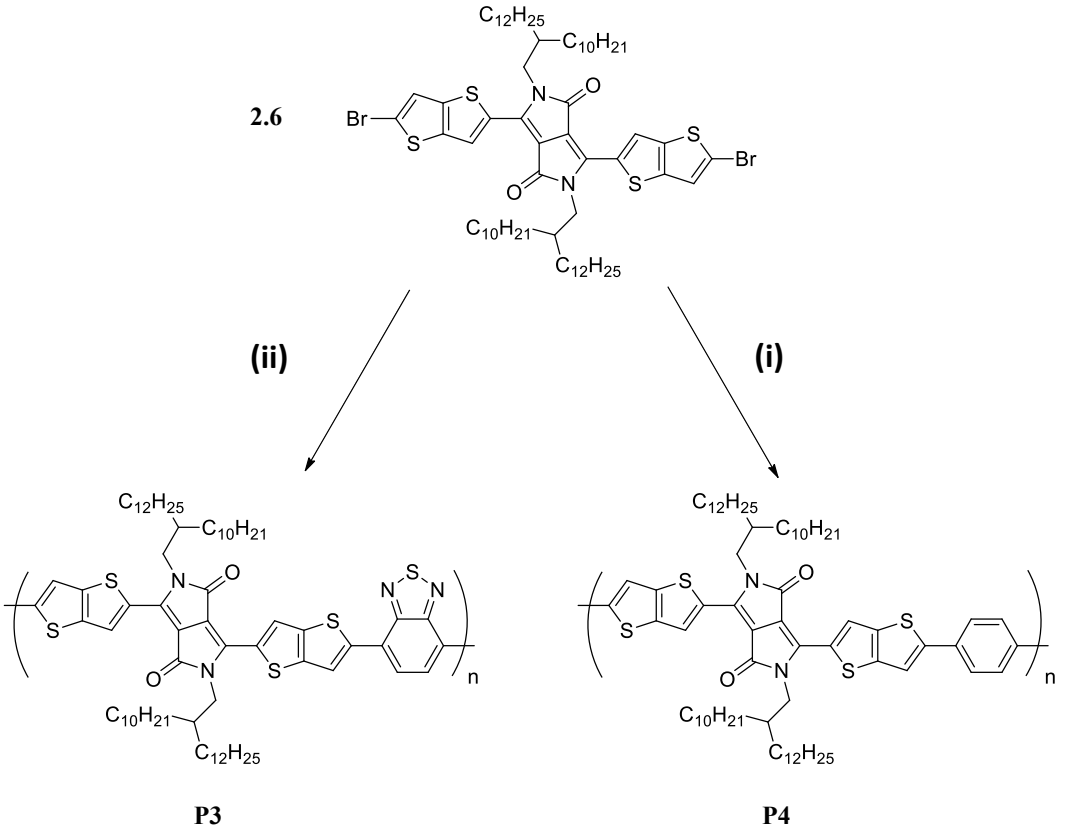

Figure 2.8. Synthesis of polymers **P3** and **P4** by palladium-catalysed Suzuki co-polymerisation of **2.6**. *Reagents and conditions*: **(i)** 4,7-bis(4,4,5,5-tetramethyl-1,3,2-dioxabrolan-2-yl)-benzothiadiazole, K_2CO_3 / PhMe, Aliquat 336, $Pd_2(PPh_3)_4$, 120 ºC. **(ii)** 1,4-di(4,4,5,5-tetramethyl-1,3-dioxaboralane)benzene, K_3PO_4 / PhMe, Aliquat 336, $Pd_2(dba)_3$, PPh_3, 120 ºC.

Co-monomers consisting of a phenyl ring borylated at the *1* and *4* positions and a benzothiadiazole unit borylated at the *4* and *7* positions were co-polymerised with equimolar amounts of the dibrominated **DPPTT** monomer **2.6** using palladium-catalysed Suzuki cross-coupling to afford **DPPTT-BT** (**P3**) and **DPPTT-P** (**P4**) co-polymers. Suzuki polymerisations are bi-phasic with the monomers and catalyst dissolved in a high boiling point organic solvent, toluene in this instance, and the base required for monomer activation dissolved in an aqueous phase. Using a phase transfer catalyst such as Aliquat 336 with vigorous stirring at 120 ºC in a sealed vial, the polymerisation is able to take place and over the course of 3 days a colour change to dark green is observed in the organic phase. The resulting polymeric solutions were worked up and purified in a similar fashion to the previously described Stille polymerisations with purification by Soxhlet extraction. Polymers were characterised

by analytical GPC in chlorobenzene and their physical properties are reported in **Table 2.2**.

Table 2.2. Physical properties of polymers **P3** and **P4**.

Polymer	M_n (kDa)[a]	M_w (kDa)[a]	PDI[a]	DP_n[a]
P3	50	78	1.6	41.0
P4	23	42	1.8	19.8

[a] M_n, M_w, PDI (M_w / M_n) and DP_n (M_n / M_0) determined by GPC at 80 ºC using low-PDI (<1.10) polystyrene standards and chlorobenzene as the eluent.

2.4. Optical and physical properties of P1 - P4

2.4.1. Optical properties

All four synthesised polymers demonstrated good solubility as demonstrated by the range of high M_n and narrow PDI values obtained (**Table 2.3**). Each of the polymers in the series exhibit broad red-shifted UV-Vis absorption profiles (**Figure 2.9**), with λ_{max} ranging from 750 nm – 800 nm. These red-shifted absorption profiles are a result of E_g values that are estimated to be relatively narrow, ranging from 1.3 – 1.5 eV. E_g values were estimated by the UV-Vis absorption onset and the LUMO levels (E_{LUMO}) by the addition of the estimated band gaps (E_g) to the experimentally determined HOMO energy levels (E_{HOMO}). Polymer E_{HOMO} values were determined experimentally by photoelectron spectroscopy in air (PESA), which is a surface technique that measures photoelectrons emitted from the surface of a polymer film under monochromatic irradiation.

As with the previously reported **DPPTT-T** co-polymer with shorter C_8C_{10} alkyl chains, **P1** has a single broad absorption. It also demonstrates very similar absorption maxima with λ_{max} at 779 nm in solution and a slightly more red-shifted 787 nm in the thin film. This shows that the slightly larger $C_{10}C_{12}$ alkyl chain, as expected, does not have a noticeable effect on the absorption profile of the polymer. The absence of a noticeable change in the shape of the absorption profile also indicates that there is not a large reduction in aggregation in going from C_8C_{10} to $C_{10}C_{12}$ alkylated material.

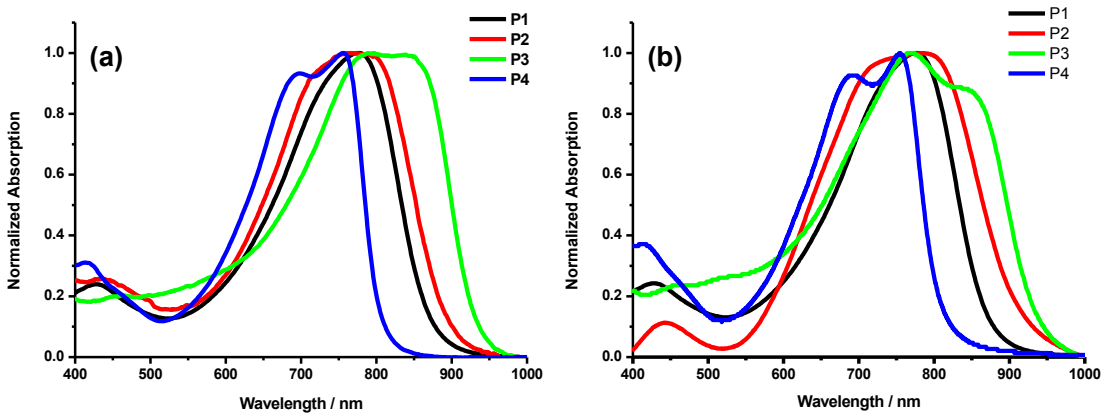

Figure 2.9. Room temperature normalised UV-Vis absorption profiles of polymers **P1** – **P4** **(a)** in dilute chlorobenzene solution and **(b)** thin film spun on glass substrates from 5 mg / mL chlorobenzene solution.

P2 compared to **P1** sees the thiophene co-monomer replaced by the more electron-rich fused thieno[3,2-*b*]thiophene unit. The increased electron density and increased quinoidal contribution results in E_{HOMO} being raised by 0.2 eV from -5.2 eV to -5.0 eV and a slight reduction in E_g from 1.4 eV to 1.3 eV. Both **P1** and **P2** show a red-shift in going from the solution to thin film spectra due to increased aggregation in the solid state, a feature that is common to conjugated polymers.[29] **P2** can also be seen to show a small broadening of the absorption profile compared to **P1** whilst the λ_{max} of **P2** remains relatively unchanged in both the solution and thin film (771 nm and 783 nm respectively). The lack of red-shift in λ_{max} by changing from thiophene to thieno[3,2-*b*]thiophene is unexpected, however there is an observable red-shift in the onset of the thin film absorption of **P2** relative to **P1** which explains the variation in E_{LUMO} values. This is absent for the solution absorption profiles and it is likely that this red-shift only being observable in the thin film is a result of the extra fused thiophene ring of the thieno[3,2-*b*]thiophene resulting in increased aggregation in the solid state relative to thiophene in **P1**.

Unlike **P1** and **P2**, **P3** and **P4,** which have benzothiadiazole and phenyl co-monomers respectively, do not exhibit a red-shifted λ_{max} in going from the solution to thin film. **P3** has a thin film λ_{max} of 774 nm whilst in solution it is 796 nm and in **P4** there is no change between solution and thin film with both λ_{max} at 755 nm. The electron-withdrawing benzothiadiazole co-monomer in **P3** lowers both E_{HOMO} and E_{LUMO} by

different amounts with a narrowing of E_g, which results in the most red-shifted absorption onsets of the series.

Table 2.3. Optical properties of polymers **P1** – **P4**.

Polymer	λ_{max} (nm) Film[a]	λ_{max} (nm) Solution[b]	E_{HOMO} (eV)[c]	E_{LUMO} (eV)[d]	E_g (eV)[d]
P1	787	779	-5.2	-3.8	1.42
P2	783	771	-5.0	-3.7	1.34
P3	774	796	-5.1	-3.8	1.32
P4	755	755	-5.1	-3.6	1.53

[a] Spin coated on glass substrates from 5 mg / mL polymer solution in chlorobenzene [b] measured in dilute chlorobenzene solution [c] HOMO energies (E_{HOMO}) determined by PESA[d] LUMO energies (E_{LUMO}) estimated by addition of thin film absorption onset onto E_{HOMO} [f] Band gap (E_g) estimated as the difference between the experimentally determined E_{HOMO} and optically estimated E_{LUMO}.

With a phenyl co-monomer unit in **P4** there is a significantly wider E_g of 1.5 eV and this widening is partly due to the reduced electron density contribution to the HOMO by the phenyl unit and partly a result of a steric clash that is known to occur between protons on adjacent thiophene and phenyl rings.[30] This can result in torsional twisting of the phenyl ring giving reduced planarity along the polymer backbone with less efficient conjugation and a broadening of E_g. This steric clash has been previously reported with similar polymer structures and it is possible to estimate its effect by TD / DFT calculations using a B3LYP / 6-31g* basis set as shown in **Figure 2.10**. The details of these calculations are further discussed in section **2.4.3**. As a result **P4** has the most blue-shifted absorption profile of each of the polymers in the series in both the thin film and solution spectra.

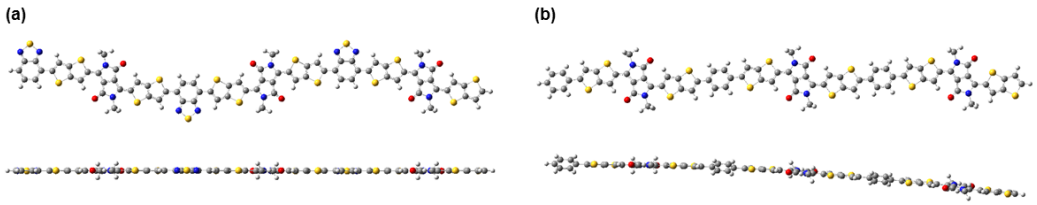

Figure 2.10. TD / DFT calculated polymer backbones and long axis linearities of polymers **(a) P3** and **(b) P4** exemplifying the backbone twist arising from the phenyl co-monomer.

A further comparison to be made is between the modalities of the absorption profiles across the series and there is a marked variation which can be related to the nature of the changing co-monomer unit. In both solution and thin film spectra, **P1** and **P2** with thiophene and thieno[3,2-*b*]thiophene units respectively, generally show single broad absorpttions. Both **P3** and **P4** have absorption structures that are significantly more bimodal compared to **P1** and **P2**, which is likely a result of vibronic coupling. As is often observed with conjugated polymers the vibronic structures are significantly more pronounced in the thin film than in the solution which is understood to be related to increased aggregation between polymer chains in the solid state.[31]

Generally when describing the role that different backbone structures play in influencing the light absorption of a polymer, λ_{max} is often quoted as a value that is indicative of the nature of this absorption. However various features can influence where this maximum lies and as a result the absorption onset can often be a more accurate descriptor when comparing two different polymer structures.[32] Considering **P1** – **P4**, the λ_{max} of the four polymers show very different trends in λ_{max} in the solution and thin films, which is likely a result of a complex interplay between the different factors described. In solution, polymer **P4** has the shortest λ_{max} at 755 nm, which shows a good match with the polymer's wider E_g, at the other extreme **P3** shows the narrowest E_g due to its electron-withdrawing co-monomer unit corresponding to the most red-shifted λ_{max} at 796 nm.

When the thin film absorption is considered the trend is not as closely related to the structure of the co-monomer unit as in solution. An example of this is with the narrowest E_g polymer **P3** (1.3 eV) which would be expected to correlate to the most red-shifted absorption profile yet has a λ_{max} that is at a shorter wavelength than both **P1** and **P2** which have wider E_g values. The trend in absorption of polymers **P1** – **P4** is better described by the absorption onsets (λ_{onset}), which is consistent with the structure of the co-monomer unit regardless of whether solution or thin film spectra are considered. **P3** has the most red-shifted onsets in solution and thin film at 931 nm and 932 nm respectively due to its narrow E_g. **P2** has the next longest wavelength λ_{onset} as it is a stronger donor unit than **P1**, which follows close after with slightly shorter wavelength λ_{onset}. **P4** with the widest E_g for the reasons previously described has the most blue shifted solution and thin film λ_{onset} values at 803 nm and 807 nm respectively.

Table 2.4. λ_{max} and λ_{onset} of polymers **P1** – **P4** in solution and thin film.

	λ_{max} (nm)		λ_{onset} (nm)	
Polymer	Film[a]	Solution[b]	Film[a]	Solution[b]
P1	787	779	872	868
P2	783	771	897	896
P3	774	796	932	931
P4	755	755	807	803

[a] Spin coated on glass substrates from 5 mg / mL polymer solution in chlorobenzene [b] measured in dilute chlorobenzene solution.

2.4.2. C_8C_{10} / $C_{10}C_{12}$ solubility comparison

2.4.2.1. Temperature dependent UV-Vis

Aggregating interactions between polymer chains can arise from local dipoles in the D / A structure as well as π - π interactions between the electron clouds of the conjugated systems. Aggregation can also be closely related to polymer solubility with more strongly aggregating polymers demonstrating poorer solubility than those with less of a tendency to aggregate. Insulating alkyl chains that are anchored to the polymer backbones serve to increase polymer solubility by disrupting these strong interactions and allowing solvent molecules between chains to solvate the materials.

Aggregation can be probed experimentally using temperature dependent UV-Vis spectroscopy in solution where absorption spectra are recorded at successive intervals of increasing temperatures. These increased temperatures are able to disrupt large aggregates resulting in changes to the absorption profile and subtle absorption features that are present at room temperature can be significantly reduced at higher temperatures due to the disappearance of the aggregates responsible.[33] **Figure 2.11** shows comparative temperature dependent UV-Vis absorption profiles in chlorobenzene of the previously synthesised **C_8C_{10}DPPTT-T** and the newly synthesised **$C_{10}C_{12}$DPPTT-T**. Beginning at 15 ºC the UV-Vis spectra of both polymers are recorded at successive temperature intervals of 10 ºC up to 85 ºC. Through superimposing the spectra recorded at each different temperature it is possible to visualise specific changes in polymer aggregation occurring at the elevated temperatures.

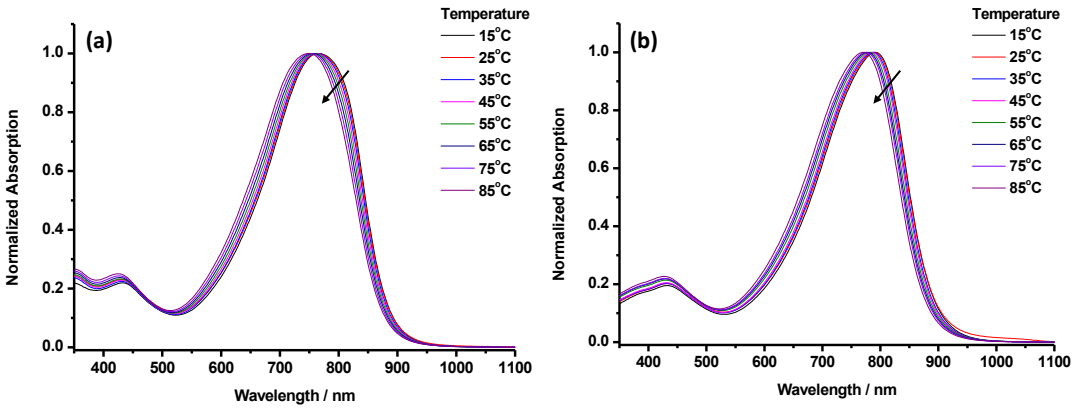

Figure 2.11. Temperature dependent UV-Vis absorption profiles of **(a)** C_8C_{10} alkylated and **(b)** $C_{10}C_{12}$ alkylated **DPPTT** polymers in dilute chlorobenzene solution.

Comparisons between the two differently alkylated polymers are shown in **Figure 2.11** and as expected demonstrate only small differences. The polymer backbone structure remains unchanged as a result of the alkyl chain extension meaning the frontier molecular orbitals and consequently the absorption profiles are almost identical. **Table 2.5** quantifies the very slight blue-shift observed with increasing temperature that is common to most polymer systems and is similar for both C_8C_{10} and $C_{10}C_{12}$. With this blue-shift at higher temperatures a very slight narrowing of the absorption can be seen, this is most pronounced at longer wavelengths with a reduction in a red-shifted shoulder as indicated by the two arrows in **Figure 2.11**. When comparing the two materials it can be seen that this shift is less pronounced when the larger $C_{10}C_{12}$ alkyl chain is employed. Whilst only a small change, it is reasonable to infer that this may be a result of reduced aggregation between polymer chains which in turn is evidence for the increased solubility of the longer alkyl chain **$C_{10}C_{12}$DPPTT-T** polymers.

Table 2.5. Temperature dependent comparison of λ_{max} in C_8C_{10} and $C_{10}C_{12}$ alkylated **DPPTT-T** polymers.

C_8C_{10}		$C_{10}C_{12}$	
Temperature (ºC)	λ_{max} (nm)[a]	Temperature (ºC)	λ_{max} (nm)[a]
15	786	15	791
25	764	25	789
35	763	35	788
45	760	45	785
55	760	55	781
65	756	65	777
75	753	75	774
85	749	85	771

[a] measured in dilute chlorobenzene solution.

2.4.2.2. XRD

X. Zhang et al. showed in 2011 how a series of **DPPT** co-polymers change the orientation of their polymer backbone relative to the plane of the substrate according to the co-monomer used.[34] By varying the co-monomer size between thiophene, thieno[3,2-*b*]thiophene and bi-thiophene they were able to tune the inversely proportional alkyl chain density along the polymer backbone. The increased alkyl chain density corresponded to a reduction in edge-on orientation of the polymer chains and it was suggested that this is a result of a reduction of interchain interactions in solution during the spin-coating of thin films. Other studies have detailed similar findings where larger or bulkier alkyl chains are employed to influence the crystallinity and orientation of polymer chains in the solid state.[35-38]

Comparison of the orientation and crystallinity of the two differently alkylated **DPPTT-T** materials was therefore of interest to further provide evidence of the increased solubility imparted by the $C_{10}C_{12}$ chain. **Figure 2.12** shows the XRD diffractograms of the two materials and it is clearly seen that the shorter chain **C_8C_{10}DPPTT-T** material is more crystalline and has a greater edge-on contribution than with the larger alkyl chain. It is likely that this is a consequence of stronger interchain interactions occurring with C_8C_{10} in solution. These stronger interactions can results in a certain amount of pre-aggregation, which can act as a driving force for the formation of edge-on orientated polymer chains. The larger $C_{10}C_{12}$ chains serve to reduce the strength of these interchain interactions, which is shown by the more

amorphous nature of the film. Reduced interactions and aggregate formation fits well with the observed improvement in solubility and the differences observed by temperature dependent UV-Vis spectroscopy in section **2.4.2.1**.

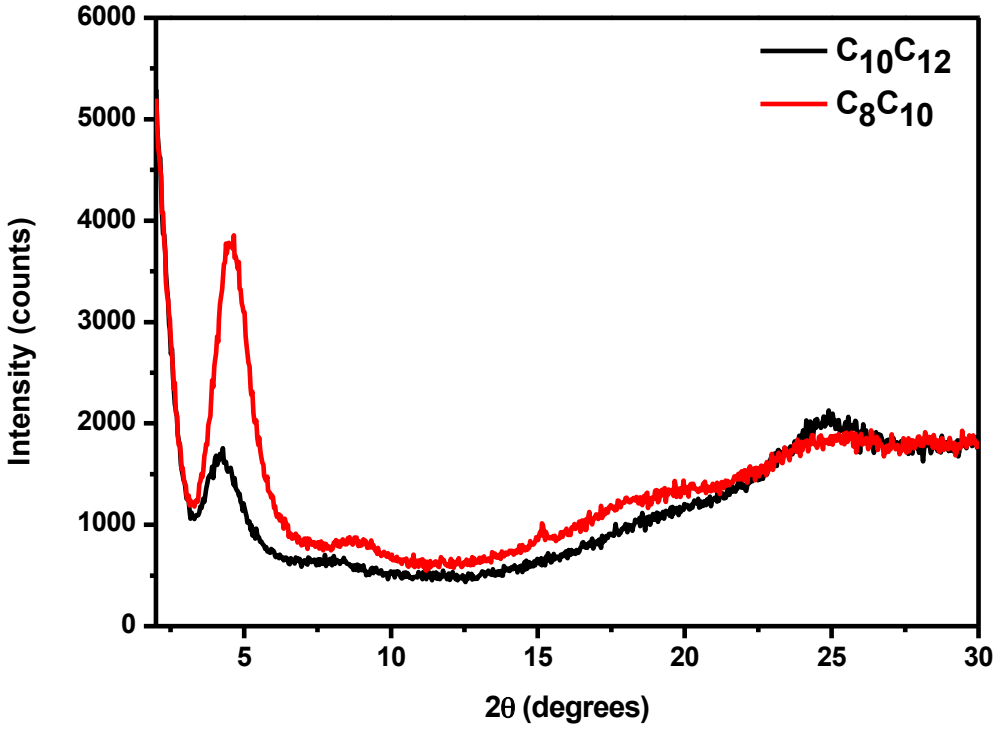

Figure 2.12. XRD diffractogram of C_8C_{10} and $C_{10}C_{12}$ alkylated **DPPTT-T** polymers. Films drop cast from 10 mg / mL chlorobenzene solutions on Si wafers and dried in air overnight.

2.4.3. Computational studies

Figure 2.13 displays frontier molecular orbital energies of **P1** – **P4** polymers experimentally determined using photoelectron spectroscopy in air (PESA) and UV-Vis absorption onsets shown in black on the lower HOMO and LUMO rows. These are compared to the computationally predicted energies using TD / DFT with a B3LYP / 6-31g* basis set shown in white on the upper rows. When comparing experimentally and computationally determined values it is often the case that there are a number of factors that DFT calculations do not account for which results in differences between the experimentally determined and computationally predicted values. However, throughout the field DFT calculations has long been shown to be an

accurate approximation to a material's energy levels and experimental trends consistently match those predicted computationally. [39,40]

The complexity of the DFT calculations used limits the modelling of materials to being performed on trimeric units, a structure that is in fact much shorter in length than the material synthesized. Therefore these calculations do not account for polymers of higher molecular weights that have reached their effective conjugation length, which would lead to a miscalculation of the material's band gap. These calculations also assume a polymer chain that is in the gas phase in a perfect vacuum which understandably leads to further inaccuracies due to the various interactions between polymer chains that are not accounted for.[41]

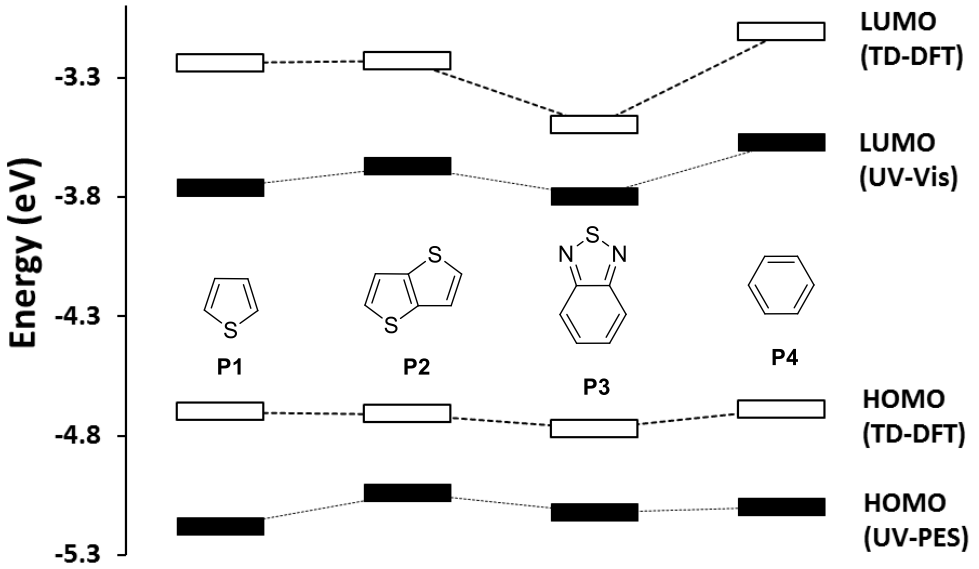

Figure 2.13. Frontier molecular orbital energy levels of polymers **P1** – **P4** predicted by UV-Vis / PESA and TD / DFT calculations with a B3LYP / 6-31g* basis set.

Similar to the absorption profiles, it is possible to rationalize the experimentally and computationally determined frontier molecular orbital energy levels in polymers **P1** – **P4** according to various factors such as co-monomer unit, polymer planarity and HOMO / LUMO backbone distribution. Additionally, the extent of HOMO and LUMO delocalisation along a polymer's backbone can also be used to infer details regarding their fundamental charge transport properties. Their distribution onto specific parts of the backbone structure can further be used to establish an understanding of HOMO and LUMO contributions made by individual donor and

acceptor units. The frontier molecular orbital distributions of **P1** - **P4** calculated using TD / DFT are shown in **Figure 2.14**. **P1** and **P2** can be seen to have highly planar backbones with HOMO and LUMO levels that are evenly distributed along the backbone to an extent that they are almost completely delocalized. The extra fused thiophene ring in **P2** imparts an increased linearity along the polymer backbone relative to the single thiophene ring in **P1**.

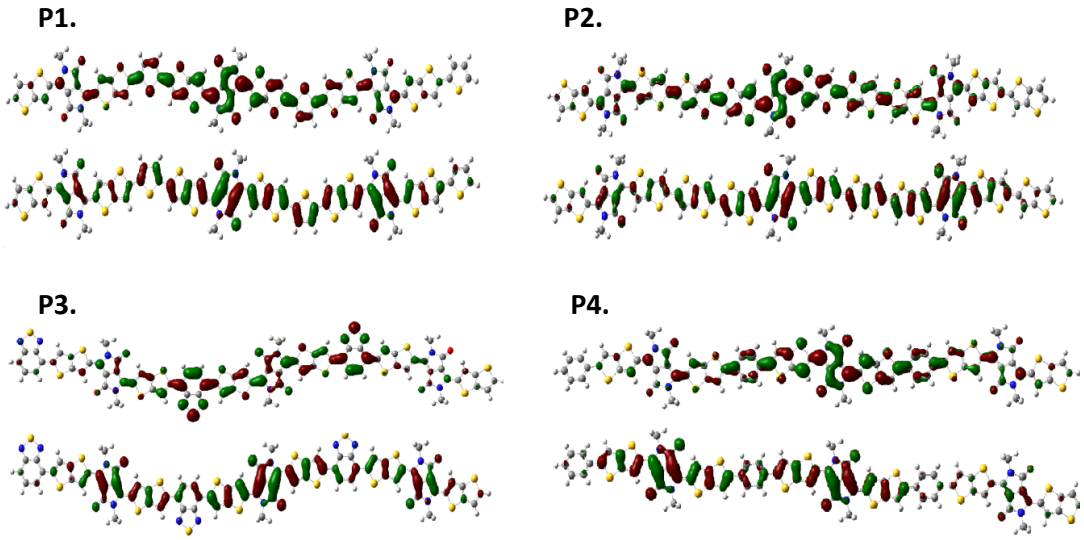

Figure 2.14. Frontier molecular orbital distribution of **P1** - **P4** calculated using TD / DFT with a B3LYP / 6-31g* basis set. HOMO and LUMO levels are shown below and above, respectively, for each polymer.

It has previously been mentioned that the electron-poor benzo[*c*][1,2,5]thiadiazole BT co-monomer unit in **P3** lowers the E_{HOMO} and E_{LUMO} by different amounts, giving values of -5.1 eV and -3.8 eV respectively, and the narrowest E_g of the series. From the energy level distributions it can be seen that LUMO of **P3** is strongly distributed onto the BT co-monomer and is therefore significantly influenced by the electron-withdrawing nature of the unit. The HOMO does not extend into the BT unit and is therefore not significantly affected by its electron-withdrawing nature giving an E_{HOMO} value that is the same as **P4**. As shown in **Figure 2.14** calculations also show a considerably increased planarity of **P3** relative to **P4** meaning there is no loss in conjugation along the polymer backbone.

Contrastingly, in **P4** the steric clash and resultant backbone twisting disrupts the polymer's conjugated system, which significantly broadens E_g to 1.5 eV and raises

E_{LUMO} to -3.6 eV. E_{HOMO} remains uninfluenced by this backbone twisting and is slightly raised relative to the thiophene analogue in **P1** which is unexpected considering the lower electron density contribution that would be expected from the phenyl ring that has been reported in previous similar studies.[15]

2.5. OPV performance of polymers P1 – P4

2.5.1. OPV device characteristics of polymers P1- P4

Bulk heterojunction organic solar cells were constructed using polymers **P1** - **P4** as the donor material in the active layers. Devices with a conventional glass/ITO/PEDOT:PSS/polymer:PC[71]BM/LiF/Al architecture were fabricated with the active layer being spin coated from a mixed solvent system of chloroform : *o*-dichlorobenzene (*o*DCB) (4 :1) containing a 1 : 2 polymer / PC[71]BM mixture. The current *vs* voltage (*J-V*) curves and the external quantum efficiency (EQE) spectra of all four polymers are shown in **Figure 2.15** with the EQE corrected device data for each polymer shown in **Table 2.6**.

The best performing devices across the series were achieved using **P1** with thiophene as a co-monomer, which demonstrated a good J_{sc} of 14.7 mA cm^{-2}, V_{oc} of 0.62 V and FF of 0.53. These values result in an overall PCE of 4.1 % that is slightly lower than the previously reported shorter chain (C_8C_{10}) analogues. Despite this reduction in performance, these are the initial devices and there remains much room for optimization which will be discussed later in this chapter.

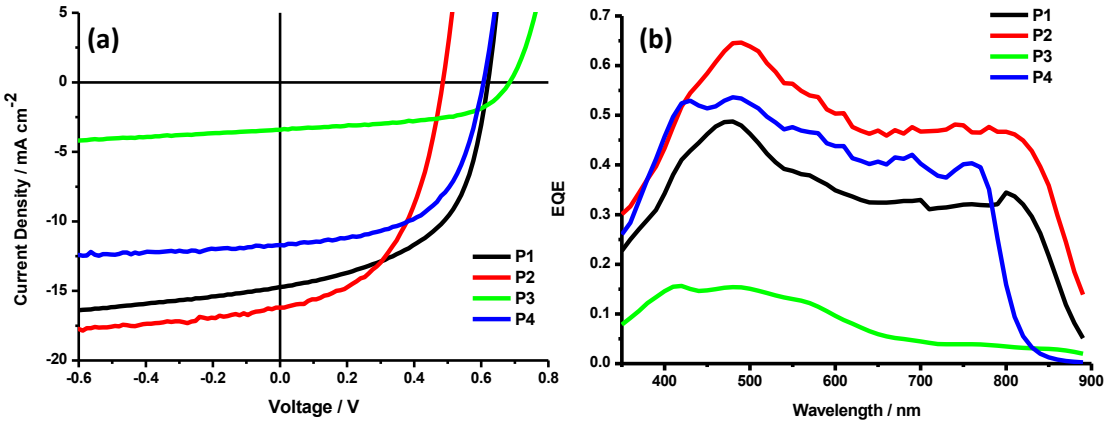

Figure 2.15. (a) *J-V* curves and **(b)** EQE spectra of polymers **P1** – **P4**.

Table 2.6. OPV device performance parameters of polymers **P1** – **P4**.

Polymer	J_{sc} (mA cm^{-2})[a]	V_{oc} (V)	FF	PCE (%)[a]
P1	12.6	0.62	0.53	4.1
P2	15.7	0.48	0.50	3.8
P3	2.9	0.68	0.55	1.1
P4	11.7	0.61	0.57	4.0

[a] EQE corrected.

The narrowing of E_g from 1.4 eV to 1.3 eV that is observed from the introduction of the thieno[3,2-*b*]thiophene co-monomer is likely the origin of the enhanced J_{sc} of 15.7 mA cm^{-2} observed with **P2**. Compared to **P1** the raised E_{HOMO} arising from the more electron-rich thieno[3,2-*b*]thiophene expectedly results in a decreased V_{oc} of 0.48 V due to the reduced energetic offset between D_{HOMO} and A_{LUMO} levels. When using a more electron-rich co-monomer to achieve E_g reduction there is often a trade-off between J_{sc} improvement through the narrowed band gap and reduction in V_{oc} due to the raised E_{HOMO} value. The FF only shows a slight reduction to 0.50, which results in a PCE of 3.8 %.

Charge separation in bulk heterojunctions is closely related to the energetic driving force between polymer and fullerene LUMO levels. It is known that if an exciton is going to dissociate at a boundary into free holes and electrons there must be a sufficient energetic offset between the LUMOs of the two materials.[424344] Without a sufficient driving force, a significant reduction in charge separation can be observed. In **P3** the electron-withdrawing benzothiadazole as a co-monomer lowers the polymer E_{LUMO} and it is likely that this results in reduced charge separation at the polymer / fullerene interfaces giving a low J_{sc} of 2.9 mA cm^{-2}. The stabilisation of E_{HOMO} also results in a significantly enhanced V_{oc} of 0.68 V, which when combined with a FF of 0.55 gives an overall efficiency of 1.1 %.

The wider band gap in **P4** with a phenyl co-monomer results in a J_{sc} of 11.7 mA cm^{-2} that is reduced compared to both **P1** and **P2**. It also demonstrates a good V_{oc} of 0.61 V, which is in agreement with the experimentally and computationally determined values that do not show the raised E_{HOMO} that would be expected in theory. The FF is the highest in the series at 0.57 and this corresponds to a promising PCE of 4 %

2.5.2. AFM

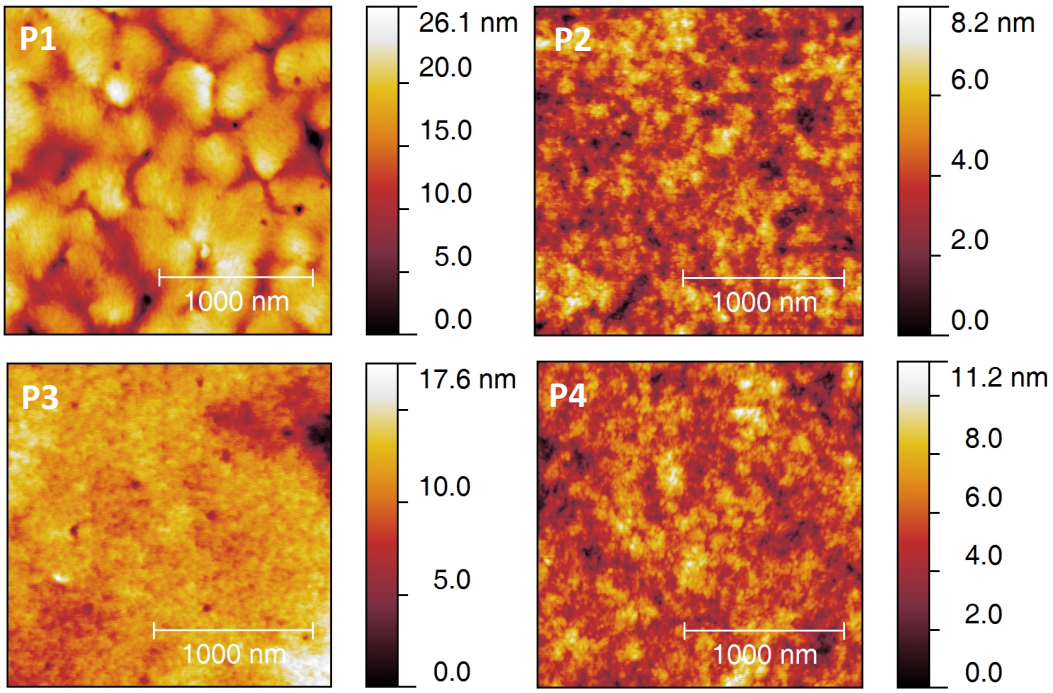

Figure 2.16. AFM phase images of films of polymer **P1** – **P4** / fullerene blend spin coated on glass under the same conditions used during device fabrication.

AFM is a surface technique that is extremely valuable for probing the surface of a polymer / fullerene blend and can provide a wealth of information regarding the extent of intermixing between the two phases which in turn can be directly related to the solar cell device parameters of each polymer. As a surface technique caution must be taken when relating a blend's surface morphology to that of the bulk material, however it is often used to great effect as an indicator of morphology and is frequently shown to be a good descriptor of a material's OPV performance.[45-48]

At first glance it is clear to see polymers **P2** and **P4** appear to have very similar morphologies whilst **P1** and **P3** are very different. Interestingly **P1** with the highest solar cell performance of 4.1 % appears to have the coarsest morphology of the polymer series with large domains that appear greater than 100 nm in size. Usually it is desirable to have a more homogeneous blend mixture of polymer and fullerene materials by AFM as this allows for increased exciton dissociation and charge transport pathways. It is not clear from these images whether these larger regions are separate domains of polymer or fullerene, which is unlikely due to high current

observed with this material, or whether they are in fact larger domains of well mixed polymer and fullerene materials.

Both **P2** and **P4** materials demonstrate very similar surface morphologies with what appears to be finely intermixed polymer and fullerene blends that are far less coarse than that of **P1**. **P3** has a considerably lower solar cell performance with PCE of 1.1 % and shows a noticeably different AFM image with a very finely dispersed morphology. On the basis that the low photocurrent is a result of the reduced charge separation due to insufficient LUMO – LUMO offset it appears that the morphology of this material would be very favourable for charge transport should the charge separation be sufficiently improved.

2.6. OFET performance of polymers P1 – P4

2.6.1. OFET device characteristics of polymers P1 – P4

Several **DPP** structures are known to demonstrate promising charge transport properties with high electron and hole transport materials reported as well as many ambipolar polymers.[49,50,9] Structural features that are general to **DPP** polymers are known to be beneficial for charge transport such as their highly planar nature combined with an ability for inter- and intra- molecular interactions. A strong D / A type back bone structure has also been shown to promote strong ordering effects between polymer chains which can facilitate interchain hopping.[51] There has also been shown to be an intramolecular planarising effect from hydrogen bonding that occurs between carbonyls on the ketopyrrole core and β-protons on the adjacent thiophene / thieno[3,2-*b*]thiophene flanking unit (**Figure 2.18**) which promotes effective conjugation and charge transport.[52]

The planarising effect of these hydrogen bonds are shown in **Figure 2.19** where optimized energies are plotted for every 10º rotation about the bond connecting the thiophene / thieno[3,2-*b*]thiophene flanking unit to the diketopyrroloyprrole core. Two global minima can clearly be seen when the dihedral angle is 0º and 360º, which represent the points at which the hydrogen bonding interactions are strongest. There is also a local minima at 180º with a significant energetic barrier to the 0º / 180º conformation where oxygen – sulfur through-space non-bonding interactions arise

due to the radially expanded nature of the sulfur atom facilitating close contact between the two atoms as well as the vacant d-orbitals situated on the sulfur atom which are able to accept electron density. It is likely that a significant amount of the polymers will be present with this orientation, which also results in a planar backbone structure and is not seen as being detrimental to the charge transport properties of the material.

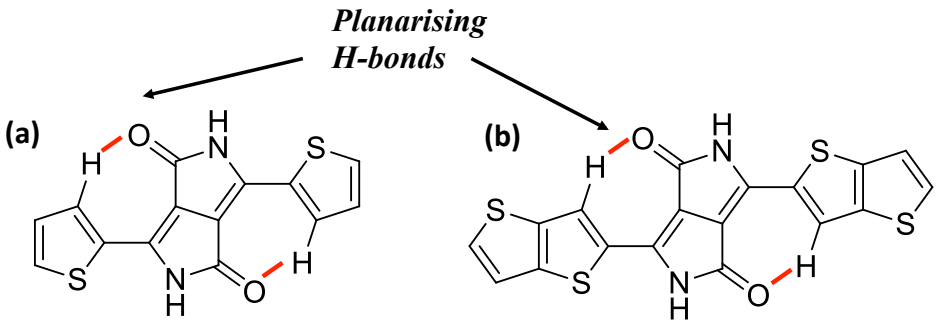

Figure 2.17. Favourable planarising hydrogen bonding interactions in **(a) DPPT** and **(b) DPPTT**.

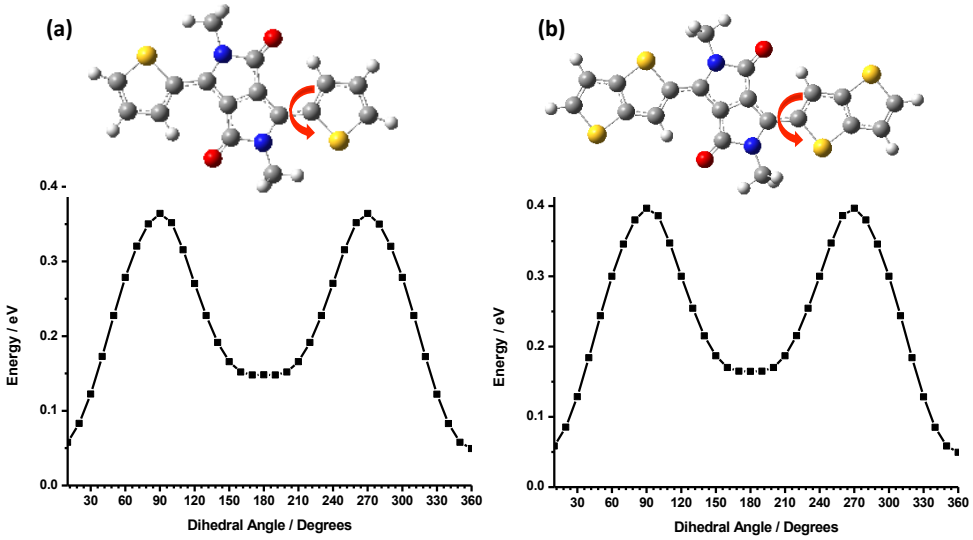

Figure 2.18. Graphical representation of optimised energies of **(a) DPPT** and **(b) DPPTT** at intervals of 10º rotation about the dihedral bond between the **DPP** core and flanking units shown by the red arrow. TD / DFT calculations calculated using a B3LYP / 6-31g* basis set.

Consequently it was of interest to investigate the charge transport properties of the newly synthesized polymers **P1** – **P4**. Top gate / bottom contact and bottom gate / bottom contact thin film OFET devices were fabricated on glass substrates with gold source / drain electrodes. The semiconducting channel was deposited by the spin coating of chlorobenzene solutions of polymers **P1** – **P4** and the various device parameters extracted and reported in **Figure 2.17** and **Table 2.7**.

In top gate / bottom contact devices polymer **P1** shows good ambipolar charge transport properties with both hole and electron mobilities greater than 0.1 cm^2 / Vs. Compared to the shorter C_8C_{10} chain analogue **P1**'s hole mobility of 0.33 cm^2 / Vs is an order of magnitude lower. However **P1** has much more well balanced charge transport with an electron mobility of 0.12 cm^2 / Vs which is approximately double the value of 0.063 cm^2 / Vs reported for C_8C_{10} **DPPTT-T**.

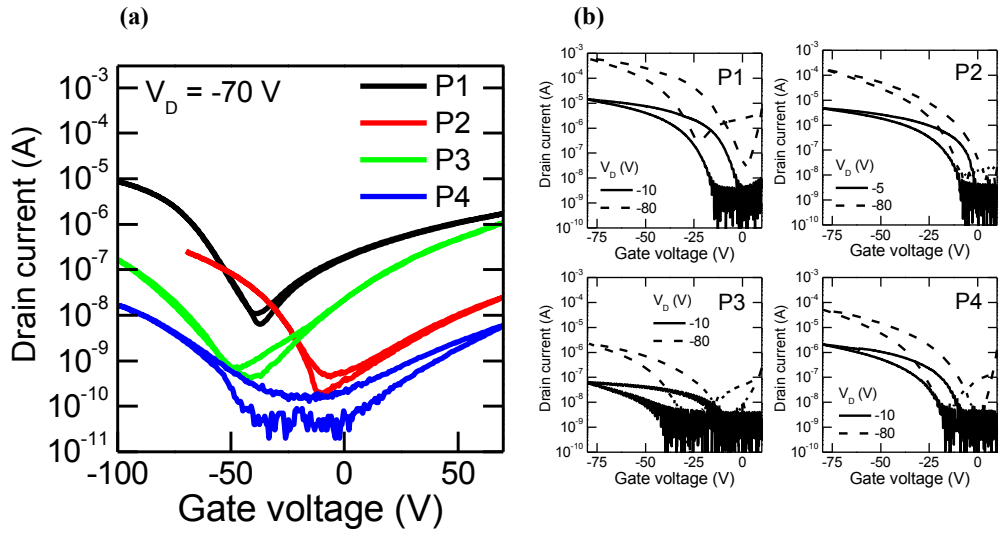

Figure 2.19. OFET transfer curves in saturation regime made using polymers **P1** – **P4** in **(a)** Top gate / bottom contact devices with channel dimensions 1 mm width, 50 µm channel length. **(b)** Bottom gate / bottom contact devices with 10 mm channel width and 10 µm channel length.

Considering it's similarities with **P1** and its highly planar structure **P2** has a surprisingly low hole and electron mobilities and poor device characteristics with a hole mobility of 1.1 x 10^{-2} cm^2 / Vs and electron mobility of 9 x 10^{-3} cm^2 / Vs. This is likely a result of the poor processability of the material arising from the intrinsic reduction in solubility due to the extra fused thiophene ring combined with the very high molecular weights of the material. Such low solution processability inevitably

adds an extra level of complication to the fabrication of devices as it proves very difficult to obtain good, homogenous polymer films.

Table 2.7. Thin film OFET device characteristics of polymers **P1** – **P4**.

Polymer	Top gate / bottom contact				Bottom gate / bottom contact	
	μ_{hole} (cm^2 / Vs)	I_{on} / I_{off} (holes)	$\mu_{electron}$ (cm^2 / Vs)	I_{on} / I_{off} (electrons)	μ_{hole} (cm^2 / Vs)	I_{on} / I_{off} (holes)
P1[a]	0.33	1×10^4	0.12	1×10^3	0.45	1×10^4
P2[b]	1.1×10^{-2}	1×10^2	9×10^{-3}	-	9×10^{-2}	1×10^4
P3[c]	3.7×10^{-2}	1×10^3	0.15	1×10^2	3×10^{-3}	10
P4[d]	8.0×10^{-3}	1×10^2	5×10^{-3}	-	6×10^{-2}	1×10^3

[a] Spin coated on glass substrates from 5 mg / mL chlorobenzene solution at 2000 rpm for 30 s. [b] Spin coated on glass substrates from 10 mg / mL chlorobenzene solution at 500 rpm for 10 s then 2000 rpm for 20s. [c] Spin coated on glass substrates from 20 mg / mL chlorobenzene solution at 500 rpm for 10 s then 2000 rpm for 20 s. [d] Spin coated on glass substrates from 10 mg / mL chlorobenzene solution at 2000 rpm for 30 s.

P3 with benzothiadiazole has a relatively low hole mobility on the same order of magnitude as **P2** but a promising electron mobility of 0.15 cm^2 / Vs. As reported in several other structures employing a benzothiadiazole ring, it is likely that the highly planar backbone structure allows for efficient charge transfer through interchain hopping whilst the sterically exposed nature of the acceptor unit facilitates short intermolecular contacts.[53] **P4** as expected is not a good candidate material for OFET devices. The twisted backbone structure disrupts the conjugation along the backbone and inhibits the transport of both electrons and holes. This is shown by the lowest hole and electron mobilities in the series of 8.0×10^{-3} cm^2 / Vs and 5×10^{-3} cm^2 / Vs respectively.

Interestingly when bottom gate / bottom contact device architecture is used with polymers **P1** – **P4**, the devices lose their ambipolarity and it is not possible to extract electron mobilities. **P2** and **P3** show improved hole mobilities relative to their values in top gate / bottom contact devices whilst **P4** shows a reduction. Similar to **P2** and **P3**, changing the device architecture of **P1** results in an enhanced hole mobility of 0.45 cm^2 / Vs which is the highest mobility of all four polymers using both device architectures.

2.6.2. AFM

In section **2.5.2** it was discussed how the morphology of a blend can be key to the understanding of how a bulk heterojunction solar cell operates and that AFM imaging can be important in establishing such an understanding. This concept can also be applied to OFET devices where a spin coated polymer film on glass can be probed to obtain information on how polymer chains arrange themselves as a bulk in a pristine film.

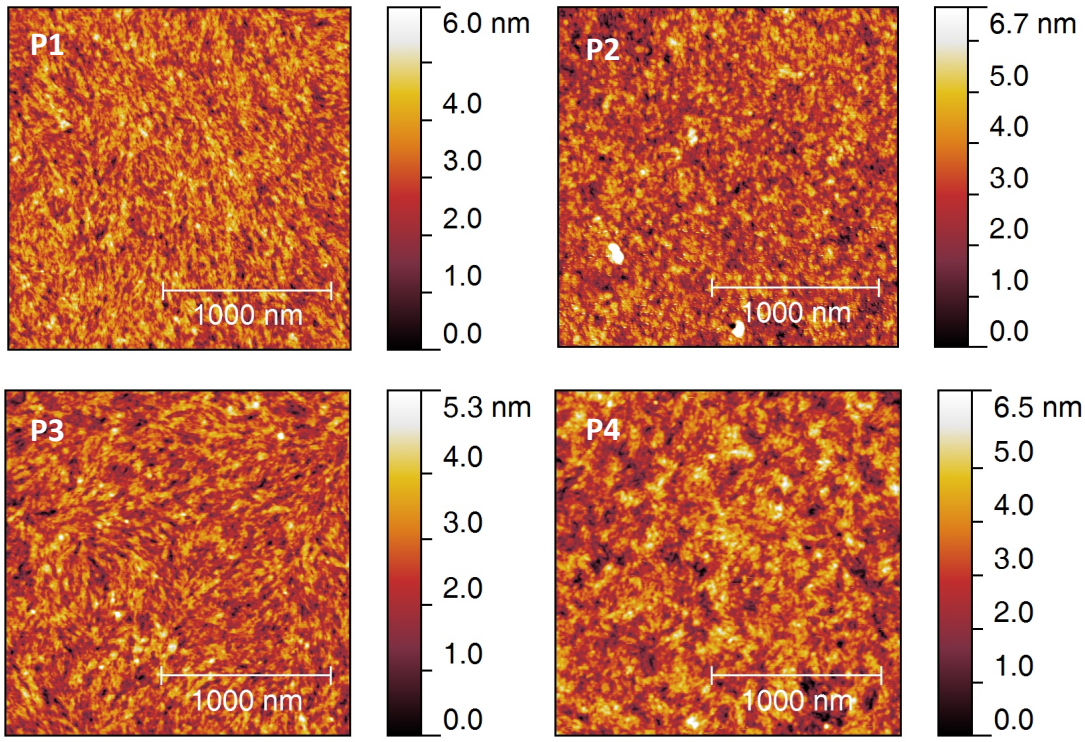

Figure 2.20. AFM phase images of films of polymers **P1** – **P4**. Spin coated on glass substrates under the same conditions used during device fabrication.

AFM images of the four pristine polymer films are shown in **Figure 2.20**, despite the large variations in the charge transport characteristics all four polymer films have remarkably similar AFM images. **P4** can be seen to be slightly different to the other three with a coarser surface morphology. This could be a result of the twisting of the polymer chains resulting in a change in the nature of the intermolecular interactions between chains, although a more comprehensive morphological study would be needed to confirm this.

2.7. Molecular weight study of P1

2.7.1. Polymer fractionation and characterisation

R. Ashraf et al. recently reported improved solar cell device characteristics in Ge / Si / C bridged **IDT-BT** polymers when fractionated by GPC into different M_n batches with narrowed PDIs.[54] This resulted in PCE enhancement from 4.4 % to 6.5 % and the improved device performance was shown to be closely related to the effect that polymer fractionation has on the polymer / fullerene blend morphology. Without the use of GPC it has long been established that higher molecular weights and narrowed PDIs can be key physical parameters towards the fabrication of high performance devices.[55] Recently *Z. Huang et al.* have shown that batch-to-batch molecular weight differences in **C_8C_{10}DPPTT-T** can strongly influence the charge separation in the blends as shown by TAS.[56] *S. Dimitov et al.* demonstrated how higher M_n **DPP** based polymers show improved efficiencies as a result of the formation of smaller PCBM domain sizes.[57] Considering the high M_n values achieved for **P1** and the inhomogeneity observed in the blend morphology it was of interest to fractionate a large batch of **P1** to attempt to tune the blend morphology and solar cell performance of the material.

GPC separates materials on the basis of differences in their hydrodynamic volume and hence can be used to separate polymer fractions of varying molecular weights from a single batch. The polymer solution is the mobile phase, which passes through microporous beads that are the stationary phase. Material with the largest hydrodynamic volume (high molecular weight material) elutes first as it does not spend as much time in the pores compared to material with a smaller hydrodynamic volume (low molecular weight material). As such, the higher molecular weight material experiences greater 'excluded volume' and a given polymer batch elutes with an molecular weight gradient. GPC can therefore be used to isolate high molecular weight and narrow PDI material providing it has sufficient solubility. Additionally it can prove effective at removing small impurities that may be silent by ^{1}H NMR or analytical GPC. For several reasons it can therefore prove a valuable tool towards improving device performance.

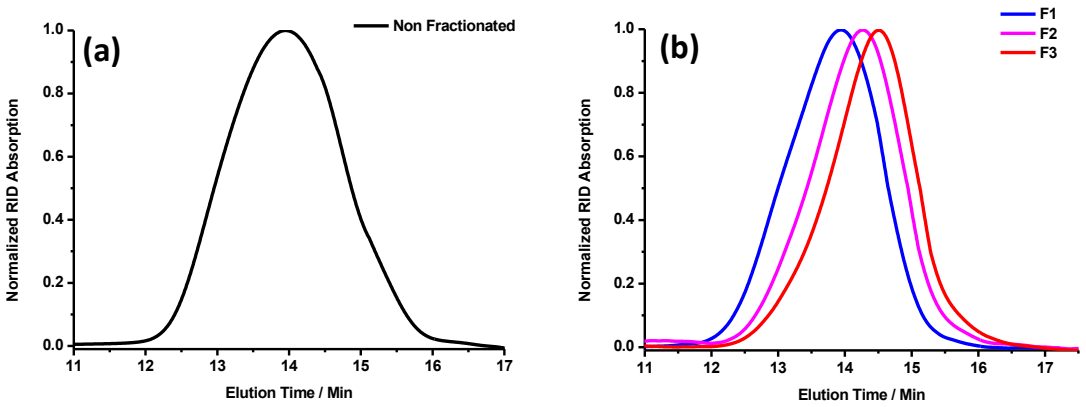

Figure 2.21. Normalised GPC elugrams of **(a)** non-fractionated and **(b)** fractionated polymer materials in chlorobenzene at 80 ºC

Table 2.8. Physical properties of **NF**/**F1**/**F2**/**F3** polymer materials.

Polymer	M_n (kDa)[a]	M_w (kDa)[a]	PDI[a]
F1	180	375	2.1
F2	120	220	1.8
F3	80	146	1.8
NF	108	273	2.5

[a] M_n, M_w and PDI (M_w / M_n) determined by GPC at 80 ºC using low-PDI (<1.10) polystyrene standards and chlorobenzene as the eluent.

A non-fractionated batch of polymer **P1** was separated over time into multiple fractions of different molecular weights by size exclusion GPC. The eluted polymer solution was separated by eye into many fractions of approximately equal volume and the three fractions of highest molecular weights **F1**, **F2** and **F3** were isolated, precipitated into methanol and dried under vacuum. **Figure 2.21** shows the normalized GPC traces for the non-fractionated (**NF)** material compared to **F1**, **F2** and **F3** and **Table 2.8** shows each of their physical properties determined by analytical GPC.

The three different batches were all isolated in high molecular weight and narrow PDI. When compared to the unpurified **P1** material, **F1** has a higher M_n and a comparable PDI, **F2** has a very slightly increased M_n but a narrowed PDI whilst **F3** has a lower M_n and narrowed PDI.

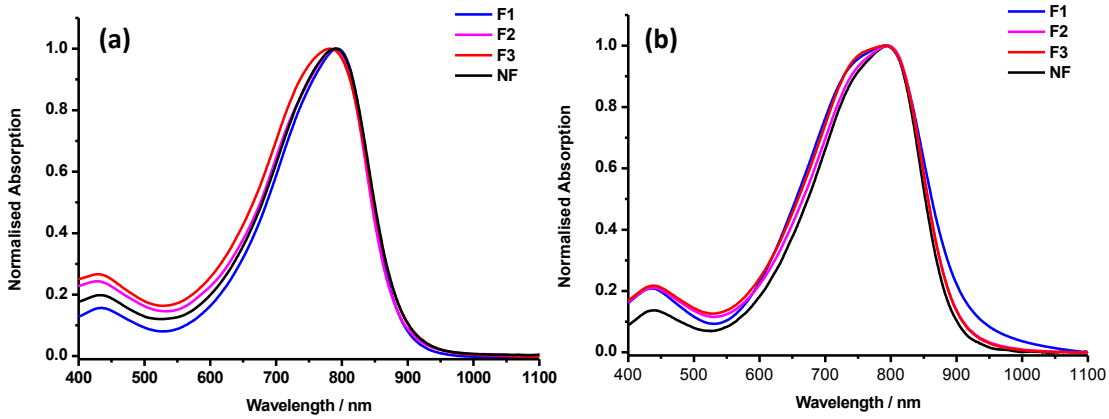

Figure 2.22. Room temperature normalised UV-Vis absorption profiles of **NF**/**F1**/**F2**/**F3** polymer materials **(a)** In dilute chlorobenzene solution and **(b)** Thin film spin coated on glass substrates from 5 mg / mL chlorobenzene solutions.

It was of interest to investigate whether the absorption profile of the polymer was affected by the fractionation process as higher molecular weights and narrowed PDIs can often lead to changes in the interactions between polymer chains which in turn can change the shape or wavelength of the absorption. The solution and thin film UV-Vis spectra of the fractionated and non-fractionated materials are shown in **Figure 2.22** with comparison of λ_{max} in **Table 2.9**. It is worth noting that the recorded λ_{max} in solution and thin film for the non-fractionated material is slightly red-shifted relative to the previous batch **P1**. This small variation can be attributed to batch-to-batch variation in polymer material, however with the same PCE achieved in both batches this variation can be interpreted not to have a significant effect on polymer OPV performance.

In solution the spectra of all three fractions are very similar to that of the **NF** material. They have the same absorption onset and broad profile shape with **F3** showing a slight broadening relative to **F1**, **F2** and **NF** material. There are also only small differences in solution λ_{max} observed. Going from **F3** to **F1** with an increase in molecular weight there is a small red-shift whilst the **NF** material comes close to the middle of the range of wavelengths, with a 1 nm shorter wavelength λ_{max} than **F2**. In the thin film however there is no such trend with **F1** having the most blue-shifted λ_{max} whilst **F2** has the most red-shifted value. **F1** also shows a noticeably red-shifted λ_{onset} relative to the other fractions, which show little variation between themselves. In addition to the lack of a significant trend in λ_{onset} or λ_{max} it can be seen that moving

towards higher molecular weights as a result of the fractionation does not result in a signficant increase in polymer aggregation.[58]

Table 2.9. λ_{max} of **NF**/**F1**/**F2**/**F3** polymer materials in solution and thin film.

Polymer	λ_{max} Solution (nm)[a]	λ_{max} Thin film (nm)[b]
F1	793	791
F2	790	796
F3	782	793
NF	789	795

[a] Measured in dilute chlorobenzene solution [b] Spin coated on glass substrates from 5 mg / mL chlorobenzene solution.

2.7.2. Solar cell device characteristics of fractionated polymer

2.7.2.1. Conventional device architecture

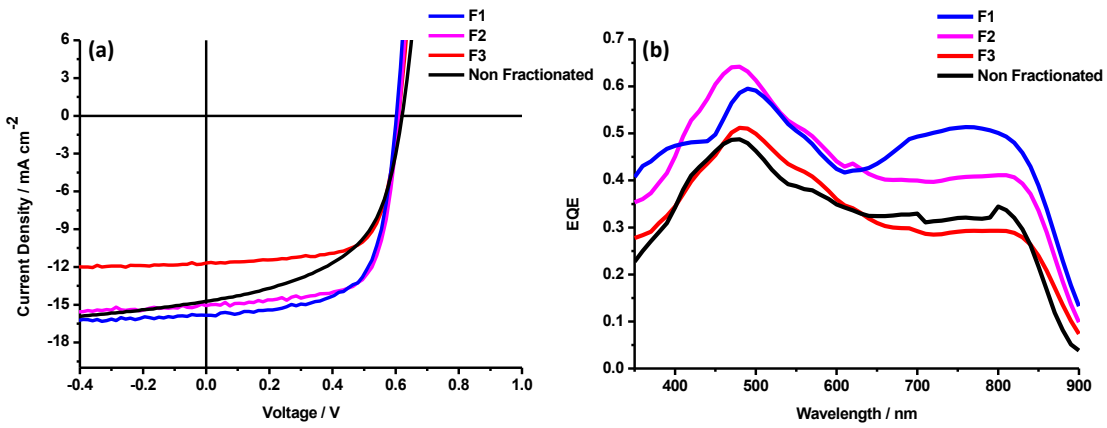

Figure 2.23. (a) *J-V* Curve and **(b)** EQE spectra of **NF**/**F1**/**F2**/**F3** polymer materials in devices with conventional architecture.

Polymer / fullerene bulk heterojunction solar cells were fabricated with the fractionated and non-fractionated polymers as the donor material using the same fabrication conditions and conventional device architecture as described in section **2.5.1**. The OPV performance of the three fractionated materials and the non-fractionated material are used to compare the effect that fractionation has on the device performance of **$C_{10}C_{12}$DPPTT-T**. The *J-V* curve and EQE spectra of the fractionation series are shown in **Figure 2.23** whilst the device data is shown in **Table 2.10**.

The **NF** material demonstrates the lowest overall solar cell device performance with an overall efficiency of 4.1 % using a conventional device architecture. There is a clear efficiency enhancement resulting from the fractionation with each of the three fractions showing improved performances ranging from 4.8 – 6.3 %.

The lowest molecular weight fraction **F3** shows a drop in M_n and a narrowing of PDI compared to the original polymer batch yet shows a significantly enhanced efficiency of 4.8 % showing that there is not a straight-forward linear relationship between M_n and device performance. The J_{sc} of the fractions appear to follow the M_n more closely with a slightly reduced value of 11.2 mA cm^{-2} for **F3** whilst the V_{oc} remains effectively unchanged. The performance enhancement can be seen to largely be arising from a significant increase in FF from 0.53 to 0.70.

F2 also shows a narrowed PDI but unlike **F3** has an increased M_n which results in a larger enhancement in efficiency with a PCE of 6.2 %. Similarly to the improvements observed with **F3** there is a largely unchanged V_{oc} at 0.61 V and an increased FF of 0.70, the further enhancement results from an improved J_{sc} of 14.6 mA cm^{-2}. The highest M_n batch **F1** has many similarities to **F2** with the same PDI of 1.8 and an increased M_n of 180 kDa. It has marginally reduced V_{oc} and FF and an enhanced J_{sc} of 15.6 mA cm^{-2}, which results in a PCE that is slightly improved at 6.3 %.

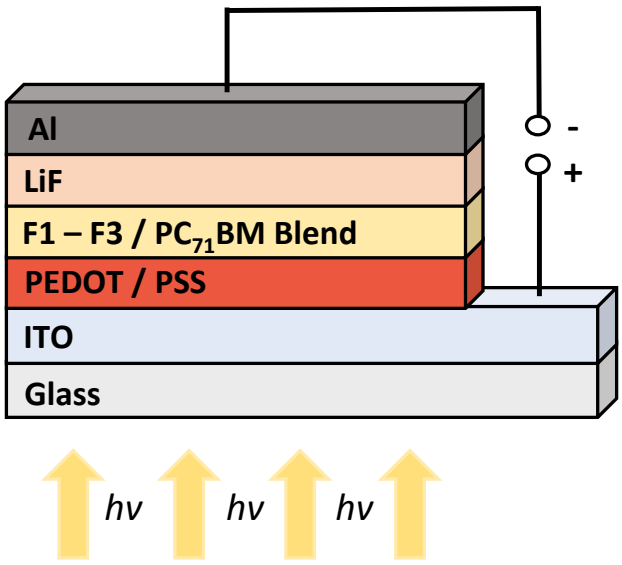

Figure 2.24. Graphical representation of the conventional device architecture used for **NF**/**F1**/**F2**/**F3** polymer materials.

Table 2.10. OPV device performance parameters of **NF**/**F1**/**F2**/**F3** polymer materials in devices with conventional architecture.

Polymer	J_{sc} (mA / cm^2)[a]	V_{oc} (V)	FF	PCE (%)[a]
F1	15.6	0.60	0.67	6.3
F2	14.6	0.61	0.70	6.2
F3	11.2	0.61	0.70	4.8
NF	12.6	0.62	0.53	4.1

[a] EQE corrected

Of all the device characteristics it appears that J_{sc} is the most sensitive to polymer M_n with an apparent direct correlation between the two that is shown for both conventional and inverted device architectures in **Figure 2.27** Overall the improvements agrees with the previous studies conducted by *R. Ashraf et al.* on analogous IDT type polymers and further surpasses the efficiency improvements reported. Through a single post-polymerisation fractionation step the two highest molecular weight fractions **F1** & **F2** have demonstrated an improvement in overall power conversion efficiency of greater than 50 %.

2.7.2.2. Inverted Device Architecture

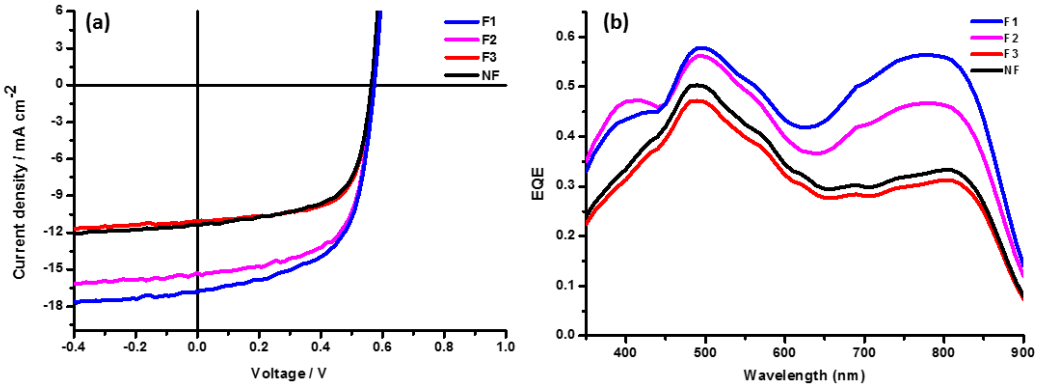

Figure 2.25. (a) *J-V* Curve and **(b)** EQE spectra of **NF**/**F1**/**F2**/**F3** polymer materials in devices with inverted architecture.

Optimisation of device architecture is often shown to be an effective route towards accessing higher solar cell performances and the performances of different polymers can vary dramatically between conventional and inverted architectures.[59] Inversion of the device architecture is shown in **Figure 2.26** whilst the *J-V* curve and EQE spectra

of the inverted devices are shown in **Figure 2.25** and the respective device data in **Table 2.11**.

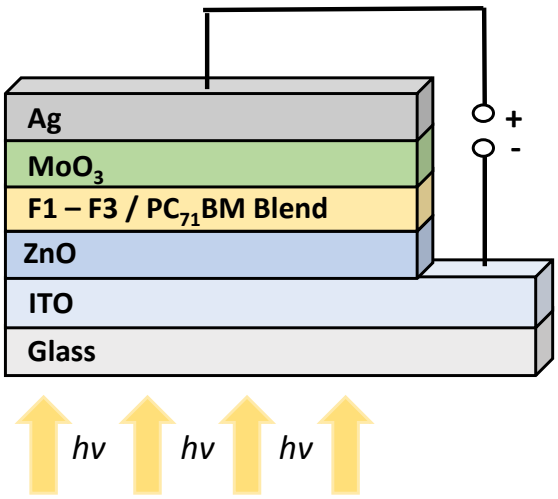

Figure 2.26. Graphical representation of the inverted device architecture used for **NF**/**F1**/**F2**/**F3** polymer materials.

Table 2.11. OPV device performance parameters for **NF**/**F1**/**F2**/**F3** polymer materials in devices with inverted architecture.

Polymer	J_{sc} (mA / cm^2)^a	V_{oc} (V)	FF	PCE (%)^a
F1	16.0	0.57	0.60	5.5
F2	14.3	0.57	0.64	5.2
F3	10.7	0.57	0.66	4.0
NF	11.4	0.56	0.63	4.0

^{a} EQE corrected

In comparison to the conventional device architecture, the original **NF** material shows both a reduction in V_{oc} (0.57 V) and J_{sc} (13.9 mA cm^{-2}) but a significantly enhanced FF of 0.63 when inverted architecture is used giving a slightly reduced overall efficiency of 4.0 %. As was observed with **F3** in conventional device architecture, going to a reduced M_n results in a drop in J_{sc} and an increase in FF whilst the V_{oc} remains relatively unchanged at 0.57 V. When all these variations are considered the outcome is an overall efficiency that is largely unchanged from the **NF** batch at 4.0 %.

With inverted device architecture **F2** shows the same improved V_{oc} as **F3** and a similarly enhanced FF relative to the **NF** batch. Following the same trend as the conventional architecture the J_{sc} is improved with a value of 14.3 mA cm^{-2}. This improved photocurrent corresponds to an efficiency of 5.2 % that is significantly

improved compared to the **NF** batch. Comparatively **F1** has a further improved J_{sc} of 16.0 mA cm^{-2} and an unchanged V_{oc} of 0.57 V whilst the FF drops to 0.60 giving a small improvement in efficiency of 5.5 %.

With both device architectures it is clear that there is not a linear correlation between M_n and OPV performance which is largely due to both FF and V_{oc} appearing to vary unpredictably in each fraction. In general the relationship with PDI seems to be more straight-forward with fractionation resulting in narrowed PDIs that correspond to improved efficiencies. As shown in **Figure 2.27**, the J_{sc} is much more sensitive to M_n and PDI than other parameters with an clear improvement in photocurrent with increased M_n for both device architectures.

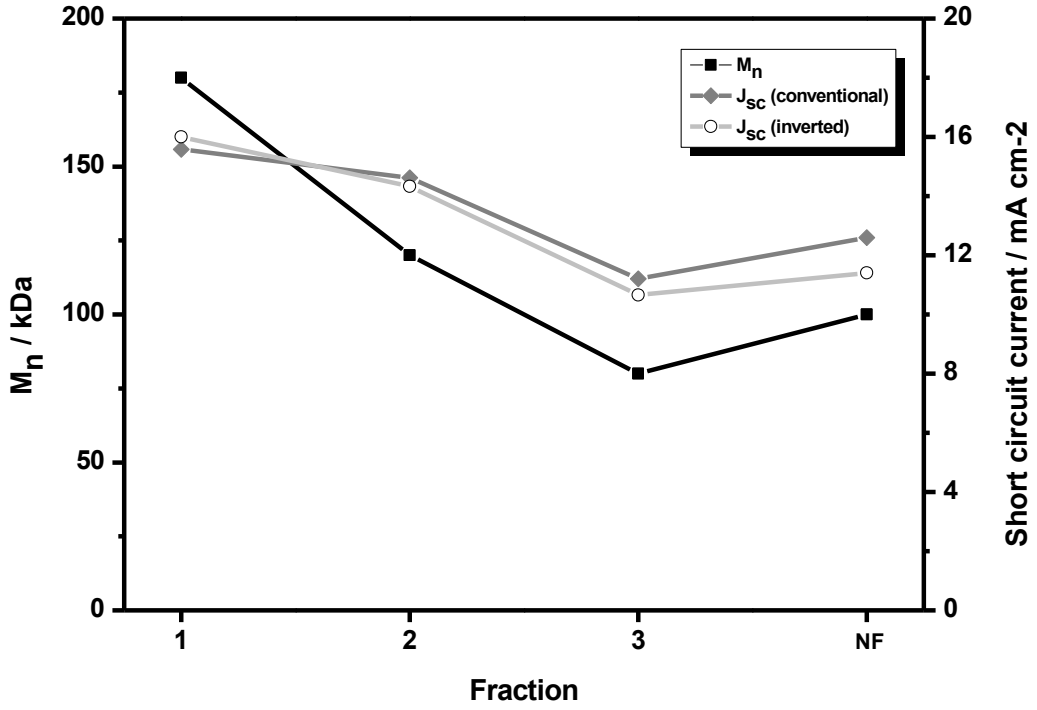

Figure 2.27. Graphical representation of the variation of J_{sc} with M_n in both conventional and inverted devices for **NF**/**F1**/**F2**/**F3** polymer materials.

2.7.3. Morphological Characterisation of Molecular Weight Study

2.7.3.1. AFM

The generation of charge in polymer / fullerene bulk heterojunction solar cells is known to be closely related to the ability of photogenerated excitons to dissociate. This is strongly influenced by the extent of intermixing between the polymer and fullerene materials. A photogenerated exciton has previously been shown to be a short-lived species with exciton diffusion only occuring over a short distance before exciton degradation or recombination occurs.[60]

Consequently blends that have a more finely intermixed blend morphology allow for a greater number of excitons to reach an interface and subsequently separate into free electron and hole charge carries within the lifetime of the short-lived exciton. In contrast, blends with a poorer intermixing of polymer and fullerene materials can often exhibit large polymer and fullerene domain sizes. This means in fewer number of excitons reaching an interface within their short lifetime and results in fewer charges being generated. AFM images of polymer / fullerene blends can therefore be valuable when evaluating the extent of this intermixing and can be used to indirectly probe how the blend materials are behaving within a bulk heterojunction solar cell.

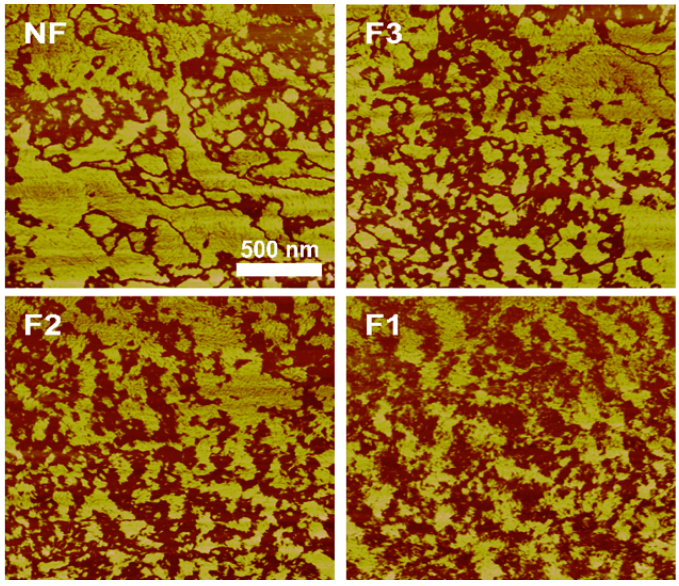

Figure 2.28. AFM phase images of polymer / fullerene blends with **NF**/**F1**/**F2**/**F3** polymer materials spin coated from a chloroform : *o*DCB mixture using the same conditions used in device fabrication.

Figure 2.28 shows AFM images of the polymer / fullerene blends of **F1**/**F2**/**F3**/**NF** materials. Relative to the three fractionated batches, the non-fractionated material can be seen to have significantly larger phase segregation and domain size. This appears to be related to the PDI of the materials with each of the three fractions having a narrowed PDI compared to the non-fractionated material, which in turn corresponds to a finer intermixing of blend morphology. In terms of device performance for both conventional and inverted device architectures this correlates to both the lowest FF and PCE.

F3 has a reduced M_n and PDI relative the **NF** material and reduced phase segregation observed by AFM although regions of large domain size are still observable. As a result of this slight improvement in blend morphology **F3** demonstrates the smallest improvement in solar cell performance with only small efficiency enhancements observed for both conventional and inverted architectures. **F2** sees the disappearance of the larger domains and this matches larger improvements in device performance for both inverted and conventional architectures as a result of improved J_{sc} values of 14.3 mA cm^{-2} and 14.6 mA cm^{-2} respectively. The blend morphology of **F1** is further improved on that of **F2** giving an increase in photocurrent to 16.0 mA cm^{-2} however a small drop in FF means that only slight efficiency improvements are observed in both cases.

Figure 2.29 shows a histogram of the average domain sizes approximated from the AFM blend images and can be seen to support the above statement. The **NF** blends appear to have a very large range of domain sizes with the largest population of domain sizes being around 30 nm. The histogram of **F3** has a similarly diffuse shape, although slightly narrowed in comparison to **NF** but with the largest population of domain sizes being slightly larger at around 35 nm. This agrees with the smallest improvement in OPV performance of **F3** and the surface morphology image that is most similar to that of **NF**. In further agreement with the OPV performances and surface image morphologies **F2** and **F1** see substantial changes with significantly narrowed distributions of domain sizes on average around 10 nm in size for **F2** and 5 nm for **F1**. With the limitations in exciton diffusion lengths previously discussed it is clear that these reduced domain sizes are closely related to an increased amount of excitons reaching a D / A boundary for dissociation which is in turn the reason for the significantly enhanced photocurrents of **F1** and **F2** devices.

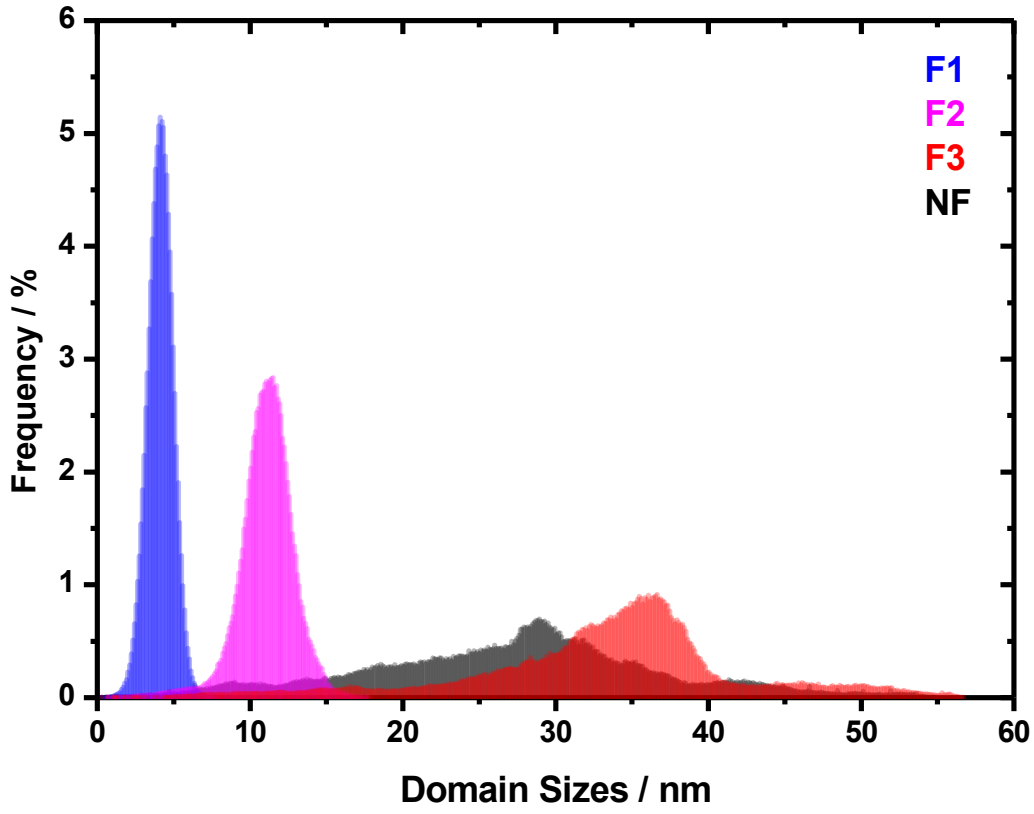

Figure 2.29. Average domain size of **NF**/**F1**/**F2**/**F3** polymer materials approximated by AFM.

2.7.3.2. XRD

X-ray diffraction (XRD) can provide a wealth of information on the nature and strength of interactions between polymer chains in addition to information on the orientation of polymer chains relative to the substrate, both of which have been shown to be closely related to various physical properties including molecular weight and polydispersity.[61,62] To further probe this it was of interest to probe the fractionation series and **Figure 2.29** shows XRD diffractograms of fractions **NF**/**F1**/**F2**/**F3** materials.

Each of the four materials show an out-of-plane reflection peak at 2θ = ~ 4º that is characteristic of lamellar *d*-spacing (100 peak) which translates to an interlamellar distance of approximately 21.5 Å. This has the lowest intensity for the **NF** material with the most crystalline material being **F3** with the lowest M_n of the three purified fractions whilst the two highest molecular weight fractions **F1** and **F2** have intensities

that are approximately half that of **F3**. This would suggest that there is not a simple relationship between polymer crystallinity, M_n or device performance.

It has previously been shown, and is probed further in Chapter Three and Chapter Four, that crystallinity is important in a variety of OPV performance parameters of **DPPTT-T** polymers and it is clear that fractionation induces an increase in crystallinity likely as a result of a reduction in polydispersity.[63-65] There is also a smaller crystalline peak at 2θ = ~ 8º characteristic of second order (200) crystallinity and this peak is indicative of increased crystallinity that is much more pronounced for **F3** which is in agreement with the greater intensity of the **F3** (100) peak.

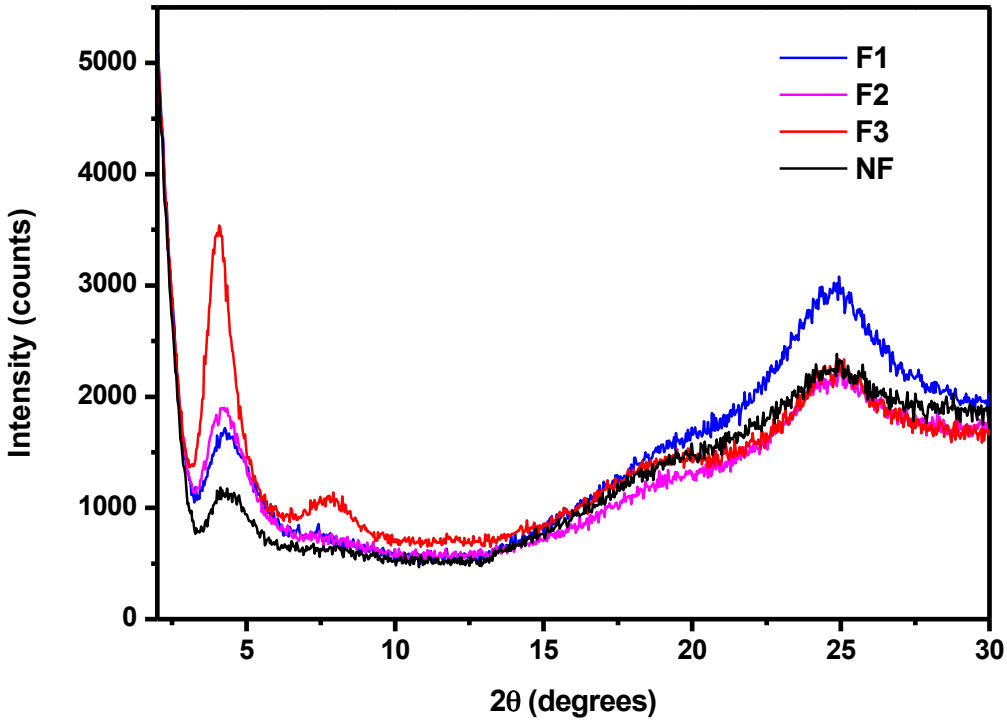

Figure 2.30. XRD diffractogram of films of **NF**/**F1**/**F2**/**F3** polymer materials drop cast from 10 mg / mL chlorobenzene solutions on Si wafers and dried in air overnight.

A low angle diffraction peak at 2θ = ~ 25º is clearly observable which is characteristic of π - π stacking between polymer chains and indicates the presence of material with a face-on orientation of the backbone plane to the plane of the substrate. Such an orientation can be favourable for vertical charge transport, a feature that is known to be advantageous for OPV applications. This peak is of similar intensity for **NF**, **F2** and **F3** materials but shows a sizeable increase for the highest M_n and best performing material **F1**.

2.8. Conclusion and outlook

The design, synthesis, and characterization of four novel **DPP** based polymers are described. Through employing a $C_{10}C_{12}$ branched alkyl chain it is demonstrated how the greater solubility imparted from the larger alkyl chain facilitates the synthesis of a larger range of co-polymer structures in higher molecular weights and narrowed polydispersities, a valuable tool towards the synthesis of solution processable **DPP** polymers. When used as the donor material in polymer : fullerene bulk heterojunction solar cells, efficiencies of up to 4 % are achieved in un-optimised devices. As the conducting channel in thin film organic transistors, promising ambipolar mobilities as high as 0.45 cm^2 / Vs are demonstrated with varying device architectures investigated.

Investigation into optimisation of the most promising polymer (**$C_{10}C_{12}$DPPTT-T**) for OPV applications as determined by initial device performance parameters is demonstrated. Through precise polymer fractionation using GPC polymer **P1** is separated into three different molecular weight fractions. Fractionation gives material of even narrowed polydispersities and higher molecular weights and subsequent incorporation of the varying molecular weight fractions into polymer : fullerene bulk heterojunction solar cells and subsequent optimisation through comparison of conventional and inverted device architecture gives impressive enhancement of solar cell performance. Short circuit currents are enhanced from 12.6 mA cm^2 to values approaching 16 mA cm^2 giving a dramatic increase in power conversion efficiency of in excess of 50 % from 4.1 % to 6.3 % in conventional architecture and 5.5 % with inverted device architecture. An efficiency enhancement is observed even in **F3** where there is a reduction in molecular weight which demonstrates the importance of PDI in addition to molecular weight as a physical parameter that can influence device performance. Photocurrent improvement is also seen to closely follow molecular weight at values far above the polymer's effective conjugation length and the improved device performances correlate well with improved intermixing of the polymer / fullerene blends.

Using alkyl chain modification to access higher molecular weight material combined with a single post polymerisation fractionation step and subsequent device optimisation an effective route towards optimisation the performance of a promising **DPP** polymer for OPV applications is demonstrated.

Further work into the effect of fractionation on polymers for OPV applications would be desirable to establish to what extent the performance can be increased with narrower weight distributions and larger molecular weights. It would also be of interest to examine how the OFET device performances of DPP and other polymers, are effected by such a fractionation.

2.9. References

1. D. Moghe, P. Yu, C. Kanimozhi, S. Patil and S. Guha, *Appl. Phys. Lett.*, 2011, **99**, 233307.
2. L. Chen, D. Deng, Y. Nan, M. Shi, P. K. L. Chan and H. Chen, *J. Phys. Chem. C*, 2011, **115**, 11282–11292.
3. C. Kanimozhi, N. Yaacobi-Gross, K. W. Chou, A. Amassian, T. D. Anthopoulos and S. Patil, *J. Am. Chem. Soc.*, 2012, **134**, 16532–16535.
4. J. C. Bijleveld, R. A. M. Verstrijden, M. M. Wienk and R. A. J. Janssen, *J. Mater. Chem.*, 2011, **21**, 9224–9231.
5. M. M. Wienk, M. Turbiez, J. Gilot and R. A. J. Janssen, *Adv. Mater.*, 2008, **20**, 2556–2560.
6. J. C. Bijleveld, A. P. Zoombelt, S. G. J. Mathijssen, M. M. Wienk, M. Turbiez, D. M. de Leeuw and R. A. J. Janssen, *J. Am. Chem. Soc.*, 2009, **131**, 16616–16617.
7. H. Bronstein, Z. Chen, R. S. Ashraf, W. Zhang, J. Du, J. R. Durrant, P. S. Tuladhar, K. Song, S. E. Watkins, Y. Geerts, M. M. Wienk, R. A. J. Janssen, T. Anthopoulos, H. Sirringhaus, M. Heeney and I. McCulloch, *J. Am. Chem. Soc.*, 2011, **133**, 3272–3275.
8. W. Li, T. Lee, S. J. Oh and C. R. Kagan, *ACS Appl. Mater. Interface*s, 2011, **3**, 3874–3883.
9. P.-T. Wu, F. S. Kim and S. A. Jenekhe, *Chem. Mater.*, 2011, **23**, 4618–4624.
10. F. P. V. Koch, J. Rivnay, S. Foster, C. Müller, J. M. Downing, E. Buchaca-Domingo, P. Westacott, L. Yu, M. Yuan, M. Baklar, Z. Fei, C. Luscombe, M. A. McLachlan, M. Heeney, G. Rumbles, C. Silva, A. Salleo, J. Nelson, P. Smith and N. Stingelin, *Prog. Polym. Sci.*, 2013, **38**, 1978–1989.
11. T.-Y. Chu, J. Lu, S. Beaupré, Y. Zhang, J.-R. Pouliot, J. Zhou, A. Najari, M. Leclerc and Y. Tao, *Adv. Funct. Mater.*, 2012, **22**, 2345–2351.
12. T. Higashihara and E. Goto, *Polym. J.*, 2014, **46**, 381–390.
13. H. A. Bronstein and C. K. Luscombe, *J. Am. Chem. Soc.*, 2009, **131**, 12894.
14. Z. N. Bao, W. K. Chan, and L. P. Yu, *J. Am. Chem. Soc.*, 1995, **117**, 12426–12435.
15. J. C. Bijleveld, V. S. Gevaerts, D. Di Nuzzo, M. Turbiez, S. G. J. Mathijssen, D. M. de Leeuw, M. M. Wienk and R. A. J. Janssen, *Adv. Mater.*, 2010, **22**, 242–246.
16. P. Sonar, S. P. Singh, Y. Li, M. S. Soh and A. Dodabalapur, *Adv. Mater.*, 2010, **22**, 5409.
17. T. Potrawa and H. Langhals, *Chem. Ber.*, 1987, **120**, 1075–1078.
18. C. J. H. Morton, R. Gilmour, D. M. Smith, P. Lightfoot, A. M. Z. Slawin and E. J. MacLean, *Tetrahedron*, 2002, **58**, 5547–5565.
19. E. Ripaud, D. Demeter, T. Rousseau, E. Boucard-Cétol, M. Allain, R. Po, P. Leriche and J. Roncali, *Dye. Pigment.*, 2012, **95**, 126–133.
20. S. Talukdar, J.-L. Hsu, T.-C. Chou and J.-M. Fang, *Tetrahedron Lett.*, 2001, 42, 1103–1105.
21. D. F. DeTar, *J. Org. Chem.*, 1980, **45**, 5174–5176.

22. S. A. Gevorgyan and F. C. Krebs, *Handbook of Thiophene-Based Materials*, 673–693.
23. M. Jayakannan, J. L. J. van Dongen and R. A. J. Janssen, *Macromolecules*, 2001, **34**, 5386–5393.
24. T. Kirschbaum, R. Azumi, E. Mena-Osteritz and P. Bauerle, *New J. Chem.*, 1999, **23**, 241–250.
25. T. Kirschbaum, C. A. Briehn and P. Bauerle, *J. Chem. Soc. Perkin Trans. 1*, 2000, 1211–1216.
26. S. Tierney, M. Heeney and I. McCulloch, *Synth. Met.*, 2005, **148**, 195–198.
27. C. J. Brabec, A. Cravino, D. Meissner, N. S. Sariciftci, T. Fromherz, M. T. Rispens, L. Sanchez and J. C. Hummelen, *Adv. Funct. Mater.*, 2001, **11**, 374–380.
28. K. Vandewal, K. Tvingstedt, A. Gadisa, O. Inganas and J. V Manca, *Nat. Mater.*, 2009, **8**, 904–909.
29. T.-Q. Nguyen, I. B. Martini, J. Liu and B. J. Schwartz, *J. Phys. Chem. B*, 1999, **104**, 237–255.
30. C. B. Nielsen, M. Turbiez and I. McCulloch, *Adv. Mater.*, 2012, **25**, 1859-1880
31. W. R. Salaneck, R. H. Friend and J. L. Brédas, *Phys. Rep.*, 1999, **319**, 231–251.
32. P. J. Brown, D. S. Thomas, A. Kohler, J. S. Wilson, J.-S. Kim, C. M. Ramsdale, H. Sirringhaus and R. H. Friend, *Phys. Rev. B: Condens. Matter Mater. Phys.*, 2003, **67**, 064203/1–064203/16.
33. G. Dufresne, J. Bouchard, M. Belletête, G. Durocher, and M. Leclerc, *Macromolecules*, 2000, **33**, 8252–8257.
34. X. Zhang, L. J. Richter, D. M. DeLongchamp, R. J. Kline, M. R. Hammond, I. McCulloch, M. Heeney, R. S. Ashraf, J. N. Smith, T. D. Anthopoulos, B. Schroeder, Y. H. Geerts, D. A. Fischer, and M. F. Toney, *J. Am. Chem. Soc.*, 2011, **133**, 15073–15084.
35. M. Ahmida, S. Dufour, H.-S. Li, H. Kayal, R. Schmidt, C. E. DeWolf and S. H. Eichhorn, *Soft Matter*, 2013, **9**, 811–819.
36. R. Mondal, N. Miyaki, H. A. Becerril, J. E. Norton, J. Parmer, A. C. Mayer, M. L. Tang, J.-L. Brédas, M. D. McGehee and Z. Bao, *Chem. Mater.*, 2009, **21**, 3618–3628.
37. C. Muller, C. P. Radano, P. Smith and N. Stingelin-Stutzmann, *Polymer*, 2008, **49**, 3973–3978.
38. J. M. Szarko, J. C. Guo, Y. Y. Liang, B. Lee, B. S. Rolczynski, J. Strzalka, T. Xu, S. Loser, T. J. Marks, L. P. Yu and L. X. Chen, *Adv. Mater.*, 2010, **22**, 5468–5472.
39. N. Blouin, A. Michaud, D. Gendron, S. Wakim, E. Blair, R. Neagu-Plesu, M. Belletete, G. Durocher, Y. Tao and M. Leclerc, *J. Am. Chem. Soc.*, 2008, **130**, 732–742.
40. P. M. Beaujuge, H. N. Tsao, M. R. Hansen, C. M. Amb, C. Risko, J. Subbiah, K. R. Choudhury, A. Mavrinskiy, W. Pisula, J.-L. Brédas, F. So, K. Müllen and J. R. Reynolds, *J. Am. Chem. Soc.*, 2012, **134**, 8944–8957.
41. T. M. McCormick, C. R. Bridges, E. I. Carrera, P. M. DiCarmine, G. L. Gibson, J. Hollinger, L. M. Kozycz and D. S. Seferos, *Macromolecules*, 2013, **46**, 3879–3886.
42. H. Ohkita, S. Cook, Y. Astuti, W. Duffy, S. Tierney, W. Zhang, M. Heeney, I. McCulloch, J. Nelson, D. D. C. Bradley and J. R. Durrant, *J. Am. Chem. Soc.*, 2008, **130**, 3030–3042.
43. M. C. Scharber, D. Wuhlbacher, M. Koppe, P. Denk, C. Waldauf, A. J. Heeger and C. L. Brabec, *Adv. Mater.*, 2006, **18**, 789.
44. P. W. M. Blom, V. D. Mihailetchi, L. J. A. Koster and D. E. Markov, *Adv. Mater.*, 2007, **19**, 1551–1566.
45. L. Y. Park, A. M. Munro and D. S. Ginger, *J. Am. Chem. Soc.*, 2008, **130**,15916–15926.
46. H. Hoppe, M. Niggemann, C. Winder, J. Kraut, R. Hiesgen, A. Hinsch, D. Meissner and N. S. Sariciftci, *Adv. Funct. Mater.*, 2004, **14**, 1005–1011.
47. F. Liu, Y. Gu, J. W. Jung, W. H. Jo and T. P. Russell, *J. Polym. Sci. Part B: Polym. Phys.*, 2012, **50**, 1018–1044.

48. C. Groves, O. G. Reid and D. S. Ginger, *Acc. Chem. Res.*, 2010, **43**, 612–620.
49. Z. Chen, M. J. Lee, R. Shahid Ashraf, Y. Gu, S. Albert-Seifried, M. Meedom Nielsen, B. Schroeder, T. D. Anthopoulos, M. Heeney, I. McCulloch and H. Sirringhaus, *Adv. Mater.*, 2012, **24**, 647–52.
50. J. Lee, A. R. Han, J. Kim, Y. Kim, J. H. Oh and C. Yang, *J. Am. Chem. Soc.*, 2012, **134**, 20713–20721.
51. S. Holliday, J. E. Donaghey and I. McCulloch, *Chem. Mater.*, 2013, **26**, 647–663.
52. J. Liu, B. Walker, A. Tamayo, Y. Zhang and T.-Q. Nguyen, *Adv. Funct. Mater.*, 2013, **23**, 47–56.
53. I. McCulloch, R. S. Ashraf, L. Biniek, H. Bronstein, C. Combe, J. E. Donaghey, D. I. James, C. B. Nielsen, B. C. Schroeder and W. Zhang, *Acc. Chem. Res.*, 2012, **45**, 714-722
54. R. S. Ashraf, B. C. Schroeder, H. A. Bronstein, Z. Huang, S. Thomas, R. J. Kline, C. J. Brabec, P. Rannou, T. D. Anthopoulos, J. R. Durrant and I. McCulloch, *Adv. Mater.*, 2013, **25**, 2029–2034.
55. K. H. Hendriks, G. H. L. Heintges, V. S. Gevaerts, M. M. Wienk and R. A. J. Janssen, *Angew. Chemie Int. Ed.*, 2013, **52**, 8341–8344.
56. Z. Huang, E. C. Fregoso, S. Dimitrov, P. S. Tuladhar, Y. W. Soon, H. Bronstein, I. Meager, W. Zhang, I. McCulloch and J. R. Durrant, *J. Mater. Chem. A*, 2014, Submitted.
57. S. D. Dimitrov, Z. Huang, F. Deledalle, C. B. Nielsen, B. C. Schroeder, R. S. Ashraf, S. Shoaee, I. McCulloch and J. R. Durrant, *Energy Environ. Sci.*, 2014, **7**, 1037-1043.
58. R. Noriega, J. Rivnay, K. Vandewal, F. P. V Koch, N. Stingelin, P. Smith, M. F. Toney and A. Salleo, *Nat. Mater.*, 2013, **12**, 1038–1044.
59. S. K. Hau, H.-L. Yip and A. K.-Y. Jen, *Polym. Rev.*, 2010, **50**, 474–510.
60. H. Hoppe and N. S. Sariciftci, *J. Mater. Chem.*, 2006, **16**, 45–61.
61. A. Zen, M. Saphiannikova, D. Neher, J. Grenzer, S. Grigorian, U. Pietsch, U. Asawapirom, S. Janietz, U. Scherf, I. Lieberwirth and G. Wegner, *Macromolecules*, 2006, **39**, 2162–2171.
62. W. Ma, J. Y. Kim, K. Lee and A. J. Heeger, *Macromol. Rapid Commun.*, 2007, **28**, 1776–1780.
63. B. D. Olsen, S.-Y. Jang, J. M. Luning, and R. A. Segalman, *Macromolecules*, 2006, **39**, 4469–4479.
64. P. Kohn, S. Huettner, H. Komber, V. Senkovskyy, R. Tkachov, A. Kiriy, R. H. Friend, U. Steiner, W. T. S. Huck, J.-U. Sommer and M. Sommer, *J. Am. Chem. Soc.*, 2012, **134**, 4790–4805.
65. Y. W. Soon, S. Shoaee, R. S. Ashraf, H. Bronstein, B. C. Schroeder, W. Zhang, Z. Fei, M. Heeney, I. McCulloch, and J. R. Durrant, *Adv. Funct. Mater.*, 2014, **24**, 1474–1482.

Chapter Three

Alkyl Chain Branching Point Manipulation In Thieno[3,2-*b*]thiophene Flanked Diketopyrrolopyrrole Polymers For Use in Organic Solar Cells and Field Effect Transistors

3.1. Introduction

As demonstrated in Chapter Two, it is clear from initial OPV and OFET devices made both in the literature and in the previous work described in this thesis that thieno[3,2-*b*]thiophene flanked diketopyrrolopyrrole (**DPPTT**) polymers are an excellent candidate material for the rational design of high performance organic electronic materials. Through extension of the alkyl chain length from C_8C_{10} to $C_{10}C_{12}$ it was previously possible to increase the solubility, molecular weight and polydispersity of various **DPPTT** based polymers, which exemplified how modification of the insulating alkyl chains can be essential in optimizing polymer performance.

The choice of solubilising alkyl chains generally fall into two categories; linear or branched. Branched alkyl chains are often favoured in solar cell applications whereas linear chains can prove more successful in transistor applications. Branching of the chains at a position away from the polymer backbone ensures that disruption of the strong interchain $\pi - \pi$ interactions is maximised and that the material can be solubilised. Linear alkyl chains can interdigitate which facilitates closer intermolecular packing of polymer chains which can be favourable for many polymer properties and characteristics. However this can also come at the cost of reduced solubility and as a result, polymers that are known to be less soluble are often designed with branched alkyl chains to ensure solubility.

Throughout the literature, the use of branched alkyl chains is almost exclusively limited to those in which the branching point is located at a position with one linear carbon atom between the point of alkylation and the point of branching. Predominantly this is due to the commercial availability of the 2-ethylhexanol, 2-octyldodecanol and 2-decyltetradecanol precursors. In 2011 *Z. Bao et al.* reported the use of siloxane-terminated linear alkyl chains attached to a series of isoindigo-based polymers which gave large enhancements in OFET mobilities. The bulky terminal trimethylsilane groups provide branching characteristics after a long linear portion which allows for the closer packing of polymers.[1] This remained the only example of manipulation of alkyl chain branching until *J. Pei et al.* successfully demonstrated the effect of moving the alkyl chain branching position further from the polymer backbone in a series of di-phenyl isoindigo polymers (**Figure 3.1**).[2] It was shown that through careful consideration of the alkyl chain branching position significant

increased in the charge transport properties in OFET devices could be realised. This was attributed to increased material crystallinity through tighter interchain stacking. The same group, and others, have also recently published further reports of this effect upon the OFET performance in isoindigo based polymers and naphthalene diimide (NDI) small molecules to establish the expansion of the alkyl branching position as a key synthetic parameter for the design of semiconducting polymers.[3-6]

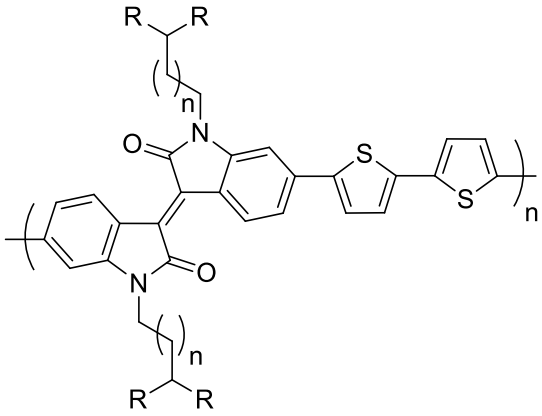

Figure 3.1. Manipulation of alkyl chain branching point in di-phenyl isoindigo polymers for OFET applications as reported by *J. Pei et al.*[2]

Despite these promising results it is yet to be shown whether these improvements in device characteristics and solubility will be reflected in OPV applications. A systematic study of the effect that such a branching point manipulation would have on solar cell performance is therefore of great interest to the field and would likely benefit the future design of candidate OPV materials.

3.2. Aim

Through the design and synthesis of two new branched alkyl halide chains, attachment of these new alkyl chains to thieno[3,2-*b*]thiophene diketopyrrolopyrrole (**Figure 3.2)** and their subsequent co-polymerisation with various co-monomers it is hoped that a novel series of extended branching position polymers will shed new light on the role of branched alkyl chains in organic solar cell devices. **DPP** based polymers, especially **DPPTT** polymers are known to exhibit strong π - π interactions between polymer chains with a tendency to aggregate in both solution and thin films. Consequently, such a modification that can influence the manner in which these

interactions occur has high potential to influence a number of optical and physical properties of the polymers.

These new alkyl chains, denoted *Cn* where *n* corresponds to the number of linear carbon atoms between alkylation and branching, should serve to increase the interactions between polymer chains due to the extended linear portion of the alkyl chains facilitating a less sterically hindered conjugated backbone whilst also improving the solubility through increasing their spatial size. Initially through co-polymerisation with thiophene, it will be possible to directly compare how such a manipulation will affect the solubility, morphology, energetic and physical properties of the resultant polymers.

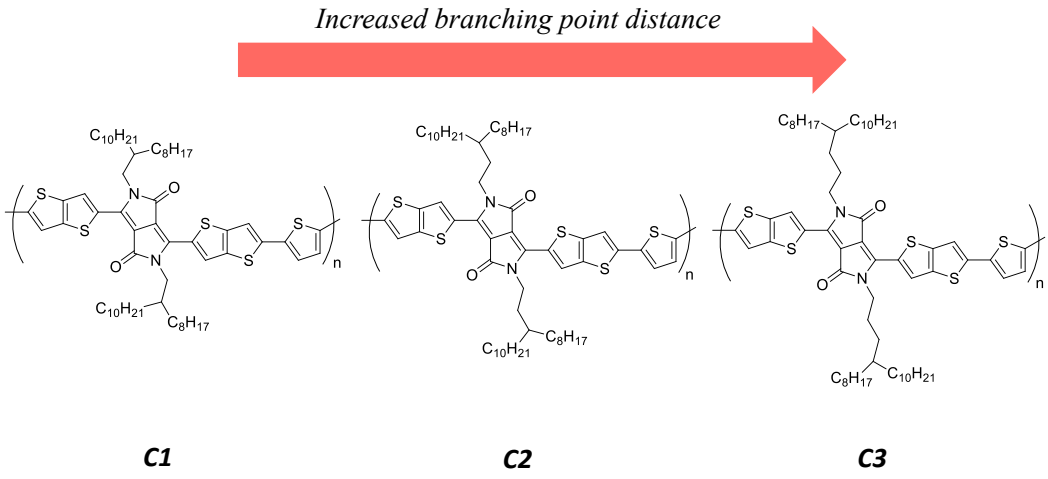

Figure 3.2. Proposed **DPPTT-T** series in which the alkyl chain branching position is systematically moved further from the polymer backbone.

These changes in polymer properties will be correlated to the differences in performance of the materials in polymer / fullerene bulk heterojunction (BHJ) solar cells and thin film OFET devices. Further to co-polymerisation with thiophene, the most promising previous co-monomer partners will also be examined for the new ***C2*** unit; in Chapter Two the phenyl co-monomer unit (**P4**) was shown to be as high performing as thiophene in BHJ solar cells whilst previous literature demonstrates the **DPPTT** homo-polymer as another promising material. Incorporation of the novel ***C3*** moeity in chalcogenophene (Thiophene, Selenophene and Tellurophene) based co-polymers will also be investigated to shine light on their potential in organic electronic applications and develop an understanding of chalcogen heavy atom substitution structure-property relationships.

3.3. Synthesis of polymers P5 – P10

3.3.1. Alkyl chain synthesis

3.3.1.1. Synthesis of *C2* alkyl chain 3-octyl-1-tridecyl iodide 3.3

The commercially available 2-octyl-1-dodecanol was brominated using NBS under conditions previously described to afford the equivalent alkyl bromide **3.1**. This was converted to the corresponding alkyl magnesium bromide by reaction with magnesium in diethyl ether using a single flake of iodine as an initiator. The highly reactive Grignard reagent was quenched with powdered paraformaldehyde and worked up under acidic conditions to afford the extended branching position alcohol 3-octyl-1-tridecanol **3.2 (Figure 3.3)**.

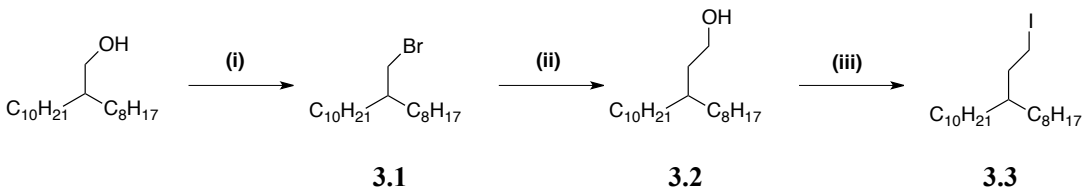

3.1 **3.2** **3.3**

Figure 3.3. Synthesis of ***C2*** alkyl chain 3-octyl-1-tridecyl iodide **3.3** *Reagents and conditions*: **(i)** NBS, PPh_3, DCM, 0 ºC **(ii)** Mg, paraformaldehyde, reflux **(iii)** PPh_3, I_2, imidazole, 0 ºC.

As shown in **Figure 3.4** this transformation was identified by the disappearance of a doublet at 3.47 ppm, corresponding to the CH_2 protons adjacent to the bromide, to be replaced by a more downfield shifted triplet at 3.62 ppm in the ^{1}H NMR of **3.2**. The extended alcohol was then converted to the better leaving group (iodide) for subsequent attachment to the **DPPTT** core under conditions analogous to the initial bromination using iodine in combination with imidazole and triphenylphosphine. The formation of 3-octyl-1-tridecyl iodide **3.3** was identified by a shift of the CH_2 triplet to 3.22 ppm due to the less electronegative iodide functionality.

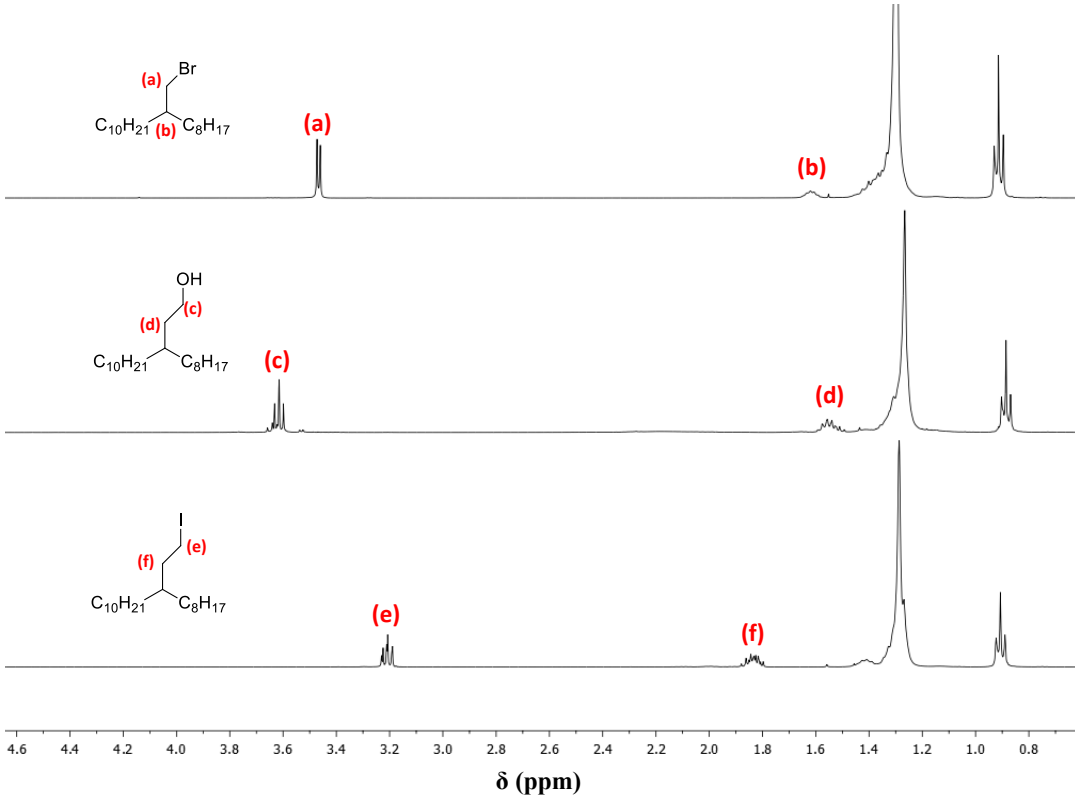

Figure 3.4. ^{1}H NMR in $CDCl_3$ at 25 ºC of compounds **3.1**, **3.2** and **3.3** showing the characteristic changes associated with each transformation.

3.3.1.2. Synthesis of *C3* alkyl chain 4-octyl-1-tetradecyl iodide 3.8

As shown in **Figure 3.5**, commercially available diethyl malonate was deprotonated at the acidic C*H* position between the two carbonyl groups using the strongly basic sodium ethoxide. The previously synthesised 2-octyl-1-dodecyl bromide **3.1** was then slowly added to the resultant malonate anion solution. Nucleophilic substitution of the malonate ion for the bromide group afforded the C_8C_{10} malonic ester **3.4**. This transformation was identified by ^{1}H NMR showing the disappearance of the CH_2 doublet adjacent to the bromide group at 3.47 ppm to be replaced by a triplet at 3.44 ppm due to the formation of the carbonyl flanked tertiary C*H* peak as well as the appearance of the quartet at 4.21 ppm representing the four ethyl CH_2 protons in the attached malonic ester group (**Figure 3.6**).

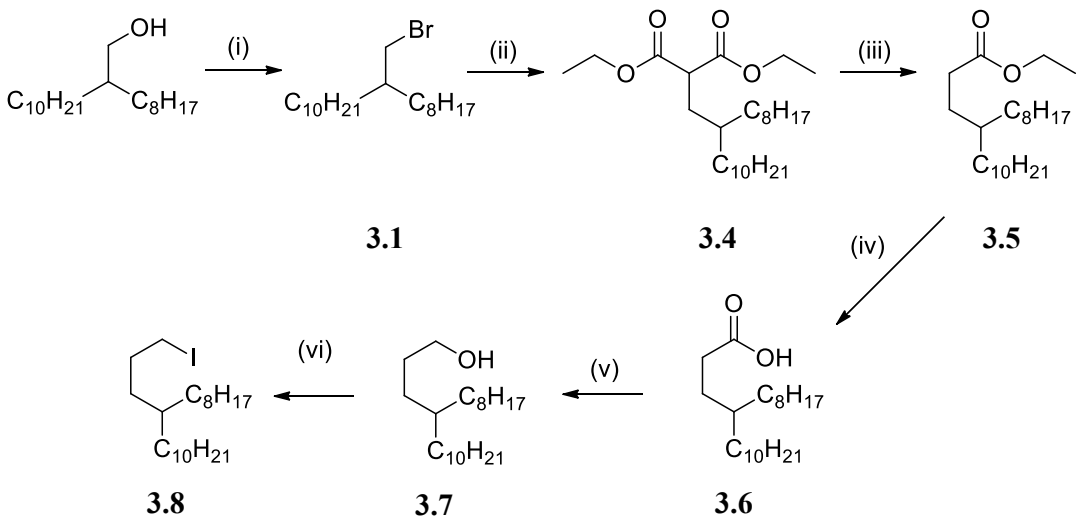

Figure 3.5. Synthesis of ***C3*** alkyl chain 4-octyl-1-tetradecyl iodide **3.8**. *Reagents and conditions*: **(i)** NBS, PPh_3, DCM, 0 ºC **(ii)** Na^+EtO^-, diethyl malonate **(iii)** NaCl, DMSO, 180 ºC **(iv)** NaOH, EtOH, reflux **(v)** $LiAlH_4$, THF, reflux **(vi)** PPh_3, I_2, imidazole, DCM, 0 ºC.

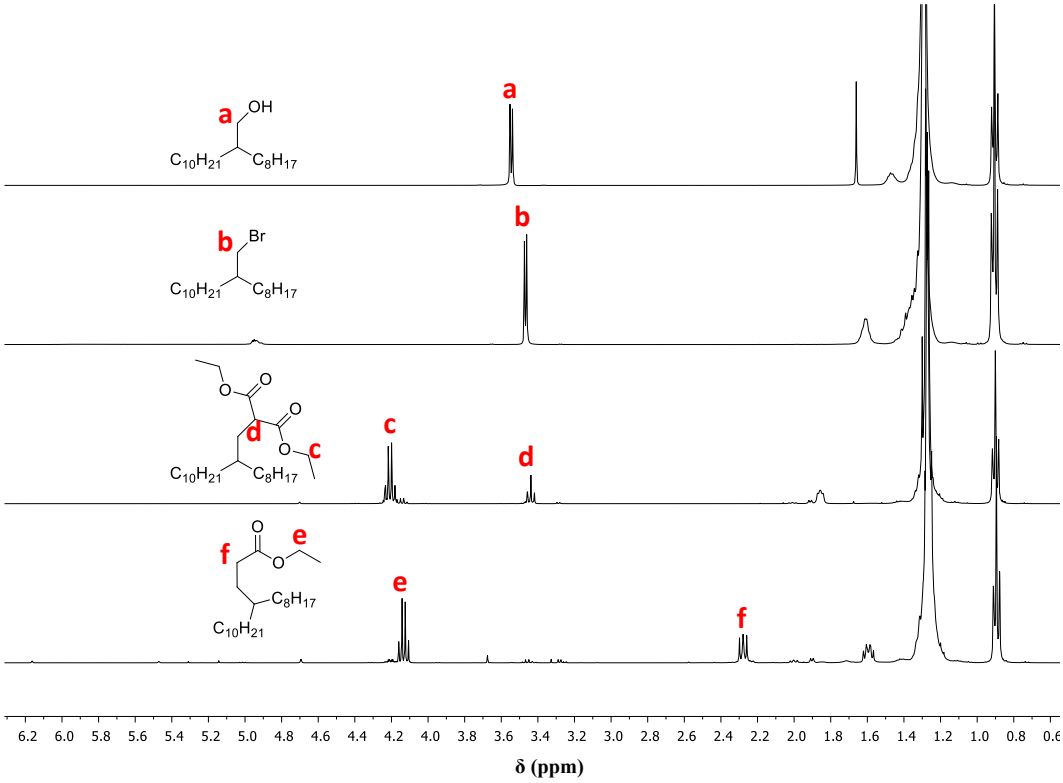

Figure 3.6. ^1H NMR in $CDCl_3$ at 25 ºC of compounds **3.1**, **3.4**, **3.5** showing the characteristic changes associated with each transformation.

The malonic ester **3.4** was converted to the corresponding mono-ester by Krapcho decarboxylation using NaCl in DMSO at 180 ºC. A polar aprotic solvent was used to stabilise the anionic intermediate and a high temperature was needed due to the relatively weak nucleophilicity of the Cl^- anion. The reaction proceeds via attack of the ester ethyl group by the free chloride ions resulting in the formation of gaseous chloroethane. The resultant CO_2^- group is then able to leave as gaseous CO_2 by resonance stabilisation of the anionic charge onto the remaining adjacent ester group, which provides an entropic driving force for the decarboxylation. The product **3.5** was identified using ^{1}H NMR by disappearance of the tertiary C*H* triplet peak at 3.44 ppm to be replaced by a CH_2 triplet peak at 2.28 ppm due to the presence of one, as opposed to the previous two, flanking carbonyls (**Figure 3.7**). There is also the changing integration of the CH_2 quartet from 4H to 2H confirming the loss of one ethyl ester group.

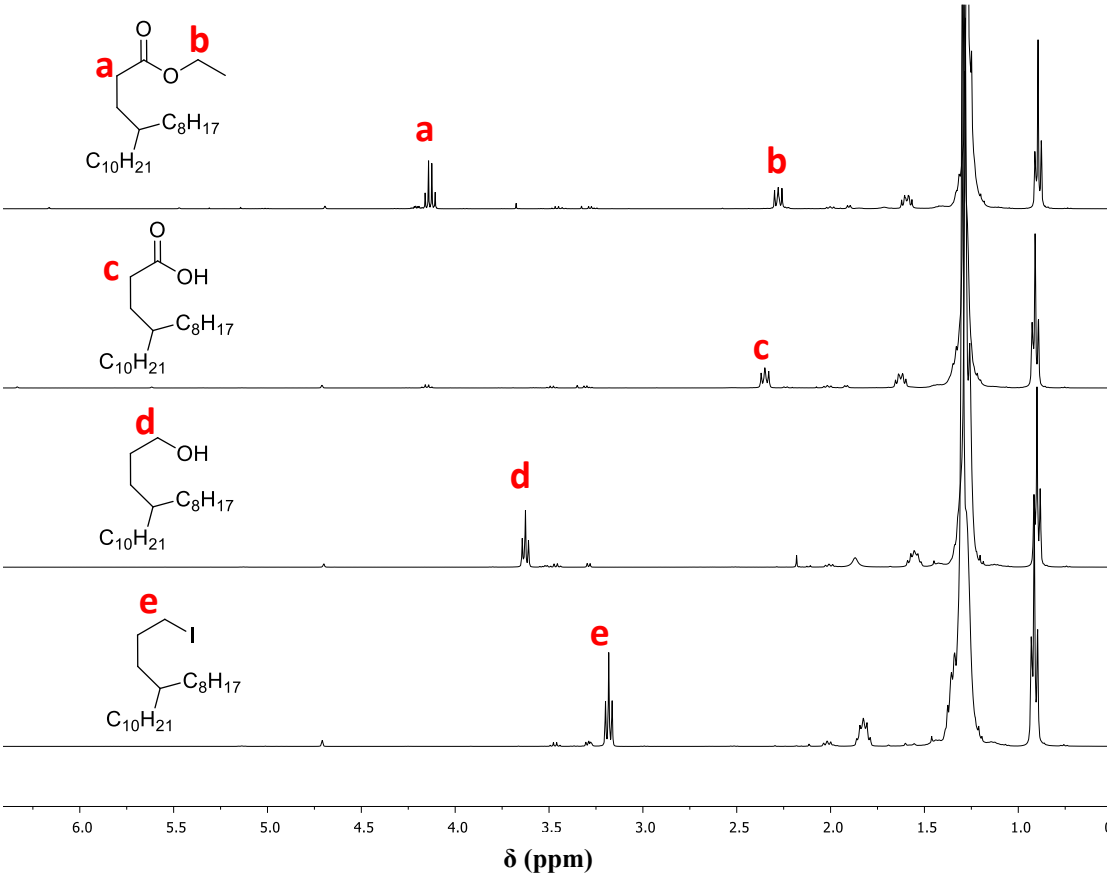

Figure 3.7. ^{1}H NMR in $CDCl_3$ at 25 ºC of compounds **3.5**, **3.6**, **3.7** and **3.8** showing the characteristic changes associated with each transformation.

Following decarboxylation the ester group was hydrolysed to the corresponding carboxylic acid **3.6** by elimination of ethanol using mildly basic conditions. The transformation was identified by the disappearance of the ethyl CH_2 quartet at 4.21 ppm in the ^{1}H NMR spectrum to be replaced by a triplet at 2.35 ppm indicating the CH_2 protons adjacent to the acid functionality. The resulting acid was converted to the corresponding alcohol **3.7** using lithium aluminium tetrahydride with care being taken to add the reducing agent at a steady rate. The formation of the alcohol **3.7** was confirmed by the presence of a triplet peak at 3.63 ppm in the ^{1}H NMR spectrum, corresponding to the CH_2 peak adjacent to the hydroxyl functionality. The alcohol was subsequently converted to the corresponding alkyl iodide **3.8** using the mild conditions as previously described. The transformation was confirmed by a shift of the CH_2 peak in the ^{1}H NMR spectrum to 3.18 ppm (**Figure 3.7**).

3.3.2. Monomer synthesis

The **DPPTT** core was reacted with the corresponding alkyl iodide (**3.3** or **3.8**) under standard DPP S_N2 alkylation conditions detailed earlier in the thesis. The moving of the branching position further from the halogen leaving group to ***C2*** and ***C3*** positions affords higher yielding alkylation steps than the original branched chains due to the electrophilic centres being less sterically hindered by the C_8H_{17} and $C_{10}H_{21}$ alkyl groups. ^{1}H NMR shows both ***C2*** and ***C3*** alkylations affording two aromatic doublets and a singlet of equal integration. Following purification the alkylated monomers were brominated using elemental bromine and purified by column chromatography to afford the final ***C2*** and ***C3*** monomers. As with the **DPPTT** synthesis described in Chapter Two this transformation is identified by a change in the aromatic region of the ^{1}H NMR to give two singlets showing the α-protons of the thieno[3,2-*b*]thiophene units being replaced by bromine atoms. There was a slight increase in polarity with increased branching point distance as observed during purification by column chromatography which is likely as a result of the more sterically exposed polar carbonyl functionalities, this was also observed with branching point manipulation in isoindigo polymers in previous publications by *J. Pei et al.*[2,6]

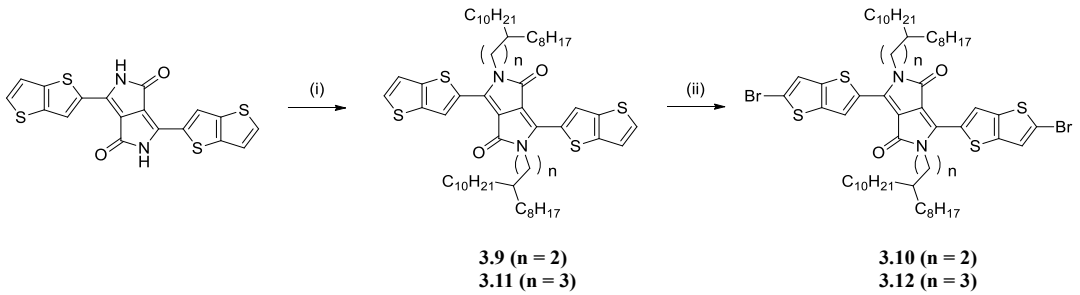

Figure 3.8. Synthesis of brominated **DPPTT** monomers **3.10** and **3.12** with the extended branching position ***C2*** and ***C3*** alkyl chains. *Reagents and conditions*: **(i)** K_2CO_3, DMF, 18-crown-6, compound **3.3** or **3.8**, 120 ºC **(ii)** Br_2, $CHCl_3$, 80 ºC.

3.3.3. Polymer synthesis

3.3.3.1. *C2* co-polymer synthesis

In Chapter Two a wide range of co-polymers of different **DPPTT** co-monomers were investigated and the two highest performing co-monomers were shown to be thiophene and phenyl units which gave unoptimised PCEs of 4.1 % and 4.0 % respectively. Because these were shown to be good co-monomers for **DPPTT** polymers, polymerisations with di- stannylated thiophene by Stille coupling and di-borylated phenyl units by Suzuki coupling were repeated with the ***C2*** alkylated monomer **3.10** under the same conditions (**Figure 3.9.**). Following standard polymer work-up and extraction into chlorobenzene the polymer's physical characteristics were obtained and are reported in **Table 3.1**.

The newly employed alkyl chains impart an observed increase in solubility during the polymerisation process, indicated by the high M_n and PDI values of the isolated polymers**.** A further consequence of the increased solubility was that when polymerisations were attempted using equimolar ratios of co-monomers only a dark green gel was obtained that was completely insoluble in common laboratory solvents even at elevated temperatures. It is speculated that the increased solubility of the monomers and resulting oligomers resulted in the synthesis of very high molecular weight materials to a point where it is not possible to re-dissolve the material following polymerisation. To counteract this effect the stoichiometry used in the polymerisation was offset to give a molar ratio of 1.05 : 1 (T : **DPP**) with a view to

targeting slightly lower M_n material that was more soluble. The specific polymer chemistry implications of this are discussed in more detail in section **3.3.3.3**.

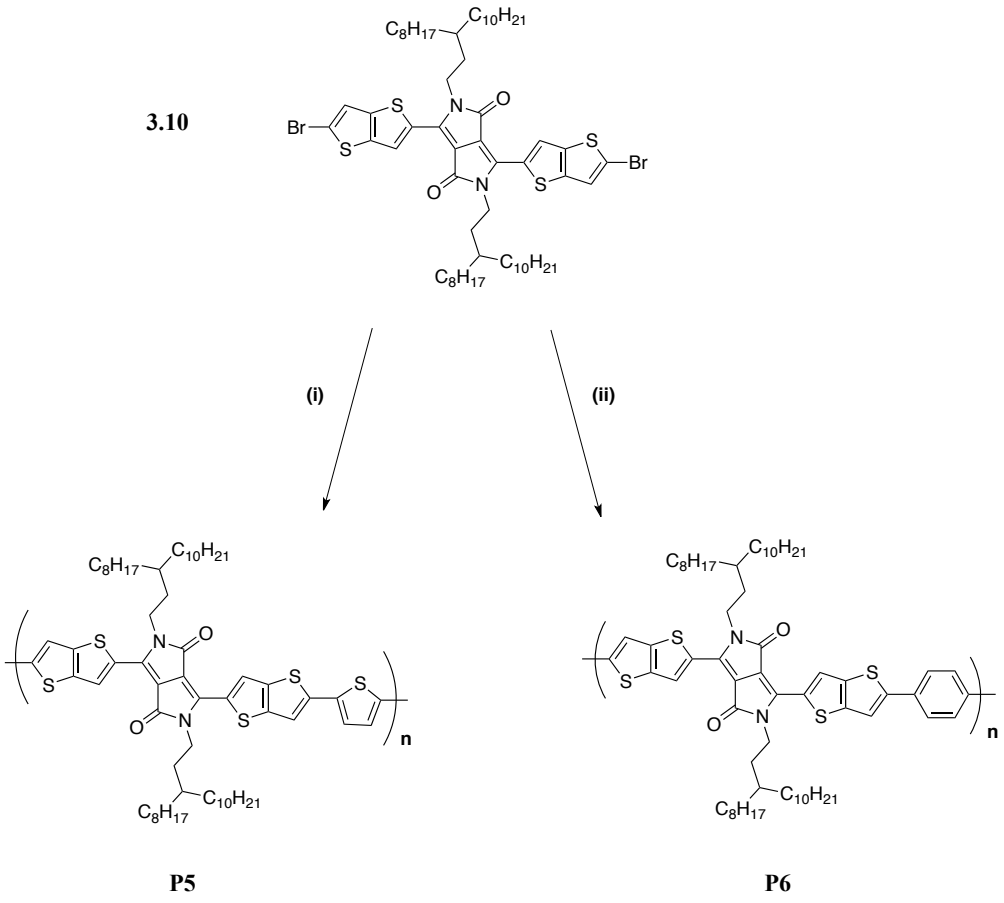

Figure 3.9. Synthesis of polymers **P5** and **P6** from **3.10** by palladium-catalysed Stille and Suzuki co-polymerisations of **3.10**. *Reagents and conditions*: **(i)** PhCl, $Pd_2(dba)_3$, P(*o*Tol)$_3$, 2,5-bis(trimethylstannyl)thiophene, µW **(ii)** PhMe, K_3PO_4, Aliquat 336, $Pd_2(dba)_3$, PPh_3, 1,4-di(4,4,5,5-tetramethyl-1,3-dioxaboralane)benzene, 120 ºC.

3.3.3.2. *C2* homo-polymer synthesis

For the original **DPPTT** publication previously introduced, in addition to the thiophene co-polymer a homo-polymer was also synthesised which demonstrated good solar performance with a PCE of 3.0 % and OFET electron mobilities of 0.30 cm^2 / Vs. Building on this, the potential of **DPPTT** homo-polymers was further investigated by Stille-like homo-polymerisation of the ***C2*** monomer **3.10** using hexamethylditin $(Sn(Me_3))_2$. The physical properties of the new homo-polymer **P7** are

reported alongside **P5** (T) and **P6** (Ph) in **Table 3.1**. Homo-polymerisation has been shown with other **DPP** structures to afford materials with good charge transport properties due to the intrinsic planarity of **DPP** unit, whilst the flanking donor units of the electron-deficient core ensures that **DPP** homo-polymers retain their D / A type backbone structure and exhibit much of the same properties as their co-polymer counterparts.

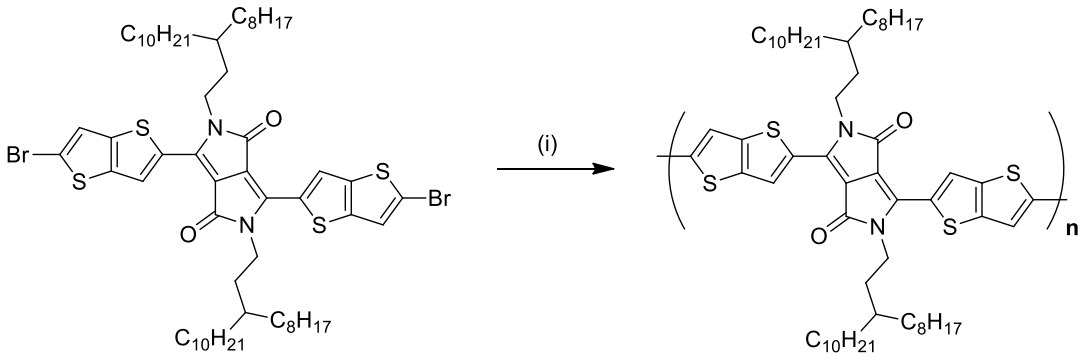

3.10 **P7**

Figure 3.10. Synthesis of polymer **P7** by palladium-catalysed homo-polymerisation of **3.10**. *Reagents and conditions*: $(Sn(Me_3))_2$, $Pd_2(PPh_3)_4$, CuI, THF / NMP, reflux.

A recent study by *R. Janssen et al.* was undertaken to investigate the role that homo-couplings play as defects in conventional **DPP** co-polymeristions.[7] Whilst the purpose of this work was to evaluate the detrimental effects these homo-couplings have on OPV performance when present as impurities during a co-polymerisation, the findings provide a useful insight into the differences between homo-coupled and cross-coupled systems. A series of **DPPT** co-polymers were synthesised with molar homo-coupling ratios from 5 % to 20 % and it was shown that in comparison to cross-couplings, homo-couplings result in increased E_{HOMO}, stabilised E_{LUMO}, and a narrowed E_g. Such features may be desirable to varying extents for the development of this new series of polymers.

One significant difference to earlier discussed co-polymerisations can be seen with the density of the alkyl chains along the polymer backbone. Removing the non-alkylated co-monomers from the equation creates a significantly increased density of alkyl chains and as a result the solubility is high. However this increased density can

also mean alkyl chains are much closer to one another and result in steric congestion which can be detrimental to the interactions between polymer chains.[89] The increased alkyl chain density can be crudely estimated by considering the mass of alkyl chain as a proportion of the total mass of the repeat unit which shows that going from the thiophene co-polymer to the homo-polymer corresponds to a 5 % increase in alkyl chain density.

Table 3.1. Physical properties of polymers **P5** (T), **P6** (Ph) and **P7** (Homo).

Polymer	M_n (kDa)[a]	M_w (kDa)[a]	PDI[a]	DP_n[a]
T	45	83	1.8	41.6
Ph	76	133	1.7	70.5
Homo	34	68	2.0	34.0

[a] M_n, M_w, PDI (M_w / M_n) and DP_n (M_n / M_0) determined by GPC at 80 ºC using low-PDI (<1.10) polystyrene standards and chlorobenzene as the eluent.

3.3.3.3. *C3* co-polymer synthesis

The brominated ***C3*** co-monomer **3.10** was co-polymerised with thiophene by palladium-catalysed Stille coupling using the conditions previously described. Again it was not possible to obtain soluble polymers when equimolar amounts of monomers were used and a stoichiometric offset was required in order to achieve polymers that were of high molecular weight within the window of solubility of the material.

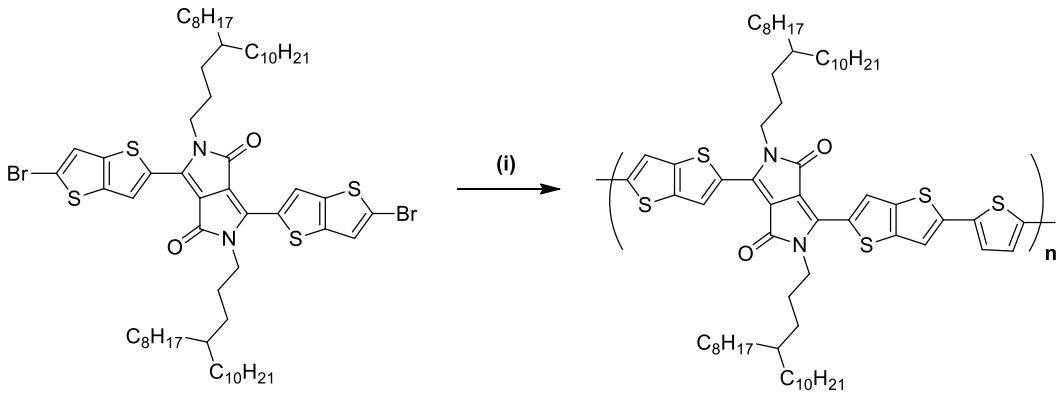

3.10 **P8**

Figure 3.11. Synthesis of polymer **P8** by palladium-catalysed Stille coupling of **3.10**. *Reagents and conditions*: **(i)** PhCl, $Pd_2(dba)_3$, P(*o*Tol)$_3$, 2,5-bis(trimethylstannyl)thiophene, μW.

These difficulties encountered are likely due to extension of the linear part of the chain resulting in a more sterically exposed polymer backbone giving increased π-π interactions between polymer chains. Such increased interactions can result in polymers in the solid state that are bound too tightly for re-dissolution. This effect is likely to be proportional to polymer M_n so the previously described targeting of lower M_n material is an attempt to counterbalance these stronger interactions.

As explained in Chapter One, for step-growth polymerisations with bi-functional monomers such as those used within this thesis, the degree of polymerisation DP_n for a given monomer conversion (p) is described by the Carothers equation. As the conversion of monomers is increased towards $p = 1$ the value of DP_n, is also increased. Therefore the usual approach towards the synthesis of high molecular weight polymers from bifunctional monomers is to use as close to equimolar quantities as is possible within the experimental error of the measurements. In theory, when this results in a DP_n that is too high for a polymer to be soluble, it is possible to exert a degree of control over DP_n by varying the stoichiometric ratio of the monomers. Assuming complete monomer conversion ($p = 1$), when one monomeric species is in excess the Carothers equation becomes

$$\boldsymbol{DP_n = \frac{1+r}{1-r}} \qquad \textbf{Equation 2.1.}$$

Where **r** corresponds to the ratio of the monomers to one another.

It can be calculated that if a polymer of high molecular weight is desired, taking $DP_n = 100$ as an example then a molar ratio of approximately $r = 0.98$ is required. With this in mind, initial polymerisations were attempted with $r = 0.99, 0.98, 0.97$ resulting in only insoluble solid material. A polymer with good M_n and solubility wasn't achieved until a large stoichiometric offset of $r = 0.93$ (1.07 : 1.00, T : **DPP**) was used. Using the above equations this value would be expected to give $DP_n < 30$, yet the value was calculated to be much higher, indicating that on the small laboratory scale the errors associated with measuring molar ratios means it is difficult to follow the Carother's equation and trial and error is in fact more successful.

3.3.3.4. *C3* chalcogenophene co-polymer synthesis

As the complexity in design of conjugated polymers continues to accelereate, with an ongoing strive to develop novel structures, the role of heteroatomic substitution becomes increasingly valuable as a means for providing variety.[10] Examples are frequently encountered where thiophene, pyrrole and furan rings are readily interchanged to target specific properties and features.[11]

In **DPP** structures this variation can take place at the heterocycles of the flanking unit and / or the heterocycles of the co-monomer unit. A very recent example saw the substitution of a pyridine ring into the flanking units which resulted in extremely high electron mobilities of 6.3 cm^2 / Vs.[12] The nitrogen of the pyridine was carefully positioned to remove the steric clash arising from protons in an analogous phenyl ring whilst the electron-withdrawing nature of the pyridine rings serves to stabilise polymer LUMO levels. Furan flanked **DPP** has also been well reported with hole mobilities as high as 1.54 cm^2 / Vs recently obseved. As a co-monomer the furan ring has also been shown to result in a blue-shifted absorption profile due to its increased oxidation potential and reduced aromaticity.[13,14]

Selenophene has also been used in this role, flanking the **DPP** unit (**DPPSe**), the resultant co-polymers adopted a highly planar structure showing good amibipolar OFET mobilities compared to its thiophene counterpart.[15] Other selenophene based polymers frequently report narrowed band gaps and increased crystallinity as a result of the substitution, whilst with selenophene and bi-selenophene co-monomers high hole mobilities and good ambipolarity have been observed in **DPP**-type polymers[16-19] In OPV applications, selenophene containing materials give a range of reported efficiencies which are generally reduced compared to the thiophene analogues due to the reduction in V_{oc}.[20-24]

In comparison to the rising number of selenophene containing systems in semiconducting organic materials, there has been little work investigating the electronic properties of the next heavier chalcogen based heterocycle tellurophene. This can partly be attributed to the difficulties associated with it's synthesis as well as its resultant toxicity.[25] There have been several studies on the characterisation of tellurophene conjugated polymers and recently a few examples of their application in organic electronic devices have been demonstrated. *D. Choi et al.* reported **DPPT** co-

polymers containing tellurophene co-monomers that give impressive hole mobilities of 1.78 cm^2 / Vs whilst in another paper using the same tellurophene containing structural motif the same group demonstrated a creative biosensing application where the redox properties of the tellurium heteroatom are used for the detection of reactive oxygen species.[26-28] Despite these promising findings, the evaluation of similar polymers in OPV applications remains almost non-existent except for a single study by *W. H. Jo et al.* published during the preparation of this thesis in which a series of low band gap isoindigo polymers were synthesised containing thiophene, selenophene and tellurophene co-monomers. Substitution with selenophene afforded the best performing OPV devices with PCEs as high as 5.7 % whilst the tellurophene containing co-polymer demonstrated the lowest efficiencies due to coarse blend morphology as a result of high material crystallinity, which contrastingly resulted in the highest OFET hole mobilities of the series.[29]

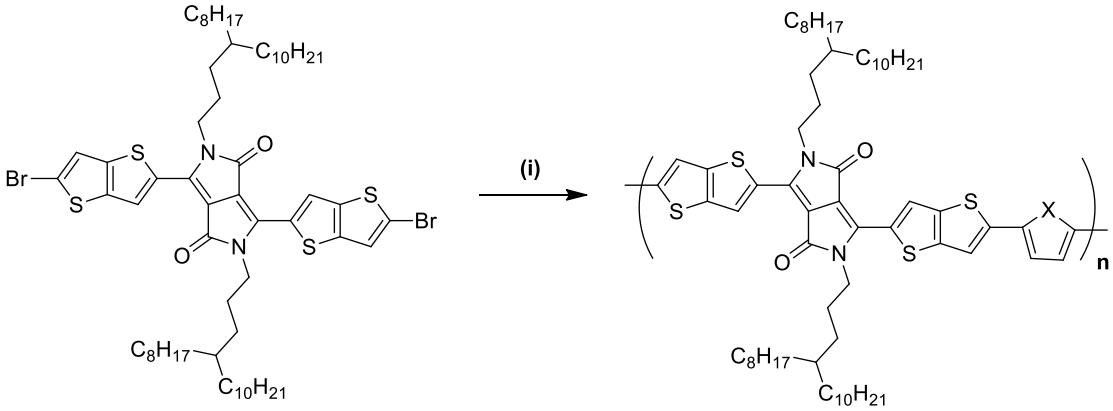

3.10

P9 (X = Se)
P10 (X = Te)

Figure 3.12. Synthesis of polymers **P9** and **P10** by palladium-catalysed Stille coupling of **3.10**. *Reagents and conditions*: **(i) P9** PhCl, $Pd_2(dba)_3$, P(*o*Tol)$_3$, 2,5-bis(trimethylstannyl) selenophene, µW. **P10** PhCl, $Pd_2(dba)_3$, P(*o*Tol)$_3$, 2,5-bis(trimethylstannyl)tellurophene, µW.

Due to this lack of a detailed study of tellurophene containing semiconducting polymers or of a general chalcogenophene comparison for organic electronic applications it was of interest to investigate the effect that chalcogen heteroatom substitution would have on the optical, physical and device properties of **DPP** materials. A parallel study in our group by *M. Planells et al.* shows the optical and electronic properties in different cyclopentadithiophene (**CPDT**) polymers, without

consideration of device performances, and these results will be also be compared and considered.[30] Through co-polymerisation with chalcogenophenes of increasing heteroatom size it is anticipated that the optical band gap will be narrowed due to stabilisation of E_{LUMO} as the chalcogenophene aromatic character decreases. It is also of interest to observe the effect on the morphology and crystallinity of the resultant polymers to see if a larger heteroatom results in increased heteroatom-heteroatom interactions affording a more crystalline polymer system.

Due to a combination of high OPV performance and good solution processability, the ***C3* DPP** co-monomer was chosen for this investigation (**Figure 3.12**). Di-stannylated selenophene and tellurophene co-monomers were co-polymerised with the **DPP** monomer using the microwave assisted palladium-catalysed Stille coupling conditions previously described and the resulting co-polymers were compared to the previous ***C3*** alkylated **P8** (T) polymer mentioned earlier. All three co-monomers afforded polymers of comparably high M_n (T = 80 kDa, Se = 95 kDa and Te = 91 kDa) and narrow PDIs (T = 1.9, Se = 2.5 and Te = 3.0) as shown in **Table 3.2** thus allowing for a reasonably accurate comparative study across the series. There is a slight broadening of mass distributions with heavier heteroatomic substitution, as indicated by the increased PDI values, which could be a result of greater aggregation in solution during the polymerisation process in going from T to Se to Te. The optical and physical properties as well as device performance of this polymer series will be described later in Section **3.6**

Table 3.2. Physical properties of polymers **P8** (T), **P9** (Se) and **P10** (Te).

Polymer	M_n (kDa)[a]	M_w (kDa)[a]	PDI[a]	DP_n[a]
T	80	154	1.9	72.0
Se	95	238	2.5	82.0
Te	91	272	3.0	75.4

[a] M_n, M_w, PDI (M_w / M_n) and DP_n (M_n / M_0) determined by GPC at 80 ºC using low-PDI (<1.10) polystyrene standards and chlorobenzene as the eluent.

3.4. DPPTT-T *C1* - *C3* co-polymer comparison

3.4.1. Optical properties

The two new co-polymers **P5** (***C2***) and **P8** (***C3***) were both synthesised in high M_n with low PDIs as described in previous sections **3.3.3.1** and **3.3.3.3** and by comparison with the previously synthesised **DPPTT-T** (***C1***) polymer it is possible to establish a direct comparison of the new alkyl chain branching position. The molecular weights that can be achieved within the window of solubility for each material increase with extended branching position with ***C2*** and ***C3*** having M_n 45 kDa and 80 kDa respectively whilst weight distribution of the two new polymers is also significantly reduced with both new materials showing reduced PDIs of less than 2.

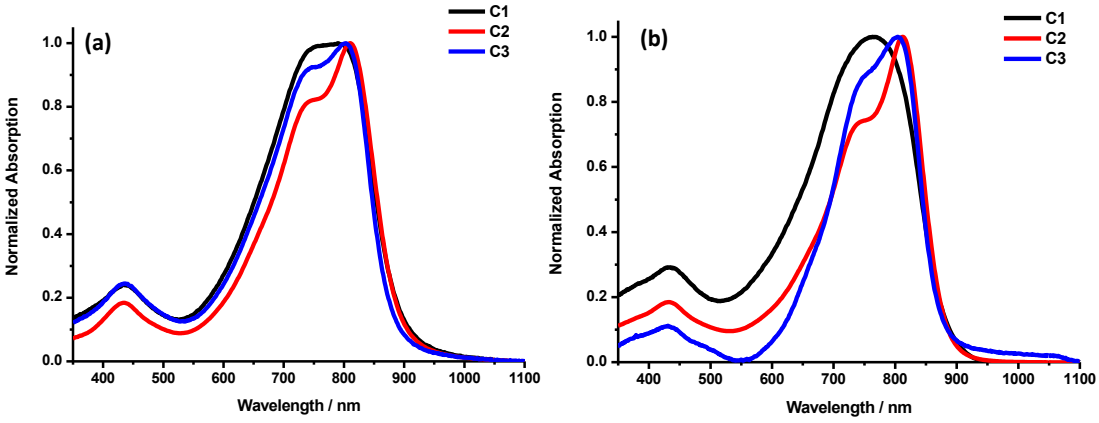

Figure 3.13. Room temperature normalised UV-Vis absorption profile of ***C1*** – ***C3*** polymers **(a)** thin films spun on glass substrates from 5 mg / mL chlorobenzene solution and **(b)** dilute chlorobenzene solution.

The solution and thin film UV-Vis spectra of polymers ***C1*** – ***C3*** are shown in **Figure 3.13**. In both spectra it can be seen that changing the branching position of the alkyl chain does not significantly affect the absorption profile. This is to be expected, as there is likely to be little to no change in the molecular orbital energies arising from such a transformation. There are however some noticeable changes in the shape of the absorption profile with the two new polymers showing a more significantly aggregated absorption profile.

C2 demonstrates the most aggregation with ***C3*** showing slightly less and ***C1*** demonstrating very little aggregation. This can be seen to have an influence on λ_{max}, with ***C2*** showing the most red-shifted λ_{max} at 812 nm and 810 nm in solution and thin

film respectively as a result of being the most aggregating material whilst ***C1*** with the least observable aggregation has the most blue-shifted λ_{max} at 764 nm and 790 in solution and thin film respectively. It is likely that this increased aggregation is a combination of the higher molecular weights and the more sterically exposed polymer backbone, although this does not appear to show a linear correlation with branching point distance.

E_{HOMO}, E_{LUMO} and E_g values are shown in **Table 3.3** and from these approximations it can be seen that across the branching point series there is no significant variation between frontier molecular orbital energy levels or optical band gaps. It is therefore reasonable to assume that any observable changes in polymer properties across the series cannot be attributed to energetic effects.

Table 3.3. Optical properties of ***C1*** - ***C3*** polymers.

Polymer	λ_{max} (nm) Film[b]	Solution[c]	E_{HOMO} (eV)[d]	E_{LUMO} (eV)[e]	Eg (eV)[f]
C1[a]	790	764	-5.1	-3.7	1.4
C2	810	812	-5.1	-3.7	1.4
C3	803	804	-5.1	-3.7	1.4

[a] ***C1*** polymer obtained for comparison from Dr Hugo Bronstein [b] thin films spin coated on glass substrates from 5 mg / mL chlorobenzene solution [c] in dilute chlorobenzene solution [d] HOMO energies (E_{HOMO}) determined by PESA [e] LUMO energies (E_{LUMO}) estimated by addition of thin film absorption onset onto E_{HOMO} [f] Band gap (E_g) estimated as the difference between the experimentally determined E_{HOMO} and optically estimated E_{LUMO}.

3.4.2. OPV devices

3.4.2.1. Device data

The OPV performance of the newly synthesised ***C2*** and ***C3*** polymers relative to ***C1*** were evaluated in polymer / fullerene bulk heterojunction solar cells using the same general fabrication conditions previously describe in Chapter One. A direct comparison across the series can therefore be made of the effect the manipulation of branching point has on the various OPV device performance parameters. Agreeing with the principle that it is a value dictated by the energetic offset between donor E_{HOMO} and acceptor E_{LUMO}, the V_{oc} across the branching point series remains almost

entirely unchanged. The FF can be seen to loosely follow the trends in aggregation from ***C1*** – ***C3*** with the most aggregated ***C2*** showing the largest value, although these variations are not large enough to be considered significant.

The most dramatic consequence of varying the alkyl chain branching position can be seen with the J_{sc}, moving from ***C1*** branching to ***C2*** branching corresponds to a significant enhancement in photocurrent from 15.1 mA cm^{-2} to 18.8 mA cm^{-2} whilst ***C3*** demonstrates a slightly smaller improvement with a value of 17.5 mA cm^{-2}. As was also observed with FF values, J_{sc} can be correlated to the variations in aggregation observed by UV-Vis spectroscopy, with the most aggregated ***C2*** material giving the largest photocurrent, which could suggest that in this instance the interchain interactions that result in aggregation may also be favourable for photocurrent generation in the new materials.

Figure 3.14 (b) shows the EQE spectra of the three polymers in the series where it can be seen that the improved photocurrent arises from increased absorption right across the spectral window indicating that both the polymer donor and the fullerene acceptor are demonstrating improved photon absorption. These various improvements result in significant PCE enhancements, the highest of which is observed in ***C2*** with a PCE of 7.1 %, a 34 % improvement from 5.3 % PCE in ***C1***. Whilst not as dramatic, ***C3*** also has an improved efficiency of 6.4 %.

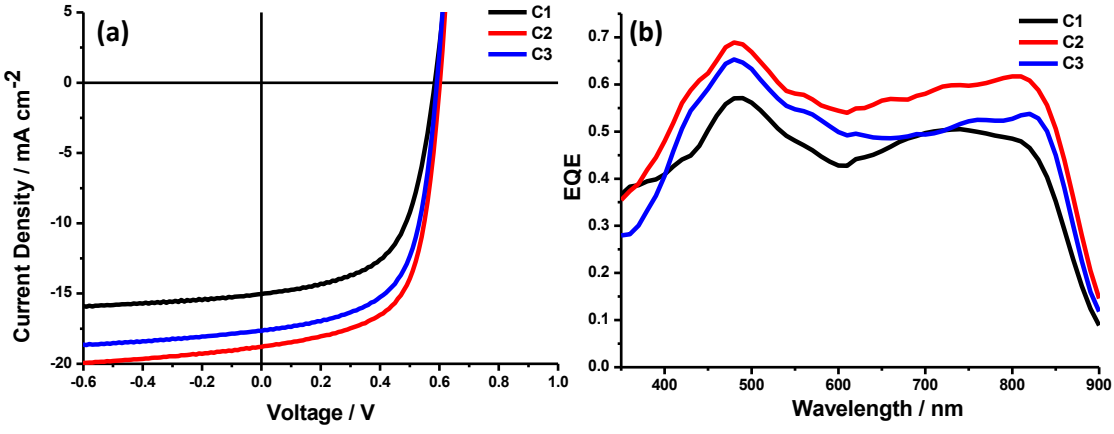

Figure 3.14. (a) *J-V* curves and **(b)** EQE spectra for polymers ***C1*** - ***C3*** polymers.

Table 3.4. OPV device performance characteristics of ***C1*** **-** ***C3*** polymers.

Polymer	J_{sc} (mA / cm^2)[a]	V_{oc} (V)	FF	PCE (%)[a]
C1	15.1	0.59	0.59	5.3
C2	18.7	0.60	0.63	7.1
C3	17.5	0.59	0.62	6.4

[a] EQE corrected.

3.4.2.2. Grazing incidence x-ray diffraction

Having observed the improved solar cell performance of ***C2*** and ***C3*** relative to ***C1***, and the differences in M_n, PDI and aggregation across the series, it was of interest to probe what effect the manipulation of branching positions has on the morphological arrangement of the donor and acceptor materials in the active blend layer.

The benefits of XRD were described and experimentally demonstrated in chapter two where crystallinity was shown to be a valuable tool towards describing the photovoltaic performance of a material. Furthermore, the use of a Synchrotron light source can harness X-rays that are at least five orders of magnitude more intense than the best laboratory source and can therefore be especially valuable for visualising a material's crystallinity.[31] The high energy collimated X-rays allow for ultra-fast diffraction studies of polymer materials with signal to noise ratios and resolutions that are much higher than regular XRD and can therefore provide much a greater depth of information on a material's microstructure.

Using polymers ***C1*** – ***C3***, polymer / fullerene blends were spin coated using the same donor / acceptor ratio, solvent system and spin speeds used in solar cell devices to closely mimic the condition of the bulk heterojunction active layer. The polymer / fullerene blends were then probed by 2D grazing incidence x-ray diffraction (GIXD) using high energy Synchrotron light source. The component of the scattering vector parallel to the substrate is given by Q_{xy} and the component perpendicular to the substrate is q_z. The 2D GIXD patterns of ***C1*** – ***C3*** are shown in **Figure 3.15** whilst the line cuts in Q_{xy} **(a)** and q_z **(b)** are shown in **Figure 3.16**. In addition to peaks associated with the pure polymers, the GIXD patterns can also be seen to contain a diffraction halo peak near 1.33 Å^{-1} associated with the PC[71]BM amorphous phase.

In general there is an observed increase in crystallinity of the new ***C2*** and ***C3*** polymer materials as a result of moving the branching position. The three polymers can be seen to show a set of alkyl stacking peaks, located at 0.65 $Å^{-1}$ for *C1*, 0.62 $Å^{-1}$ for *C2* and 0.63 $Å^{-1}$ for ***C3*** (**Figure 3.16 (a)).** The intensity of the alkyl stacking peaks increases with branching point distance, the most substantial increase being seen with ***C2***. Additionally, analysis of the (200) lamellar peak intensities in the q_z direction for the polymer blend films shows a significant increase in ***C2*** relative to ***C1*** whilst ***C3*** remains relatively unchanged. There is also a diffraction feature around 1.79 $Å^{-1}$ which is in the same approximate region as the π-stacking peak found in neat polymer films, this is significantly increased in intensity going to ***C2*** and ***C3*** which may be as a result of the further branching position leading to an increased amount of π-stacking within the blend. Whilst it is not possible to draw a quantitative comparison from these diffractograms, a qualitative comparison of intensities would indicated that an increased branching point distance imparts an increased crystallinity of the polymer material in the polymer / fullerene blend which are likely the cause of the enhanced OPV device characteristics.

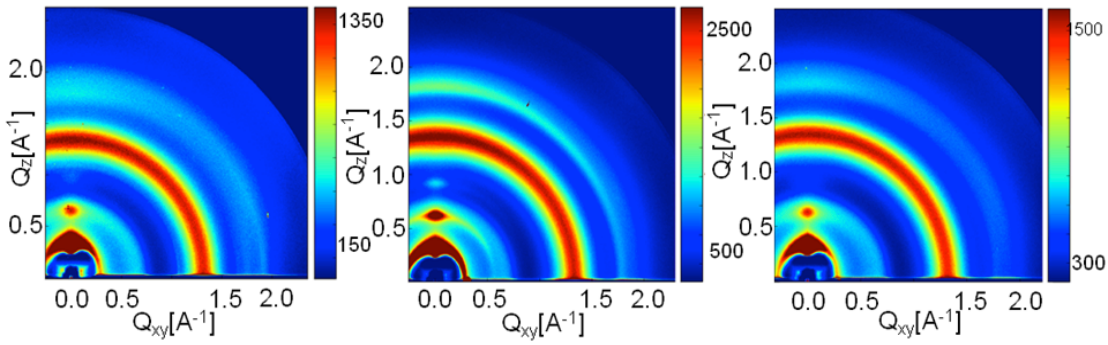

Figure 3.15. GIXD diffractograms of ***Cn*** / PC[71]BM blends using **(a)** ***C1*** **(b)** ***C2*** and **(c)** ***C3*** polymers. Blends were fabricated using the same conditions as in device fabrication.

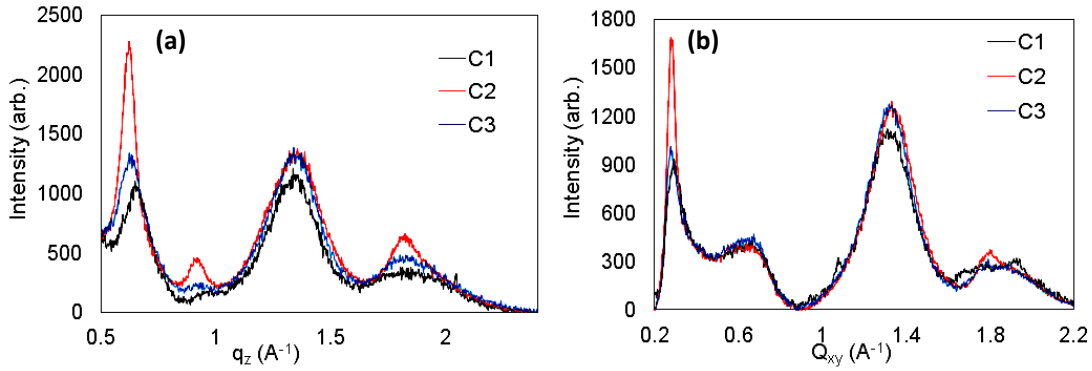

Figure 3.16. GIXD diffractograms of ***Cn*** / PC[71]BM blend films with line cuts in the **(a)** q_z and **(b)** Q_{xy} directions.

3.4.3. OFET devices

3.4.3.1. Device data

C1 has previously been shown to be an excellent hole transport material in thin film OFET devices and the high short circuit currents observed in section **3.4.2** indicate ***C2*** and ***C3*** have the potential to exhibit similar results. Top gate / bottom contact OFET devices were therefore fabricated with polymers ***C1*** – ***C3*** as the semiconducting channel with the extracted device performance parameters shown in **Table 3.5**.

The polymers again show good hole transport properties with μ_{hole} values on the order of 1 x 10^{-2} cm^2 / Vs. When considering the performance of ***C1*** an immediate observation can be made that μ_{hole} at 0.014 cm^2 / Vs, is significantly reduced compared to that which is first reported in the literature. There are several possible reasons for this variation in measured values, the literature ***C1*** material and the ***C1*** material reported in this study are polymers from two different batches, something that can lead to any number of variations in physical properties. The resultant OFET devices are also the product of two different transistor laboratories meaning there are a number of additional variations to consider despite using similar fabrication conditions. Most significantly it is important to note that the devices fabricated for the ***C1*** – ***C3*** series are un-optimised and fabricated with a view to examining the effect of branching point variation on various performance parameters and it is likely that a full

investigation into optimisation of fabrication conditions, thermal annealing and device architecture would yield significantly improved values.

As shown in **Table 3.5**, the hole mobilities of the three polymers can be seen to be strongly influenced by the alkyl chain branching point position. Going from ***C1*** to ***C2*** an approximate four-fold increase in μ_{hole} from 1.4 x 10^{-2} cm^2 / Vs to 5.2 x 10^{-2} cm^2 / Vs is observed. From ***C2*** to ***C3*** there is a further slightly smaller increase up to 6.6 x 10^{-2} cm^2 / Vs. Similar to the improved photocurrent in OPV devices it is clear that an expanded branching position is highly desirable, although unlike with the OPV photocurrents and efficiencies the OFET mobilities seem to show a more linear correlation with a gradual increase in device performance with the progression from ***C1*** to ***C3***. Whilst these improvements in hole mobilities are generally in agreement with the earlier reported isoindigo study, in this instance there can be seen to be a linear increase from ***C1*** – ***C3***, whereas previously there was reported to be an odd / even type effect where ***C1*** and ***C3*** branching showed significantly higher hole mobilities than ***C2*** and ***C4***.

Table 3.5. Thin film OFET device characteristics of polymers ***C1*** - ***C3***.

Polymer	μ_{hole} (cm^2 / Vs)[a]	V_{th} (V)[b]	I_{on} / I_{off}[b]
C1	0.014	-20	~5 x 10^2
C2	0.052	-17	~1 x 10^3
C3	0.066	-15	~1 x 10^3

[a] Highest effective hole mobilities measured in the saturation regime [b] Threshold voltages (V_{th}) and on / off ratios (I_{on} / I_{off}) extracted from the linear regime (V_D = - 5V).

3.4.3.2. Grazing incidence x-ray diffraction

As was described for polymer / fullerene blends and previously in Chapter Two, a thorough examination of a material's crystallinity can be invaluable when evaluating their intermolecular interactions and device performance. The semiconducting channels in OFET devices are fabricated from spin-coating of a polymer solution and pristine polymer films can therefore be used as a good approximation of the charge transport properties, providing the polymer film is spin coated using the same conditions that were used in device fabrication.

There is a marked increase in polymer crystallinity with increased branching point distance shown in **Figure 3.17**. Again the scattering vector parallel to the substrate plane is given by Q_{xy} whilst the perpendicular component given by q_z. As was observed in the blends there is an increase in intensity of the (200) with both ***C2*** and ***C3*** showing larger peaks. It can also be seen in **Figure 3.18** that increased branching point distance results in a shift of the (200) peak to slightly lower q, ***C1*** is located at $q_z = 0.62$ Å^{-1}, ***C2*** at 0.60 Å^{-1} whilst ***C3*** is at 0.59 Å^{-1}.

A significant increase in π-stacking intensity in both ***C2*** and ***C3*** compared to ***C1*** can be seen as shown by the peak at around 1.75 Å^{-1} whilst there also appears to be a relationship between the branching position and the orientation of the polymer backbone relative to the substrate. ***C1*** exhibits predominantly edge-on orientation relative to the plane of the substrate, whilst ***C2*** and ***C3*** can be seen to exhibit a mixture of both edge-on and face-on indicating that the extension of branching positions beyond ***C1*** encourages a more face-on orientation. It is possible that the increased hole mobilities observed in ***C2*** and ***C3*** are related to these changes in backbone orientation. The lamellar stacking peaks are shifted towards slightly lower q than the positions previously described in the blends indicating that the lamellar spacing is slightly wider in the pristine films than in the blends. The increased crystallinity across the series combined with the dramatic increase in π-stacking supports the idea that increasing the linear portion of the alkyl chain in ***C2*** and ***C3***, which affords a more sterically exposed conjugated backbone, facilitates much stronger intermolecular interactions between polymer chains and enhances charge carrier transport characteristics.

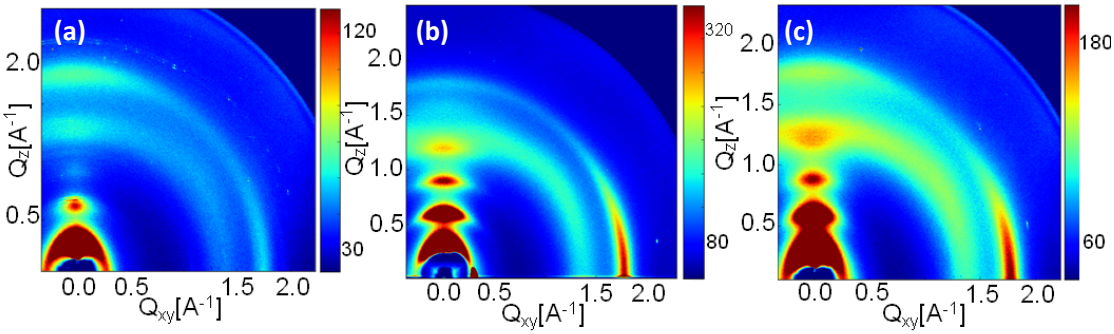

Figure 3.17. GIXD diffractograms of **(a)** ***C1***, **(b)** ***C2*** and **(c)** ***C3*** polymer films. Spin coated using the same conditions as in device fabrication.

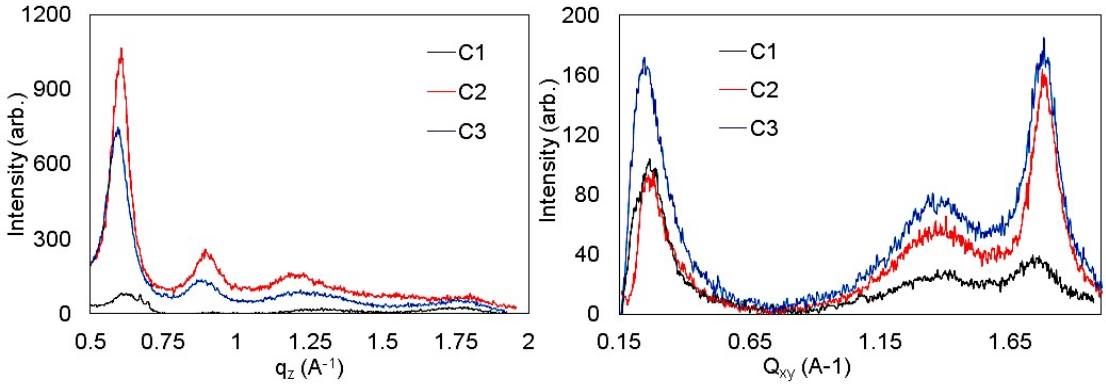

Figure 3.18. GIXD diffractograms of ***C1*** – ***C3*** polymer films with line cuts in the **(a)** q_z and **(b)** Q_{xy} directions.

3.5. *C2* co- and homo- polymer comparison

3.5.1. Optical properties

The UV-Vis absorption profiles of the three newly synthesised ***C2*** alkylated polymers are shown in **Figure 3.19** with their comparative optical properties reported in **Table 3.6**. Each polymer has a shoulder at shorter wavelengths due to aggregation and there are noteable red-shifts of λ_{onset} in going from solution to thin film despite λ_{max} not showing this trend. The differences between the absorption profiles and the frontier molecular orbital energies can be rationalised according to polymer backbone structural variations. **P7** (Homo) has the narrowest E_g value of 1.32 eV due to enhanced molecular orbital hybridisation giving increased E_{HOMO} and stabilised E_{LUMO} values. This gives the most red-shifted absorption profile with λ_{max} at 867 nm and 869 nm in solution and thin film respectively. In comparison **P5** (T) has a slightly lower energy E_{HOMO} of -5.10 eV and a raised E_{LUMO} of -3.71 eV. This results in the next red-shifted absorption profile due to a slightly wider E_g of 1.39 eV with λ_{max} of 812 nm and 810 nm in solution and thin film. Due to the steric clash in **DPPTT-P** polymers previously discussed in Chapter Two **P6** (Ph) has the lowest energy E_{HOMO} and highest energy E_{LUMO} values which gives the widest band gap in the series with an E_g value of 1.47 eV. This widening gives the most blue-shifted absorption profile with λ_{max} of 759 nm and 761 nm in solution and thin film respectively.

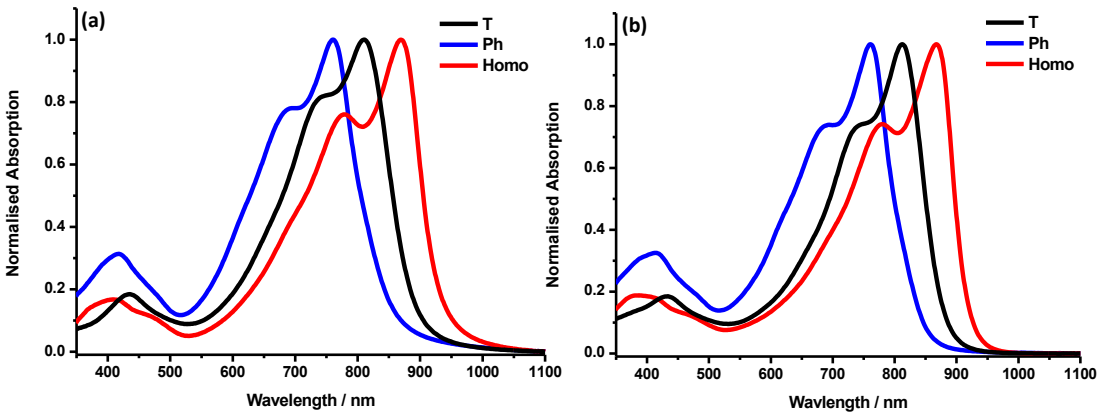

Figure 3.19. Room temperature normalised UV-Vis absorption profiles of polymers **P5** (T), **P6** (Ph) and **P7** (Homo) **(a)** thin films spun on glass substrates from 5 mg / mL chlorobenzene solution **(b)** in dilute chlorobenzene solution.

Table 3.6. Optical properties of polymers **P5** (T), **P6** (Ph) and **P7** (Homo).

Polymer	λ_{max} (nm) Film[a]	Sol.[b]	E_{HOMO} (eV)[c]	E_{LUMO} (eV)[d]	E_g (eV)[f]
T	810	812	-5.10	-3.71	1.39
Ph	761	759	-5.13	-3.66	1.47
Homo	869	867	-5.07	-3.75	1.32

[a] thin films spin coated on glass substrates from 5 mg / mL chlorobenzene solution [b] in dilute chlorobenzene solution [c] HOMO energies (E_{HOMO}) determined by PESA [d] LUMO energies (E_{LUMO}) estimated by addition of thin film absorption onset onto E_{HOMO} [f] Band gap (E_g) estimated as the difference between the experimentally determined E_{HOMO} and optically estimated E_{LUMO}.

3.5.2. OPV device data

Bulk heterojunction solar cells were fabricated using the ***C2*** alkylated polymer series **P5** – **P7** with PC[71]BM the *J-V* curve and EQE spectra are shown in **Figure 3.20** whilst the device performance parameters are shown in **Table 3.7**. The **P5** (T) polymer previously discussed can be seen to be the best performing co-polymer in this series with the highest J_{sc} and PCE values of 18.7 mA cm^{-2} and 7.1 % respectively. In comparison the phenyl co-polymer **P6** exhibits a slight increase in V_{oc} compared to **P5** (T) from 0.60 V to 0.63 V due to stabilisation of E_{HOMO} giving a greater energetic offset with the acceptor LUMO. However there is also a significant

reduction in J_{sc} due to the polymer's wider band gap which results in an overall drop in PCE from 7.1 % to 4.1 %. The homo-polyer **P7** also sees an improved V_{oc} relative to the thiophene co-polymer despite its slightly raised E_{HOMO} which would normally be expected to result in a reduction in V_{oc}. The significant narrowing of E_g in **P7** (Homo) results in poor charge separation due to an insufficient D_{LUMO} - A_{LUMO} offset which is illustrated in **Figure 3.20 (b)** by the largely reduced EQE in the region of polymer absorption. This results in a J_{sc} of 11.9 mA cm^{-2} which is the lowest in the series and corresponds to an overall PCE of 4.4 % that is greater than **P6** (Ph) but lower than **P5** (T).

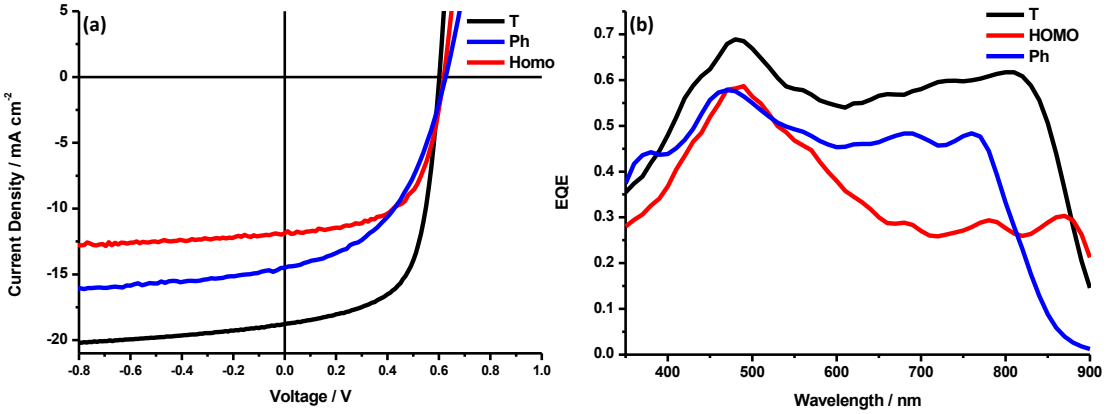

Figure 3.20. (a) *J-V* curves and **(b)** EQE spectra of polymers **P5** (T), **P6** (Ph) and **P7** (Homo).

Table 3.7. OPV device performance parameters of polymers **P5** (T), **P6** (Ph) and **P7** (Homo).

Polymer	J_{sc} (mA cm^{-2})[a]	V_{oc} (V)	FF	PCE (%)[a]
T	18.7	0.60	0.63	7.1
Ph	14.0	0.63	0.47	4.1
Homo	11.9	0.62	0.60	4.4

[a] EQE corrected.

Due to the relatively low OPV performance of these new ***C2*** alkylated polymers **P6** (Ph) and **P7** (Homo) in comparison to the thiophene co-polymer, a further investigation into their properties was not undertaken with greater emphasis placed upon the variation of co-monomers in ***C3*** alkylated polymers in the next section.

3.6. *C3* co-polymer comparison

3.6.1. Chalcogenophene optical and physical property comparison

Figure 3.21 shows solution and thin film UV-Vis absorption profiles of the chalcogenophene substituted series from thiophene to selenophene and tellurophene. In both the solution and thin film spectra there are clear observable trends as group VI of the periodic table is descended. Going from thiophene to selenophene corresponds to a more radially expanded heteroatom and a heterocycle with reduced aromatic character. This results in a narrowing of E_g and a red-shifting of the absorption profile. In solution λ_{max} goes from 804 nm (T) to 832 nm (Se), whilst in the thin film there is a shift from 803 nm (T) to 831 nm (Se). There is also a similar, slightly smaller, red-shift in the λ_{onset} in both spectra.

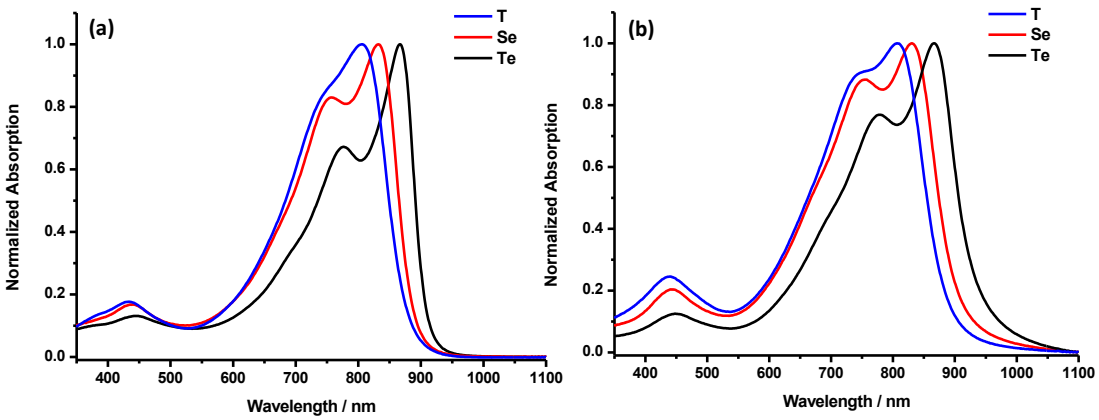

Figure 3.21. Room temperature normalised UV-Vis absorption profile of polymers **P8** (T), **P9** (Se) and **P10** (Te) **(a)** dilute chlorobenzene solution **(b)** thin films spin coated on glass substrates from 5 mg / mL chlorobenzene solution.

Going from selenophene to tellurophene continues this trend showing a further red-shift in absorption profile with λ_{max} of 866 nm for both solution and thin film spectra. It can also be seen that these experimentally determined spectra closely match the computationally predicted absorption spectra calculated using TD / DFT calculations with B3LYP / 6-31g* (H, C, S, N, O atoms) and SDD ECP (Se, Te atoms) basis sets set shown in section **3.6.3**.

In addition to the red-shifting of λ_{max} and λ_{onsets}, there is also a clear trend in the aggregation of the chalcogenophene containing co-polymers as observed by the UV-Vis absorption spectra. Descending group VI gives polymers with an increased

tendency to aggregate as indicated by shoulders seen in the absorption profiles. This is likely a heavy atom effect where the more radially expanded atomic orbitals of the larger heteroatoms are able to associate more strongly with those on other polymer chains. These varying interactions occurring in the materials are further discussed using XRD and AFM in sections **3.8.1** and **3.8.2**.

E_{HOMO}, E_{LUMO} and E_g estimations are shown in **Table 3.7**. Generally in this thesis E_{HOMO} and E_{LUMO} values will be described to 1 decimal place as this is often the most accurate manner in which to interpret PESA data, however for the benefit of probing heteroatomic substitution E_{HOMO} values to 2 decimal places will be considered, as there are only slight variations across the series. Increasing the heteroatomic size in the chalcogenophene co-monomer corresponds to a small but consistent raising of E_{HOMO} and similar size reductions in E_{LUMO} values. The lowest lying E_{HOMO} and highest E_{LUMO} values are observed for the thiophene containing co-polymer with an E_{HOMO} value of -5.08 eV and an E_{LUMO} of -3.69 eV. Moving to the row IV selenophene atom sees a slightly raised E_{HOMO} value of -5.07 eV and a stabilised E_{LUMO} value of -3.70 eV, a further increase in chalcogen size with tellurophene results in the highest E_{HOMO} value of -5.05 eV and the lowest E_{LUMO} value of -3.73 eV. Consequently E_g shows a small narrowing with increasing heteroatomic size with thiophene showing the broadest E_g at 1.39 eV and Te the narrowest at 1.32 eV. These small but observable trends are consistent with the very recently published chalcogenophene study by *M. Planells et al.* in **CPDT** based polymers.[30]

Table 3.8. Optical properties of polymers **P8** (T), **P9** (Se) and **P10** (Te).

	λ_{max} (nm)				
Polymer	Film[a]	Solution[b]	E_{HOMO} (eV)[c]	E_{LUMO} (eV)[d]	E_g (eV)[e]
T	803	804	-5.08	-3.69	1.39
Se	831	832	-5.07	-3.70	1.37
Te	866	866	-5.05	-3.73	1.32

[a] thin film spin coated on glass substrates from 5 mg / mL chlorobenzene solution [b] dilute chlorobenzene solution [c] HOMO energies (E_{HOMO}) determined by PESA [d] LUMO energies (E_{LUMO}) estimated by addition of thin film absorption onset to E_{HOMO} [e] Band gap (E_g) estimated as the difference between the experimentally determined E_{HOMO} and optically estimated E_{LUMO}.

3.6.2. Temperature dependent UV-Vis comparison

Room temperature UV-Vis spectroscopy of the thiophene, selenophene and tellurophene containing polymers indicate a significant variation in aggregate formation across the series. **P8** with a thiophene co-monomer demonstrates the least tendency for aggregation of the three polymers, indicated by the near Gaussian shape of the largest absorption peak. Going to heavier heteroatoms sees the Gaussian shape of the absorption reduced with an absorption shoulder at lower wavelengths that becomes more prominent with increased chalcogen atom size.

This increased tendency for aggregation can be accurately identified using temperature dependent UV-Vis spectroscopy as shown in **Figure 3.22**. The absorption spectra of dilute chlorobenzene solutions of **P8** (T), **P9** (Se) and **P10** (Te) are recorded at successive increasing temperature intervals of 10 ºC and the each spectra superimposed to demonstrate the change in aggregation at elevated temperatures.

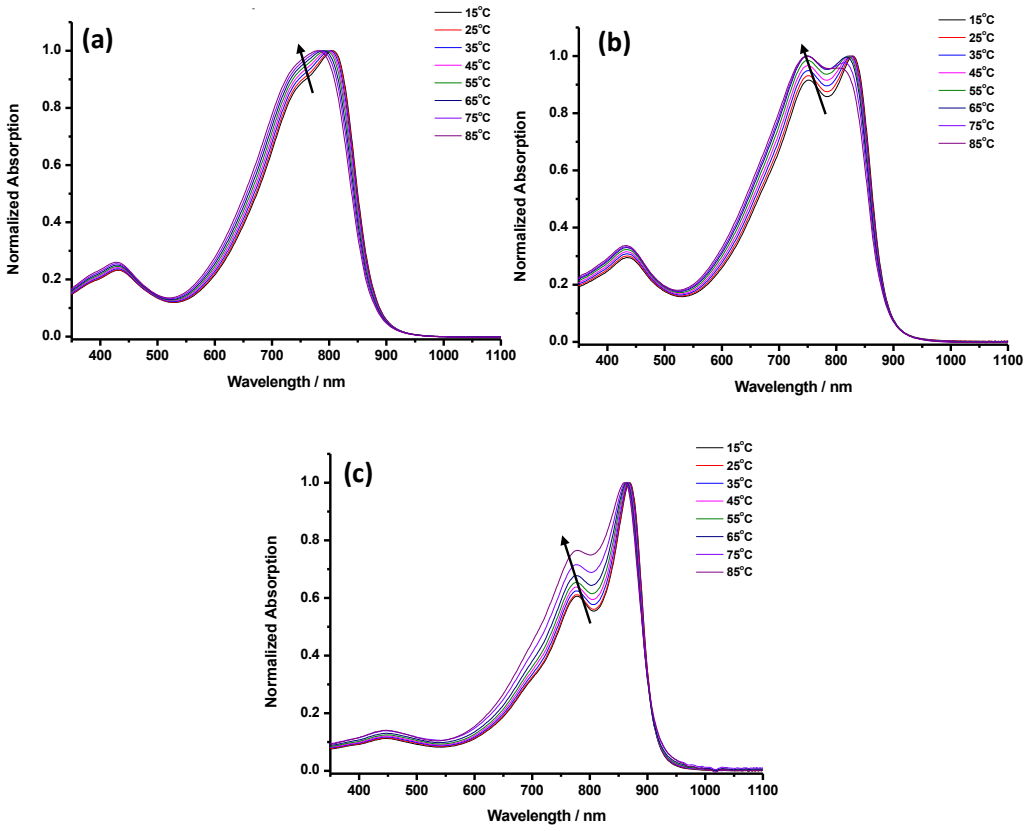

Figure 3.22. Temperature dependent UV-Vis absorption profiles of polymers **(a) P8** (T) **(b) P9** (Se) and **(c) P10** (Te) in dilute chlorobenzene solution.

The least aggregated polymer **P8**, with thiophene, shows a shift to an almost entirely Gaussian shape with the small absorption shoulder that is present at room temperature disappearing, indicating that any aggregates are almost fully disrupted at such elevated temperatures. The selenophene containing polymer **P9** shows a similar trend with the longer wavelength shoulder being greatly reduced and absorption profile assuming a slightly blue-shifted position at elevated temperatures as a consequence of this reduction in aggregation. **P10** with the tellurophene co-monomer is the most strongly aggregating material and the dominant absorption can be seen to be moving towards a more Gaussian shape at higher temperatures, however even at 85 ºC there remains a significant shoulder to the absorption indicating a tendency to aggregate even at elevated temperatures.

3.6.3. Chalcogenophene DFT calculations

It is clear from the previously discussed optoelectronic properties of the chalcogenophene series that there are observable energetic variations resulting from chalcogen substitution and it is therefore of interest to evaluate these variations computationally in order to establish a validity in the conclusions that are drawn from these materials.

Previous calculations in this thesis have been processed using a B3LYP / 6-31g* basis set, one that is valid for DFT approximations involving C, H, N, O and S atoms. For this basis set, there are a number of parameters that are present with larger Se and Te atoms that are not accounted for. As such, for the Se and Te containing co polymers the more complex SDD ECP basis set must be used. The resultant energy level distributions are shown in **Figure 3.24** and E_{HOMO}, E_{LUMO} and E_g values shown in **Table 3.8** whilst the computationally predicted UV-Vis absorption spectra are shown in **Figure 3.23**. The predicted absorption profiles of the three polymers can be seen to closely match the experimentally determined trend in the previous section, showing a small red-shift in λ_{max} with increased chalcogen atom size.

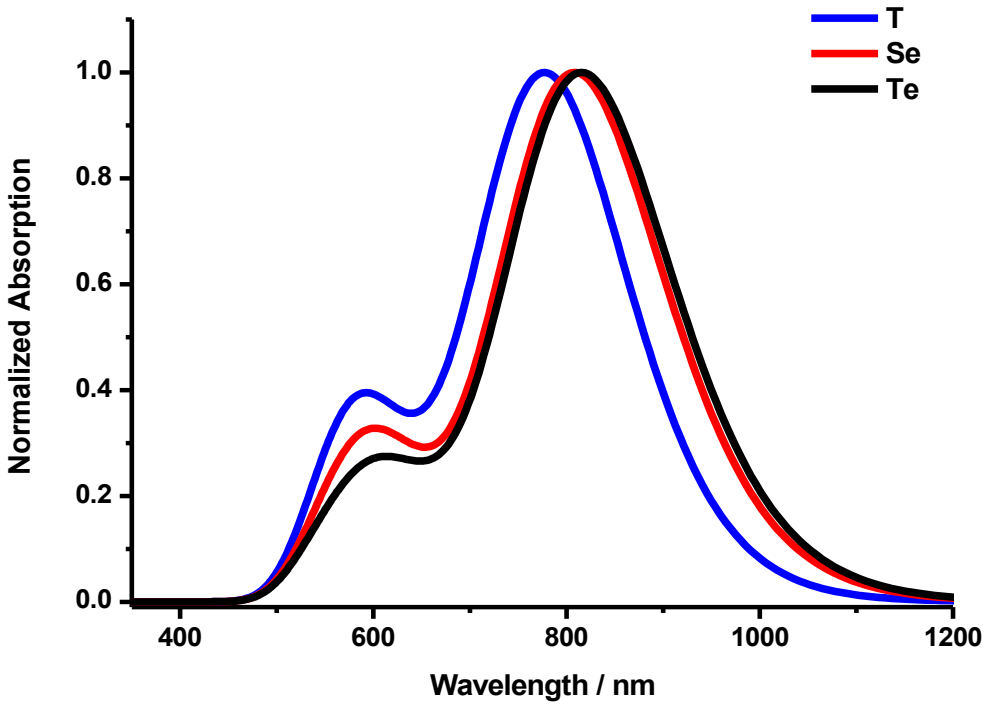

Figure 3.23. Computationally predicted UV-Vis absorption profiles of polymers **P8** (T), **P9** (Se) and **P10** (Te) calculated using TD / DFT calculations with B3LYP / 6-31g* (H, C, S, N, O atoms) and SDD ECP (Se, Te atoms) basis sets.

The predicted frontier molecular orbital energy levels of the chalcogenophene series are shown in **Figure 3.24** and can generally be seen to follow the trend observed experimentally. Whilst the increase is smaller than experimental values indicate, the predicted E_{HOMO} again shows an increase in energy with increasing heteroatom size corresponding to the reduction in aromaticity across the series. The predicted E_{LUMO} values also match estimated values with an E_{LUMO} stabilisation going from T to Se to Te and E_g values that show a similar narrowing across the series.

Looking at the backbone distributions in **Figure 3.23** each of the three polymers have planar backbones with linear long axis linearities. All three polymers can also be seen to have evenly distributed HOMO and LUMO energy levels indicating good delocalisation along the polymer backbone structures.

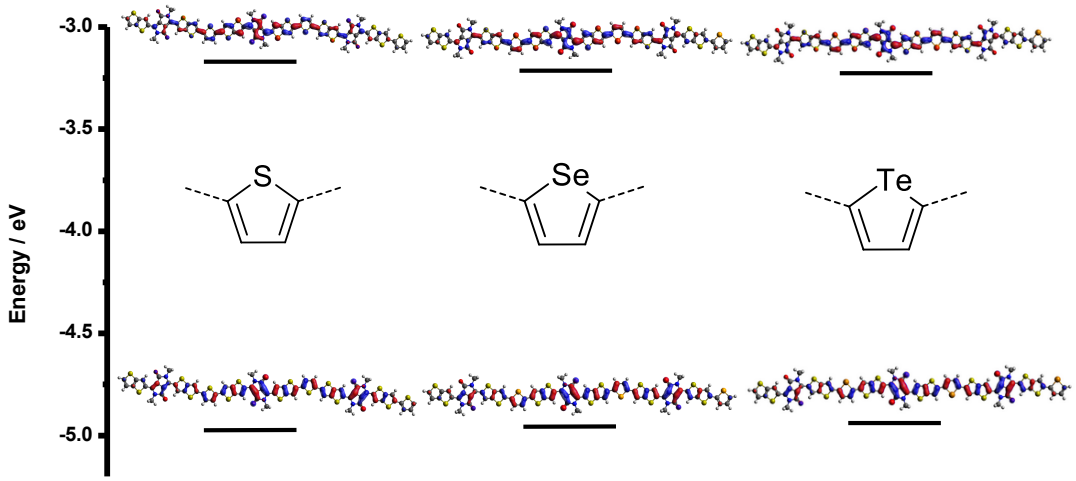

Figure 3.24. Computationally predicted frontier molecular orbital energy levels of polymers **P8** (T), **P9** (Se) and **P10** (Te) calculated using TD / DFT calculations with B3LYP / 6-31g* (H, C, S, N, O atoms) and SDD ECP (Se, Te atoms) basis sets.

Table 3.9. TD / DFT predicted frontier molecular orbital energy levels of polymers **P8** (T), **P9** (Se) and **P10** (Te).

Chalcogen	E_{HOMO} (eV)[a]	E_{LUMO} (eV)[a]	E_g (eV)[a]
T	-4.97	-3.15	1.82
Se	-4.96	-3.20	1.76
Te	-4.95	-3.21	1.74

[a] calculated using TD / DFT calculations with B3LYP / 6-31g* (H, C, S, N, O atoms) and SDD ECP (Se, Te atoms) basis sets.

3.7. Chalcogenophene OPV comparison

3.7.1. Conventional device architecture

Polymer / fullerene bulk heterojunction solar cells were fabricated with polymers **P8** (T), **P9** (Se) and **P10** (Te) as the donor material to establish a relationship between chalcogen atom substitution and OPV performance. Compared to the previous ***C1*** – ***C3*** comparison, a more in depth investigation with both PC[61]BM and PC[71]BM fullerenes and device architecture variation was undertaken to add further data to the detailed comparison between the different chalcogenophenes.

Figure 3.25 shows the *J-V* curves and EQE spectra with both PC[61]BM and PC[70]M using conventional device architecture and **Table 3.9** displays the

respective performance parameters for each device. Despite the similar acceptor energy levels the V_{oc} of the three materials are generally slightly higher when PC[61]BM is used whilst both acceptors can be seen to closely follow the observed trend in E_{HOMO} with a reduced V_{oc} across the series. **P8** (T) shows the highest values of 0.61 V (PC[61]BM) and 0.59 V (PC[71]BM) as a result of the lowest lying E_{HOMO} of the series. **P9** (Se) is next highest with the selenophene co-momoner affording a V_{oc} of 0.59 V (PC[61]BM) and 0.57 V (PC[71]BM) whilst **P10** (Te) with the highest E_{HOMO} due to the least aromatic tellurophene co-monomer gives the lowest V_{oc} of 0.53 V observed with both acceptors.

The photocurrent values show a similar trend with **P8** (T) showing the largest J_{sc} values of 16.7 mA cm^{-2} (PC[61]BM) and 19.0 mA cm^{-2} (PC[71]BM) whilst **P10** (Te) has the lowest values at 12.1 mA cm^{-2} (PC[61]BM) and 16.2 mA cm^{-2} (PC[71]BM). This is likely a result of the narrowing of the optical band resulting in a reduced offset between the donor and acceptor LUMOs and reduced charge separation. There is a substantial increase in photocurrent, an average of around 3.3 mA cm^{-2}, when PC[71]BM is used as an acceptor as opposed to PC[61]BM. This substitution of fullerenes has previously been shown to be highly effective strategy for increasing the photocurrent of the resultant devices due to the larger fullerene exhibiting stronger light absorption. This is demonstrated by a comparison of the two EQE spectra in **Figure 3.25 (a)(ii)** and **(b)(ii)** which show an increase in absorption in the fullerene region of the spectrum for PC[71]BM ranging from approximately 65 - 80 % compared to 50 – 60 % for PC[61]BM.

Device FF values also show an increase in going from PC[61]BM to PC[71]BM for each of the three chalcogenophene polymers suggesting that there could also be an increased miscibility between the polymer and fullerene materials. These FF values decrease with heavier atom substitution, which is potentially a consequence of increased crystallinity inhibiting percolation pathways to the electrodes. These variations in performance parameters with differing fullerenes and chalcogenophene co-monomers give good maximum PCE values for T, Se and Te of 7.0 %, 6.5 % and 5.0 % respectively.

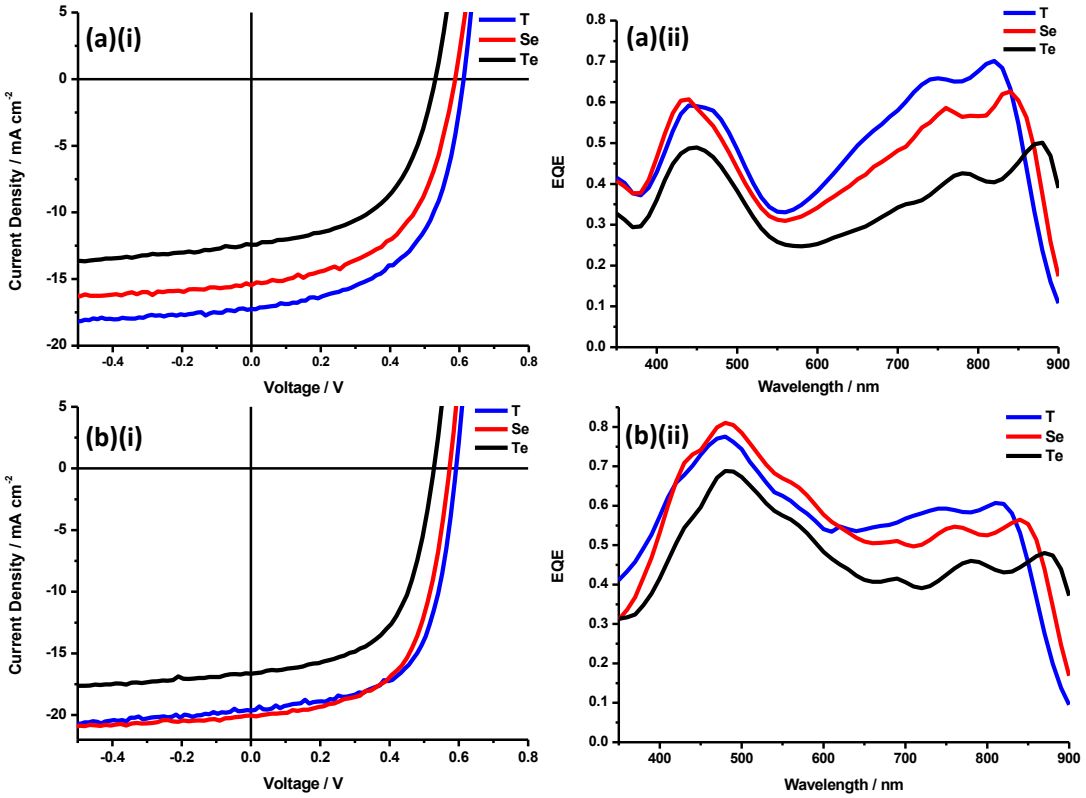

Figure 3.25. (a) Polymer / PC[61]BM **(i)** *J-V* curve and **(ii)** EQE spectra **(b)** Polymer / PC[71]BM **(i)** *J-V* curve and **(ii)** EQE spectra for polymers **P8** (T), **P9** (Se) and **P10** (Te) using conventional device architecture.

Table 3.10. OPV device performance parameters of polymers **P8** (T), **P9** (Se) and **P10** (Te) with both PC[61]BM and PC[71]BM fullerene acceptors using conventional device architecture.

Polymer	Fullerene	J_{sc} (mA / cm^2)[a]	V_{oc} (V)	FF	PCE (%)[a]
T	PC[61]BM	16.7	0.61	0.56	5.7
Se	PC[61]BM	15.5	0.59	0.54	4.9
Te	PC[61]BM	12.1	0.53	0.53	3.4
T	PC[71]BM	19.0	0.59	0.62	7.0
Se	PC[71]BM	19.1	0.57	0.60	6.5
Te	PC[71]BM	16.2	0.53	0.58	5.0

[a] EQE corrected.

3.7.2. Inverted device architecture

Inversion of the device architecture of **DPP** based polymers in Chapter Two yielded promising results, although device performance improvements compared to using conventional architecture were not observed. **Figure 3.26** shows the *J-V* curve and EQE spectra of the chalcogenophene series when inverted device architecture is employed and the corresponding device data is shown in **Table 3.10**. As with conventional device architecture in the previous section, devices with both PC[61]BM and PC[71]BM fullerenes as acceptors were investigated.

The V_{oc} and J_{sc} values with both acceptors follow the same trends as in conventional architecture with the highest values observed for thiophene, 0.61 V (PC[61]BM) and 0.58 V (PC[71]BM), and the lowest values for tellurophene 0.52 V (PC[61]BM) and 0.52 V (PC[71]BM). The V_{oc} values are of similar sizes for both inverted and conventional devices whilst there is more of a variation of J_{sc} across the different architecture and fullerene combinations. An improvement in the absorption resulting from substitution of PC[61]BM for PC[71]BM is again observed, with J_{sc} values greater than 20 mA cm^{-2} for both T and Se co-monomers when devices containing the larger fullerene are considered. The thiophene co-polymer shows a largely increased FF of 0.61 (PC[61]BM) and 0.68 (PC[71]BM) which results in significant efficiency improvements compared to conventional architectures with high PCE of 6.5 % (PC[61]BM) and 8.15 % (PC[71]BM). Se and Te co-polymers also show an increased overall efficiency with inverted architecture, showing PCE values of 5.0 % (PC[61]BM) and 6.8 % (PC[71]BM) for Se and 3.8 % (PC[61]BM) and 5.0 % (PC[71]BM) for Te. These improvements with inversion of device architecture are in contrast to the findings of the comparisons between conventional and inverted devices with **DPP** polymers in Chapter Two where a drop in efficiency was observed.

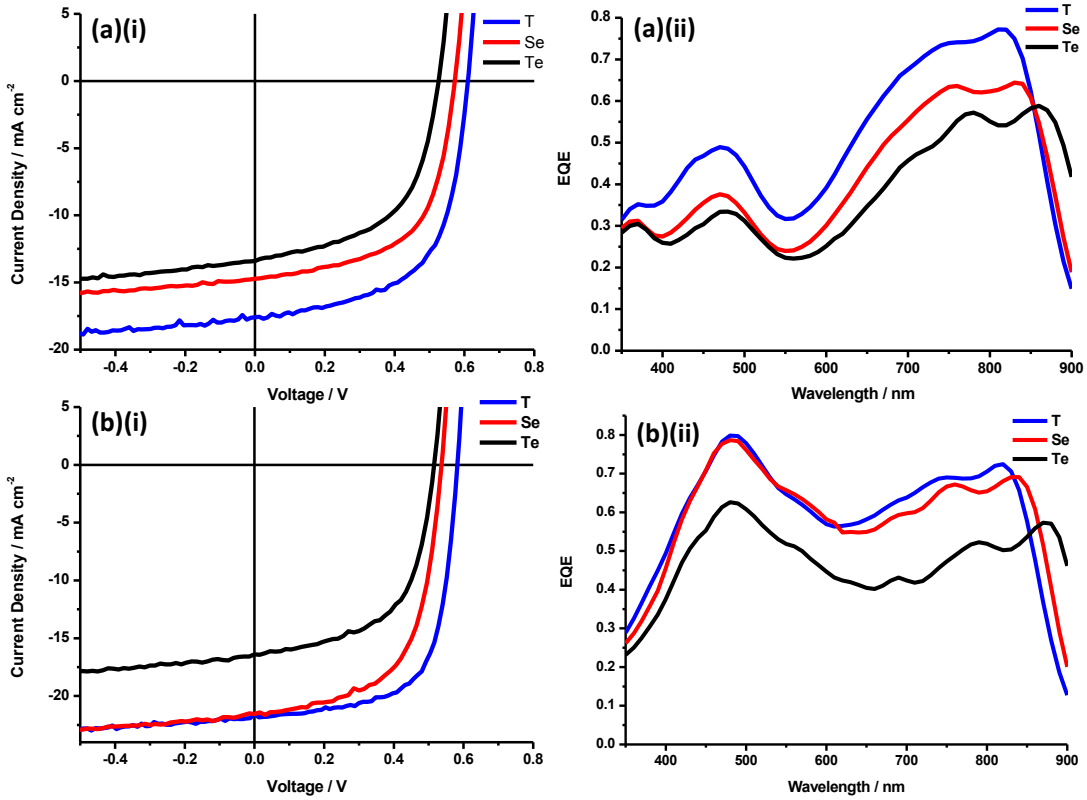

Figure 3.26. (a) Polymer / PC[61]BM **(i)** *J-V* curve and **(ii)** EQE spectra **(b)** Polymer / PC[71]BM **(i)** *J-V* curve and **(ii)** EQE spectra for polymers **P8** (T), **P9** (Se) and **P10** (Te) using inverted device architecture.

Table 3.11. OPV device performance parameters of polymers **P8** (T), **P9** (Se) and **P10** (Te) with both PC[61]BM and PC[71]BM fullerenes using inverted device architecture.

Polymer	Fullerene	J_{sc} (mA / cm^2)[a]	V_{oc} (V)	FF	PCE (%)[a]
T	PC[61]BM	17.6	0.61	0.61	6.5
Se	PC[61]BM	14.6	0.57	0.60	5.0
Te	PC[61]BM	13.2	0.53	0.55	3.8
T	PC[71]BM	20.7	0.58	0.68	8.2
Se	PC[71]BM	20.5	0.54	0.61	6.8
Te	PC[71]BM	16.3	0.52	0.59	5.0

[a] EQE corrected.

3.7.3. Tandem devices

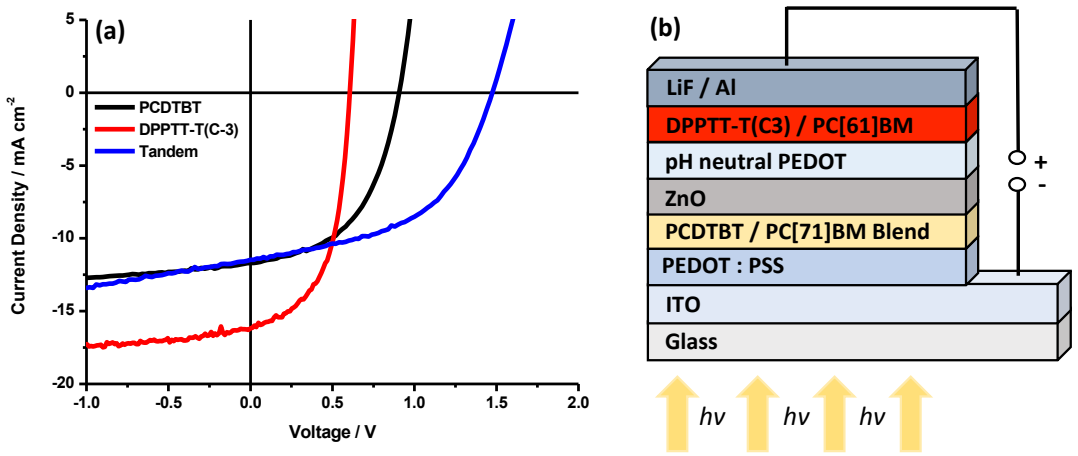

Figure 3.27. Tandem device **(a)** *J-V* curve and **(b)** device architecture using polymer **P8** in combination with **PCDTBT** co-polymer.

Recent advancements in multi-junction OPV devices has resulted in the progression of device performance parameters to ever increasing PCEs. Whilst device fabrication is by definition more complex, with multi-layer deposition required during device fabrication, there are several benefits of having two active material layers. By combining a wide band gap material and a narrow band gap material it is possible to cover a larger part of the solar flux spectrum, whilst the V_{oc} of tandem devices is significantly enhanced due to the greater in-built voltage of the devices.

The best performing material of this chapter **P8** was used as a narrow band gap material in combination with the wide band gap **PCDTBT** polymer in a tandem device with the structure shown in **Figure 3.27 (b).** The *J-V* curves of the individual polymer single junction solar cells and the tandem device are shown in **Figure 3.27 (a)**, the V_{oc} of the tandem device can be seen to have a high value of 1.47 V that is the sum of the V_{oc} values of the two individual single junction devices. The J_{sc} value of 11.5 mA cm^{-2} of the tandem device is reduced in comparison to the single junction devices despite a larger range of the visible spectrum being covered. Despite the reduction in J_{sc} the improved V_{oc} results in a significantly enhanced overall efficiency of 8.6 %.

Table 3.12. Tandem device characteristics using **P8** and **PCDTBT** polymers.

Polymer	J_{sc} (mA / cm^2)	V_{oc} (V)	FF	PCE (%)
PCDTBT:PC[71]BM[a]	11.7	0.90	0.51	5.4
DPPTT-T(*C3*):PC[61]BM	16.2	0.60	0.55	5.3
Tandem	11.5	1.47	0.51	8.6

[a] **PCDTBT** polymer provided by Dr. Raja Shahid Ashraf.

3.8. Chalcogenophene morphology

3.8.1. Chalcogenophene XRD

The chalcogenophene substituted polymers were shown by UV-Vis spectroscopy at room temperature and elevated temperatures to vary significantly in terms of intermolecular interactions with thiophene and selenophene containing polymers showing fairly similar behaviour whilst tellurophene containing material demonstrated a marked difference. An XRD study was performed to evaluate how these interactions relate to the crystalline behaviour of each polymer in the solid state.

The diffractogram of the three polymers can be seen in **Figure 3.28** with each of the three polymers showing a first order (100) lamellar stacking peak at around $2\theta = 4.1^{o}$ that is of similar intensity for both **P8** (T) and **P9** (Se), but is approximately five times more intense for **P10** (Te). There is also a second order (200) reflection at around $2\theta = 8.2^{o}$ that is again of much greater intensity for **P10** (Te) than **P8** (T) and **P9** (Se) as well as a small third order (300) reflection at $2\theta = 12.3^{o}$ that is present only in the tellurophene containing co-monomer. These correspond to lamellar stacking distances of approximately 21.5 Å and interestingly the heavy atom substitution does not result in significant variation in these stacking distances. In general **P8** (T) and **P9** (Se) are both of similar crystallinity whilst **P10** (Te) is significantly more crystalline suggesting that the heteroatom-heteroatom interactions between tellurium atoms on different polymer chains are greater than with selenophene.

These findings are also in agreement with the previous data (UV-Vis / OPV) discussed in this chapter where similar behaviour is observed for **P8** (T) and **P9** (Se) whilst **P10** (Te) behaves slightly different. It is likely that the increased crystallinity resulting from the tellurophene co-monomer is detrimental to the OPV performance

of resultant device due to more crystalline polymer domains reducing fullerene intermixing in the donor / acceptor blend layers.

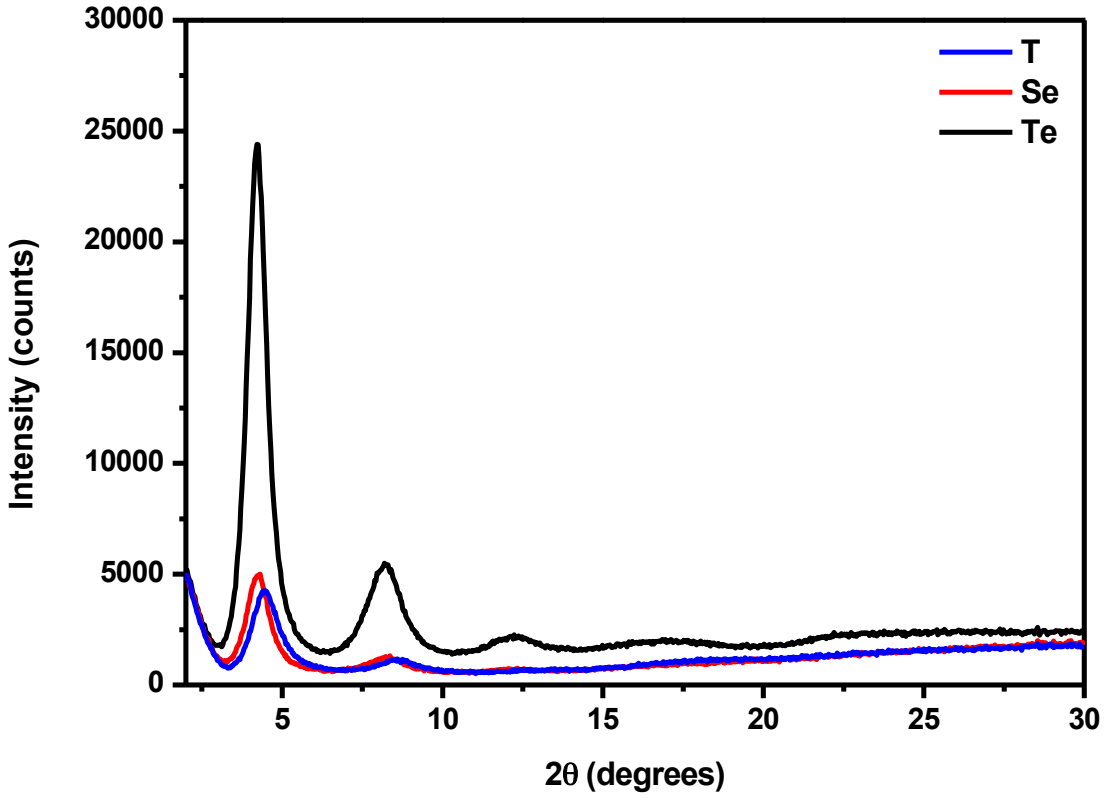

Figure 3.28. XRD diffractograms of **P8** (T), **P9** (Se) and **P10** (Te) polymer films drop cast on Si wafers from 10 mg / mL chlorobenzene solution.

3.8.2. Chalcogenophene AFM

AFM imaging was used to investigate any changes in surface morphology across the series in both the neat film and polymer / fullerene blends to see if there are any observable trends that can be related to the different polymer device performances. **Figure 3.29** shows the AFM images of the three different chalcogenophene co-polymers, pristine polymer films and conventional and inverted devices with both PC[C61]BM and PC[71]BM fullerenes were probed.

The pristine polymer film of **P10** (Te) appears slightly more ordered than **P8** (T) and **P9** (Se) indicative of the increased crystallinity observed in XRD diffractograms. Conventional devices show similar trends across the series with both fullerenes and there does not appear to be dramatic variation between the different co-monomer

units. However, it can be seen that with **P10** (Te) the blends exhibit slightly coarser morphologies which is supported by the increased average domain sizes for Te and this apparent reduction in blend intermixing with Te appears larger when PC[71]BM is used. With inverted device architectures there is no observable trend with PC[61]BM but with the larger PC[71]BM fullerene the Te containing polymer appears to have a less finely intermixed blend morphology which is again not reflected in the average domain sizes.

A changing of the blend morphologies between conventional and inverted devices, when both fullerenes are used, is one of the most noticeable differences shown by the AFM data in this study, with inverted devices exhibiting observably larger domain sizes. It is widely known that the use of different material interlayers in OPV devices not only modifies electrode work functions but can also result in a wide range of blend morphologies due to the changing surface energies of these interfactial layers.[32,33] Such a variation of interlayers between conventional and inverted devices is likely to be the reason behind these different blend morphologies. Despite the inverted devices appearing to have coarser polymer / fullerene blends this is not detrimental to the OPV performance as there was a general improvement with inversion of architecture observed in section **3.7.2**.

Whilst small changes in the AFM morphologies can be speculated, the variations between different co-monomers are not dramatic enough to draw conclusions that support the much larger variations in OPV device parameters and it is therefore likely that previously observed variations in light absorption and energy level alignments are more significant contributors to the different performances.

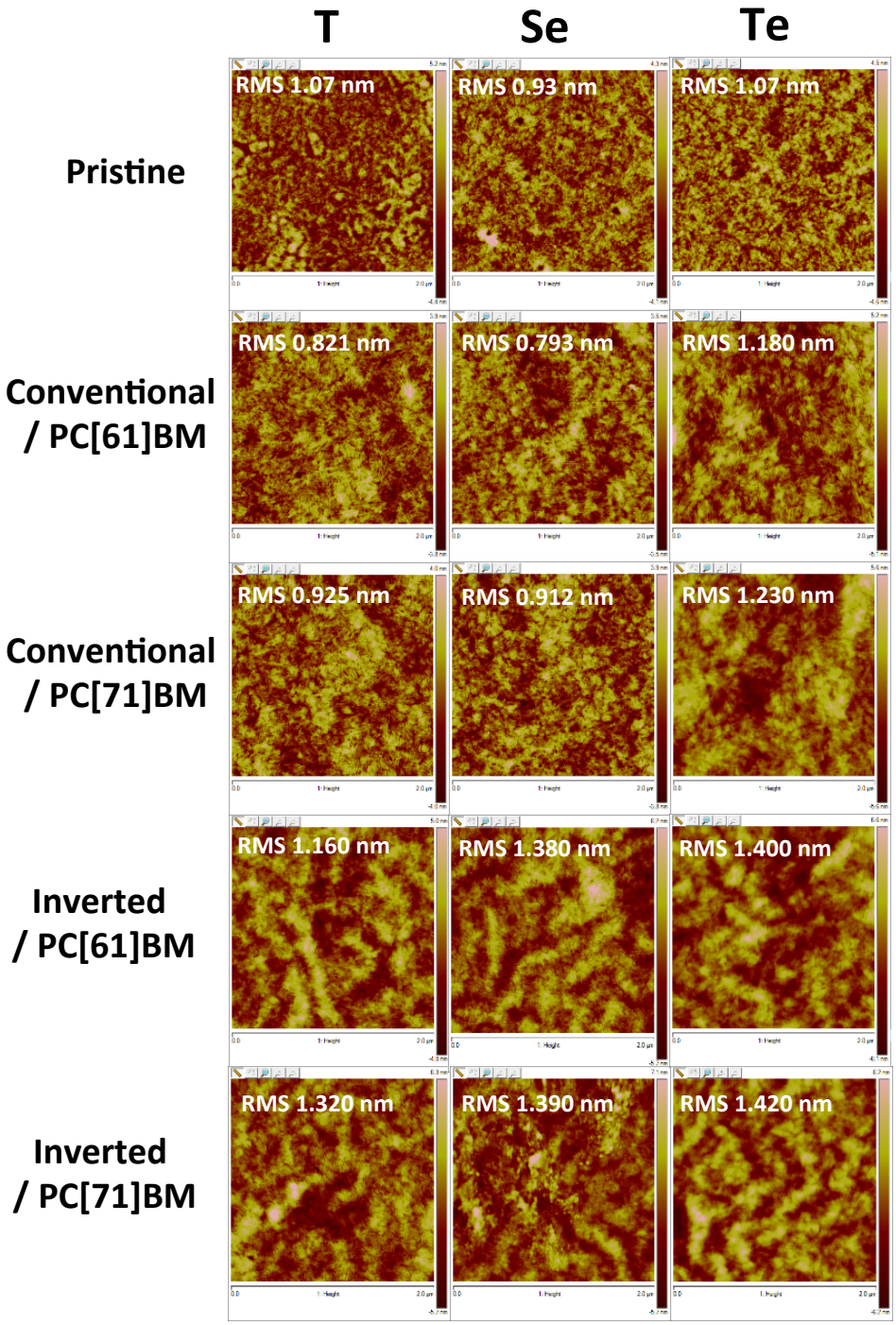

Figure 3.29. AFM images of polymers **P8** (T), **P9** (Se) and **P10** (Te) pristine polymer films and conventional / inverted device architectures with both PC[61]BM and PC[71]BM fullerene acceptors.

3.9. Conclusion and outlook

Two new branched alkyl chains, ***C2*** and ***C3***, were synthesised where the branching position is systematically moved further from the polymer main chain, thus increasing the linear portion of the alkyl chain. The new alkyl chains imparted an increased solubility which afforded higher molecular weight and narrowed PDI material whilst the molecular orbital energy levels remained unchanged. When used as the donor material in bulk heterojunction solar cells the ***C2*** and ***C3*** polymers resulted in a largely enhanced photocurrent compared to ***C1*** which gave a significant improvement in solar cell efficiency from around 5.5 % to around 7.0 %. A similar trend in improvement was observed with hole mobilities in thin film OFETs. The thiophene co-polymers of ***C1***, ***C2*** and ***C3*** were probed by GIXD using a synchrotron light source and it was shown that ***C2*** and ***C3*** branching resulted in a significant increase in polymer crystallinity in both the neat polymer films and polymer / fullerene blends which is likely the reason for the improved device performances. The neat polymer films also showed an increased amount of face-on orientation of the polymer chains relative to the substrate which can also be seen to contribute to the increased OFET mobilities.

New co-monomer variations of the ***C2*** and ***C3*** alkyl chains were also investigated, the homo-polymer of ***C2*** was synthesised in addition to co-polymerisation with a phenyl co-monomer. Of the three ***C2*** polymers it was found that the thiophene co-monomer was the best performing material by a considerable amount with a PCE of 7.1 % compared to 4.1 % and 4.4 % for the homo-polymer and phenyl co-monomer respectively. Building upon the high performance of ***C3*** and the lack of literature precedence for chalcogenophene comparison in organic electronics, the equivalent selenophene and tellurophene co-polymers were synthesised and compared computationally and experimentally to the original thiophene co-polymer. Descending the periodic group gives a reduction in aromaticity resulting in slight increases in E_{HOMO} and reduction in E_{LUMO} with the resultant narrowing of E_g giving red-shifted absorption profiles. Comparison of the three chalcogenophene polymers with differing fullerene acceptors and device architectures showed V_{oc} and J_{sc} to generally drop with increasing heteroatomic size. Despite these drops, high performing solar cells were obtained with efficiencies as high as 8.2 % for thiophene, 6.8 % for

selenophene and 5 % for tellurophene whilst an initial tandem device was investigated with ***C3*** thiophene which exhibited a highly promising PCE of 8.6 %.

For the ***C3*** thiophene co-polymer these device performances are close to the current leaders of **DPP** based polymers and the field of OPV in general whilst at the time of writing this thesis the selenophene and tellurophene co-polymers give the highest performing OPV devices reported for each of the respective heterocycles.

Further work to demonstrate this branching point effect in other conjugated polymers for OPV applications would be highly desirable for the field whilst further understanding of the effect of chalcogen substitution could be developed by incorporation of the heteromatic substitution into the flanking aromatic unit of the DPP core.

3.10. References

1. J. Mei, D. H. Kim, A. L. Ayzner, M. F. Toney and Z. Bao, *J. Am. Chem. Soc.*, 2011, **133**, 20130–20133.
2. T. Lei, J.-H. Dou and J. Pei, *Adv. Mater.*, 2012, **24**, 6457–6461.
3. T. Lei, J.-H. Dou, X.-Y. Cao, J.-Y. Wang, and J. Pei, *Adv. Mater.*, 2013, **25**, 6589–6593.
4. F. Zhang, Y. Hu, T. Schuettfort, C. Di, X. Gao, C. R. McNeill, L. Thomsen, S. C. B. Mannsfeld, W. Yuan, H. Sirringhaus and D. Zhu, *J. Am. Chem. Soc.*, 2013, **135**, 2338–2349.
5. T. Lei, J.-Y. Wang and J. Pei, *Chem. Mater.*, 2014, **26**, 594-603.
6. J.-H. Dou, Y.-Q. Zheng, T. Lei, S.-D. Zhang, Z. Wang, W.-B. Zhang, J.-Y. Wang and J. Pei, *Adv. Funct. Mater.*, 2014, ASAP, DOI: 10.1002/adfm.201401822
7. K. H. Hendriks, W. Li, G. H. L. Heintges, G. W. P. van Pruissen, M. M. Wienk and R. A. J. Janssen, *J. Am. Chem. Soc.*, 2014, **136**, 11128 – 11133.
8. X. Zhang, L. J. Richter, D. M. DeLongchamp, R. J. Kline, M. R. Hammond, I. McCulloch, M. Heeney, R. S. Ashraf, J. N. Smith, T. D. Anthopoulos, B. Schroeder, Y. H. Geerts, D. A. Fischer and M. F. Toney, *J. Am. Chem. Soc.*, 2011, **133**, 15073 – 15084.
9. R. J. Kline, D. M. DeLongchamp, D. A. Fischer, E. K. Lin, L. J. Richter, M. L. Chabinyc, M. F. Toney, M. Heeney and I. McCulloch, *Macromolecules*, 2007, **40**, 7960–7965.
10. Y. Shin, J. Liu, J. J. Quigley, H. Luo and X. Lin, *ACS Nano*, 2014, 8, 6089-6096.
11. J. Liu, B. Walker, A. Tamayo, Y. Zhang and T.-Q. Nguyen, *Adv. Funct. Mater.*, 2013, **23**, 47–56.
12. B. Sun, W. Hong, Z. Yan, H. Aziz, and Y. Li, *Adv. Mater.*, 2014, **26**, 2636–2642.
13. Y. Li, P. Sonar, S. P. Singh, W. Zeng and M. S. Soh, *J. Mater. Chem.*, 2011, **21**, 10829–10835.
14. J. C. Bijleveld, B. P. Karsten, S. G. J. Mathijssen, M. M. Wienk, D. M. de Leeuw and R. A. J. Janssen, *J. Mater. Chem.*, 2011, **21**, 1600–1606.

15. A. J. Kronemeijer, E. Gili, M. Shahid, J. Rivnay, A. Salleo, M. Heeney and H. Sirringhaus, *Adv. Mater.*, 2012, **24**, 1558–1565.
16. M. Shahid, T. McCarthy-Ward, J. Labram, S. Rossbauer, E. B. Domingo, S. E. Watkins, N. Stingelin, T. D. Anthopoulos and M. Heeney, *Chem. Sci.*, 2012, **3**, 181–185.
17. J. S. Ha, K. H. Kim, and D. H. Choi, *J. Am. Chem. Soc.*, 2011, **133**, 10364–10367.
18. H.-W. Lin, W.-Y. Lee and W.-C. Chen, *J. Mater. Chem.*, 2012, **22**, 2120–2128.
19. J. Lee, A. R. Han, J. Kim, Y. Kim, J. H. Oh and C. Yang, *J. Am. Chem. Soc.*, 2012, **134**, 20713–20721.
20. A. A. B. Alghamdi, D. C. Watters, H. Yi, S. Al-Faifi, M. S. Almeataq, D. Coles, J. Kingsley, D. G. Lidzey and A. Iraqi, *J. Mater. Chem. A*, 2013, **1**, 5165–5171.
21. M. Shahid, R. S. Ashraf, Z. Huang, A. J. Kronemeijer, T. McCarthy-Ward, I. McCulloch, J. R. Durrant, H. Sirringhaus and M. Heeney, *J. Mater. Chem.*, 2012, **22**, 12817–12823.
22. M. Heeney, M. Al-Hashimi, I. McCulloch, W. Zhang and R. Hamilton, *238th ACS National Meeting Washington DC United States 2009*, 2009.
23. C.-C. Chang, C.-P. Chen, H.-H. Chou, C.-Y. Liao, S.-H. Chan and C.-H. Cheng, J. *Polym. Sci. Part A: Polym. Chem.*, 2013, **51**, 4550 – 4557.
24. H.-Y. Chen, S.-C. Yeh, C.-T. Chen and C.-T. Chen, *J. Mater. Chem.*, 2012, **22**, 21549–21559.
25. D. P. Sweat and C. E. Stephens, *J. Organomet. Chem.*, 2008, **693**, 2463–2464.
26. T. M. McCormick, A. A. Jahnke, A. J. Lough and D. S. Seferos, *J. Am. Chem. Soc.*, 2012, **134**, 3542–3548.
27. A. A. Jahnke, G. W. Howe and D. S. Seferos, *Angew. Chemie Int. Ed.*, 2010, **49**, 10140–10144.
28. M. Kaur, D. S. Yang, K. Choi, M. J. Cho and D. H. Choi, *Dye. Pigment.*, 2014, **100**, 118–126.
29. E. H. Jung, S. Bae, T. W. Yoo and W. H. Jo, *Polym. Chem.*, 2014, ASAP, DOI: 10.1039/C4PY00791C
30. M. Planells, B. C. Schroeder and I. McCulloch, *Macromolecules*, 2014, ASAP, **DOI:** 10.1021/ma5014308
31. M. H. J. Koch and J. Bordas, *Nucl. Instruments Methods Phys. Res.*, 1983, **208**, 461–469.
32. T.-H. Lai, S.-W. Tsang, J. R. Manders, S. Chen and F. So, *Mater. Today*, 2013, **16**, 424–432.
33. J. H. Park, T.-W. Lee, B.-D. Chin, D. H. Wang and O. O. Park, *Macromol. Rapid Commun.*, 2010, **31**, 2095–2108.

Chapter Four

New Thieno[3,2-*b*]thiophene Based Isoindigo Polymers For Organic Field Effect Transistor Applications

4.1. Introduction

Indigo is a naturally occurring blue organic pigment which has been used commercially as a dye worldwide for thousands of years.[1,2] The structure consists of two ketopyrrole rings, which are fused to flanking phenyl groups and connected via a carbon-carbon double bond (**Figure 4.1 (b)**). Despite its lack of apparent conjugation through the structure it has still been shown to be an effective unit for organic semiconductors, with several ambipolar OFET devices reported.[3,4] In comparison, isoindigo sees the alkene and keto groups swapping position on the pyrrole ring giving it a more efficiently conjugated backbone.[5] As with the similar **DPP** unit, structural variations can be made to both the flanking unit and *N*-alkyl chain. The synthesis of the isoindigo unit has been reported since the 1980's however its application as an acceptor unit in organic electronics did not come until 2010 when *J. Reynolds et al*. reported a di-phenyl isoindigo small molecule structure (**Figure 4.1 (b)**) that demonstrated OPV efficiencies around 2 %.[6,7] The di-phenyl isoindigo unit has since been shown to be an effective building block for semiconducting materials in both small molecule and polymer based OFET devices.[8-12]

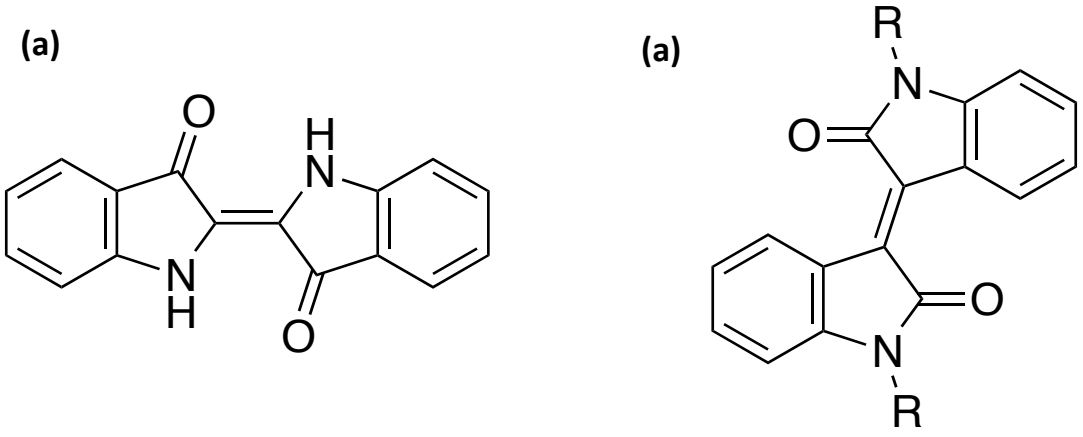

Figure 4.1. Chemical structures of (di-phenyl) **(a)** indigo **(b)** isoindigo.

Various structural modifications to the core isoindigo unit have since been reported. The progression to a di-thienyl isoindigo (**iIT**) unit was reported by *R. Ashraf et al.* in 2012 and the new bis-lactam unit was co-polymerised with an electron-deficient benzothiadiazole unit which gave thin film OFET devices with high hole mobilities > 0.1 cm^2 / Vs.[13] The fused structure of the **iIT** core results in a planar unit with highly efficient conjugation, which can be favourable for charge transport properties.

Additionally, the enhanced conjugation and increased quinoidal contribution of the thiophene donor groups affords polymers with narrow optical band gaps and red-shifted absorption profiles.[14,15] A consequence of the electron-deficient nature of the unit's core results in a D / A backbone structure in a similar fashion to the previously discussed **DPP** polymers, in which off-axis dipoles in combination with the various planarising features results in strong intermolecular interactions between polymer chains.[16]

Whilst there are a wealth of isoindigo materials reported throughout the literature there still remains a number of aromatic units that are yet to be incorporated into the fused isoindigo core.[17,18] To date the flanking units have also so far been restricted to single aromatic rings, primarily phenyl or thiophene, with no investigations into the effect that extension of the fused core has on device performance. This can be identified as a gap in isoindigo research and the synthesis of an isoindigo acceptor unit that is extended to incorporate further fused rings would have significant impact potential.

4.2. Aim

A multi-step synthesis of a new thieno[3,2-*b*]thiophene based isoindigo unit (**iITT**) with branched alkyl chains will be targeted with a view to developing the first example of a conjugated six fused ring isoindigo system. Subsequent co-polymerisation by palladium-catalysed Stille and Suzuki coupling with a variety of conjugated co-monomer partners will afford a series of semiconducting polymers with great potential in thin film OFET applications. A series of co-monomers will be chosen according to some of the most promising literature reports as well as the earlier findings of this thesis. Full characterisation of the optical and physical properties of the polymer series will be reported. The polymers will be screened for OFET device performances, which will be discussed in conjunction with a full morphological study to establish a thorough understanding of the novel isoidigo unit **iITT**.

It is hoped that through the introduction of the thieno[3,2-*b*]thiophene unit, the fused nature of the isoindigo core will be extended, facilitating enhanced delocalisation and

hybridisation of molecular orbitals for charge transport. The thieno[3,2-*b*]thiophene unit is also highly planar by definition and as such the resultant solution processable D / A type polymers should demonstrate strong intermolecular association in the solid state desirable for OFET applications. The performance of this novel unit is expected to rival those previously reported for the di-phenyl and di-thienyl equivalents.[19,20]

4.3. Synthesis of iITT polymers P11 – P13

4.3.1. Alkyl chain synthesis

The fused nature of the thieno[3,2-*b*]thiophene unit is likely be of detriment to the solubility of resultant polymers due to the increased amount of unfunctionalised aromaticity compared to previous isoindigo systems containing single aromatic rings. The solubilising alkyl chains must therefore be carefully considered to ensure sufficient disruption of the strong interchain interactions between aromatic systems and guarantee solution processability. Considering the excellent solubility observed in Chapter One with similar **DPP** polymers, the larger $C_{10}C_{12}$ branched alkyl group was chosen.

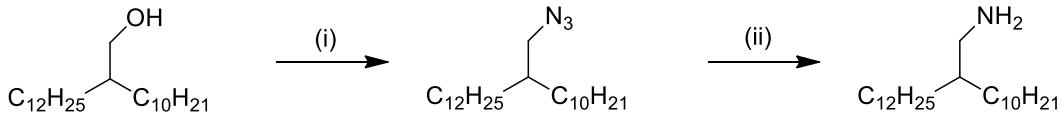

4.1 **4.2**

Figure 4.2. Synthesis of compound **4.2.** *Reagents and conditions:* **(i)** DIAD, diphenylphosphoryl azide, PPh_3, THF, RT **(ii)** $LiAlH_4$, THF, reflux.

As shown in **Figure 4.2** the commercially available 2-octyl-dodecanol was converted to the corresponding branched alkyl azide using diisopropyl azodicarboxylate (DIAD), triphenylphosphine (PPh_3) and diphenylphosphoryl azide in THF at room temperature in a modification of the Mitsunobu reaction.[21,22] Aqueous work-up followed by column chromatography (hexanes) afforded the corresponding alkyl azide **4.1** in good purity. Azides readily eliminate diatomic nitrogen and the resultant azide group was reduced to the alkyl amine 2-decyl-1-tetracedylamine **4.2** by careful addition of $LiAlH_4$. Due to the exothermic nature of the reduction, care was taken to

add the reducing agent dropwise whilst the reaction was monitored for the build-up of internal pressure arising from the elimination of gaseous N_2 as a side product.

As shown in **Figure 4.3** the alkyl functional group interconversions in this synthesis were identified by changes in the ^{1}H NMR chemical shift of the doublet corresponding to the CH_2 protons adjacent to the different functionalities. A gradual shift to a less downfield shift is observed due the changing electronegativities with each functional group interconversion.

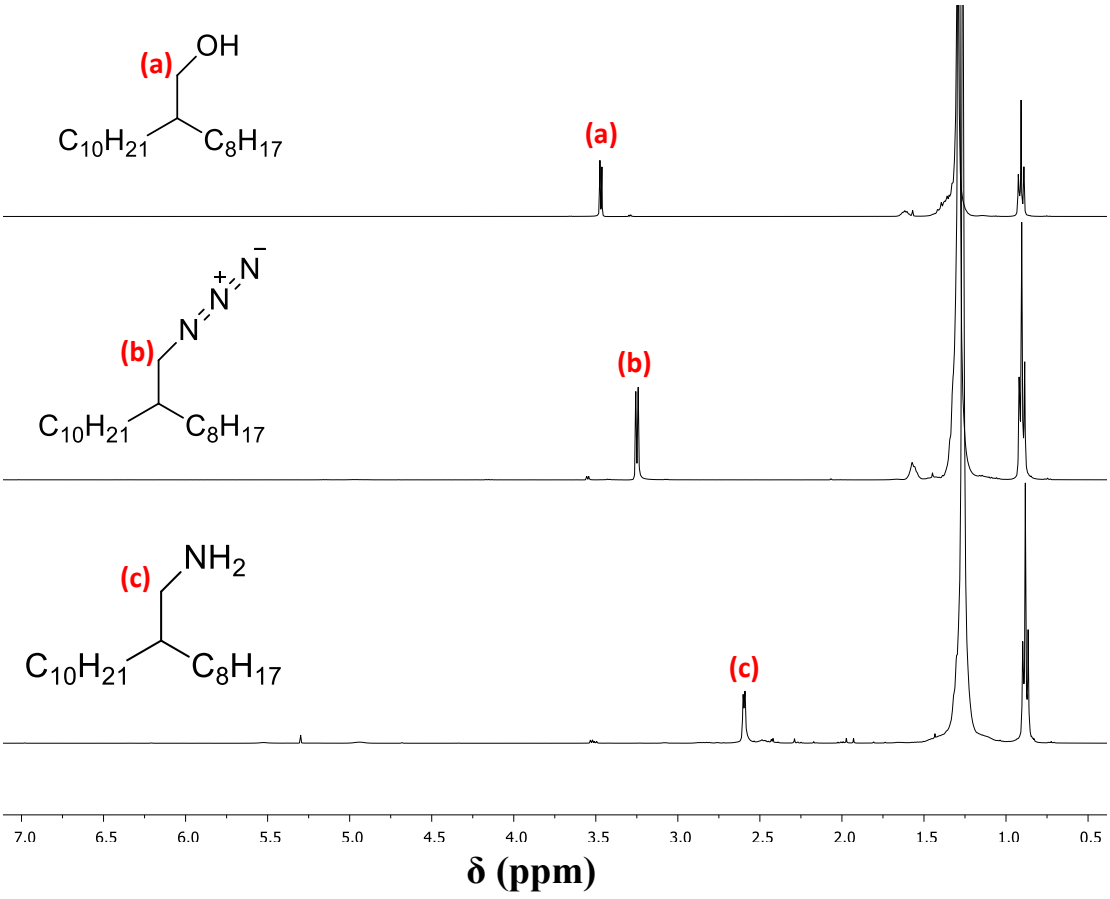

Figure 4.3. ^{1}H NMR in $CDCl_3$ at 25 ºC of compounds **4.1** and **4.2** showing the characteristic changes associated with each transformation.

4.3.2. iITT monomer synthesis

Commercially available thieno[3,2-*b*]thiophene was di-brominated at the two alpha positions under mild conditions using the versatile brominating agent *n*-bromosuccinimide (NBS) in dimethylformamide (DMF) to afford 2,5-dibromo-thieno[3,2-*b*]thiophene **4.3**. Recrystallization ensured the pure product was isolated from any starting material and mono-bromo impurities as confirmed by the transformation of two doublets into a singlet at 7.21 ppm in the aromatic region of the ^{1}H NMR (**Figure 4.5**). The di-brominated product 2,5-dibromo-thieno[3,2-*b*]thiophene **4.3** was next thoroughly dried and lithiated using *n*BuLi at -78 ºC in diethyl ether with care taken to ensure that one equivalent of organolithium reagent was added dropwise to avoid the formation of any di-lithiated species. Quenching at -78 ºC with excess chlorotrimethylsilane afforded the asymmetric TMS protected (5-bromothieno[3,2-*b*]thiophen-2-yl)trimethylsilane **4.4** via substitution of the lithiated aromatic for the chloride leaving group. The solution was warmed slowly to room temperature, worked-up under aqueous conditions and separated from any di-TMS protected species by column chromatography using hexane as the eluent. The transformation was confirmed by the change from one singlet to two doublets in the aromatic region of the ^{1}H NMR (**Figure 4.5**). Additionally, the appearance of the CH_3 peak of 9H intensity at 0.38 ppm shows the three methyl groups in the TMS protecting group.

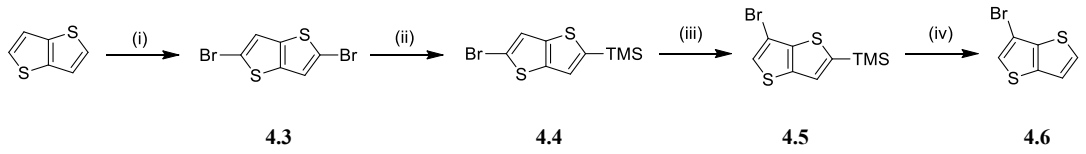

Figure 4.4. Synthesis of compound **4.6.** *Reagents and Conditions*: **(i)** NBS, DMF **(ii)** *n*BuLi, Et_2O, TMSCl, -78 °C **(iii)** LDA, Et_2O, -78 °C **(iv)** TBAF, THF, 0 °C.

The purified TMS protected product was transformed into (6-bromothieno[3,2-*b*]thiophen-2-yl)trimethylsilane **4.5** using the 'Halogen Dance' reaction in diethyl ether where lithium diisopropyl amide solution (LDA) was added at -78 ºC to afford the migration of the bromine from the *5*- to the *6*- position. After 30 min the solution was quenched at -78 ºC with ammonium chloride and warmed to room temperature. The crude product was purified by column chromatography in hexane with ^{1}H NMR

of the (6-bromothieno[3,2-*b*]thiophen-2-yl)trimethylsilane **4.5** product showing the conversion of two aromatic doublets at 7.28 ppm and 7.27 ppm to singlets at 7.40 ppm and 7.30 ppm.

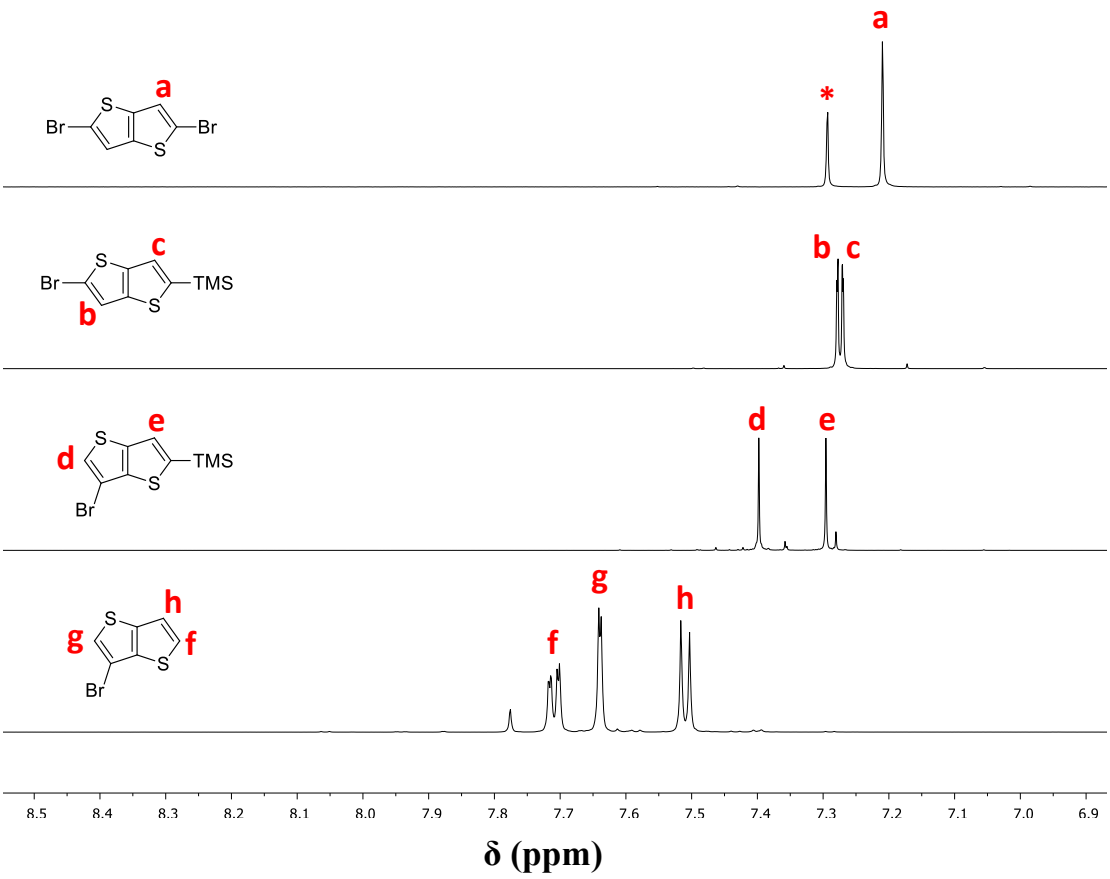

Figure 4.5. ^{1}H NMR at 25 °C of compounds **4.3** ($CDCl_3$), **4.4** ($CDCl_3$), **4.5** ($CDCl_3$), and **4.6** (Acetone-d_6) showing the characteristic changes associated with each transformation. * $CHCl_3$.

Facile deprotection of the TMS group was achieved using an excess of the deprotecting agent tertiary butylammonium fluoride (TBAF) in THF at 0 ºC, the formation of the strong Si-F bond in the fluoro trimethylsilane by-product providing a driving force for deprotection with the high yielding removal of the trimethylsilane group. Removal of salts by column chromatography in hexane afforded the 3-bromo-thieno[3,2-*b*]thiophene **4.6** product showing three aromatic peaks at 7.71 ppm, 7.64 ppm and 7.51 ppm and the disappearance of the TMS peak at 0.38 ppm in the ^{1}H NMR spectrum.

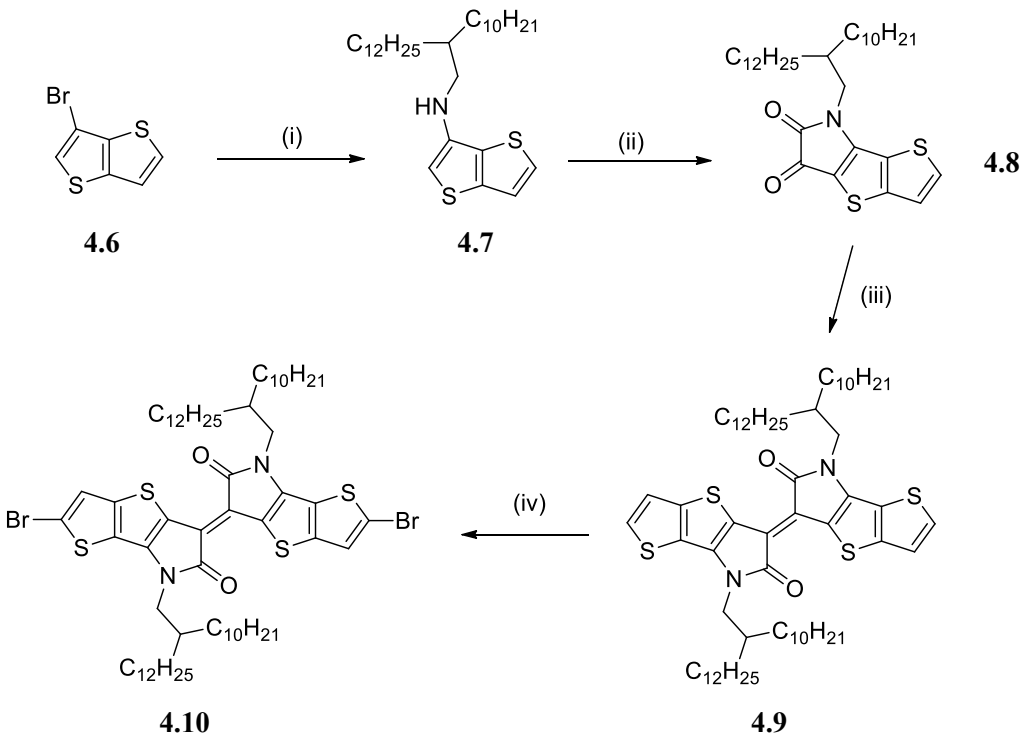

Figure 4.6. Synthesis of compound **4.10.** *Reagents and Conditions*: **(i)** 2-decyltetradecyl amine **3.2**, Cu, CuI, K_3PO_4, dimethyl aminoethanol, 80 °C **(ii)** oxalyl chloride, TEA, DCM, -10 °C **(iii)** Lawesson's Reagent, *o*-xylene, 60 °C **(iv)** NBS, THF, -10 °C.

The above synthesised compounds 3-bromo-thieno[3,2-*b*]thiophene **4.6** and 2-decyl-1-tetracedylamine **4.2** were combined in an Ullmann coupling reaction using copper and copper iodide as catalysts to replace the bromine in the thieno[3,2-*b*]thiophene *3* position with the branched alkyl amine. Column chromatography purification with hexane as the eluent afforded the pure product **4.7** with three sharp peaks in the ^{1}H NMR aromatic region identifying the thieno[3,2-*b*]thiophene unit, a broad singlet at 3.56 ppm indicating the N*H* proton and a doublet at 3.13 ppm corresponding to the NCH_2 of the alkyl chain (**Figure 4.7**).

The substituted amine **4.7** was acylated with oxalyl chloride which subsequently ring closed onto the electron-rich thieno[3,2-*b*]thiophene *2* position to afford the alkylated dicarbonyl compound **4.8**. This was again separated from any remaining starting material by column chromatography with DCM as the eluent. The ring closure was identified by the disappearance of the aromatic singlet peak as well as a downfield shift of the alkyl chain protons (**Figure 4.7**). The dicarbonyl compound was dimerised using Lawesson's reagent in *o*-xylene to give the isoindigo dimer **4.9** with care taken

to use exactly half an equivalent of the thio-compound to ensure maximum yield from the dimerization. This reaction is known to proceed exclusively to the *E* isomer, which is confirmed by the presence of only eight sp^2 carbons in the ^{13}C NMR indicating no *Z* isomer to be present. The dimer was then di-brominated under mild conditions using NBS in THF to afford the final di-brominated monomer **4.10**, which was rigorously purified by column chromatography to ensure a high yielding polymerisation.

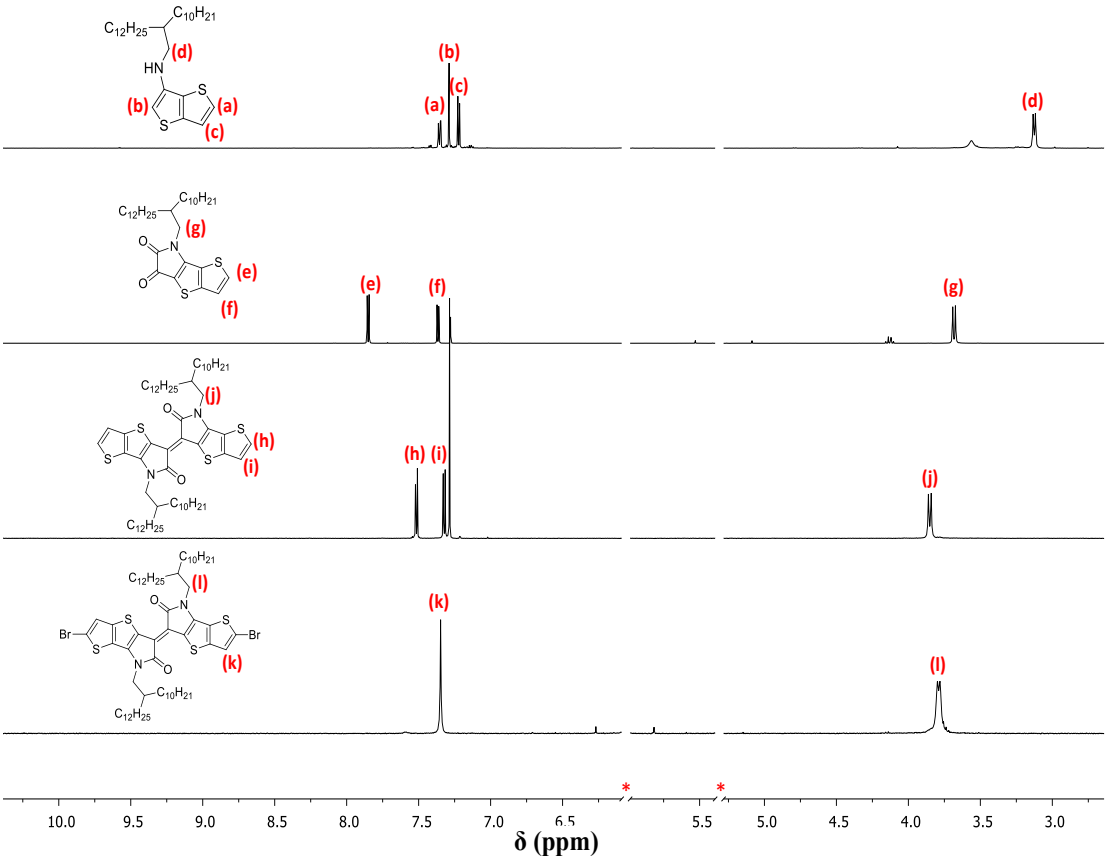

Figure 4.7. ^1H NMR at 25 ºC of compounds **4.7** ($CDCl_3$), **4.8** ($CDCl_3$), **4.9** ($CDCl_3$) and **4.10** (TCE-d_2) showing the characteristic changes associated with each transformation. * indicates solvent peak removed for demonstrative purposes.

4.3.3. iITT polymer synthesis

4.3.3.1. Suzuki coupling

Due to previous reports of good ambipolar performance of polymers consisting of benzothiadiazole co-monomers, the new brominated isoindigo monomer **4.10** was first co-polymerised with the di-borylated benzothiadiazole monomer using the standard Suzuki coupling conditions discussed in both Chapter Two and Chapter Three.[23] The dark green monomer solution turned dull green / black in colour as the polymerisation progressed over the course of three days and was worked up and purified using previously described standard conditions. The large $C_{10}C_{12}$ alkyl chain ensured the resultant polymer **P11 (iITT-BT**) was fully soluble in chloroform at room temperature. The recovered polymeric material was found to have a smaller, slightly lower M_n shoulder by analytical GPC and this was removed using preparative GPC to afford a more Gaussian GPC distribution of material with higher M_n and narrower PDI as reported in **Table 4.1**.

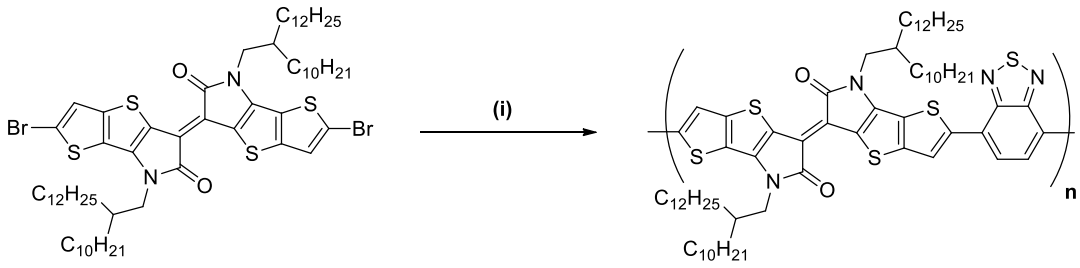

4.10 **P11 (iITT-BT)**

Figure 4.8. Synthesis of polymer **P11** (**iITT-BT**) from **4.10** by palladium-catalysed Suzuki coupling. *Reagents and conditions:* **(i)** Toluene / Aliquat 336, $Pd_2(PPh_3)_4$, K_2CO_3, 120 °C.

4.3.3.2. Stille coupling

Monomer **4.10** was also co-polymerised via Stille coupling with di-stannylated thiophene and di-stannylated bi-thiophene monomers (**Figure 4.9**) which were both chosen to function as conjugated, co-planar spacers that are often incorporated in high performing organic semiconducting materials.[24] Conditions similar to those previously described in Chapters Two and Three for **DPP** Stille coupling were used

with slight modification to the maximum temperature reached in the microwave. Since this was the first example of a microwave-assisted polymerisation of isoindigo in which coupling occurs at a thienyl position and the temperature range of the reaction is unknown, the maximum temperature was lowered to 180 ºC.

Following polymerisation with di-stannylated thiophene, work-up and Soxhlet extraction into chloroform afforded the dull green / black polymer **P12** (**iITT-T**) which again showed good solubility in common chlorinated laboratory solvents such as chloroform and chlorobenzene. Polymerisation with bi-thiophene yielded similar results, affording the polymer **P13** (**iITT-2T**). For consistency of comparison to the BT analogue, both of these polymers synthesised by Stille coupling were also purified by preparative GPC to afford materials with good M_n and narrow PDI. The physical data of the two polymers compared to **P11** (**iITT-BT**) synthesised by Suzuki coupling is shown in **Table 4.1**. It is worth noting that all three polymers were isolated in lower molecular weights than previous chapters, as indicated by the reduced DP_n values, however they are each of similar M_n which enables a fair comparison of the effects arising from different co-monomer units.

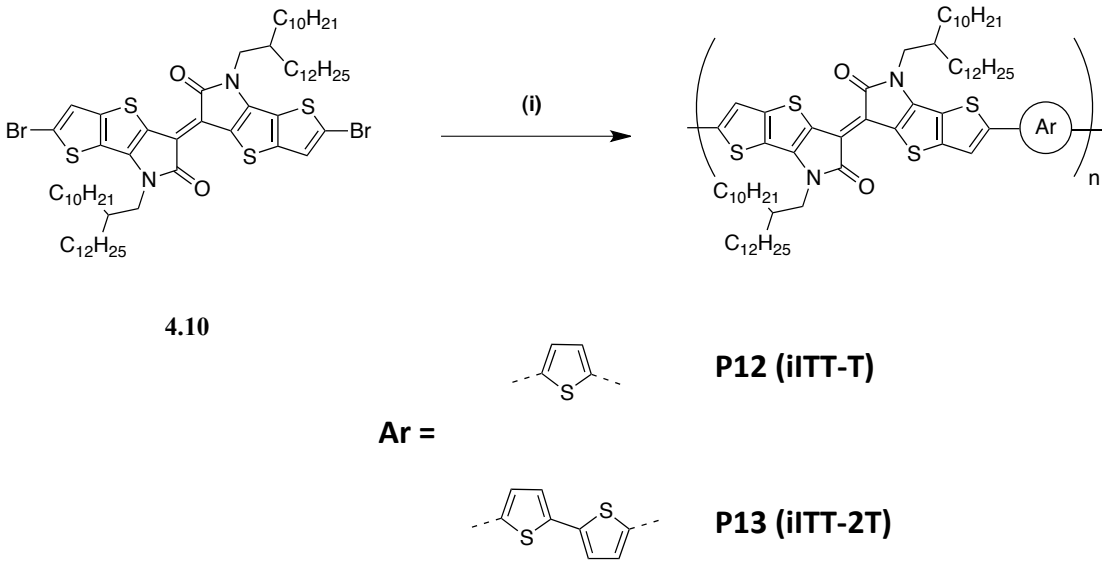

4.10

Figure 4.9. Synthesis of polymers **P12** (**iITT-T**) and **P13 (iITT-2T**) from **4.10** by palladium-catalysed Stille coupling. *Reagents and conditions:* **(i) P12** PhCl, $Pd_2(dba)_3$, P(*o*Tol)$_3$, 2,5-bis(trimethylstannyl)thiophene, µW **(ii) P13** PhCl, $Pd_2(dba)_3$, P(*o*Tol)$_3$, 5,5'-bis(trimethyl stannyl)-2,2'-bithiophene, µW.

Table 4.1. Physical properties of **iITT** polymers.

Polymer	M_n (kDa)[a]	M_w (kDa)[a]	PDI[a]	DP_n[a]
iITT-BT	17	27	1.6	14.3
iITT-T	30	67	2.3	26.3
iITT-2T	20	41	2.1	16.4

[a] Determined by M_n, M_w, PDI (M_w / M_n) and DP_n (M_n / M_0) determined by GPC at 80 ºC using low-PDI (<1.10) polystyrene standards and chlorobenzene as the eluent.

4.4. Optical properties of iITT polymers

The three newly synthesised polymers **iITT-BT**, **iITT-T** and **iITT-2T** can all be seen to have very broad, red-shifted UV-Vis absorption profiles that encroach into the near-IR region of the electromagnetic spectrum (**Figure 4.10**). The position of the individual spectra can be rationalised according to the choice of co-monomer unit in both solution and thin film with both the λ_{max} and λ_{onset} following the same trend (**Table 4.2**).

The BT containing co-polymer shows the most red-shifted absorption profile of the series with λ_{max} at 914 nm and 926 nm in solution and thin film respectively. The BT co-monomer is a strong acceptor unit due to its highly electron-withdrawing characteristics resulting in a significant stabilisation of both E_{HOMO} and E_{LUMO} by different amounts. In comparison, the choice of thiophene as a co-monomer gives less red-shifted absorption spectra with λ_{max} at 897 nm and 909 nm, in solution and thin film, due to the more electron-rich nature of the thiophene unit. Bi-thiophene as a co-monomer sees the lowest wavelength absorption profiles, λ_{max} in solution is 864 nm and 875 in the thin film, with the extra thiophene spacer resulting in a widened E_g.

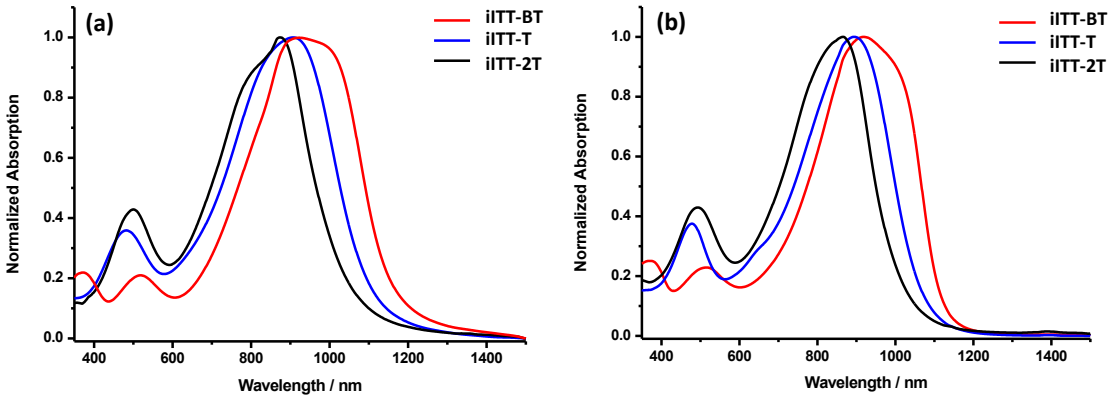

Figure 4.10. Room temperature normalised UV-Vis absorption profiles of **iITT** polymers **(a)** thin film spun on glass substrates from 5 mg / mL chlorobenzene solution and **(b)** in dilute chlorobenzene solution.

Table 4.2. Thin film and solution λ_{max} of **iITT** polymers.

Polymer	λ_{max} (nm)	
	Thin film[a]	Solution[b]
iITT-BT	926	914
iITT-T	909	897
iITT-2T	875	864

[a] thin film spun on glass substrates from 5 mg / mL chlorobenzene solution [b] dilute chlorobenzene solution.

As with previously characterised polymers E_{HOMO} values for the **iITT** polymer series were determined by PESA, E_g by the onset of absorption in the thin film and E_{LUMO} by the addition of estimated E_g to E_{HOMO} values. Due to its strong acceptor features BT demonstrated the deepest E_{HOMO} value of -4.9 eV as well as the deepest E_{LUMO} value of -3.9 eV which results in an extremely narrow estimated E_g of 1.05 eV. The more electron-rich thiophene co-monomer, with the less red-shifted absorption, sees both E_{HOMO} and E_{LUMO} raised in comparison to BT. E_{HOMO} is increased by 0.1 eV to -4.8 eV whilst E_{LUMO} is raised by a larger 0.2 eV to -3.7 eV giving a slightly wider E_g of 1.13 eV. Using a bi-thiophene co-monomer sees energy levels similar to the thiophene polymer with an E_{HOMO} of -4.8 eV and a slightly raised E_{LUMO} of -3.6 eV. This corresponds to a further E_g broadening with an estimated value of 1.19 eV matching the shorter wavelength absorption profile.

Table 4.3. Optical properties of **iITT** polymers.

Polymer	E_{HOMO} (eV)[a]	E_{LUMO} (eV)[b]	Eg (eV)[c]
iITT-BT	-4.9	-3.9	1.05
iITT-T	-4.8	-3.7	1.13
iITT-2T	-4.8	-3.6	1.19

[a] HOMO energies (E_{HOMO}) determined PESA [b] LUMO energiess (E_{LUMO}) estimated by addition of thin film absorption onset onto E_{HOMO} [c] Band gap (E_g) estimated as the difference between the experimentally determined E_{HOMO} and optically estimated E_{LUMO}.

4.5. DFT calculations

TD / DFT calculations have proved valuable throughout previous sections of this thesis in modelling the behaviour of newly synthesised polymer structures. Through comparing these calculations to experimental findings the predicted values have continually matched the experimentally determined trends and are essential when validating the conclusions that are made on a material's behaviour.

Again using TD / DFT calculations with a B3LYP / 6-31g* basis set the new **iITT** polymer series was computationally modelled. The predicted frontier molecular orbital energies were extracted and compared to the experimental values estimated using PESA and UV-Vis data. The comparison is shown in **Figure 4.11** and the predicted values presented in **Table 4.4**. For each of the three polymers the predicted E_{HOMO} and E_{LUMO} values can be seen to follow the same general trend as the observed values. In agreement with the PESA values, T and 2T containing polymers are shown to have the same E_{HOMO} values with the BT co-monomer resulting in a value that is 0.1 eV lower in energy. E_{LUMO} values also closely follow those estimated in **Table 4.3**, BT as a co-monomer is calculated to give a 0.2 eV E_{LUMO} reduction in comparison to T which in turn is calculated to be 0.1 eV less than 2T. With both frontier orbital energy levels being calculated to exhibit the same trend as the experimentally determined values, it follows that the trend in E_g values is also comparable with a broadening from the narrowest E_g co-polymer BT to the widest E_g co-polymer 2T again being observed.

Table 4.4. Calculated frontier molecular orbital energy levels and optical band gaps of **iITT** polymers.

Polymer	HOMO (eV)[a]	LUMO (eV)[a]	Eg (eV)[a]
iITT-BT	-4.7	-3.5	1.17
iITT-T	-4.6	-3.3	1.31
iITT-2T	-4.6	-3.2	1.33

[a] predicted using TD / DFT calculations with a B3LYP / 6-31g* basis set.

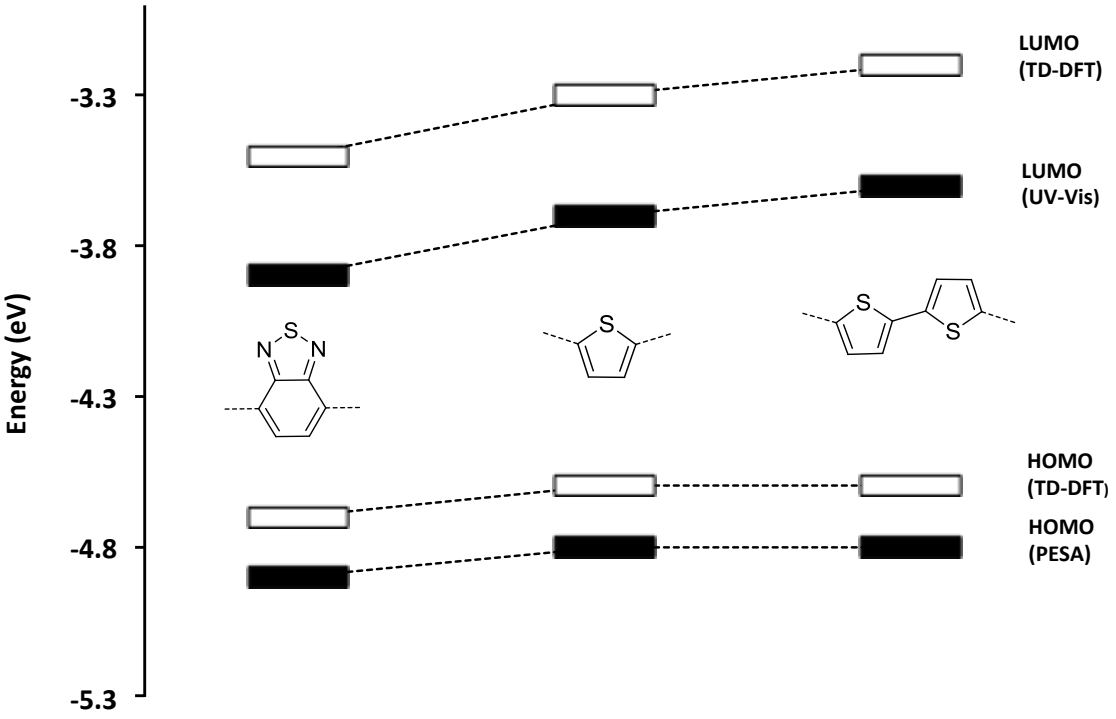

Figure 4.11. Comparison of experimentally determined and computationally predicted frontier molecular orbital energy levels of polymers **iITT** polymers.

The predicted backbone conformations are shown in **Figure 4.12** and the molecular orbital distributions shown in **Figure 4.13. iITT-BT** has a highly planar structure due to the coplanar nature of the benzothiadizole co-monomer whilst the thiophene and bi-thiophene co-monomers result in slightly decreased planarities with torsional angles between co-monomers of 5.2° for **iITT-T** and 7.6° for **iITT-2T**.

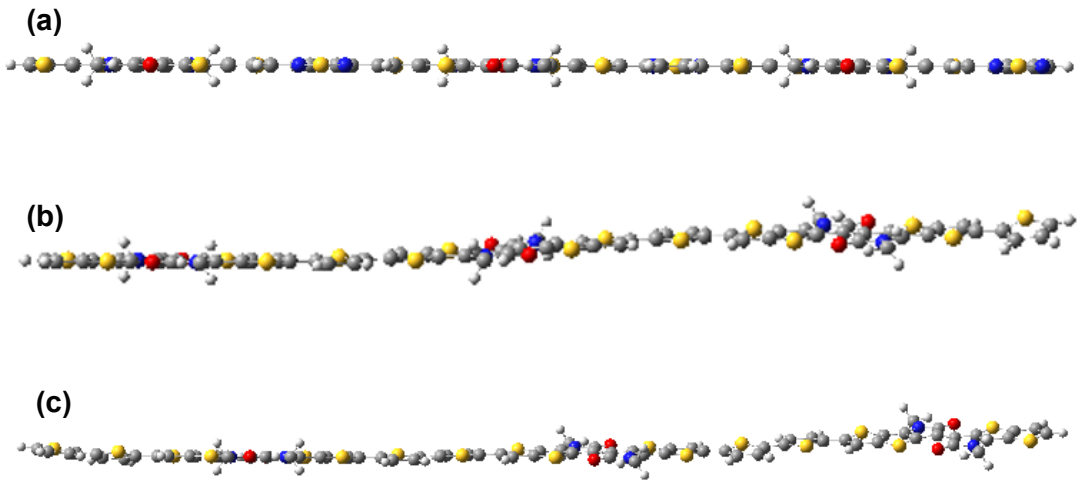

Figure 4.12. Computationally predicted backbone planarities of **iITT** polymers **(a) iITT-BT**, **(b) iITT-T** and **(c) iITT-2T**.

Whilst all three polymers show good delocalisation of molecular orbitals as a result of the highly fused structures, there is also an influence of co-monomer unit on the extent of HOMO and LUMO energy level distribution along the polymer chain. **iITT-BT** has a HOMO level that does not delocalise onto the electron-deficient thiadiazole unit compared to the LUMO level which has a large contribution from the co-monomer which is mirrored by a larger stabilisation of E_{LUMO} than E_{HOMO}. There is little difference between the delocalisation of orbitals for **iITT-T** and **iITT-2T** polymers with both structures demonstrating highly delocalised energy levels, which is desirable for effective charge transport pathways. There is however a slight difference in the long axis linearities with the **iITT-T** having a noticeable 'kink' in the backbone at the thiophene spacer whilst **iITT-2T** is completely linear as with the BT co-monomer unit.

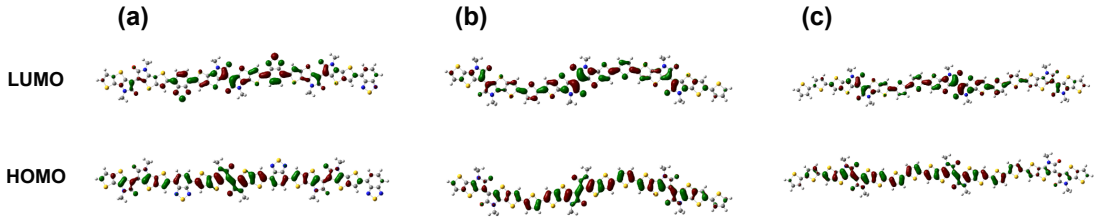

Figure 4.13. Computationally predicted long axis linearities of **iITT** polymers **(a) iITT-BT**, **(b) iITT-T** and **(c) iITT-2T**.

4.6. OFET device data

In Chapter One the mechanism for charge generation in OPV devices was discussed and it was highlighted that a sufficient energetic offset between donor and acceptor LUMOs is required to separate excitons into free charge carriers. The minimum energetic offset is often estimated to be around 0.3 eV and with PC[71]BM (E_{LUMO} = 3.9 eV) this would mean that the donor E_{LUMO} levels required should be greater in energy than those estimated for the **iITT** series (**Figure 4.14**). Consequently polymer / fullerene blends of **iITT** polymers and PC[71]BM are unlikely to have sufficient driving force for charge separation and therefore were not evaluated in OPV devices.[25,26]

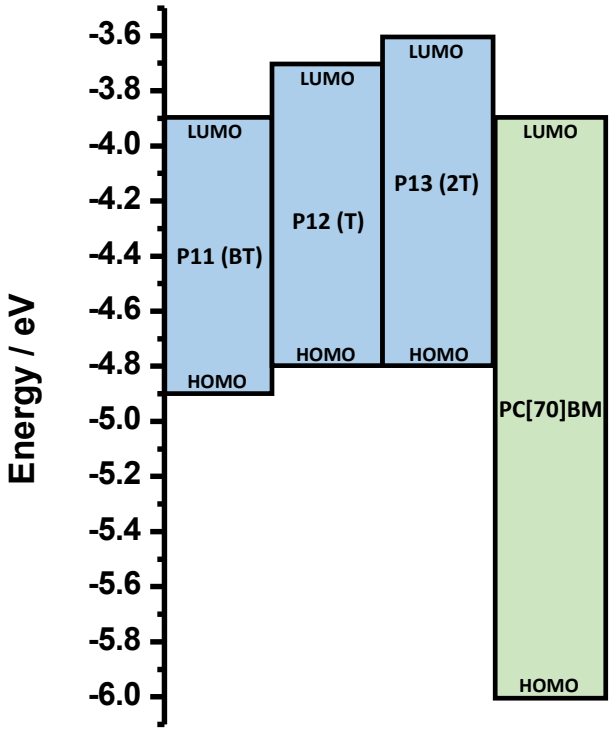

Figure 4.14. Frontier molecular orbital energy levels of **iITT** polymers compared to PC[71]BM demonstrating the insufficient energetic offset between donor and acceptor E_{LUMO} for OPV applications.

The material requirements of candidate polymer materials for thin film OFET applications were also discussed in Chapter One and the importance of polymer planarity and energy level alignment with electrodes were highlighted. By meeting these, and other requirements, the structures of the **iITT** co-polymer series has the

potential to deliver high performances. Thus, top gate / bottom contact devices were fabricated to evaluate the charge transfer characteristics of **iITT** co-polymers.

Typical transfer characteristics recorded at V_D = - 60 V for **iITT-BT**, **iITT-T** and **iITT-2T** are shown in **Figure 4.15** and the output characteristics are shown in **Figure 4.16**. The average charge carrier mobilities and threshold voltages determined from the square root of the saturation transfer curve are summarised in **Table 4.5**. Each device was annealed at 100 ºC, 200 ºC and 300 ºC for 1 hour in an inert atmosphere, as many previously reported isoindigo and **DPP** polymers have shown substantial morphological and mobility improvements upon annealing.[27,28] High temperature annealing conditions were possible as differential scanning calorimetry (DSC) (section **4.7**) shows that each of the polymers in the series showed no significant degradation or melting up to 300 ºC.

Each of the **iITT** polymers exhibits good ambipolar charge transport properties with significant improvements observed at elevated annealing temperatures. Interestingly the dominant transport mode changes with co-monomer unit allowing tuning of charge transport properties through structural variations. **iITT-BT** has higher electron mobilities, **iITT-T** shows equally balanced electron and hole mobilities and **iITT-2T** has higher hole than electron mobilities. The improvements observed with annealing are generally larger when annealing temperature is increased from 100 ºC to 200 ºC with only small further increases observed from 200 ºC to 300 ºC.

iITT-BT demonstrates the best overall performance with hole mobilities that show an increase from 0.1 cm^2 / Vs at 100 ºC to 0.3 cm^2 / Vs at 200 ºC and 0.4 cm^2 / Vs at 300 ºC and electron mobilities that are on the same order of magnitude which go from 0.2 cm^2 / Vs at 100 ºC to 0.5 cm^2 / Vs at 200 ºC and 0.7 cm^2 / Vs at 300 ºC. It was previously mentioned that polymers containing a benzothiadiazole co-monomer unit frequently exhibit higher electron mobilities. This is due to the LUMO stabilisation facilitating electron injection from the high work function electrode which is complimented by the highly planar backbone structure facilitating charge transfer through interchain hopping.[29]

Introduction of a thiophene co-monomer sees the disappearance of the superior electron mobilities to be replaced by mobilities that are generally balanced for holes and electrons. At 100 ºC devices show fairly low hole and electron mobilities with

both giving values of 0.01 cm^2 / Vs, these values are largely increased by approximately two orders of magnitude when the annealing temperature is increased to 200 ºC with electron and hole mobilities of 0.2 cm^2 / Vs and this is unchanged when the annealing temperature is further increased to 300 ºC. Bi-thiophene in **iITT-2T** results in devices with dominant hole transport and again there are large improvements between 100 ºC and 200 ºC / 300 ºC with maximum hole and electron mobilities of 0.4 cm^2 / Vs and 0.1 cm^2 / Vs respectively. These observed charge carrier mobility improvements at elevated annealing temperatures are in agreement with similar effects that have been observed in recent **DPP** polymer structures.[30,31]

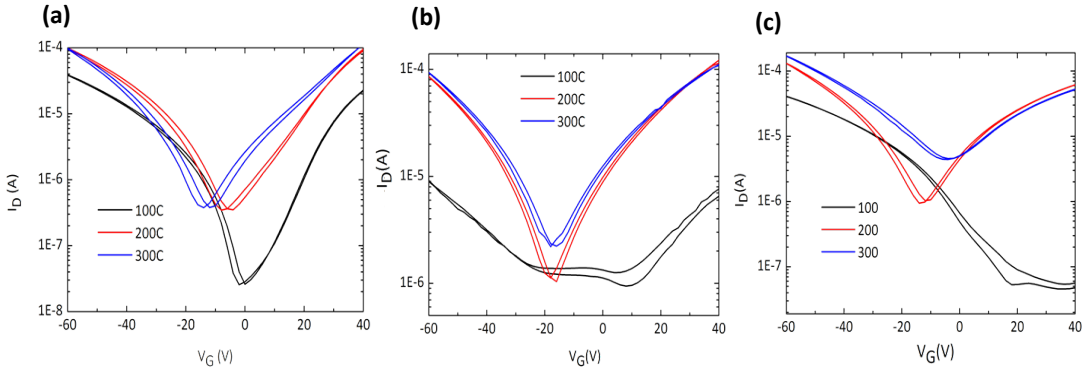

Figure 4.15. Transfer characteristics of top gate / bottom contact OFET devices (L = 20 µm, W = 1 mm) with polymers **(a) iITT-BT (b) iITT-T** and **(c) iITT-2T** as the semiconducting channel. Devices were annealed at different temperatures and measured at V_D = -60 V.

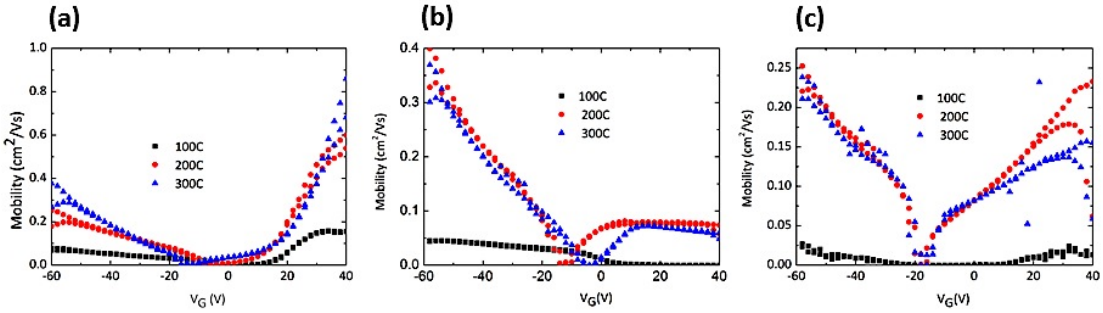

Figure 4.16. Output curves of top gate / bottom contact OFET devices (L = 20 µm, W = 1 mm) with polymers **(a) iITT-BT (b) iITT-T** and **(c) iITT-2T** as the semiconducting channel annealed at 100 ºC, 200 ºC and 300 ºC.

Table 4.5. Thin film OFET device characteristics of **iITT** polymers.

Polymer	T_{anneal} (ºC)[a]	μ_e (cm^2 / Vs)[b]	μ_h (cm^2 / Vs)[b]	V_{th} (electrons) (V)[b]	V_{th} (holes) (V)[b]
iITT-BT	100	0.2	0.1	14	-10
	200	0.5	0.3	12	-13
	300	0.7	0.4	13	-20
iITT-T	100	0.01	0.01	7	-32
	200	0.2	0.2	-18	-24
	300	0.2	0.2	-24	-22
iITT-2T	100	-	0.01	n/a	3
	200	0.1	0.4	-18	-25
	300	0.1	0.4	-11	-21

[a] Annealed for 1 h in an inert atmosphere [b] Average values determined from the square root of the saturation transfer curve.

4.7. Morphology

OFET mobilities of the new **iITT** polymers were observed to increase largely with high temperature annealing with increases by up to two orders of magnitude observed in some cases. To determine the origin of these large improvements, pristine polymer films spin coated using the same solvent systems and spin speeds and annealed at 100 ºC, 200 ºC and 300 ºC, were probed using out of plane x-ray diffraction (XRD) scattering and atomic force microscopy (AFM) shown in **Figure 4.17** and **4.18** respectively.

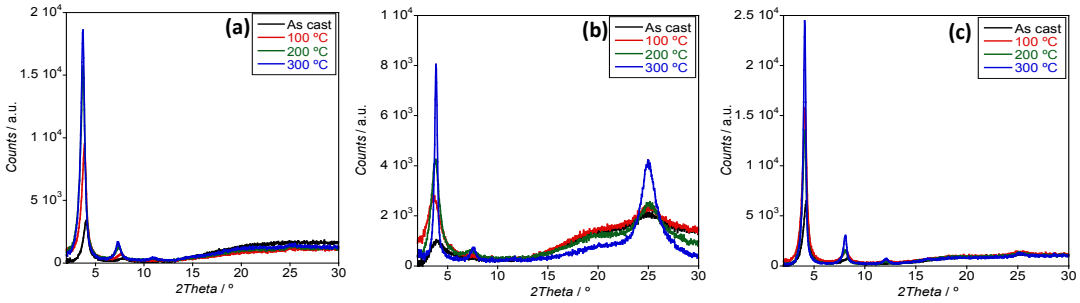

Figure 4.17. Out of plane XRD diffractograms of polymers **(a) iITT-BT (b) iITT-T (c) iITT-2T** drop cast on Si wafers using the same solvent systems and concentrations as used in OFET device fabrication.

For each of the three polymers there is a large increase in polymer crystallinity observed with progression to higher annealing temperatures, which matches the increased charge carrier mobilities observed in section **4.6**. There is a strong first order (100) lamellar stacking peak $2\theta = 4.1^{\circ}$ in all three polymers indicative of a significant number of polymer chains adopting an edge-on orientation relative to the substrate plane. There is also a second order (200) reflection at $2\theta = 8.2^{\circ}$ that is present in all three films but has greater intensity with **iITT-BT** and **iITT-2T** and both of these (100) and (200) peaks show similar increases with high temperature annealing. A small third order peak (300) can be seen at $2\theta = 13.3^{\circ}$ at higher annealing temperatures with the two most crystalline systems **iITT-BT** and **iITT-2T**. These (100), (200) and (300) peaks correspond to lamellar stacking distances of approximately 21.5 Å and their reduced intensities in **iITT-T** is married with the appearance of a broad π - π stacking peak at $2\theta = 25.0^{\circ}$ that corresponds to a stacking distance of 3.6 Å.

The broader peak that is present in **iITT-T** also shows increased intensity with annealing and suggests an observably different orientation of polymer chains indicating the presence of strong π - π stacking in the film that is often characteristic of a significant amount of polymer chains that have a face-on orientation to the substrate. Such an enhancement in face-on orientation with the introduction of a thiophene spacer is in agreement with previous studies on similar **DPP** polymers.[32] An observation can be made that the two **iITT-BT** and **iITT-2T** polymers with no face-on contribution both show highly linear long-axis linearities whilst **iITT-T** with a significant face-on contribution demonstrates a non-linear kinked / s-shaped conformation. It is possible that this contributes towards the manner in which the polymer chains orientate themselves relative to the substrate plane, although a more thorough investigation into the relationship between long axis linearities and backbone orientation would be required to develop this beyond an observation.

The breadth of a diffraction peak is known to be inversely proportional to crystallite size which can be approximated using the Full Width Half Maximum (FWHM) of the diffraction peaks using the Scherrer equation.[33] The values obtained cannot be considered to be highly accurate due to the number of assumptions made in the equation, such as uniformity of crystallite shapes, however when comparing diffractions from different structures it can be useful for the approximate estimation

of relative crystallite sizes or coherence lengths. Considering signals when an annealing temperature of 300 ºC is used, the sharpest (100) lamellar stacking peak can be seen for **iITT-2T**, which corresponds to the largest approximate crystallite size of around 30 nm. Next largest is **iITT-BT** which has a calculated approximate crystal size of 20 nm whilst the broadest peak is seen for **iITT-T** with comparatively small crystal sizes of around 6 nm. The crystal sizes from using a thiophene spacer are therefore significantly smaller which is likely a result of the variation of polymer backbone orientation relative to the substrate plane with a mixture of edge-on and face-on orientated polymers preventing the formation of larger crystallite structures.

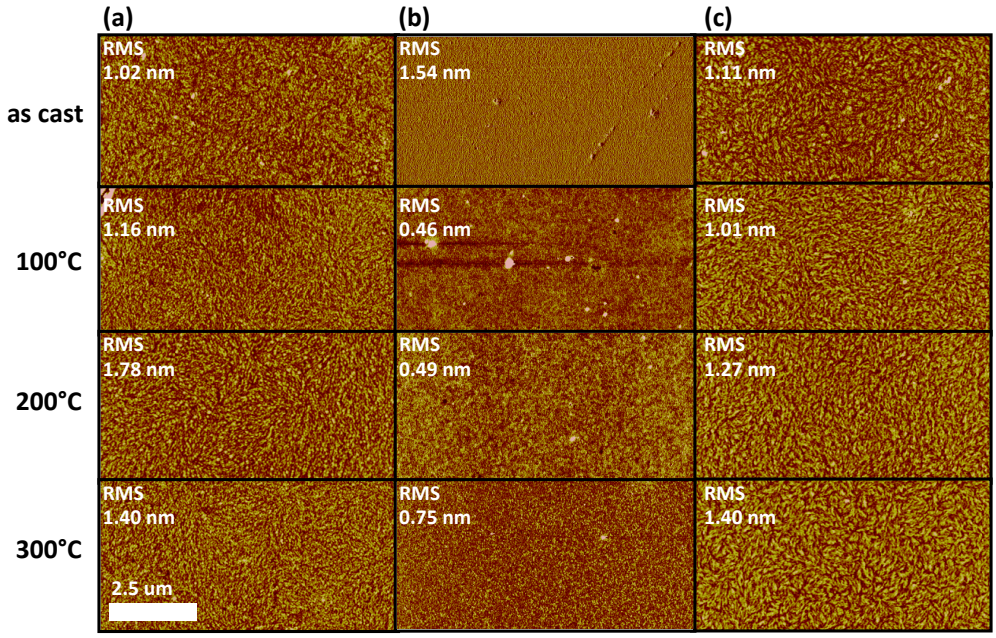

Figure 4.18. AFM phase images of polymers **(a) iITT-BT (b) iITT-T** and **(c) iITT-2T** spin coated on glass substrates using the same solvent systems and concentrations as used in OFET device fabrication.

The AFM images of the three polymers across the range of increasing annealing temperatures shown in **Figure 4.18** do not show a discernable change in surface morphology / roughness as the films progress to higher annealing temperatures. Both **iITT-BT** and **iITT-2T** show very similar surface roughness with little change at higher temperatures. In comparison **iITT-T** gives a slightly smoother, less fibrillar polymer film that shows a more pronounced change with annealing to a coarser polymer film. Whilst it is always difficult to strongly relate the surface of polymer films observed by AFM to their bulk behaviour as a solid, it is possible that this

change in film microsctructure is a result of the change in chain orientation observed by XRD with the appearance of a strong π - π stacking peak at high temperatures.

When treating polymers to device processing conditions in which high temperatures are used it is important to have confidence that such temperatures are not causing polymer degradation or melting. These effects would result in significant changes to the bulk material, which would mean that any observations made at these elevated temperatures are not necessarily an accurate representation of a particular polymer's physical and structural properties. There are many thermochemical techniques that can be used to evaluate any changes that occur with increased temperatures of which Differential scanning calorimetry (DSC) is one of the more versatile. Phase transitions and material degradation have associated enthalpic changes that are exo- or endo-thermic in nature. By heating a material and a reference pan in parallel and monitoring the comparative heat flow, any changes in the material relative to the empty reference pan with heating can be detected as changes in heat flow and depending on their magnitude and direction can be assigned to a specific phase transition such as alkyl chain melt, polymer melt, glass transition temperature and crystallisation.

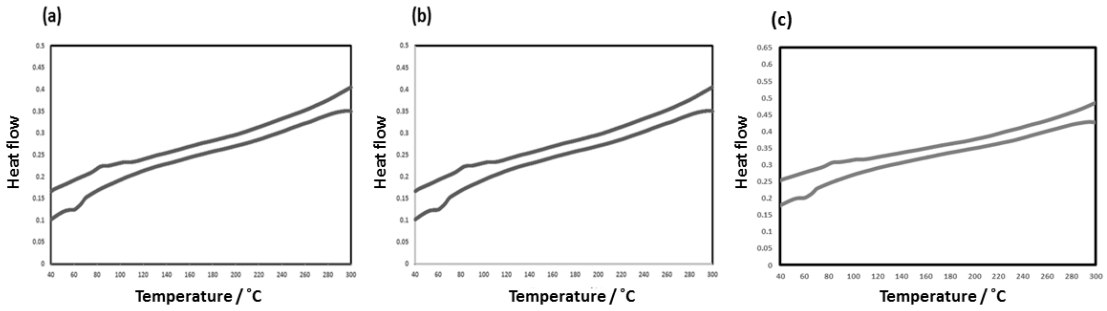

Figure 4.19. DSC scans of **iITT** polymers **(a) iITT-BT**, **(b) iITT-T** and **(c) iITT-2T** heated from 0 – 300 ºC with a heating rate of 10º / min.

Figure 4.19 shows the DSC traces of the three new **iITT** polymers. Excluding the instrumental artefacts below 100 ºC present for each material, the traces can be seen to be largely featureless. Considering the previously discussed crystallinity observable by XRD diffractograms, these featureless DSC scans are clearly not indicative of amorphous materials. It can be inferred however that there is no observable melting of the materials or significant polymer / impurity degradation occurring at the high

temperatures used for device annealing providing extra validity for the device performances and physical characterisations carried out at 100 ºC, 200 ºC and 300 ºC.

4.8. Photothermal deflection spectroscopy

Photothermal deflection spectroscopy (PDS) is a highly sensitive surface averaged absorption technique that has recently been applied to the characterisation of conjugated polymers.[34] It can be used effectively to investigate the energetic disorder of a polymer material which can be related to charge transport properties observed and in turn complement the observations on structural disorder made by XRD.

The technique is performed on pristine polymer films, which have been annealed at 200 ºC and exploits the heating effect observed in a sample upon the absorption of monochromatic light. This heating effect is due to photoexcitation creating a thermal gradient in front of the sample's surface and is enhanced using a surrounding inert liquid. The heating results in a refractive index gradient through which a continuous wave laser is passed that skims the sample's surface. The presence of the refractive index gradient at the sample's surface deflects the laser beam from its original path, which is detected using a quadrant detector connected to a lock-in amplifier. The amount of deflection of the laser beam is proportional to the amount of light that is absorbed and is recorded as a function of excitation wavelength and by scanning through different wavelengths the complete absorption spectra is obtained.

Through measurement of the absorption tail in the extended region below the band edge, where absorption decreases exponentially with energy, Urbach energies of the different materials can be extracted from the sharpness of this absorption tail as a measure of the energetic disorder in the polymer films. PDS measurements were performed on pristine polymers films annealed at 200 ºC, with an in-built experimental error of 5 meV. Urbach energies of 44 meV for BT, 49 meV for T and 55 meV for 2T were obtained for the **iITT** series and can be seen to correspond to materials with similar degrees of energetic disorder (**Figure 4.20**). These values are comparable to other well-known highly crystalline polymer systems such as **PBTTT** which demonstrate similar Urbach energies and charge carrier mobilities.[19,35] Within

the error range, the extracted Urbach energies can be considered to be in good agreement with the trend in mobility reported across the polymer series in **Table 4.5**.

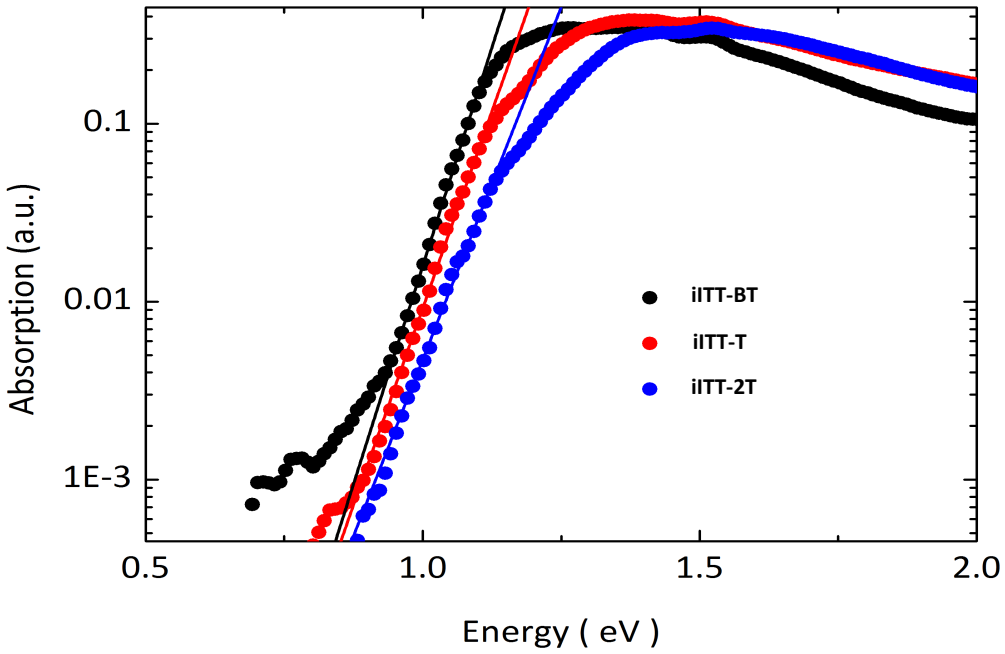

Figure 4.20. Normalized photothermal deflection spectroscopy (PDS) spectra of **iITT** polymers. Fits used for the extraction of the Urbach energy are shown as solid lines.

4.9. iIP-BT / iIT-BT / iITT-BT comparison.

To further examine the relative properties and behaviour of the new **iITT** polymer series, it was of interest to draw comparisons with existing di-phenyl (**iIP**) and di-thienyl (**iIT**) flanked structures. Taking the best performing BT co-polymer in the series, the frontier molecular orbitals and backbone confirmations were modelled using TD / DFT calculations with a B3LYP / 6-31g* basis set for **iIP-BT**, **iIT-BT** and **iITT-BT** co-polymers. The new **iITT** properties and the literature **iIP** / **iIT** properties are compared to evaluate the influence of flanking unit variation.

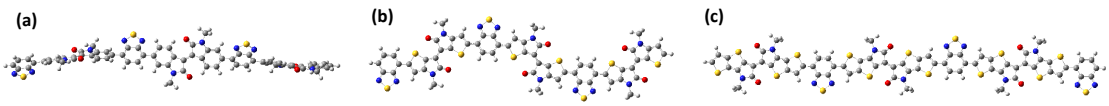

Figure 4.21. Computationally predicted long axis linearities of **iITT** polymers **(a) iIP-BT (b) iIT-BT (c) iITT-BT (P11)**.

Figure 4.21 shows the calculated long-axis linearities of the three isoindigo polymers. Transitioning from a phenyl to thiophene and the newly synthesised thieno[3,2-*b*]thiophene based structure shows a remarkable variation in the backbone arrangements. **iIP** shows a highly twisted, almost helical structure due to the steric clash between the phenyl and BT protons. The torsional angle arising due to this clash is calculated to be around 37º and the resultant disruption in conjugation is likely to be a significant contributor to the relatively high predicted and observed E_g values. **iIT** on the other hand sees a disappearance of this steric clash with a long-axis linearity that appears in plane whilst demonstrating a fairly non-linear 's' type confirmation along the length of the molecule. Moving to **iITT** sees the 's' type kinks in the backbone disappear due to the introduction of the highly fused thieno[3,2-*b*]thiophene unit which is likely to be favourable for the overlap of π-orbitals along the backbone.

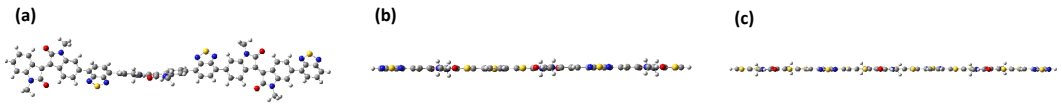

Figure 4.22. Computationally predicted edge-on backbone confirmations of **iITT** polymers **(a) iIP-BT (b) iIT-BT (c) iITT-BT (P11)**.

The edge-on polymer backbone planarities can be seen in **Figure 4.22** and **iIP** again can be seen to be highly twisted which is likely to be unfavourable for interactions, such as D / A contacts between polymer chains preventing the formation of ordered polymer channels essential for charge transport pathways. Additionally the twisting is highly detrimental for the conjugation along the chain which gives reduced π orbital overlap and impedes the transport of holes and electrons to the electrodes. It can be seen in **(b)** and **(c)** the extent of the planarising effect arising from the introduction of thiophene and thieno[3,2-*b*]thiophene units with both polymers demonstrating almost completely planar backbones. This is known to be advantageous for the close stacking of polymers resulting in highly ordered films favourable for interchain hopping charge transport.[36]

Figure 4.23 shows the calculated frontier molecular orbital and optical band gap energies of the three different isoindigo polymers and the molecular orbital backbone distributions are also given. The predicted and literature values are tabulated in **Table**

4.6 along with the reported hole and electron mobilities. It is worth noting when drawing comparisons between the new structure and literature results that there are of course variations between the device fabrication and processing conditions. For example the reported mobilities are extracted from bottom gate / top contact devices annealed at 150 ºC for the **iIP** polymer whilst the **iIT** and **iITT** values are from top gate / bottom contact devices devices annealed at 300 ºC. Therefore a comparison between the three polymers can not be taken as absolute.

It can be seen that the E_{HOMO}'s of **iIP-BT**, at -5.7 eV and -5.4 eV for the observed and calculated values, are dramatically lower than that of **iIT-BT** (-4.8 eV and -4.6 eV) and **iITT-BT** (-4.9 and -4.7 eV) which is a consequence of the reduced electron density of the phenyl ring relative to the other units which combined with the electron-withdrawing nature of the BT co-monomer has a significant stabilising effect. The other two more electron-rich flanking units are raised in energy with an E_{HOMO} value of -4.8 eV and -4.7 eV for thiophene and -4.9 eV and -4.7 eV for thieno[3,2-*b*]thiophene. Interestingly **iITT** is stabilised relative to **iIT** which is in contrast to the same comparison between **DPPT** and **DPPTT** which shows a raised E_{HOMO} for **DPPTT**.[37]

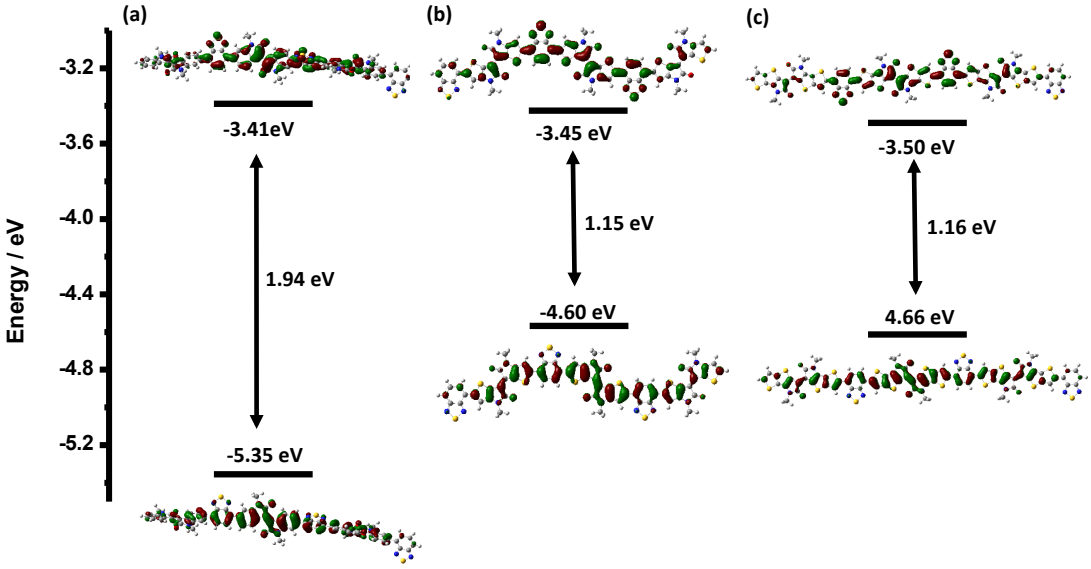

Figure 4.23. Computationally predicted frontier molecular orbital energy levels and optical band gaps of **iITT** polymers **(a) iIP-BT (b) iIT-BT (c) iITT-BT**.

The three predicted E_{LUMO} values also show similar trends with a stabilisation from the more electron-rich unit from a predicted -3.41 eV with **iIP-BT** to -3.45 eV with

iIT-BT and -3.50 eV with **iITT-BT**. A similar trend is observed experimentally with thiophene and thieno[3,2-*b*]thiophene having greater quinoidal contribution due to their reduced aromaticity compared to the phenyl unit whilst the E_{LUMO} of **iITT-BT** is further stabilised due to its extended π-system. The band gaps reflect these energetic changes, as well as being influenced by the varying degrees of conformational planarity, with **iIP-BT** showing a significantly wider band gap than the other two. Whilst **iIT-BT** and the new **iITT-BT** are predicted to have the same optical band gap, experimentally **iIT-BT** shows the narrower E_g with a value of 0.9 eV compared to 1.1 eV for **iITT-BT**.

The mobilities of each polymer are shown in **Table 4.6** with **iIP-BT** showing good electron transport of 0.2 cm^2 / Vs, but no hole transport is observed which is possibly a result of the twisting of the polymer backbone resulting in polymer films that have significantly lower reported crystallinity. **iIT** and **iITT** structure motifs show much greater crystallinity in the polymer films with a large broad π – π stacking peak in **iIT** reported. This disappears in the **iITT-BT** polymer film which instead shows an order of magnitude increase in the intensity of the lamellar (100) peak in going from **iIT** to **iITT** and the appearance of a significantly sized (200) peak. This is indicative of a much more crystalline polymer film as well as a changing preference of polymer chain orientation from face on to edge on which supports the findings that a large portion of edge on orientated chains in **iITT** polymers is preferential for high charge transport mobilities. These highly crystalline films in **iITT-BT** compared to **iIT-BT** are matched by a doubling of hole mobility to 0.4 cm^2 / Vs and a seven-fold increase in electron mobility to 0.7 cm^2 / Vs. The small E_{LUMO} stabilisation across the series does not correspond to an overall linear increase in electron mobilities, which indicates that the observed improvements are likely to be influenced more by increases in crystallinity than by improved charge injection to polymer LUMO levels.

Table 4.6. Observed and computationally predicted frontier molecular orbital's and charge carrier mobilities of literature **iIP-BT**, **iIT-BT** compared to the newly reported **iITT-BT (P11)**.

Polymer	E_{HOMO} (eV)		E_{LUMO} (eV)		Eg (eV)		μ_h (cm^2 / Vs)	μ_e (cm^2 / Vs)
	Obs.	Calc.[a]	Obs.	Calc.[a]	Obs.	Calc.[a]		
iIP-BT[b]	-5.7	-5.4	-3.5	-3.4	2.1	1.9	-	0.2[b]
iIT-BT[c]	-4.8	-4.6	-3.9	-3.5	0.9	1.2	0.2[c]	0.1[c]
iITT-BT	-4.9	-4.7	-3.8	-3.5	1.1	1.2	0.4[e]	0.7[e]

[a] TD / DFT calculations using a B3LYP / 6-31g* basis set [b] bottom gate / top contact devices annealed at 150 ºC reported by *C. Yang et al.*[38] [c] top gate / bottom contact devices annealed at 300 ºC reported by *R. Ashraf et al.*[13] [e] top gate / bottom contact devices annealed at 300 ºC.

4.10. Conclusion and outlook

The design and synthesis of a new thieno[3,2-*b*]thiophene containing isoindigo unit (**iITT**) is reported via a multi-step synthesis analogous to the previously reported thienyl-isoindigo synthesis. This is the first reported synthesis of a conjugated fused six ring isoindigo system where the extention of the fused ring system serves to enhance molecular orbital delocalistaion. Once synthesised, the **iITT** moiety was co-polymerised by palladium-catalysed Stille and Suzuki coupling polymerisations with benzothiadiazole, thiophene and bi-thiophene to afford a series of three new semiconducting conjugated polymers with optical band gaps as narrow as 1.05 eV in the case of **iITT-BT**.

Each of the polymers in the series were shown to be good ambipolar materials when used in thin film OFET devices. These polymers were stable to temperatures as high as 300 ˚C and showed significant improvements in charge carrier mobilities as these elevated temperatures with hole mobilities as high as 0.4 cm^2 / Vs and electron mobilities as high as 0.7 cm^2 / Vs. The three polymers were found to be planar, highly crystalline systems by XRD and PDS analysis with the mobility improvements at high temperatures being matched by a significant enhancement in this crystallinity as shown by XRD.

A computational and literature study of the new **iITT-BT** co-polymer compared with previously reported **iIP-BT** and **iIT-BT** co-polymers showed **iIT-BT** and **iITT-BT** to

have similar energy levels and narrow band gaps in comparison to **iIP-BT**. Comparison of OFET mobilities showed the new **iITT-BT** to have the highest hole and electron mobilities of the three structures thus identifying the new **iITT** motif to be one of the most promising isoindigo structures for OFET applications reported to date.

Further expoloration of co-monomer structures and device architectures would be desirable to establish a more comprehensive understanding of the structure's potential whilst combining the new alkyl branching point design principle to this new isoindigo structure would likely yield improved device performances. It is also likely that these narrow bandgap polymers would perform well in tandem solar cell devices if used in combination with a wide bandgap polymer that has a complimentary absorption profile.

4.11. References

1. E. Steingruber, *Ullmann's Encyclopedia of Industrial Chemistry*, 2000.
2. E. D. Głowacki, G. Voss, L. Leonat, M. Irimia-Vladu, S. Bauer and N. S. Sariciftci, *Isr. J. Chem.*, 2012, **52**, 540–551.
3. M. Irimia-Vladu, E. D. Głowacki, P. A. Troshin, G. Schwabegger, L. Leonat, D. K. Susarova, O. Krystal, M. Ullah, Y. Kanbur, M. A. Bodea, V. F. Razumov, H. Sitter, S. Bauer and N. S. Sariciftci, *Adv. Mater.*, 2012, **24**, 375–380.
4. I. V Klimovich, L. I. Leshanskaya, S. I. Troyanov, D. V Anokhin, D. V Novikov, A. A. Piryazev, D. A. Ivanov, N. N. Dremova and P. A. Troshin, *J. Mater. Chem. C*, 2014, **2**, 7621-7631.
5. L. A. Estrada, R. Stalder, K. A. Abboud, C. Risko, J.-L. Brédas and J. R. Reynolds, *Macromolecules*, 2013, **46**, 8832–8844.
6. C. Papageorgiou and X. Borer, *Helv. Chim. Acta*, 1988, **71**, 1079–1083.
7. J. Mei, K. R. Graham, R. Stalder and J. R. Reynolds, *Org. Lett.*, 2010, **12**, 660–663.
8. K. R. Graham, P. M. Wieruszewski, R. Stalder, M. J. Hartel, J. Mei, F. So and J. R. Reynolds, *Adv. Funct. Mater.*, 2012, **22**, 4801–4813.
9. T. Lei, J.-H. Dou, Z.-J. Ma, C.-H. Yao, C.-J. Liu, J.-Y. Wang and J. Pei, *J. Am. Chem. Soc.*, 2012, **134**, 20025–20028.
10. J. Mei, D. H. Kim, A. L. Ayzner, M. F. Toney and Z. Bao, *J. Am. Chem. Soc.*, 2011, **133**, 20130–20133.
11. T. Lei, J.-H. Dou, Z.-J. Ma, C.-J. Liu, J.-Y. Wang and J. Pei, *Chem. Sci.*, 2013, **4**, 2447–2452.
12. R. Stalder, J. Mei, J. Subbiah, C. Grand, L. A. Estrada, F. So and J. R. Reynolds, *Macromolecules*, 2011, **44**, 6303–6310.
13. R. S. Ashraf, A. J. Kronemeijer, D. I. James, H. Sirringhaus and I. McCulloch, *Chem. Commun.*, 2012, **48**, 3939–3941.
14. G. W. P. Van Pruissen, F. Gholamrezaie, M. M. Wienk and R. A. J. Janssen, *J. Mater. Chem.*, 2012, **22**, 20387–20393.
15. Y. Koizumi, M. Ide, A. Saeki, C. Vijayakumar, B. Balan, M. Kawamoto and S. Seki, *Polym. Chem.*, 2013, **4**, 484–494.

16. T. Lei, Y. Cao, X. Zhou, Y. Peng, J. Bian and J. Pei, *Chem. Mater.*, 2012, **24**, 1762–1770.
17. E. Wang, W. Mammo and M. R. Andersson, *Adv. Mater.*, 2014, **26**, 1801–1826.
18. R. Stalder, J. Mei, K. R. Graham, L. A. Estrada and J. R. Reynolds, *Chem. Mater.*, 2013, **26**, 664–678.
19. I. McCulloch, M. Heeney, C. Bailey, K. Genevicius, I. MacDonald, M. Shkunov, D. Sparrowe, S. Tierney, R. Wagner, W. Zhang, M. L. Chabinyc, R. J. Kline, M. D. McGehee and M. F. Toney, *Nat. Mater.*, 2006, **5**, 328–333.
20. Z. Chen, M. J. Lee, R. Shahid Ashraf, Y. Gu, S. Albert-Seifried, M. Meedom Nielsen, B. Schroeder, T. D. Anthopoulos, M. Heeney, I. McCulloch and H. Sirringhaus, *Adv. Mater.*, 2012, **24**, 647–52.
21. O. Mitsunobu and M. Yamada, *Bull. Chem. Soc. Jpn.*, 1967, **40**, 2380–2382.
22. H. Loibner and E. Zbiral, *Helv. Chim. Acta*, 1976, **59**, 2100–2113.
23. G. Kim, A.-R. Han, H. R. Lee, J. H. Oh and C. Yang, *Phys. Chem. Chem. Phys.*, 2014, ASAP, DOI: 10.1039/C4CP01787K.
24. A. Facchetti, *Chem. Mater.*, 2010, **23**, 733–758.
25. A. B. Tamayo, X.-D. Dang, B. Walker, J. Seo, T. Kent and T.-Q. Nguyen, *Appl. Phys. Lett.*, 2009, **94**, 103301.
26. J.-L. Brédas, D. Beljonne, V. Coropceanu, and J. Cornil, *Chem. Rev.*, 2004, **104**, 4971–5004.
27. J. Shin, H. A. Um, D. H. Lee, T. W. Lee, M. J. Cho and D. H. Choi, *Polym. Chem.*, 2013, **4**, 5688–5695.
28. J. Fan, J. D. Yuen, M. Wang, J. Seifter, J.-H. Seo, A. R. Mohebbi, D. Zakhidov, A. Heeger and F. Wudl, *Adv. Mater.*, 2012, **24**, 2186–2190.
29. J. Smith, R. Hamilton, I. McCulloch, N. Stingelin-Stutzmann, M. Heeney, D. D. C. Bradley and T. D. Anthopoulos, *J. Mater. Chem.*, 2010, **20**, 2562–2574.
30. Y. Li, S. P. Singh and P. Sonar, *Adv. Mater.*, 2010, **22**, 4862–4866.
31. P. Sonar, S. P. Singh, Y. Li, M. S. Soh and A. Dodabalapur, *Adv. Mater.*, 2010, **22**, 5409.
32. X. Zhang, L. J. Richter, D. M. DeLongchamp, R. J. Kline, M. R. Hammond, I. McCulloch, M. Heeney, R. S. Ashraf, J. N. Smith, T. D. Anthopoulos, B. Schroeder, Y. H. Geerts, D. A. Fischer and M. F. Toney, *J. Am. Chem. Soc.*, 2011, **133**, 15073–15084.
33. U. Zhokhavets, T. Erb, H. Hoppe, G. Gobsch and N. S. Sariciftci, *Thin Solid Films*, 2006, **496**, 679–682.
34. L. Goris, K. Haenen, M. Nesládek, P. Wagner, D. Vanderzande, L. De Schepper, J. D'haen, L. Lutsen and J. V Manca, *J. Mater. Sci.*, 2005, **40**, 1413–1418.
35. A. J. Kronemeijer, V. Pecunia, D. Venkateshvaran, M. Nikolka, A. Sadhanala, J. Moriarty, M. Szumilo and H. Sirringhaus, *Adv. Mater.*, 2014, **26**, 728–733.
36. H. Bronstein, Z. Chen, R. S. Ashraf, W. Zhang, J. Du, J. R. Durrant, P. S. Tuladhar, K. Song, S. E. Watkins, Y. Geerts, M. M. Wienk, R. A. J. Janssen, T. Anthopoulos, H. Sirringhaus, M. Heeney and I. McCulloch, *J. Am. Chem. Soc.*, 2011, **133**, 3272–3275.
37. C. B. Nielsen, M. Turbiez, and I. McCulloch, *Adv. Mater.*, 2012, **25**, 1859-1880.
38. G. Kim, A.-R. Han, H. R. Lee, J. Lee, J. H. Oh and C. Yang, *Chem. Commun.*, 2014, **50**, 2180–2183.

Chapter Five

Experimental

5.1. General Experimental

The following chemicals were prepared as stock laboratory co-monomers by Dr. Bob Schroeder according to literature procedures; 2,5-bis(trimethylstannyl)thiophene, 2,5-bis(trimethylstannyl)selenophene, 2,5-bis(trimethylstannyl)tellurophene, 4,7-bis(4,4,5,5-tetramethyl-1,3,2-dioxaborolan-2-yl)benzothiadiazole, 5,5'-bis(trimethylstannyl)-2,2'-bithiophene, 1,4-di(4,4,5,5-tetramethyl-1,3-dioxaboralane)benzene.[1-5]

Polymer **DPPTT-T** (***C1***) used for comparison in Chapter Three was provided by Dr. Hugo Bronstein.[6]

All reagents and solvents were purchased from Sigma Aldrich, VWR, Apollo Scientific or TCI and were used without any further purification. Dry solvents for anhydrous reactions were purchased from Sigma Aldrich and no further attempt at drying them was made. All reactions were carried out under an inert Argon atmosphere unless otherwise stated. ^{1}H NMR and ^{13}C NMR spectra were recorded on a BRUKER 400 spectrometer in $CDCl_3$ solution at 25 ºC unless otherwise stated. Electrospray mass spectrometry was performed with a Thermo Electron Corporation DSQII mass spectrometer. Number-average (M_n) and weight-average (M_w) molecular weights were determined with an Agilent Technologies 1200 series GPC in chlorobenzene at 80 °C using two PL mixed B columns in series and calibrated against narrow PDI (< 1.10) polystyrene standards. A customer build Shimadzu recSEC system was used to fractionate polymers in Chapter Two, the system comprises a DGU-20A3 degasser, an LC-20A pump, a CTO-20A column oven, an Agilent PLgel 10μm MIXED-D column and a SPD-20A UV detector. UV-Vis absorption spectra were recorded on a UV-1601 Shimadzu UV-Vis spectrometer. Column chromatography was carried out on silica gel (for flash chromatography, VWR), thin layer chromatography (TLC) was performed on Merck aluminium-backed plates pre-coated with silica (0.2 mm, 60 F254). Microwave experiments were performed in a Biotage initiator v.2.3. Photo Electron Spectroscopy in Air (PESA) measurements were recorded with a Riken Keiki AC-2 PESA spectrometer with a power setting of 5 nW and a power number of 0.5. Thin films for PESA and UV-Vis were prepared by spin-coating a solution of the sample on glass substrates from chlorobenzene at a concentration of 5 mg / mL unless otherwise stated. DSC experiments were carried out with a TA Instruments DSC Q20 under nitrogen

atmosphere.

Atomic force microscopy (AFM) was carried out using a Dimension 3100 atomic force microscope in close contact (tapping, 2 x 2μm) mode. Specular X-ray diffraction (XRD) was carried out using a PANalytical X'Pert PRO MRD diffractometer equipped with a nickel-filtered Cu-Kα1 beam and X'Celerator detector, using current I = 40 mA and accelerating voltage U = 40 kV. Two-dimensional grazing incidence X-ray diffraction (2D GIXD) in Chapter Three was performed at the Stanford Synchrotron Radiation Laboratory (SSRL) at beam line 11-3. Diffraction patterns are collected using an incident beam of 12.7 keV, with a grazing angle of 0.1°, and are expressed as a function of scattering vector $q=4\pi\sin(\theta)/\lambda$ where θ is the scattering angle and λ is the x-ray wavelength. Q_{xy} is the component of the scattering vector parallel to the substrate plane and q_z is the component perpendicular to the substrate plane.

BHJ solar cells were fabricated with a conventional or inverted device configuration. Conventional; (ITO/PEDOT:PSS/polymer:PC[71]BM/LiF/Al), inverted; (ITO/ZnO/ Polymer:PC[71]BM/MoO_3/Ag). Devices were tested under simulated 100 mW / cm^2 AM1.5G illumination. Devices were in all cases prepared with a polymer : PC[71]BM blend ratio of 1 : 2 and solution processed from a chloroform : *ortho*-dichlorobenzene (4 : 1) solvent mixture. The external quantum efficiency (EQE) was used to correct the current density *vs* voltage data before extracting values. Tandem solar cell devices were fabrication under the same conditions as single junction devices with the extra layers deposited as follows; Ph neutral PEDOT from water/IPA solution, ZnO nanoparticles from IPA solution. Both active layers were spin coated from polymer : fullerene (1 : 2) solutions in dichlorobenzene.

OFET device values reported are average values taken from multiple devices. Top gate / bottom contact devices in Chapter Two; all film preparation steps were carried out under an inert atmosphere. The 2 $Å^{-2}$ cm glass slides were cleaned in a DECON90 deionized (DI) water solution in an ultrasonic bath twice for 10 min and then rinsed with DI water. To help with the adhesion of the gold on the glass substrate, 5 nm of aluminum was evaporated prior to the evaporation of 25 nm of gold. Polymeric chlorobenzene solution and substrates were heated to processing temperature followed by spin-coating for 10 s at 500 rpm followed by 30 − 60 s at 2000 rpm. The

films were then dried at 100 °C for 5 min. A perfluorinated polymer (commercial name CYTOP from Ashani Glass) was used as gate dielectric and applied via spin-coating for 60 s at 2000 rpm and cured at 100 °C for 90 min. 50 nm aluminum was evaporated on top of the dielectric as a gate electrode. Bottom Gate / bottom contact devices in Chapter Two; Photolithographicly prepatterned bottom gate bottom contact (200 nm SiO2 over Si+) substrates with gold electrodes were used. Substrates were cleaned in an ultrasonic bath (acetone 10 min and isopropanol 10 min). The devices were spun from the same solution concentrations and processing parameters as described for top gate devices. Bottom gate / top contact OFET devices in Chapter Three; thin films were fabricated on heavily doped silicon wafers, with thermally grown 200 nm SiO_2 as a gate dielectric. The substrate was treated with an octadecyltrichlorosilane (OTS) self-assembled monolayer after a 20 minute UV-ozone treatment. The active layer was deposited by spin-coating the polymers from 1,2-dichlorobenzene in a 0.5 wt % solution. 60 nm of gold was evaporated as a top contact. Channel lengths varied from 0.7 to 1.5 mm and channel widths from 40 to 200 um. All transistor measurements were performed in vacuum, and mobility was evaluated in the saturation regime at +/-60V. Samples were brought into air before the vacuum measurement.

Top-gate / bottom contact OFET devices in Chapter Four; polymer films were fabricated on glass substrates with Ti/Au (10 nm / 30 nm) evaporated on photo-lithographically defined electrodes. The iITT- polymers were deposited by spin coating from a 10 mg / mL dichlorobenzene (DCB) solution and were annealed for 1 h at 100 ºC, 200 ºC or 300 ºC, respectively. After annealing, the films were quenched on a cold metal surface and a 300 nm thick PMMA dielectric layer was spin-coated on top. A 20 nm thick gold layer was then evaporated through a shadow mask to define the transistor's top-gate. After fabrication the FETs were measured using an Agilent 4155B Semiconductor Parameter Analyser (SPA). To guarantee reproducibility, all fabrication steps as well as the measurement were performed in an N_2 glove box.

Photothermal deflection spectroscopy (PDS) measurements were performed on films prepared on quartz substrates, under identical conditions. PDS is a highly sensitive surface averaged absorption measurement technique that makes use of the heating effect on the sample upon absorption of monochromatic light, which creates a thermal

gradient in front of the sample surface. An inert liquid (Fluorinert FC-72, 3M Corporation) surrounding the sample enhances this thermal gradient. This gradient further results in a refractive index gradient through which a continuos wave laser is passed, skimming the sample surface. Deflection of the laser was detected using a quadrant detector connected to a lock-in amplifier (Stanford Resarch SR830). The amount of deflection of the laser beam, which is proportional to the amount of light absorbed is recorded as a function of the monochromatic excitation wavelength and by scanning through different wavelengths the complete absorption spectrum is obtained

5.2. Compounds synthesised in Chapter Two

Thieno[3,2-*b*]thiophene-2-carboxaldehyde 2.1

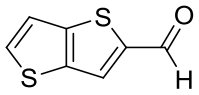

2.5 M *n*BuLi in hexanes (15.69 mL, 39.22 mmol) was added dropwise to a stirring solution of thieno[3,2-*b*]thiophene (5.00 g, 35.66 mmol) in anhydrous THF (40 mL) at -78 ºC. After stirring for 30 minutes at -78 ºC DMF (4 mL, 51.88 mmol) was added dropwise and the resultant solution stirred for a further 30 minutes. Upon warming to room temperature the reaction was quenched with sat. NH_4Cl (aq) and the organic material extracted into Et_2O. The combined organic layers were dried over $MgSO_4$ and concentrated by rotary evaporation to afford the title compound thieno[3,2-*b*]thiophene-2-carbaldehyde (4.19 g, 24.91 mmol, 69.78 %) as a brown solid which was used without further purification. ^{1}H NMR (400 MHz, $CDCl_3$): δ 10.00 (s, 1H), 7.98 (s, 1H,), 7.73 (d, J = 5.4 Hz, 1H), 7.36 (d, J = 5.3 Hz, 1H). ^{13}C NMR (100 MHz, $CDCl_3$): δ 183.6, 144.6, 137.9, 133.9, 129.1, 122.9, 120.2. m/z (EI^+) 168 (M^+).

Thieno[3,2-*b*]thiophene-2-carbonitrile 2.2

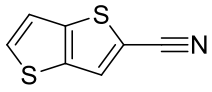

I_2 (12.5 g, 49.25 mmol) was added to a solution of stirring thieno[3,2-*b*]thiophene carbaldehyde **2.1** (5.56 g, 33.05 mmol) in ammonia water (50 mL, 28 % solution) acetonitrile (200 mL) and THF (50 mL) at 10 ºC and the solution was warmed to room temperature overnight with stirring. TLC (hexanes : chloroform, 1 : 3) was used to confirm no starting material remained and any excess I_2 was quenched with sat. Na_2SO_3 (aq) (50 mL). The organic material was extracted into Et_2O, dried over $MgSO_4$, and concentrated by rotary evaporation to afford the title compound as an off-white solid which was used without further purification (4.74 g, 28.69 mmol, 86.81 %). ^{1}H NMR (400 MHz, $CDCl_3$): δ 7.83 (d, *J* = 0.6, 1H), 7.74 (d, *J* = 5.3, 1H), 7.33 (dd, *J* = 5.3 0.6, 1H). ^{13}C NMR (100 MHz, $CDCl_3$): δ 143.4, 138.3, 133.6, 129.7, 119.4, 114.6, 110.2. m/z (EI^+) 165 (M^+).

3,6-di(thieno[3,2-*b*]thiophen-2-yl)pyrrolo[3,4-*c*]pyrrole-1,4(2*H*,5*H*)-dione 2.3

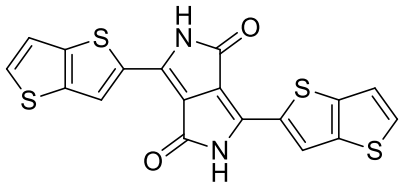

Sodium (1.08 g, 47.2 mmol) and iron (III) chloride (~40 mg) was added to 30 mL of 2-methyl-2-butanol and the mixture was heated with stirring to reflux for 2 hours until the sodium was fully consumed. Upon cooling to 85 ºC thieno[3,2-*b*]thiophene-2-carbonitrile **2.2** (5.17 g, 31.33 mmol) was added followed by a diluted solution of diisopropyl succinate (2.51 g, 12.41 mmol) in methanol (10 mL). After stirring at 120 ºC for 2 hours, the reaction was cooled to 50 ºC before the addition of methanol (50 mL) and subsequent quenching with aqueous acetic acid (20 mL). The resultant suspension was filtered under vacuum and washed with water (2 x 100 mL), methanol (2 x 100 mL), acetone (2 x 100 mL) and hexane (2 x 50 mL) to afford the title compound as an insoluble black solid which was used without further purification (4.70 g, 11.41 mmol, 91.04 %).

2-decyl-1-tetradecyl bromide 2.4

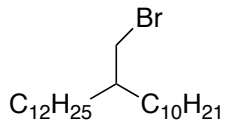

NBS (37.64g, 211 mmol) was added portion-wise to a stirring solution of 2-decyl-1-tetradecanol (50 g, 140.98 mmol) and PPh_3 (48.07 g, 183.28 mmol) in DCM (350 mL) at 0 °C. The solution was stirred warmed to room temperature over 2 hours, quenched with sat. $Na_2S_2O_3$ (aq) (50 mL), extracted into Et_2O and the combined organic phases were dried over $MgSO_4$ and concentrated by rotary evaporation. The crude product was purified by a short silica column (hexane) and subsequent concentration by rotary evaporation afforded the title compound as a colourless oil (53.57 g, 128.30 mmol, 91 %). ^{1}H NMR (400 MHz, $CDCl_3$): δ 3.47 (d, *J* = 4.6 Hz, 2H), 1.62 (m, 1H), 1.30 (bm, 40H), 0.92 (t, *J* = 6.8 Hz, 6H). ^{13}C NMR (100 MHz, $CDCl_3$) δ 39.5, 32.6, 32.0, 29.8, 29.7, 29.6, 29.4, 26.6, 22.7, 14.1. m/z (EI^+) 338 $(M\text{-}Br)^+$.

2,5-Bis(2-decyl-1-tetradecyl)-3,6-di(thieno-[3,2-*b*]thiophen-2-yl)pyrrole[3,4-*c*]pyrrole 1,4(2*H*,5*H*)-dione 2.5

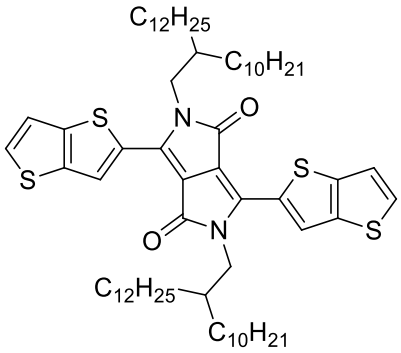

2-decyl-1-tetradecyl bromide **2.4** (16.85 g, 40.36 mmol) was added to a solution of 3,6-di(thieno[3,2-*b*]thiophen-2-yl)pyrrole[3,4-*c*]pyrrole-1,4(2*H*,5*H*)-dione **2.3** (5.00 g, 12.12 mmol), K_2CO_3 (5.58 g, 40.36 mmol), and 18-crown-6 (~40 mg) in dry DMF (150 mL). The solution was heated with stirring at 120 °C for 18 hours and subsequently cooled to room temperature. Solvent was removed by rotary evaporation to afford the crude product which was purified by column chromatography (hexanes :

chloroform, 3 : 1) to afford the title compound as a dark purple solid (4.61 g, 4.24 mmol, 35 %). ^{1}H NMR (400 MHz, $CDCl_3$): δ 9.32 (s, 2H), 7.63 (d, J = 5.2 Hz, 2H), 7.35 (d, J = 5.1 Hz, 2H), 4.10 (d, J = 7.8 Hz, 4H), 1.98 (m, 2H), 1.40−1.20 (m, 80H), 0.92−0.86 (m, 12H). ^{13}C NMR (100 MHz, $CDCl_3$): δ 140.6, 140.3, 132.0, 131.2, 127.6, 119.3, 108.4, 46.6, 37.9, 32.0, 31.2, 30.1, 29.7, 29.7, 29.6, 29.4, 26.2, 22.7, 14.1. m/z calculated for $C_{66}H_{104}N_2O_2S_4$ (M^+) 1084.7, 1085.7, 1086.7, 1086.7; found 1084.8, 1085.8, 1086.8, 1087.8.

3,6-Bis(2-bromothieno[3,2-*b*]thiophen-5-yl)-2,5-bis(2-decyl-1-tetradecyl)pyrrolo[3,4-*c*]pyrrole-1,4(2*H*,5*H*)-dione 2.6

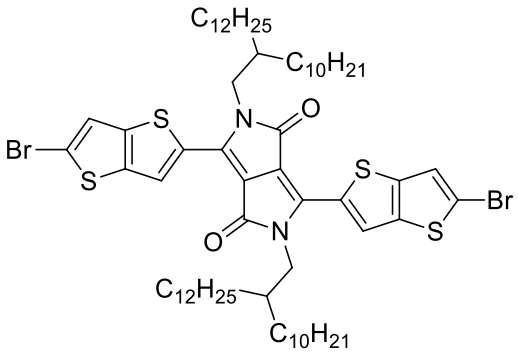

To a stirring solution of 2,5-bis(2-dodecyl-1-tetradecyl)-3,6-di(thieno[3,2-*b*]-thiophen-2-yl)pyrrole[3,4-*c*]pyrrole-1,4(2*H*,5*H*)-dione (2.00 g, 1.84 mmol) in chloroform (50 mL) was added a solution of bromine (0.59 g, 3.68 mmol) in chloroform (5 mL) dropwise. The solution was refluxed for 2 h and then cooled to 0 °C before quenching with saturated $Na_2S_2O_3$ (aq) (50 mL). The organic layer was separated, dried over $MgSO_4$, and concentrated by rotary evaporation to afford the crude product which was purified by column chromatography using (hexanes : chloroform, 3 : 1) to give the title compound as a dark purple/blue solid (1.56 g, 1.25 mmol, 68 %). ^{1}H NMR (400 MHz, $CDCl_3$): δ 9.24 (s, 2H), 7.35 (s, 2H), 4.07 (d, J = 7.7 Hz, 4H), 1.57 (s, 2H) 1.35 - 1.15 (m, 80H), 0.91 - 0.87 (m, 12H, CH_3). ^{13}C NMR (100 MHz, $CDCl_3$): δ 161.5, 142.0, 140.4, 140.2, 130.5, 126.8, 122.1, 119.0, 108.4, 46.6, 37.9, 32.0, 31.2, 30.1, 29.8, 29.7, 29.7, 29.6, 29.4, 26.3, 22.7, 14.2. m/z calculated for $C_{66}H_{102}Br_2N_2O_2S_4$ (M^+) 1242.5, 1243.5, 1244.5; found 1242.6, 1243.6, 1244.6.

$C_{10}C_{12}$DPPTT-T (P1)

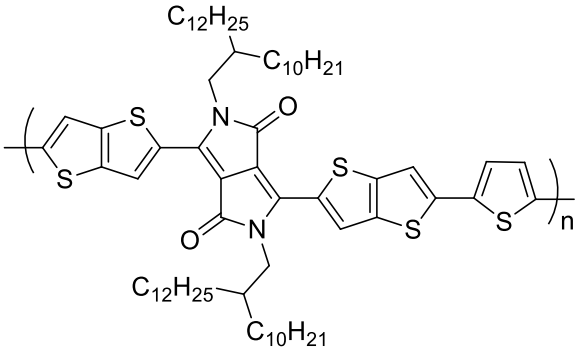

To a microwave vial was added 3,6-bis(2-bromothieno[3,2-*b*]thiophen-5-yl)-2,5-bis(2 dodecyl-1-tetradecyl)pyrrolo[3,4-*c*]pyrrole-1,4(2*H*,5*H*)-dione **2.6** (0.24 g, 0.19 mmol) and 2,5-bis(trimethylstannyl)thiophene (0.08 g, 0.19 mmol) in chlorobenzene (1.7 mL). The solution was degassed before the addition of $Pd_2(dba)_3$ (4 mg) and P(*o*Tol)$_3$ (5 mg). Following further degassing the microwave vial was sealed and the reaction mixture was heated in a microwave in successive intervals of 5 min at 100 °C, 5 min at 140 °C, 5 min at 160 °C, 10 min at 180 °C, and finally 20 min at 200 °C. After cooling to room temperature the reaction mixture was poured into vigorously stirred methanol, and the resulting polymeric precipitate filtered. The polymeric precipitate was purified by Soxhlet extraction first in acetone (24 h), hexane (24 h), chloroform (24 h), and finally chlorobenzene (24 h). The chlorobenzene fraction was concentrated by rotary evaporation, suspended in methanol, and filtered to afford the title polymer as a dark green solid (92 mg, 42 %).

GPC (chlorobenzene): M_n = 148 kDa, M_w = 385 kDa, PDI = 2.6.

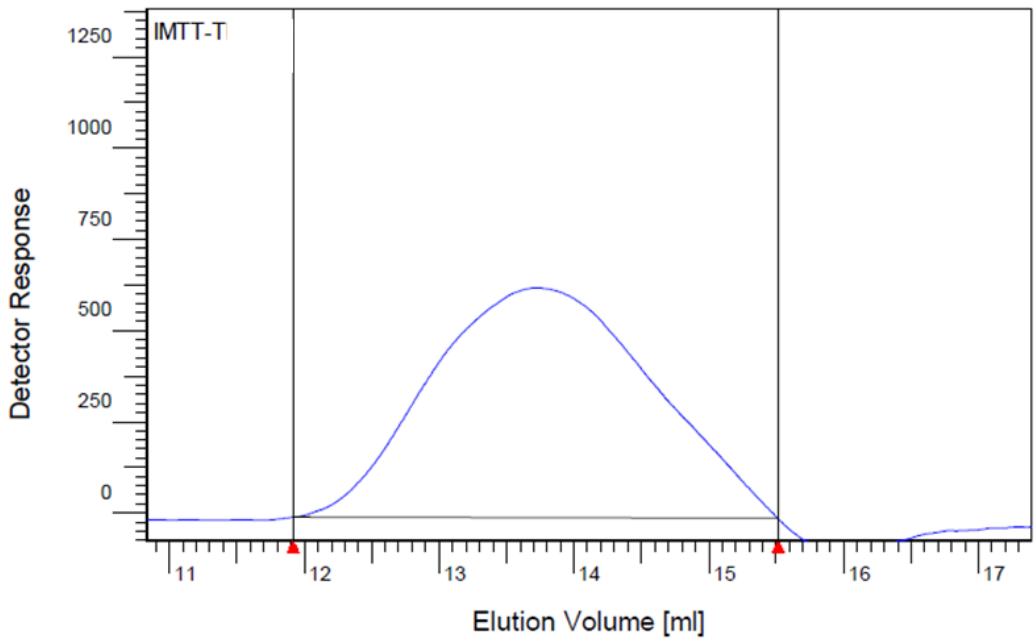

Figure 5.1. GPC trace of polymer **P1** in chlorobenzene at 80 °C.

$C_{10}C_{12}$DPPTT-TT (P2)

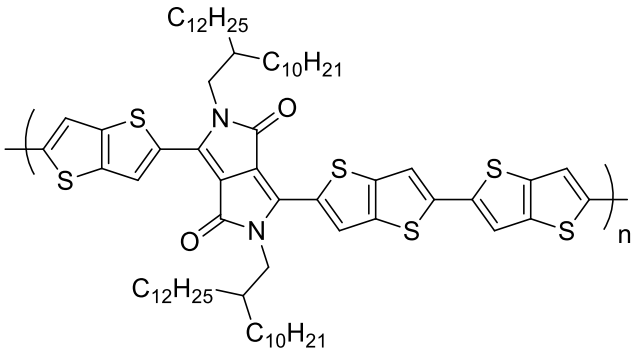

To a microwave vial was added 3,6-bis(2-bromothieno[3,2-*b*]thiophen-5-yl)-2,5-bis(2-dodecyl-1-tetradecyl)-pyrrolo[3,4-*c*]pyrrole-1,4(2*H*,5*H*)-dione **2.6** (0.19 g, 0.15 mmol) and 2,5-bis(trimethylstannyl)thieno[3,2-*b*]thiophene (0.07 g, 0.15 mmol) in chlorobenzene (1.7 mL). The solution was degassed before the addition of $Pd_2(dba)_3$ (4 mg) and P(*o*Tol)$_3$ (5 mg). Following further degassing the vial was sealed, and the reaction mixture was heated in a microwave in successive intervals of 5 min at 100 °C, 5 min at 140 °C, 5 min at 160 °C, 10 min at 180 °C, and finally 20 min at 200 °C. After cooling to room temperature, the reaction mixture was poured into vigorously stirring methanol and the polymeric precipitate was filtered. The filtrate was purified

by Soxhlet extraction first in acetone (24 h), hexane (24 h), chloroform (24 h), and finally chlorobenzene (24 h). The chlorobenzene fraction was concentrated by rotary evaporation, suspended in methanol, and filtered to afford the title polymer as a dark green solid (105 mg, 61 %).

GPC (chlorobenzene): M_n = 100 kDa, M_w = 280 kDa, PDI = 2.8.

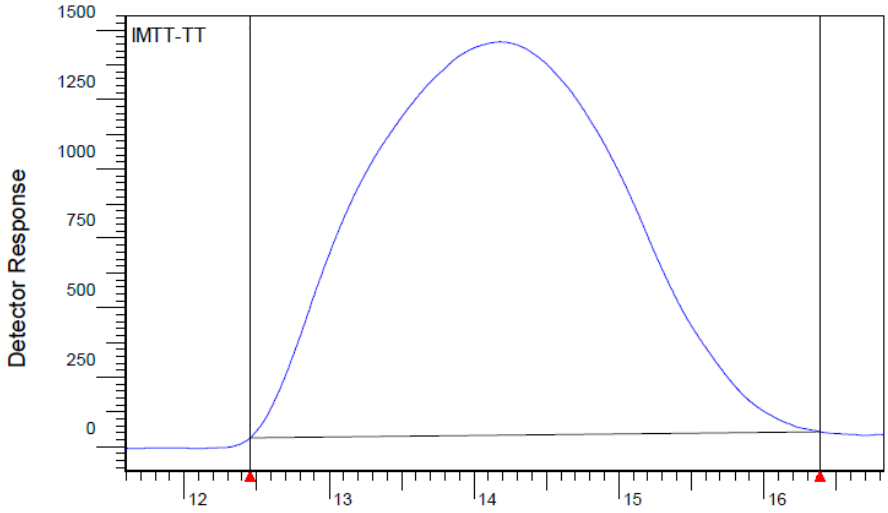

Figure 5.2. GPC trace of **P2** in chlorobenzene at 80 °C.

$C_{10}C_{12}$DPPTT-BT (P3)

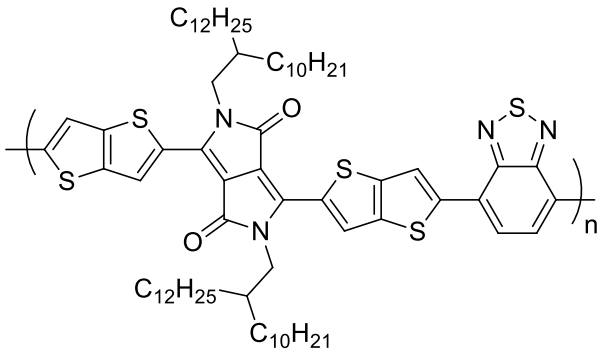

To a microwave vial was added 3,6-bis(2-bromothieno[3,2-*b*]thiophen-5-yl)-2,5-bis(2-dodecyl-1-tetradecyl)-pyrrolo[3,4-*c*]pyrrole-1,4(2*H*,5*H*)-dione **2.6** (0.18 g, 0.14 mmol) and 4,7-bis(4,4,5,5-tetramethyl-1,3,2-dioxabrolan-2-yl)-benzothiadiazole (0.06 g, 0.14 mmol) followed by a thoroughly degassed solution of Aliquat 336 (2 drops) in toluene (6 mL). The solution mixture was further degassed with stirring for 30 min

before $Pd(PPh_3)_4$ (15 mg) was added which was again degassed for a further 30 min. 2 M K_2CO_3 (aq) (2 mL) was added, and the microwave vial was sealed and heated with vigorous stirring at 120 °C for 3 days. After cooling to room temperature the reaction mixture was poured into vigorously stirred methanol, and the resulting polymeric precipitate was filtered. The filtrate was purified by Soxhlet extraction first in acetone (24 h), hexane (24 h), chloroform (24 h), and finally chlorobenzene (24 h) to afford the title polymer as a dark green / blue solid (45 mg, 26 %).

GPC (chlorobenzene): M_n = 50 kDa, M_w = 78 kDa, PDI = 1.5.

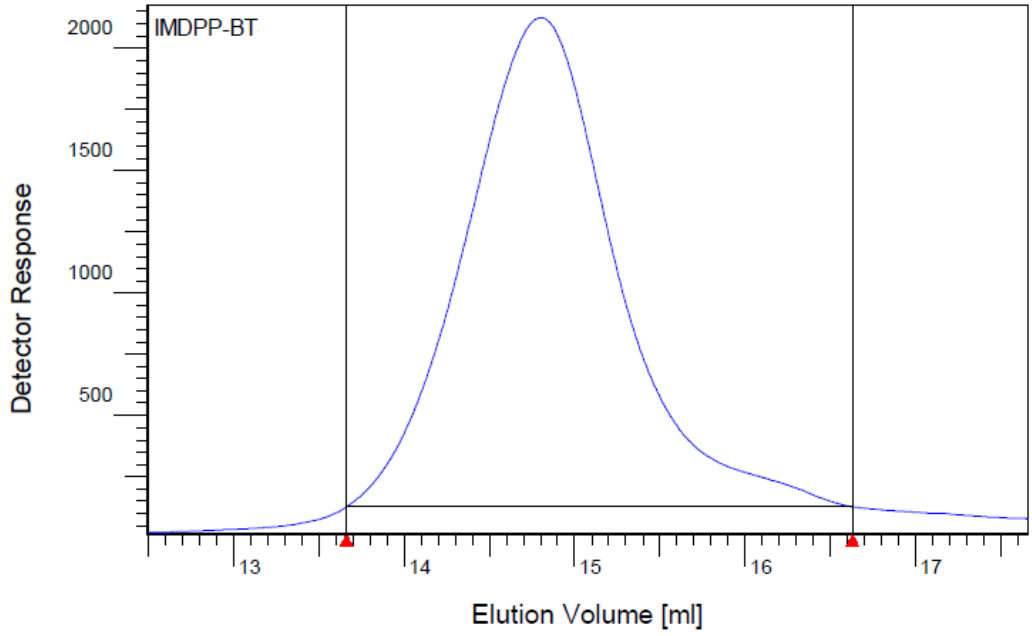

Figure 5.3. GPC trace of polymer **P3** in chlorobenzene at 80 °C.

$C_{10}C_{12}$DPPTT-P (P4)

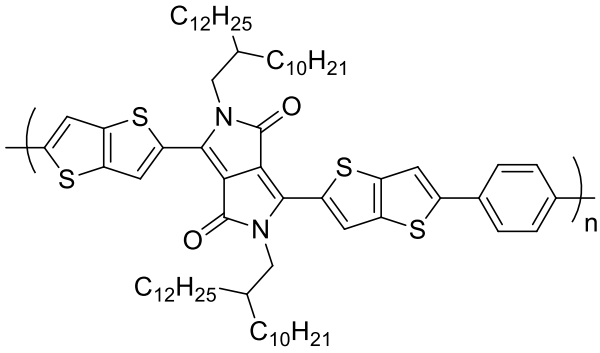

To a microwave vial was added 3,6-bis(2-bromothieno[3,2-*b*]thiophen-5-yl)-2,5-bis(2-dodecyl-1-tetradecyl)-pyrrolo[3,4-*c*]pyrrole-1,4(2*H*,5*H*)-dione **2.6** (0.17 g, 0.14 mmol) and 1,4-di(4,4,5,5-tetramethyl-1,3-dioxaboralane)benzene (0.046 mg, 0.139 mmol) followed by a thoroughly degassed solution of Aliquat 336 (2 drops) in toluene (6 mL). The solution was further degassed with stirring for 30 minutes before the addition of $Pd_2(dba)_3$ (10 mg) and PPh_3 (7 mg) followed by degassing for a further 30 minutes. K_3PO_4 (221 mg) in water (0.5 mL) was added, and the vial was sealed and heated for 3 days at 120 °C with vigorous stirring. After cooling to room temperature the reaction mixture was poured into vigorously stirring methanol, and the resulting polymeric precipitate was filtered. The filtrate was purified by Soxhlet extraction first in acetone (24 h), hexane (24 h), chloroform (24 h), and finally chlorobenzene (24 h). The chlorobenzene fraction was concentrated by rotary evaporation, suspended in methanol, and filtered to afford the title polymer as a dark green solid (68 mg, 42 %).

GPC (chlorobenzene): M_n = 23 kDa, M_w = 42 kDa, PDI = 1.8.

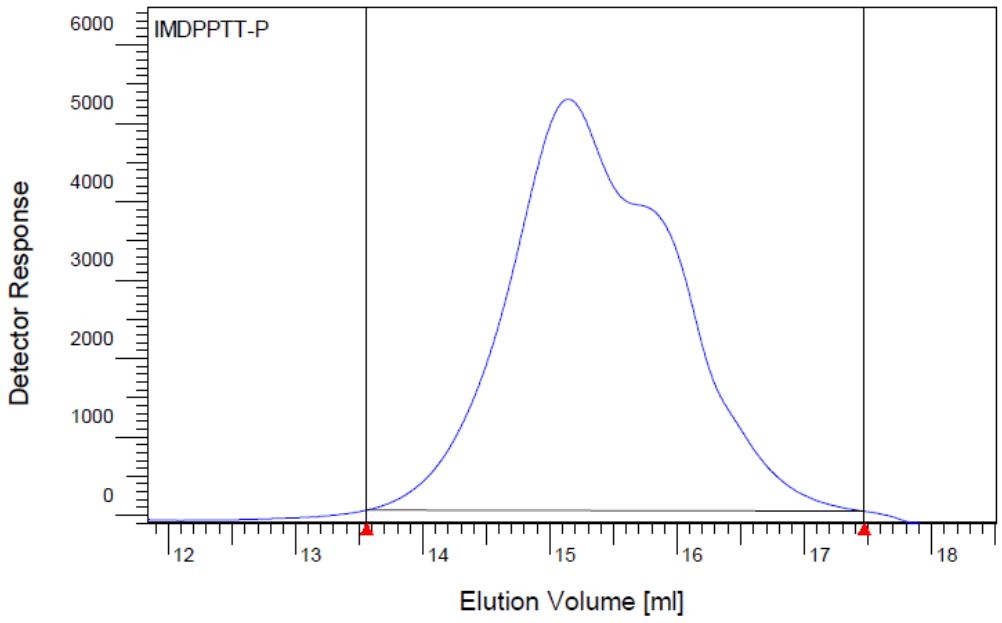

Figure 5.4. GPC trace of polymer **P4** in chlorobenzene at 80 °C.

5.3 Compounds synthesised in Chapter Three

2-octyl-1-dodecyl bromide 3.1

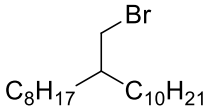

NBS (55.70 g, 217.72 mmol) was added portion-wise to a stirring solution of 2-octyl-1-decanol (50 g, 167.48 mmol) and PPh_3 (52.72 g, 200.99 mmol) in DCM (350 mL) at 0 °C. The solution was stirred at 0 °C for 2 h, quenched with sat. $Na_2S_2O_3$ (aq) (50 mL) and extracted into Et_2O. The combined organic phases were dried over $MgSO_4$, concentrated and passed through a small silica column (hexanes). Concentration by rotary evaporation afforded the title compound as a colourless oil (53.27 g, 147.34 mmol). ^{1}H NMR (400 MHz, $CDCl_3$): δ 3.46 (d, J = 4.8 Hz, 2H) 1.61 (m, 1H) 1.28 (bm, 32H), 0.90 (t, J = 6.8 Hz, 6H). ^{13}C NMR (400 MHz, $CDCl_3$): δ 39.7, 39.5, 32.6, 31.9, 29.8, 29.6, 29.6, 29.3, 29.3, 26.6, 22.7, 14.1. m/z (EI^+) 282 $(M\text{-}Br)^+$.

3-octyl-1-tridecanol 3.2

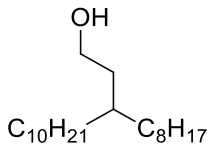

2-octyl-1docecyl bromide **3.1** (20 g, 55.33 mmol) was added dropwise to a stirring mixture of magnesium (1.48 g, 60.87 mmol) in dry Et_2O (250 mL) under argon. A flake of I_2 was added to the reaction mixture as an initiator. The reaction maintained gentle reflux until the magnesium was consumed. To the resultant Grignard reagent solution was added paraformaldehyde (2.16 g, 71.93 mmol) portion-wise. The solution was stirred at room temperature for 4 h before quenching with 1 M H_2SO_4 (50 ml), the organic layer was separated, dried over $MgSO_4$ and the solvent removed by rotary evaporation to afford the product as a colourless oil (10.90 g, 34.86 mmol, 63 %). ^{1}H NMR (400 MHz, $CDCl_3$): δ 3.61 (t, *J* = 6.7 Hz, 2H), 1.55 (m, 2H), 1.28 (bm, 33H), 0.91 (t, *J* = 6.8 Hz, 6H). ^{13}C NMR (100 MHz, $CDCl_3$): δ 62.9, 33.8, 32.8, 31.9, 30.1, 29.6, 29.5, 29.4, 26.6, 26.4, 25.8, 22.7, 14.1. m/z (EI^+) 295 $(M\text{-}H_2O)^+$.

3-octyl-1-tridecyl iodide 3.3

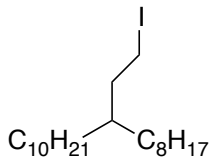

I_2 (10.64 g, 41.59 mmol) was added portion-wise to a stirring solution of 3-octyl-1-tridecanol **3.2** (10 g, 31.99 mmol), PPh_3 (10.07 g, 38.39 mmol) and imidazole (3.26 g, 47.99 mmol) in DCM (150 mL) at 0 °C. The solution was allowed to warm to room temperature over 2 hours before quenching with sat. $Na_2S_2O_3$ (aq) (50 mL). The organic phase was separated and washed with sat. $Na_2S_2O_3$ (aq) followed by water. Triphenylphosphine oxide precipitate was removed by filtration, the organic phase was dried over $MgSO_4$, concentrated and passed through a small silica column (hexanes). Concentration by rotary evaporation afforded the title compound as a colourless oil (14.41 g, 34.12 mmol, 82 %). ^{1}H NMR (400 MHz, $CDCl_3$): δ 3.23 (t, *J* = 3.8, 2H), 1.84 (m, 2H), 1.31 (m, 33H), 0.93 (t, *J* = 6.7 Hz, 6H). ^{13}C NMR (100

MHz, $CDCl_3$): δ 38.6, 38.3, 33.6, 32.9, 31.9, 30.6, 30.6, 30.0, 29.7, 29.4, 28.6, 26.4, 22.7, 14.1. m/z (EI^+) 295 $(M\text{-}I)^+$.

Diethyl- 2-octyldodecylmalonate 3.4

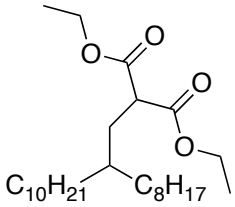

Diethyl malonate (8.06 g, 50.30 mmol) was added to a stirring solution of sodium (1.16 g, 50.30 mmol) in ethanol (100 mL). 2-octyl-1-dodecyl bromide **3.1** (20 g, 55.33 mmol) was added dropwise to the resulting sodium diethylmalonate solution and was heated at reflux for 4 hours. Upon cooling to room temperature water was added (50 mL) and the product was extracted into Et_2O, dried over $MgSO_4$ and the solvent removed by rotary evaporation to afford the title compound as a pale yellow oil (20.40 g, 46.30 mmol, 92 %) which was used without further purification. ^1H NMR (400 MHz, $CDCl_3$): δ 4.19 (q, J = 7.2 Hz, 4H), 3.42 (t, J = 7.6 Hz, 1H), 1.83 (m, 2H), 1.26 (bm, 39H), 0.88 (m, 6H). ^{13}C (100 MHz, $CDCl_3$): δ 169.8, 61.2, 50.1, 39.5, 35.4, 33.2, 32.9, 32.6, 31.9, 30.0, 29.7, 29.6, 29.3, 26.3, 22.7, 14.1. MALDI TOF (LD^+) 441 (M^+).

Ethyl-4-octyltetradecanoate 3.5

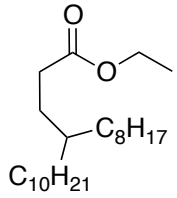

A solution of diethyl -2-octyldodecylmalonate **3.4** (20.00 g, 45.38 mmol), NaCl (10.61 g, 181.14 mmol) and water (4.08 mL, 222.69 mmol) in DMSO (150 mL) was heated with stirring at 180 °C for 24 h. Upon cooling to room temperature water (50 mL) was added and the mixture was poured into EtOAc. The organic layer was

separated, washed with water then brine, dried over $MgSO_4$ and concentrated by rotary evaporation to afford the practically title compound as a colourless oil (14.43 g, 39.03 mmol, 86 %). ^{1}H NMR (400 MHz, $CDCl_3$): δ 4.13 (q, *J* = Hz, 2H), 2.28 (m, 2H), 1.59 (m, 2H), 1.27 (bm, 36H), 0.90 (m, 6H). ^{13}C (100 MHz, $CDCl_3$): δ 174.2, 60.2, 37.0, 33.3, 31.9, 31.8, 30.1, 29.7, 29.4, 28.7, 26.6, 22. MALDI TOF (LD^+) 369 (M^+).

4-octyltetradecanoic acid 3.6

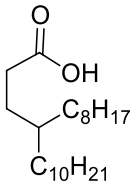

1M NaOH (30 mL) was added to a stirring solution of ethyl 4-octyltetradecanoate **3.5** (14.00 g, 37.87 mmol) in EtOH (100 mL) and the solution was heated to reflux for 6 h. Upon cooling to room temperature 2 M HCl (aq) (50 mL) was added. After 30 minutes of stirring the organic layer was extracted with EtOAc and washed with water then sat. NaCl (aq). The solution was dried over $MgSO_4$ and concentrated by rotary evaporation. Column chromatography (hexanes : EtOAc, 9 : 1) afforded the title compound as a yellow oil (8.66 g, 24.99 mmol, 66 %). ^{1}H NMR (400 MHz, $CDCl_3$): δ 2.35 (m, 2H), 1.62 (m, 2H), 1.29 (bm, 33H), 0.91 (m, 6H). ^{13}C NMR (100 MHz, $CDCl_3$): δ 180.8, 36.9, 33.2, 31.9, 31.6, 30.1, 29.7, 29.4, 28.4, 26.5, 22.7, 14.1. ES TOF (EI^+) 340 (M^+).

4-octyl-1-tetradecanol 3.7

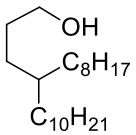

2M $LiAlH_4$ in THF (12.26 mL, 24.52 mmol) was added dropwise to a stirring solution of 4-octyltetradecanoic acid **3.6** (8.5 g, 24.52 mmol) in dry THF (50 mL) and the resulting solution was heated to reflux for 2 hours. Upon cooling to room temperature

the solution was poured carefully onto iced 1 M HCl (200 mL). The organic layer was separated, dried over $MgSO_4$ and the solvent removed by rotary evaporation before being passed through a short silica column (hexanes) affording the title compound as a colourless oil (6.24 g, 19.13 mmol, 78 %). ^{1}H NMR (400 MHz, $CDCl_3$): δ 3.63 (t, *J* = 6.6 Hz, 2H), 1.57 (m, 2H), 1.28 (m, 35H), 0.90 (t, *J* = 6.7 Hz, 6H). ^{13}C NMR (100 MHz, $CDCl_3$): δ 37.3, 33.6, 32.0, 30.2, 30.0, 29.7, 29.6, 29.4, 26.7, 22.7, 14.1. m/z (EI^+) 308 $(M\text{-}H_2O)^+$.

4-octyl-1-tetradecyl iodide 3.8

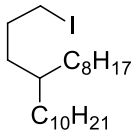

I_2 (6.12 g, 23.93 mmol) was added portion-wise to a stirring solution of 4-octyl-1-tetradecanol **3.7** (6.00 g, 18.40 mmol), PPh_3 (5.79 g, 22.09 mmol) and imidazole (1.91 g, 28.16 mmol) in DCM (50 mL) at 0 °C. The solution was allowed to warm to room temperature over 2 hours before quenching with sat. $Na_2S_2O_3$ (aq) (50 mL). The organic phase was separated and washed with sat. $Na_2S_2O_3$ (aq) followed by water. Triphenylphosphine oxide precipitate was removed by filtration, the organic phase was dried over $MgSO_4$, concentrated and passed through a small silica column (hexanes). Concentration by rotary evaporation afforded the title compound as a colourless oil (6.53 g, 15.83 mmol, 86 %). ^{1}H NMR (400 MHz, $CDCl_3$): δ 3.19 (t, *J* = 7.0 Hz, 2H), 1.81 (m, 2H), 1.28 (m, 32H), 0.91 (m, 6H). ^{13}C NMR (100 MHz, $CDCl_3$): δ 36.8, 34.6, 33.6, 32.0, 31.0, 30.1, 29.8, 29.4, 26.7, 22.7, 14.2. m/z (EI^+) 309 $(M\text{-}I)^+$.

2,5-bis(3-octyltridecyl)-3,6-di(thieno[3,2-*b*]thiophen-2-yl)pyrrole[3,4-*c*]pyrrole-1,4(2*H*,5*H*)-dione 3.9

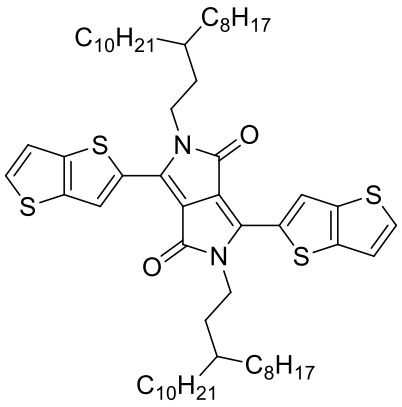

3-octyl-1-tridecyl iodide **3.3** (6.82 g, 16.14 mmol) was added to a solution of 3,6-di(thieno[3,2-*b*]thiophen-2-yl)pyrrole[3,4-*c*]pyrrole-1,4(2*H*,5*H*)-dione **2.3** (2.00 g, 4.85 mmol), K_2CO_3 (2.23 g, 16.14 mmol) and 18-crown-6 (~10 mg) in dr DMF (100 mL). The solution was heated with stirring at 120 °C for 18 hours before cooling to room temperature. Solvent was removed by rotary evaporation and the crude product purified by column chromatography (hexanes : chloroform, 3 : 1) to afford the title compound as a dark purple solid (1.55 g, 1.55 mmol, 32 %).^{1}H NMR (400 MHz, $CDCl_3$): δ 9.30 (s, 2H), 7.62 (d, J = 5.2 Hz, 2H), 7.32 (d, J = 5.3 Hz, 2H), 4.15 (m, 4H), 1.73 (m, 4H), 1.26 (bm, 66H), 0.89 (t, J = 6.7 Hz, 12H). ^{13}C NMR (400 MHz, $CDCl_3$): δ 161.28, 143.21, 140.43, 140.17, 132.10, 131.07, 127.39, 119.26, 108.31, 41.26, 36.08, 34.11, 33.50, 31.94, 30.09, 29.74, 29.69, 29.38, 26.64, 22.70, 14.13. MALDI TOF (LD^+) 1000.4.

3,6-bis(2-bromothieno[3,2-*b*]thiophen-5-yl)-2,5-bis(3-octyltridecyl)pyrrolo[3,4-*c*]pyrrole-1,4(2*H*,5*H*)-dione 3.10

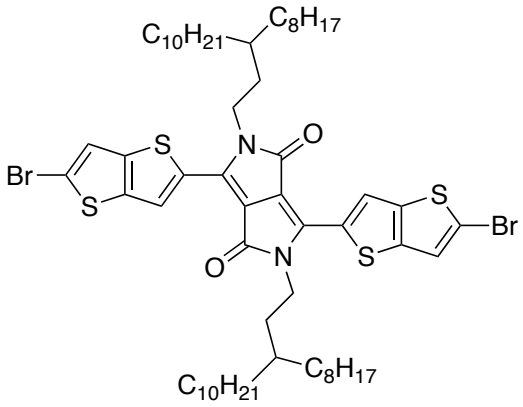

To a stirring solution of 2,5-bis(3-octyltridecyl)-3,6-di(thieno[3,2-*b*]thiophen-2-yl)pyrrole[3,4-*c*]pyrrole-1,4(2*H*,5*H*)-dione **3.9** (1 g, 0.10 mmol) in chloroform (50 mL) was added a solution of bromine (0.32 g, 2.00 mmol) in chloroform (5 mL) dropwise. The solution was refluxed for 2 hours and then cooled to 0 °C before quenching with sat. $Na_2S_2O_3$ (aq) (50 mL). The organic layer was separated and concentrated by rotary evaporation to afford the crude product which was purified by column chromatography (hexanes : chloroform, 3 : 1) to give the title compound as a dark purple/blue solid (0.79 g, 0.68 mmol, 68 %).^{1}H NMR (400 MHz, $CDCl_3$): δ 9.21 (s, 2H), 7.29 (s, 2H), 4.11 (m, 4H), 1.69 (m, 4H), 1.27 (m, 66H), 0.90 (m, J = 6.6 Hz, 12H). ^{13}C NMR (100 MHz, $CDCl_3$): δ 160.97, 141.89, 140.51, 139.69, 130.29, 126.71, 121.96, 119.06, 108.29, 41.29, 36.07, 34.04, 33.47, 31.97, 30.12, 29.78, 29.73, 29.42, 26.65, 22.73, 14.16. MALDI TOF (LD^+) 1158.6.

2,5-bis(4-octyltetradecyl)-3,6-di(thieno[3,2-*b*]thiophen-2-yl)pyrrole[3,4-*c*]pyrrole-1,4(2*H*,5*H*)-dione 3.11

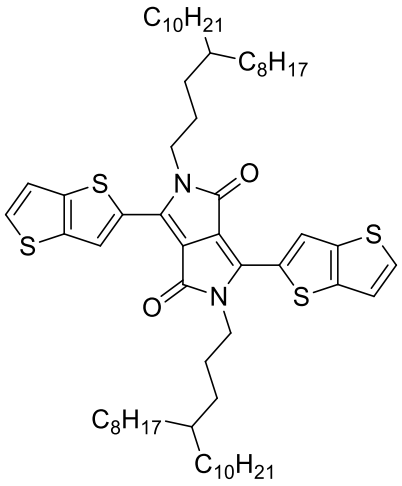

4-octyl-1-tetradecyl iodide **3.8** (7.05 g, 16.14 mmol) was added to a solution of 3,6-di(thieno[3,2-*b*]thiophen-2-yl)pyrrole[3,4-*c*]pyrrole-1,4(2*H*,5*H*)-dione (2 g, 4.85 mmol), K_2CO_3 (2.23 g, 16.14 mmol) and 18-crown-6 (~10 mg) in dry DMF (100 mL). The solution was heated with stirring at 120 °C for 18 h and then cooled to room temperature. Solvent was removed by rotary evaporation and the crude product was purified by column chromatography (chloroform : hexane, 3:1) affording the title compound as a dark purple solid (1.50 g, 1.45 mmol, 30 %). ^{1}H NMR (400 MHz, $CDCl_3$): δ 9.39 (s, 2H), 7.62 (d, *J* = 5.3 Hz, 2H), 7.32 (d, *J* = 5.3 Hz, 2H), 4.12 (m, 4H), 1.78 (m, 4H), 1.30 (bm, 70H), 0.89 (t, *J* = 6.7 Hz, 12H). ^{13}C NMR (100 MHz, $CDCl_3$): δ 161.3, 143.3, 140.5, 140.1, 132.2, 131.1, 127.6, 119.3, 108.1, 42.9, 37.2, 33.6, 31.9, 30.6, 30.1, 29.8, 29.7, 29.4, 27.3, 26.8, 22.7, 14.1. MALDI TOF (LD^+) 1028.9.

3,6-bis(2-bromothieno[3,2-*b*]thiophen-5-yl)-2,5-bis(4-octyltetradecyl)pyrrolo[3,4-*c*]pyrrole-1,4(2*H*,5*H*)-dione 3.12

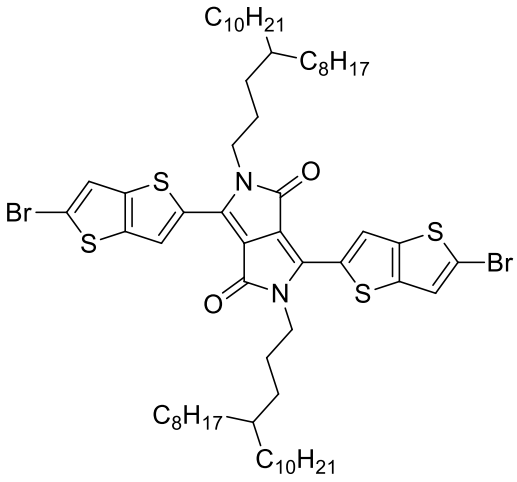

To a stirring solution of 2,5-bis(4-octyl-1-tetradecyl)-3,6-di(thieno[3,2-*b*]thiophen-2-yl)pyrrole[3,4-*c*]pyrrole-1,4(2*H*,5*H*)-dione (1.00 g, 0.97 mmol) in chloroform (50 mL) was added a solution of bromine (0.31 g, 1.94 mmol) in chloroform (5 mL) dropwise. The solution was refluxed for 2 hours and then cooled to 0 °C before quenching with sat. $Na_2S_2O_3$ (aq) (50 mL). The organic layer was separated and concentrated by rotary evaporation to afford the crude product which was purified by column chromatography (hexanes : chloroform, 3 : 1) to give the title compound as a dark purple/blue solid (0.74 g, 0.62 mmol, 64 %). ^{1}H NMR (400 MHz, $CDCl_3$): δ 9.31 (s, 2H), 7.32 (s, 2H), 4.10 (m, 4H), 1.75 (m, 4H), 1.25 (bm, 70H), 0.90 (t, J = 6.6 Hz, 12H). ^{13}C NMR (100 MHz, $CDCl_3$): δ 161.0, 142.0, 140.5, 139.5, 130.3, 126.9, 122.0, 119.2, 108.1, 42.9, 37.2, 33.5, 32.0, 30.5, 30.1, 29.8, 29.7, 29.4, 27.2, 26.8, 22.7, 14.2. MALDI TOF (LD+) 1186.8.

DPPTT-T (*C2*) P5

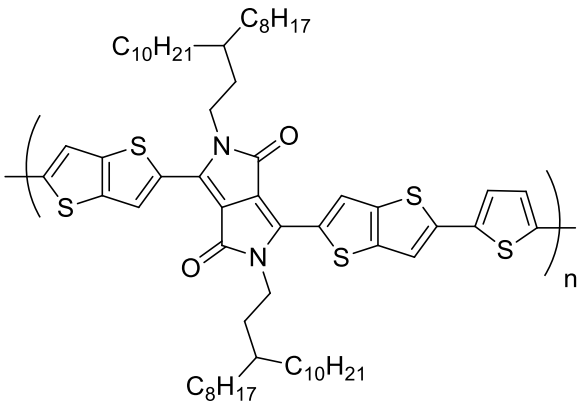

To a microwave vial was added 3,6-bis(2-bromothieno[3,2-*b*]thiophen-5-yl)-2,5-bis(3-octyltridecyl)pyrrolo[3,4-*c*]pyrrole-1,4(2*H*,5*H*)-dione **3.10** (150 mg, 0.13 mmol) and 2,5-bis(trimethylstannyl)thiophene (53.01 mg, 0.14 mmol) in chlorobenzene (1.7 mL). The solution was degassed before the addition of $Pd_2(dba)_3$ (4 mg) and P(*o*Tol)$_3$ (5 mg). Following further degassing the microwave vial was sealed and the reaction mixture was heated in a microwave in successive intervals of 5 minutes at 100 °C, 5 minutes at 140 °C, 5 minutes at 160 °C, 10 minutes at 180 °C and finally 20 minutes at 200 °C. After cooling to room temperature the reaction mixture was poured into vigorously stirring methanol and the resulting polymeric precipitate was filtered. The polymer was purified by Soxhlet extraction first in acetone (24 h), hexane (24 h), chloroform (24 h) and finally chlorobenzene (24 h). The chlorobenzene fraction was concentrated by rotary evaporation, suspended in methanol and filtered to afford the title polymer as a dark green solid (52 mg, 37 %).

GPC (chlorobenzene): M_n = 45 kDa, M_w = 83 kDa, PDI = 1.8.

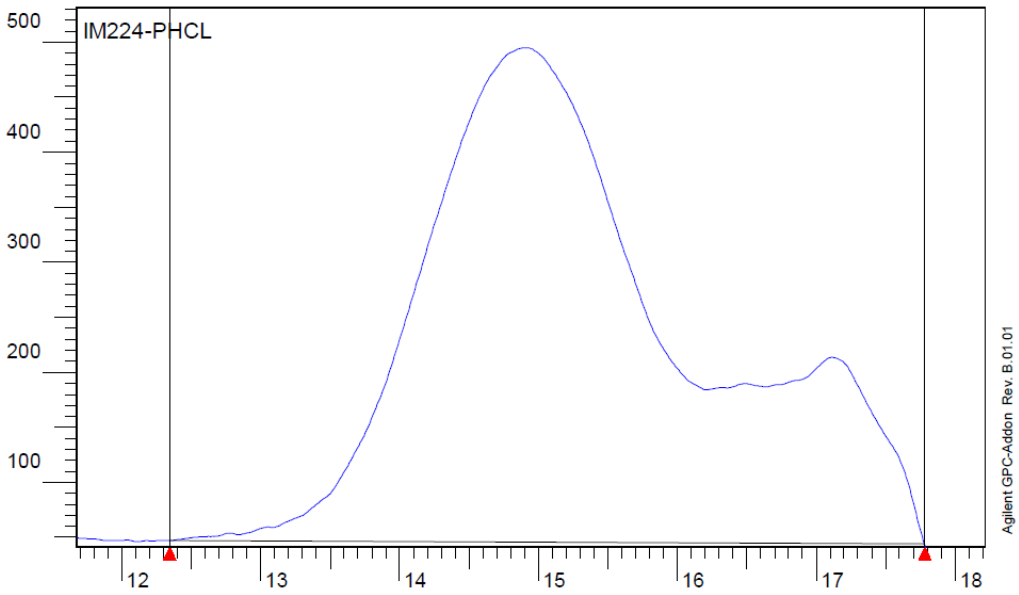

Figure 5.5. GPC trace of polymer **P5** in chlorobenzene at 80 °C.

DPPTT-Ph (*C2*) P6

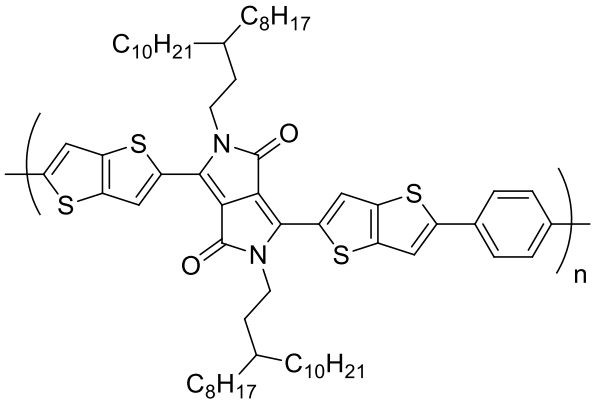

To a microwave vial was added 3,6-bis(2-bromothieno[3,2-*b*]thiophen-5-yl)-2,5-bis(3-octyltridecyl)pyrrolo[3,4-*c*]pyrrole-1,4(2*H*,5*H*)-dione **3.10** (200 mg, 0.17 mmol) and 1,4-di(4,4,5,5-tetramethyl-1,3-dioxaboralane)benzene (56.93 mg, 0.17 mmol) followed by a thoroughly degassed solution of Aliquat 336 (2 drops) in toluene (6 mL). The solution was further degassed with stirring for half an hour before the addition of $Pd_2(dba)_3$ (10 mg) and PPh_3 (7 mg) followed by degassing for a further 30 min. K_3PO_4 (221 mg) in water (0.5 mL) was added, and the vial was sealed and heated for 3 days at 120 °C with vigorous stirring. After cooling to room temperature the reaction mixture was poured into vigorously stirred methanol, and the resulting

polymeric precipitate was filtered. The filtrate was purified by Soxhlet extraction first in acetone (24 h), hexane (24 h), chloroform (24 h), and finally chlorobenzene (24 h). The chlorobenzene fraction was concentrated by rotary evaporation, suspended in methanol, and filtered to afford the title polymer (117.12 mg, 63 %) as a dark green solid.

GPC (chlorobenzene): M_n = 75 kDa, M_w = 133 kDa, PDI = 1.7

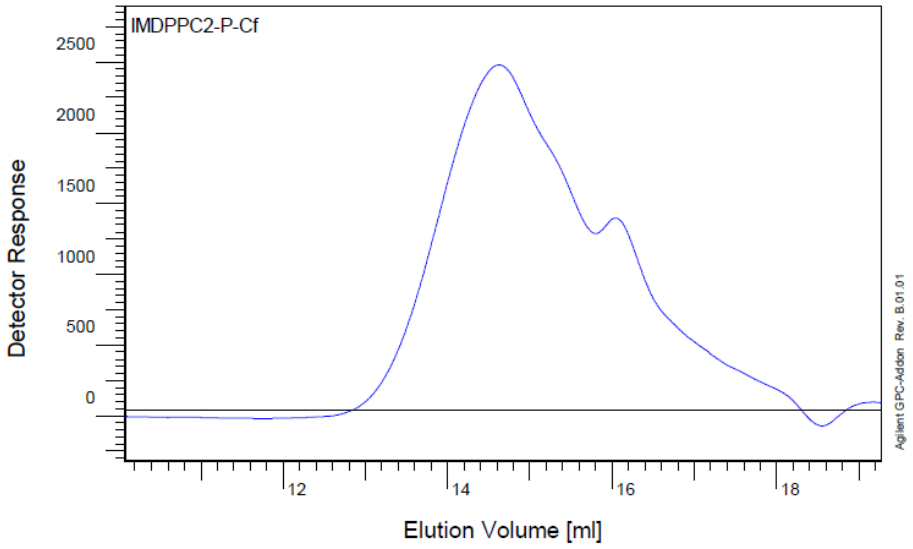

Figure 5.6. GPC of polymer **P6** in chlorobenzene at 80 °C

DPPTT-Homo (*C2*) P7

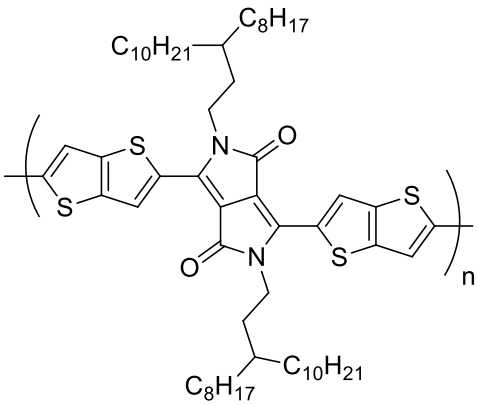

To a thoroughly degassed solution of hexamethylditin (56.52 mg, 0.17 mmol) and 3,6-bis(2-bromothieno[3,2-*b*]thiophen-5-yl)-2,5-bis(3-octyltridecyl)pyrrolo[3,4-*c*]pyrrole-1,4(2*H*,5*H*)-dione **3.10** (200 mg, 0.17 mmol) in THF (7.5 mL) and NMP

(3.75 mL) was added $Pd(PPh_3)_4$ (10 mg) and copper(I)iodide (1 mg). After degassing for a further 30 minutes the microwave vial was sealed and heated at reflux for 3 days. After cooling to room temperature the reaction mixture was poured into vigorously stirring methanol and the polymeric precipitate filtered into a Soxhlet thimble. The polymer was purified by Soxhlet extraction first in acetone (24 h), methanol (24 h), hexane (24h) and finally chloroform (24 h). The chloroform fraction was concentrated by rotary evaporation, suspended in methanol and filtered to afford the title polymer as a dark green solid (148.60 mg, 86 %).

GPC (chlorobenzene): M_n = 34 kDa, M_w = 68 kDa, PDI = 2.

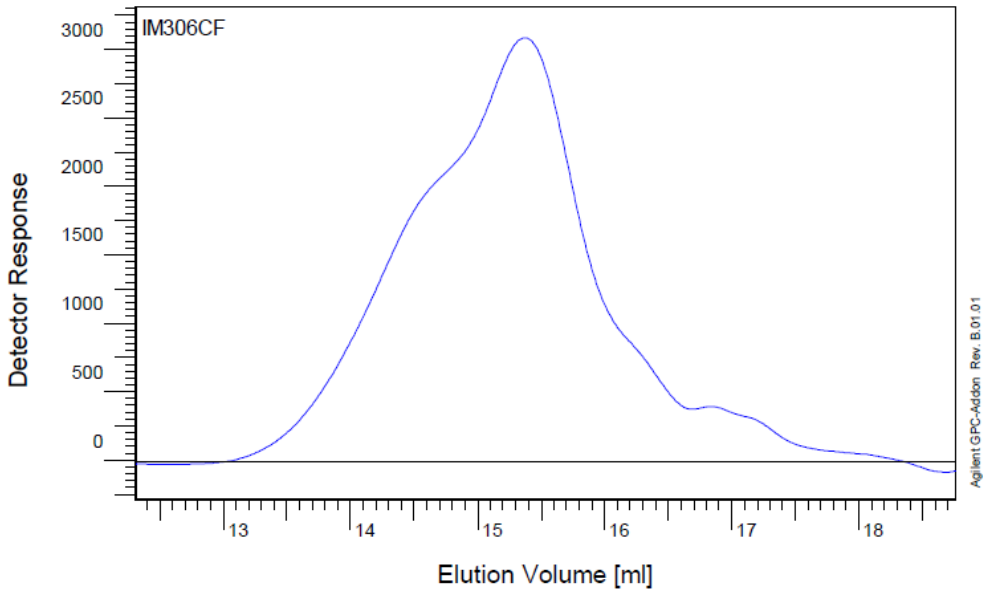

Figure 5.7. GPC trace of polymer **P7** in chlorobenzene at 80 °C.

DPPTT-T (*C3*) P8

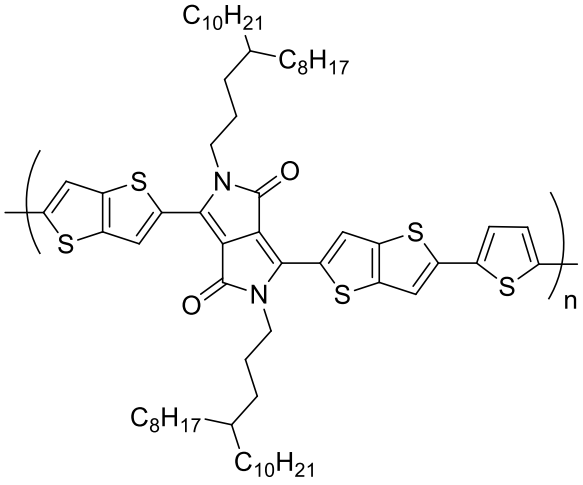

To a microwave vial was added 3,6-bis(2-bromothieno[3,2-*b*]thiophen-5-yl)-2,5-bis(4-octyltetradecyl)pyrrolo[3,4-*c*]pyrrole-1,4(2*H*,5*H*)-dione **3.12** (150 mg, 0.13 mmol) and 2,5-bis(trimethylstannyl)thiophene (51.76 mg, 0.13 mmol) in chlorobenzene (1.7 mL). The solution was degassed before the addition of $Pd_2(dba)_3$ (4 mg) and P(*o*Tol)$_3$ (5 mg). Following further degassing the microwave vial was sealed and the reaction mixture was heated in a microwave in successive intervals of 5 minutes at 100 °C, 5 minutes at 140 °C, 5 minutes at 160 °C, 10 minutes at 180 °C and finally 20 minutes at 200 °C. After cooling to room temperature the reaction mixture was poured into vigorously stirring methanol and the resulting polymeric precipitate was filtered into a Soxhlet thimble. The polymer was purified by Soxhlet extraction first in acetone (24 h), hexane (24 h), chloroform (24 h) and finally chlorobenzene (24 h). The chlorobenzene fraction was concentrated by rotary evaporation, suspended in methanol and filtered to afford the title polymer as a dark green solid (105 mg, 73 %).

GPC (chlorobenzene): M_n = 80 kDa, M_w = 154 kDa, PDI = 1.9

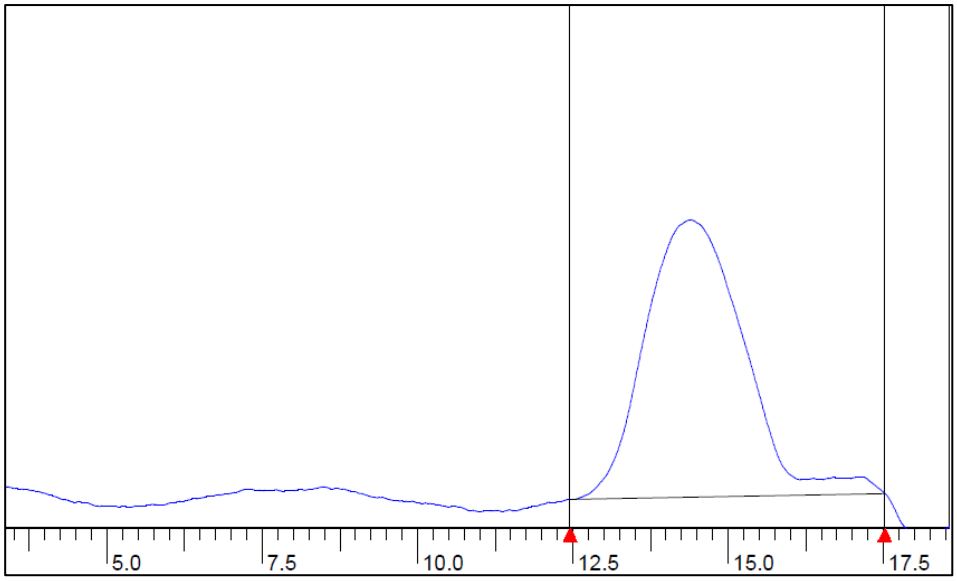

Figure 5.8. GPC trace of polymer **P8** in chlorobenzene at 80 °C.

DPPTT-Se (*C3*) P9

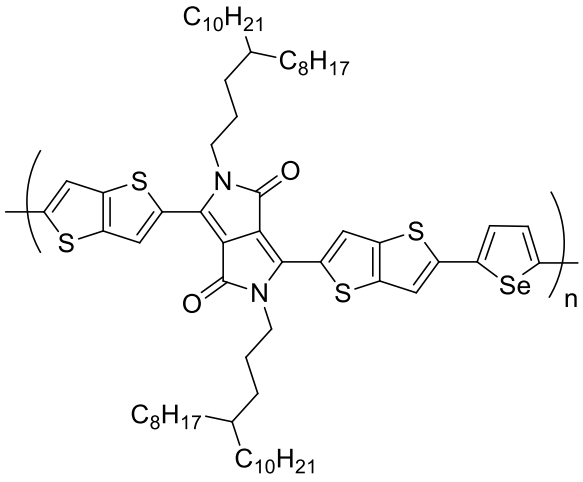

To a microwave vial was added 3,6-bis(2-bromothieno[3,2-*b*]thiophen-5-yl)-2,5-bis(4-octyltetradecyl)pyrrole[3,4-*c*]pyrrole-1,4(2*H*,5*H*)-dione **3.12** (200 mg, 0.17 mmol) and 2,5-bis(trimethylstannyl)selenophene (76.91 mg, 0.17 mmol) in chlorobenzene (1.7 mL). The solution was degassed before the addition of $Pd_2(dba)_3$ (4 mg) and P(*o*Tol)$_3$ (5 mg). Following further degassing the microwave vial was sealed and the reaction mixture was heated in a microwave in successive intervals of 5 minutes at 100 °C, 5 minutes at 140 °C, 5 minutes at 160 °C, 10 minutes at 180 °C and finally 20 minutes at 200 °C . After cooling to room temperature the reaction

mixture was poured into vigorously stirring methanol and the resulting polymeric precipitate was filtered. The polymer was purified by Soxhlet extraction first in acetone (24 h), hexane (24 h), chloroform (24 h) and finally chlorobenzene (24 h). The chlorobenzene fraction was concentrated by rotary evaporation, suspended in methanol and filtered to afford the title polymer as a dark green solid (97 mg, 65 %).

GPC (chlorobenzene): M_n = 95 kDa, M_w = 238 kDa, PDI = 2.5

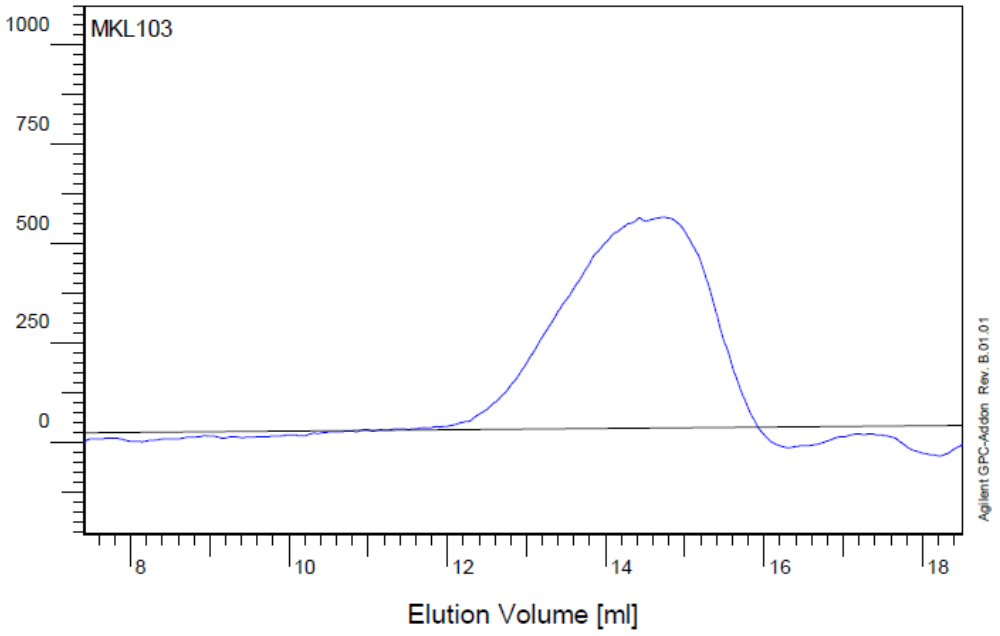

Figure 5.9. GPC trace of polymer **P9** in chlorobenzene at 80 °C.

DPPTT-Te (*C3*) P10

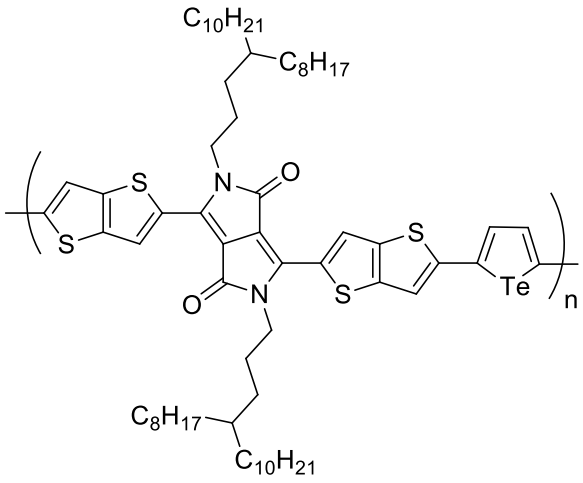

To a microwave vial was added 3,6-bis(2-bromothieno[3,2-*b*]thiophen-5-yl)-2,5-bis(4-octyltetradecyl)pyrrole[3,4-*c*]pyrrole-1,4(2*H*,5*H*)-dione **3.12** (150 mg, 0.13 mmol) and 2,5-bis(trimethylstannyl)tellurophene (63.83 mg, 0.13 mmol) in chlorobenzene (1.7 mL). The solution was degassed before the addition of $Pd(PPh_3)_4$ (10 mg). Following further degassing the microwave vial was sealed and the reaction mixture was heated in a microwave in successive intervals of 5 minutes at 100 °C, 5 minutes at 140 °C, 5 minutes at 160 °C, 10 minutes at 180 °C and finally 20 minutes at 200 °C. After cooling to room temperature the reaction mixture was poured into vigorously stirring methanol and the resulting polymeric precipitate was filtered. The polymer was purified by Soxhlet extraction first in acetone (24 h), hexane (24 h), chloroform (24 h) and finally chlorobenzene (24 h). The chloroform fraction was concentrated by rotary evaporation, suspended in methanol and filtered to afford the title polymer as a dark green solid (96 mg, 61 %).

GPC (chlorobenzene): M_n = 91 kDa, M_w = 272 kDa, PDI = 3.0.

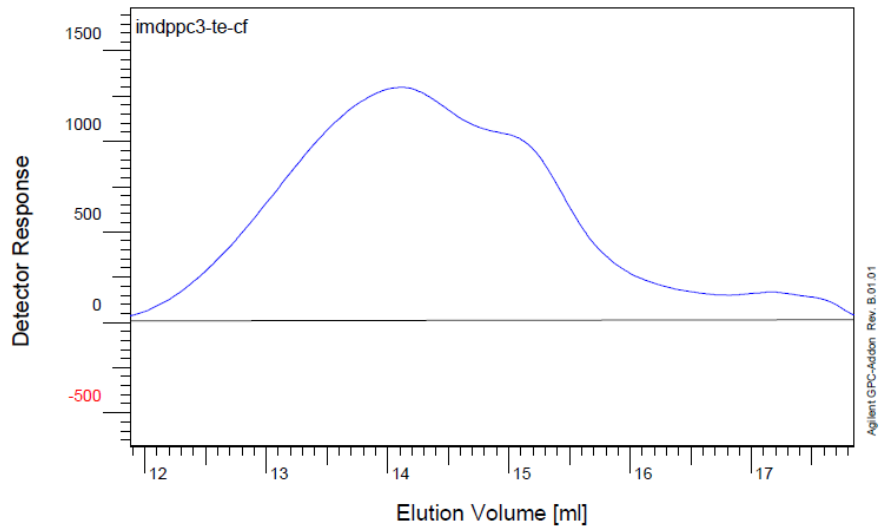

Figure 5.10. GPC trace of polymer **P10** in chlorobenzene at 80 °C.

5.4. Compounds synthesised in Chapter Four

2-decyl-1-tetradecylazide 4.1

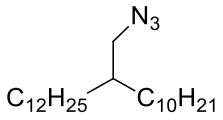

Triphenylphosphine (10.35 g, 38.48 mmol), diisopropylazodicarboxylate (7.98 g, 39.48 mmol) 1.4 and diphenylphosphoryl azide (10.86 g, 39.48 mmol) were added to a stirring solution of 2-decyl-1-tetradecanol (10.0 g, 28.20 mmol) in dry THF (150 mL) and stirred overnight at room temperature under argon. Water (100 mL) was added and the organics were extracted into hexane, which was dried over $MgSO_4$ and concentrated by rotary evaporation. The crude product was purified by column chromatography on silica (hexanes) to give the title compound as a colourless oil (6.96 g, 18.32 mmol, 65 %). ^{1}H NMR (400 MHz, $CDCl_3$): δ 3.25 (d, J = 3.2 Hz, 2H), 1.56 (m, 1H), 1.29 (bm, 40H), 0.90 (t, J = 6.7 Hz, 6H).

2-decyl-1-tetradecylamine 4.2

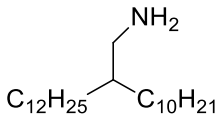

2 M Lithium aluminium hydride (8.69 mL, 17.38 mmol) was added dropwise to a stirring solution of 2-decyl-1-tetradecylazide **4.1** (6.00 g, 15.80 mmol) in dry Et_2O. The solution was heated at 60 °C for 2 hours before quenching with 1 M NaOH solution. The organic layer was separated and washed with water (3 x 150 mL), dried over $MgSO_4$ and concentrated by rotary evaporation to afford the title compound which was used without any further purification (4.69 g, 13.27 mmol, 84 %). ^{1}H NMR (400 MHz, $CDCl_3$): δ 2.60 (d, J = 4.4 Hz, 2H), 1.26 (bm, 41H), 0.88 (t, J = 6.7 Hz, 6H). ^{13}C NMR (100 MHz, $CDCl_3$): δ 46.1, 42.0, 32.1, 31.9, 30.5, 30.2, 30.0, 29.7, 27.1, 23.1, 14.4.

2,5-dibromo-thieno[3,2-*b*]thiophene 4.3

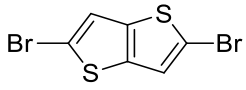

NBS (26.65 g, 149.75 mmol) was added portion-wise to a stirring solution of thieno[3,2-*b*]thiophene (10.00 g, 71.31 mmol) in DMF (150 mL) at 0 °C in the dark. After warming to room temperature over 2 hours, water (150 mL) was added and the crude product precipitate was filtered off under vacuum. Recrystallisation from EtOAc/EtOH afforded the title compound as white crystals (19.98 g, 67.03 mmol, 94 %). ^{1}H NMR (400 MHz, $CDCl_3$): δ 7.21 (s, 2H). ^{13}C NMR (100 MHz, $CDCl_3$): δ 138.6, 123.5, 113.6. GC-MS: m/z 298 (M^+)

2-bromo-6-trimethylsilyl-thieno[3,2-b]thiophene 4.4

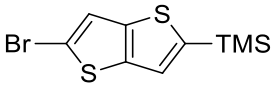

2,5-dibromothieno[3,2-*b*]thiophene **4.3** (15.00 g, 50.33 mmol) was dissolved in 250 mL of dry Et_2O at -78 °C. A 2.5 M solution of *n*BuLi (21.14 mL, 52.85 mmol) in hexanes was added dropwise to the reaction mixture. After complete addition the mixture was stirred for 30 minutes at -78 °C before being quenched by the addition of chlorotrimethylsilane (7.03 ml, 55.36 mmol). The mixture was stirred for another 15 minutes at low temperature and then warmed to room temperature. The reaction mixture was quenched by the addition of 200 mL of water. The organic layer was separated and washed subsequently with water (2 x 150 mL) and brine (1 x 150 mL). After being dried over sodium sulfate, the solution was filtered. The diethyl ether was evaporated and the recovered orange oil purified by column chromatography on silica (hexanes) to afford the title compound a pale yellow oil (12.76 g, 43.78 mmol, 87 %). ^{1}H NMR (400 MHz, $CDCl_3$): δ 7.28 (d, J = 0.7 Hz, 1H), 7.27 (d, J = 0.7 Hz, 1H), 0.38 (s, 9H). ^{13}C NMR (100 MHz, $CDCl_3$): δ 142.9, 142.8, 141.1, 125.0, 122.1, 114.5, 0.0. HRMS (EI^+): m/z calcd. for $C_9H_{11}BrS_2Si$ (M^+) 289.9255 found 289.9246.

3-bromo-6-trimethylsily-thieno[3,2-*b*]thiophene 4.5

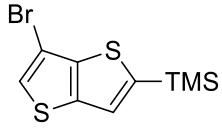

2-bromo-6-trimethylsilyl-thieno[3,2-*b*]thiophene **4.4** (10.00 g, 34.33 mmol) was dissolved in 200 mL of dry Et_2O and cooled to -78 °C. A 2.0 M LDA (22.31 mL, 44.63 mmol) in a THF / heptanes / ethylbenzene mixture was added carefully, maintaining the temperature below -70 °C. After addition the reaction mixture was slowly warmed to room temperature and stirred during 2 hours. The reaction mixture was cooled back down to -40 °C and quenched by the addition of brine (50 mL). The mixture was warmed to room temperature and the organic layer separated. The organic layer was subsequently washed with water (2 x 100 mL) and brine (1 x 100 mL) before being dried over sodium sulfate. The solvent was evaporated under reduced pressure and the recovered brown oil purified by column chromatography on silica (hexanes) to afford the title compound as a colourless oil (8.20 g, 28.1 mmol, 82 %). ^{1}H NMR (400 MHz, $CDCl_3$): δ 7.40 (s, 1H), 7.30 (s, 1H), 0.39 (s, 9H). ^{13}C NMR (100 MHz, $CDCl_3$): δ 145.4, 140.4, 126.3, 124.9, 102.5, 0.1. HRMS (EI): m/z calcd for $C_9H_{11}BrS_2Si$ (M+) 289.9255 found 289.9246.

3-bromo-thieno[3,2-*b*] thiophene 4.6

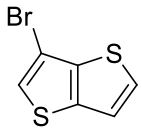

A solution of 3-bromo-6-trimethylsily-thieno[3,2-*b*]thiophene **4.5** (8.00 g, 27.46 mmol) in dry THF was cooled to -10 °C and TBAF (10.77 g, 41.19 mmol) was added portion-wise. The solution was allowed to warm to room temperature over 30 minutes before the addition of water, the product was extracted with ethyl acetate and the aqueous layer washed several times with ethyl acetate. The combined organic layers were dried over $MgSO_4$ and the solvent removed by rotary evaporation. The crude product was passed through a short silica column (hexanes) to afford the title compound as a colourless oil (5.48 g, 24.99 mmol, 91 %). ^{1}H NMR (400 MHz,

acetone-d_6): δ 7.71 (dd, *J* = 5.4, 1.4 Hz, 1H), 7.64 (d, *J* = 1.8 Hz), 7.51 (d, *J* = 5.2 Hz, 1H). ^{13}C NMR (400 MHz, acetone-d_6): δ 140.3, 139.1, 128.9, 125.2, 120.9, 101.6. GC-MS: m/z 219 (M^+).

_N_-(2-decyltetradecyl)thieno[3,2-*b*]thiophen-3-amine 4.7

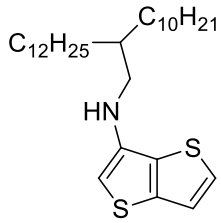

3-bromo-thieno[3,2-*b*]thiophene **4.6** (5.00 g, 22.82 mmol), copper powder (0.07 g, 1.15 mmol) copper(I)iodide (0.22 g, 1.15 mmol,) K_3PO_4 (9.69 g, 45.64 mmol) and 2-decyltetradecyl amine (12.11 g, 34.23 mmol) were heated with stirring in dimethyl aminoethanol (50 mL) at 80 °C for 48 hours. Upon cooling to room temperature, water was added and the organics extracted into hexanes. The aqueous layer was washed several times with hexanes and the organic layers combined and washed with water (100 mL) and brine (100 mL) before being dried over $MgSO_4$. The solvent was removed by rotary evaporation and the crude product was passed through a small silica column (hexanes) to afford the title compound as a light brown oil (1.67 g, 3.40 mmol, 14.89 %). ^{1}H NMR (400 MHz, $CDCl_3$): δ 7.36 (dd, *J* = 5.3, 1.4 Hz, 1H), 6.05 (d, 1H, *J* = 2.1 Hz), 3.56 (s, 1H), 3.13 (d, *J* = 6.1 Hz, 2H), 1.29 (bm, 40H), 0.91 (m, 6H). ^{13}C NMR (100 MHz, $CDCl_3$): δ 140.6, 137.8, 131.5, 125.9, 120.5, 96.5, 49.7, 37.8, 32.2, 32.0, 30.1, 29.7, 29.6, 29.4, 26.9, 26.8, 22.7, 14.2. HRMS (EI): m/z calcd for $C_{30}H_{53}NS_2$ (M+H) 492.3653 found 492.3687.

4-(2-decyltetradecyl)-4*H*-thieno[3,2-*b*]thiophene[3,2-*b*]pyrrole-5,6-dione 4.8

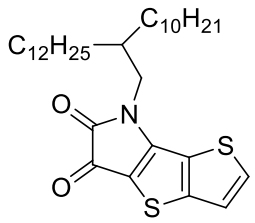

N-(2-decyltetradecyl)thieno[3,2-*b*]thiophen-3-amine **4.7** (1.50 g, 3.05 mmol) in DCM (10 mL) was added dropwise to a stirring solution of oxalyl chloride (0.50 g, 3.96 mmol) in DCM (10 mL) at -10 °C. After thirty minutes of stirring at -10 °C, triethylamine (1.39 g, 13.72 mmol) in DCM (10 mL) was added dropwise and the solution was allowed to warm to room temperature overnight. Solvent and any excess triethylamine were removed by rotary evaporation and the crude compound was purified by column chromatography on silica (DCM) to afford the title compound a bright red solid (0.68 g, 1.24 mmol, 41% yield. ^{1}H NMR (400 MHz, $CDCl_3$): δ 7.85 (d, *J* = 5.3 Hz, 1H), 7.37 (d, *J* = 5.1 Hz, 1H), 3.68 (d, *J* = 7.7 Hz, 2H), 1.9 (m, 1H), 1.25 (bm, 40H), 0.88 (m, 6H). ^{13}C NMR (100 MHz, $CDCl_3$): δ 172.6, 162.0, 157.9, 154.3, 136.9, 124.0, 121.5, 111.5, 53.43, 46.83, 38.67, 31.91, 31.32, 30.92, 29.95, 29.67, 29.62, 29.54, 29.35, 26.28, 22.69, 14.20, 14.11. HRMS (EI): m/z calcd. for $C_{32}H_{51}NO_2S_2$ (M+H) 546.3395 found 546.3448.

(*E*)-4,4'-bis(2-decyltetradecyl)-[6,6'-bithieno[3,2-*b*]thiophene[3,2-*b*]pyrrolylidene]-5,5'(4*H*,4'*H*)-dione 4.9

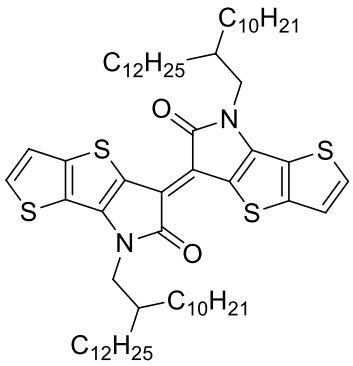

A solution of 4-(2-decyltetradecyl)-4*H*-thieno[3,2-*b*]thiophene[3,2-*b*]pyrrole-5,6-dione **4.8** (0.60g, 1.10 mmol) and Lawesson's reagent (0.11 g, 0.28 mmol) in *o*-

xylene (20 mL) were heated at 60 °C for 2 hours. After cooling to room temperature the solvent was removed by rotary evaporation and the crude product purified by column chromatography on silica (hexane : DCM, 3 : 1) to afford the title compound as a bright green solid (0.37 g, 0.35 mmol, 32 %). ^{1}H NMR (400 MHz, $CDCl_3$): δ 7.52 (d, *J* = 5.2 Hz, 2H), 7.32 (d, *J* = 5.2 Hz, 2H), 3.85 (d, *J* = 7.7 Hz, 4H), 2.04 (m, 2H), 1.24 (bm, 80H), 0.90 (m, 12H). ^{13}C NMR (100 MHz, $CDCl_3$): δ 171.1, 148.4, 143.0, 129.9, 123.6, 121.3, 121.0, 116.4, 77.4, 77.2, 77.0, 76.7, 46.5, 38.7, 32.0, 31.5, 30.0, 29.7, 29.7, 29.6, 29.4, 26.4, 22.7, 14.2. MALDI TOF (LD^{+}) 1059.2, 1060.2, 1061.2.

(*E*)-2,2'-dibromo-4,4'-bis(2-decyltetradecyl)-[6,6'-bithieno[3,2-*b*]thiophene[3,2-*b*]pyrrolylidene]-5,5'(4*H*,4'*H*)-dione 4.10

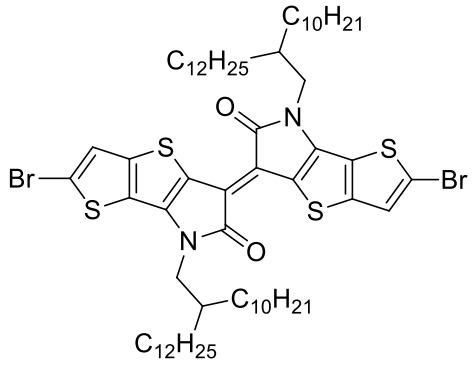

NBS (0.12 g, 0.69 mmol) in THF (2 mL) was added to a stirring solution of (*E*)-4,4'-bis(2-decyltetradecyl)-[6,6'-bithieno[3,2-*b*]thiophene[3,2-*b*]pyrrolylidene]-5,5'(4*H*,4'*H*)-dione **4.9** (0.35 g, 0.33 mmol) in THF (20 mL) at -10 °C. The reaction was monitored by TLC and quenched with water after half an hour, the product was extracted with ethyl acetate and the aqueous layer washed several times with EtOAc. The organic layers were combined, dried over $MgSO_4$ and the solvent removed by rotary evaporation to afford the crude product which was purified by column chromatography on silica (hexane : DCM, 3:1) to afford the title compound as a dark green solid (0.31 g, 0.26 mmol, 77 % yield). ^{1}H NMR (400 MHz, TCE-d_2): δ 7.35 (s, 2H), 3.80 (d, *J* = 7.7 Hz, 4H), 1.96 (m, 2H), 1.27 (bm 80H), 0.93 (m, 12H). ^{13}C NMR (100 MHz, TCE-d_2): δ 170.7, 146.8, 142.5, 123.7, 120.7, 120.5, 117.2, 115.7, 74.3, 74.1, 73.8, 46.7, 38.8, 32.1, 31.6, 30.2, 29.9, 29.7, 29.6, 26.5, 22.9, 14.4. MALDI TOF (LD+): 1218.3, 1220.3, 1221.3.

iITT-BT P11

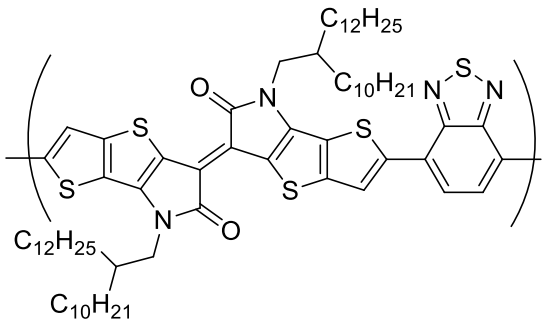

To a microwave vial was added (*E*)-2,2'-dibromo-4,4'-bis(2-decyltetradecyl)-[6,6'-bithieno[3,2-*b*]thiophene[3,2-*b*]pyrrolylidene]-5,5'(4*H*,4'*H*)-dione **4.10** (70 mg, 57 μmol) and 4,7-bis(4,4,5,5-tetramethyl-1,3,2-dioxabrolan-2-yl)benzothiadiazole (22 mg, 57 μmol). A thoroughly degassed solution of Aliquat 336 (2 drops) in toluene (1.5 mL) was subsequently added and the solution was further degassed with stirring for 30 minutes. $Pd(PPh_3)_4$ (3 mg) was added and the solution was again degassed for a 30 minutes. The microwave vial was sealed and heated to 80 °C with stirring before the addition of 2 M K_2CO_3 (aq) (0.3 mL). The biphasic mixture was then heated with vigorous stirring at 120 °C for 3 days. After cooling to room temperature the contents of the microwave vial were poured into vigorously stirring methanol and the resulting polymeric precipitate was filtered into a glass fibre Soxhlet thinble. The filtrate was purified by Soxhlet extraction first in methanol (24 h), acetone (24 h), hexane (24 h) and finally chloroform (24 h). The chloroform fraction was stirred vigorously with aqueous sodium diethyldithiocarbamate at 60 °C for 2 hours to remove any residual catalytic metal impurities, after which the chloroform layer was separated, washed with deionised water and the solvent removed by rotary evaporation. The obtained polymeric material was purified further by recycling GPC in chlorobenzene to afford the title polymer as a dark purple/black solid (56 mg, 71 %).

GPC (chlorobenzene): M_n = 17 kDa, M_w = 27 kDa, PDI = 1.6.

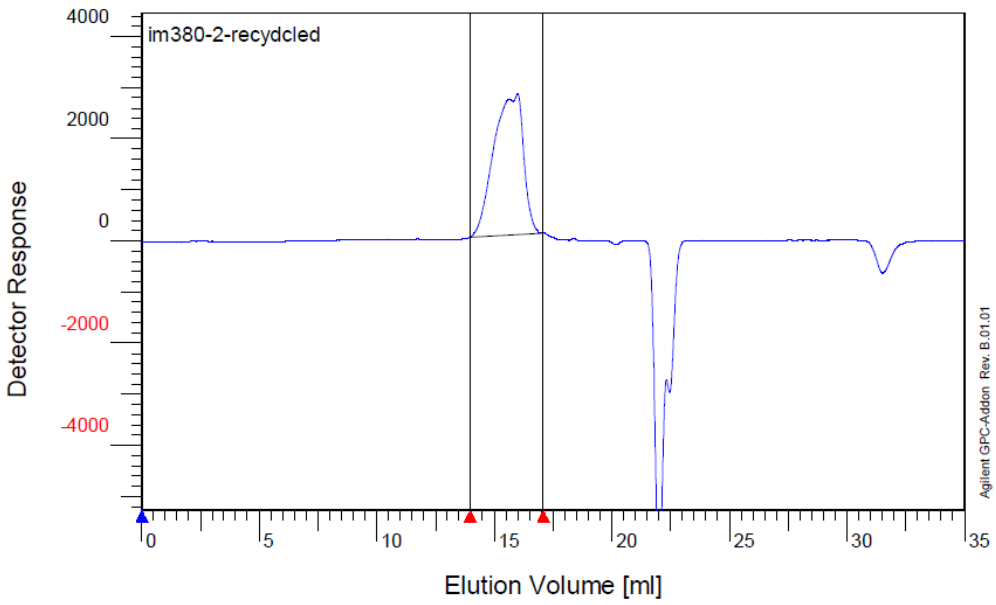

Figur 5.12. GPC trace of polymer **P12** in chlorobenzene at 80 ºC.

iITT-T P12

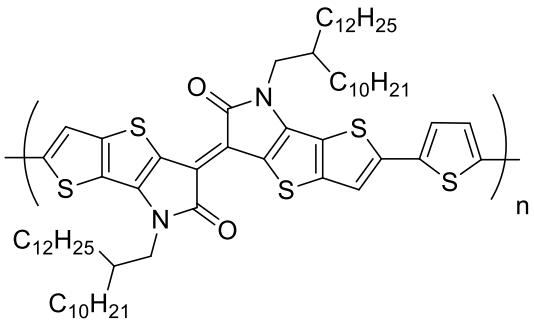

To a microwave vial was added (*E*)-2,2'-dibromo-4,4'-bis(2-decyltetradecyl)-[6,6'-bithieno[3,2-*b*]thiophene[3,2-*b*]pyrrolylidene]-5,5'(4*H*,4'*H*)-dione **4.10** (70 mg, 57 µmol) and 2,5-bis(trimethylstannyl)thiophene (24 mg, 57 µmol) in chlorobenzene (1.0 mL). The solution was thoroughly degassed before the addition of $Pd_2(dba)_3$ (2 mg) and P(*o*Tol)$_3$ (2.5 mg). The solution was further degassed and the microwave vial sealed before heating in a microwave in successive intervals of 5 min at 100 °C, 5 min at 140 °C, 5 min at 160 °C, and finally 20 min at 180 °C. After cooling to room temperature the contents of the microwave vial were poured into vigorously stirred methanol, and the resulting polymeric precipitate was filtered into a glass fibre Soxhlet thimble. The polymeric precipitate was purified by Soxhlet extraction first in

methanol (24 h), acetone (24 h), hexane (24 h), and finally chloroform (24 h). The chloroform fraction was stirred vigorously with aqueous sodium diethyldithiocarbamate at 60 °C for 2 hours to remove any residual catalytic metal impurities, after which the chloroform layer was separated, washed with deionised water and the solvent removed by rotary evaporation. The obtained polymeric material was purified further by recycling GPC in chlorobenzene to afford the title polymer as a deep purple solid (45 mg, 68 %).

GPC (chlorobenzene): M_n = 30 kDa, M_w = 67 kDa, PDI = 2.3.

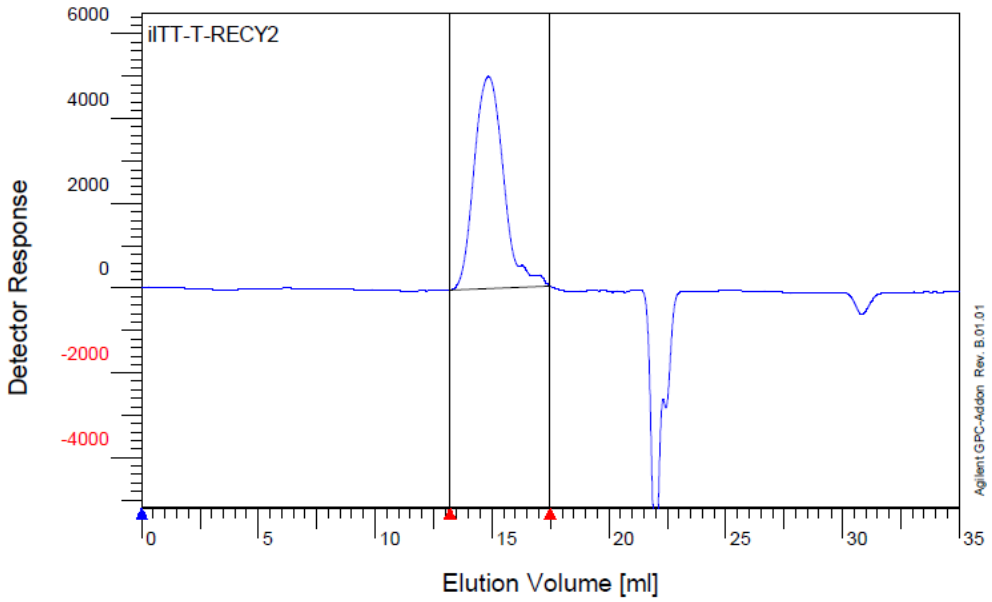

Figure 5.12. GPC trace of polymer **P12** in chlorobenzene at 80 °C.

iITT-2T P13

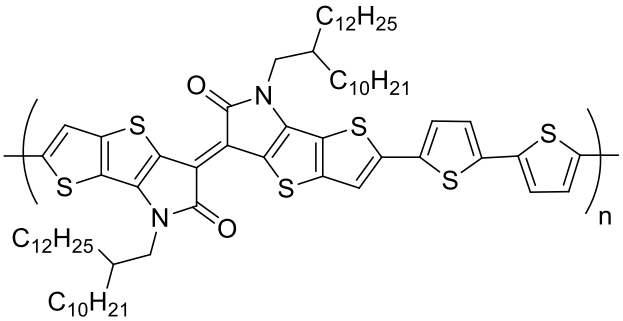

To a microwave vial was added (*E*)-2,2'-dibromo-4,4'-bis(2-decyltetradecyl)-[6,6'-bithieno[3,2-*b*]thiophene[3,2-*b*]pyrrolylidene]-5,5'(4*H*,4'*H*)-dione **4.10** (70 mg, 57

μmol) and 5,5'-bis(trimethylstannyl)-2,2'-bithiophene (28 mg, 57 μmol) in chlorobenzene (1.0 mL). The solution was thoroughly degassed before the addition of $Pd_2(dba)_3$ (2 mg) and P(*o*Tol)$_3$ (2.5 mg). The solution was further degassed and the microwave vial sealed before heating in a microwave in successive intervals of 5 min at 100 °C, 5 min at 140 °C, 5 min at 160 °C and finally 20 min at 180 °C. After cooling to room temperature the contents of the microwave vial were poured into vigorously stirred methanol, and the resulting polymeric precipitate was filtered into a glass fibre Soxhlet thimble. The polymeric precipitate was purified by Soxhlet extraction first in methanol (24 h), acetone (24 h), hexane (24 h) and finally chloroform (24 h). The chloroform fraction was stirred vigorously with aqueous sodium diethyldithiocarbamate at 60 °C for 2 hours to remove any residual catalytic metal impurities, after which the chloroform layer was separated, washed with deionised water and the solvent removed by rotary evaporation. The obtained polymeric material was purified further by recycling GPC in chlorobenzene to afford the title polymer as a deep purple/black solid (50 mg, 72 %).

GPC (chlorobenzene): M_n = 20 kDa, M_w = 41 kDa, PDI = 2.1.

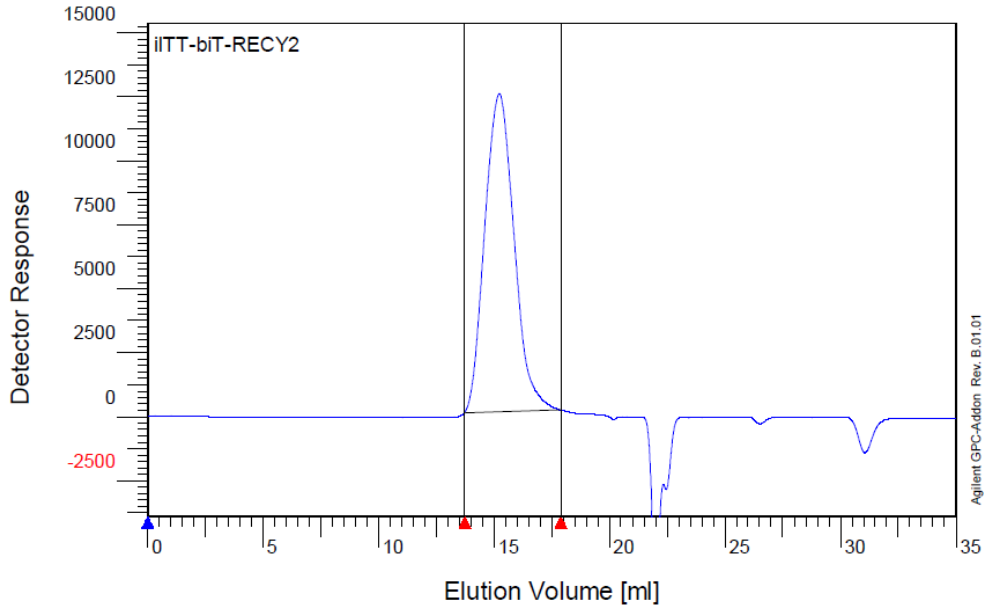

Figure 5.13. GPC trace of polymer **P13** in chlorobenzene at 80 °C.

5.5. References

1. J. Linshoeft, A. C. J. Heinrich, S. A. W. Segler, P. J. Gates and A. Staubitz, *Org. Lett.*, 2012, **14**, 5644–5647.
2. S. Haid, A. Mishra, M. Weil, C. Uhrich, M. Pfeiffer and P. Bäuerle, *Adv. Funct. Mater.*, 2012, **22**, 4322–4333.
3. M. Kaur, D. Seul Yang, J. Shin, T. Wan Lee, K. Choi, M. Ju Cho and D. Hoon Choi, *Chem. Commun.*, 2013, **49**, 5495–5497.
4. M. Zhang, H. N. Tsao, W. Pisula, C. Yang, A. K. Mishra and K. Müllen, *J. Am. Chem. Soc.*, 2007, **129**, 3472–3473.
5. C. Kleeberg, L. Dang, Z. Lin and T. B. Marder, *Angew. Chemie Int. Ed.*, 2009, **48**, 5350–5354.
6. H. Bronstein, Z. Chen, R. S. Ashraf, W. Zhang, J. Du, J. R. Durrant, P. S. Tuladhar, K. Song, S. E. Watkins, Y. Geerts, M. M. Wienk, R. A. J. Janssen, T. Anthopoulos, H. Sirringhaus, M. Heeney and I. McCulloch, *J. Am. Chem. Soc.*, 2011, **133**, 3272–3275.